Metabolic Strategies to Cope with Overcrowding in a *Pseudomonas aeruginosa* Biofilm

Jeanyoung Jo

Submitted in partial fulfillment of the
requirements for the degree of
Doctor of Philosophy
in the Graduate School of Arts and Sciences

COLUMBIA UNIVERSITY

2019

Abstract

Metabolic Strategies to Cope with Overcrowding in a *Pseudomonas aeruginosa* Biofilm

Jeanyoung Jo

Bacteria, while traditionally studied in liquid suspensions, are often found in nature as biofilms, aggregates of cells enclosed in self-produced matrices. Cells in biofilms have a fitness advantage over those that are free-living, as the biofilm lifestyle is correlated with increased resistance to various assaults, including antimicrobials, UV exposure, and dehydration. These biofilm-associated characteristics have important clinical implications, as biofilm-based bacterial infections are a major cause of morbidity in immunocompromised individuals. With this increased resiliency, however, comes a major challenge that arises during biofilm growth: the formation of resource gradients. My thesis work focused on one particular gradient, that of oxygen, which is established in biofilms formed by *Pseudomonas aeruginosa*. This bacterium has multiple mechanisms for coping with limited access to oxygen, including a highly-branched respiratory system for optimal oxygen scavenging and production and utilization of redox-active molecules called phenazines. The purpose of this thesis has been to investigate the different strategies used by *P. aeruginosa* to deal with the oxygen limitation precipitated by the biofilm lifestyle.

In Chapter 1, I will provide the necessary background for understanding the principles of redox balancing, metabolism, respiration, biofilm physiology, and phenazine utilization in *P. aeruginosa*. The work described in Chapter 2 provides evidence for the formation of a novel terminal oxidase complex that plays a biofilm-specific role in *P. aeruginosa* growth. The results in this chapter also suggest that specific terminal oxidase complexes differ in the timing of their contributions to biofilm growth and implicate the novel complex in mediating reduction of phenazines in biofilms.

Chapter 3 expands upon the principle of metabolic versatility exemplified by the results discussed in Chapter 2. The research presented in this chapter looks at how varying the source of electrons that feed into the respiratory chain influences downstream electron transfer steps,

including terminal oxidase activities and phenazine production and utilization. The data presented in Chapters 2 and 3 add to the growing body of evidence that bacterial growth in liquid culture is distinct from that in biofilms and underscores the need for more biofilm-based research that can inform treatment strategies for *P. aeruginosa* infections.

The results described in Chapter 4 take an even broader look at the strategies used by *P. aeruginosa* to sustain efficient metabolism under conditions of potential stress. An important node of central metabolism is pyruvate, which can be transformed in a number of ways. In this chapter, I will consider two pathways of pyruvate metabolism: fermentation to lactate and carboxylation to oxaloacetate. I will present data indicating that a previously-uncharacterized lactate dehydrogenase contributes to *P. aeruginosa* growth under specific growth conditions and that pyruvate carboxylation contributes to optimal progress through central metabolic pathways. I will also describe experiments that characterize the contributions of another carboxylase, previously thought to function as the pyruvate carboxylase, to *P. aeruginosa*'s ability to grow on selected nutrient sources. Finally, I will discuss how redox state informs biofilm formation in a phylogenetically distinct bacterium, *Bacillus subtilis*, highlighting the universality of redox reactions in driving metabolic processes.

In sum, the research presented in this thesis broadens our understanding of the immense respiratory and metabolic flexibility of *P. aeruginosa* and serves as an important reminder of the discrete factors that govern liquid culture and biofilm growth.

Table of Contents

List of Figures

List of Tables

Acknowledgments

I would like to sincerely acknowledge and thank everyone who propelled me throughout my Ph.D. journey.

I would like to express my gratitude for my advisor, Dr. Lars Dietrich. His support and enthusiasm for my project and growth as a scientist were second to none. Furthermore, his support of my desire to achieve and maintain a healthy work-life balance, especially during my maternity leave, was truly generous and appreciated.

I would also like to thank the members of my thesis committee, Drs. Iva Greenwald and Alexander Tzagoloff, who have provided insightful feedback and unwaveringly supported my progress through the Ph.D. program. I also extend a sincere thank you to Drs. Anuradha Janakiraman and Thomas Murray for serving as external members of my thesis committee.

I thank all past and present members of the Dietrich Lab for collectively being an intelligent and caring group of labmates. I thank Dr. Alexa Price-Whelan, who, in addition to providing invaluable feedback on my projects and writings, exemplifies what it means to be a strong woman dedicated to both science and family. I thank Dr. Yu-Cheng Lin, Lisa Kahl, William Cole Cornell, Bryan Wang, and Dr. Hassan Sakhtah for all the shared laughter, food, discussion, and angst. I also remember with love my former labmate and friend, Dr. Chinweike Okegbe, and thank him for deciding not to pursue the CcoN4 story that originated from his screen. Finally, I thank my former mentees Krista Cortez, Rachel Hainline, and Matthew Greenwald for creating the unfair standard against which I will measure all future undergraduates.

I also thank Drs. Valerie Reinke and Aurora Esquela-Kerscher, who supported me at the beginning of my scientific journey and continue to do so to this day.

I thank my husband, Ken, for being a constant source of support, comfort, friendship, and love, and for holding down the home front during the thesis writing process. I thank my beautiful son Theo for helping me to remember what is most important in life. I thank my parents, Hyae Kyung and Won Jo, for raising me to be who I am and for countless other things that cannot be

expressed in words. I thank my sister, Sueyoung, and my brother-in-law, Mark, for their encouragement, often in the form of food and drink.

Finally, I thank God for allowing me this time on earth and for His ever-present grace in my life.

Chapter 1: Introduction

1.1: Balancing life's reactions: The importance of redox homeostasis

Though life, as a concept, is difficult to define, a unique feature that can help us to understand it is homeostasis: a balanced internal condition that persists in spite of changes in the environment. Metabolism is a network of reactions that enables growth while keeping cells in this state of balance. This thesis focuses on pathways of organotrophy and aerobic respiration, in which carbon sources are metabolized to produce energy using oxygen. At one end of this scheme are the carbon sources that feed electrons into the metabolic pathways. At the other end is oxygen, which is reduced upon the final electron transfer step carried out by the terminal oxidase(s). In between the two, the respiratory chain performs a series of coordinated reactions that couple electron transfer to cellular energy generation.

When a carbon source is catabolized, it is oxidized through a series of reactions that generate reduced intracellular intermediates. Electrons released from the oxidation of carbon sources are passed through a series of carriers, each one more electronegative than the last, until they arrive at the terminal electron acceptor. In aerobically respiring organisms, this is molecular oxygen (O_2). The transfer of electrons between the membrane-associated proteins that constitute the respiratory chain is coupled to the pumping of protons across the membrane to generate an electrochemical gradient (also called the proton motive force or Δp), which ultimately drives cellular energy production in the form of adenosine triphosphate (ATP) synthesis. For these reactions to continually proceed, substrates must be regenerated and the cellular redox state must be maintained at a potential that favors catabolism.

Imbalances that disturb cellular redox homeostasis can have harmful consequences for the cell. Our lab studies the various mechanisms through which the clinically-relevant bacterium *Pseudomonas aeruginosa* maintains redox homeostasis and how redox state affects bacterial physiology. We are especially interested in learning more about the mechanisms that underlie redox homeostasis in biofilms, multicellular assemblages of bacteria encased within a self-

produced matrix (Høiby et al. 2011). *P. aeruginosa* exists as biofilms both in nature as well as in clinical environments (Hall-Stoodley, Costerton, and Stoodley 2004; Williams, Zlosnik, and Ryall 2007; Ciofu et al. 2012; Penesyan, Gillings, and Paulsen 2015). The presence of *P. aeruginosa* biofilms in the latter context is a major problem for the treatment of infections caused by this bacterium, as biofilms are more resistant to external stressors, such as antibiotic treatment, than free-living, planktonic cells (Ciofu et al. 2012). However, as cells switch from the planktonic to the biofilm mode of growth, they encounter new challenges they must overcome, perhaps the most notable being the formation of steep nutrient gradients across biofilm depth (Werner et al. 2004). Therefore, a more thorough understanding of the metabolic processes that drive biofilm formation will serve not only to broaden our understanding of the physiology of multicellularity but will also lead to more efficient ways to combat this opportunistic pathogen.

1.2: Fueling the electron transport chain: Carbon sources

P. aeruginosa is a heterotrophic, motile, Gram-negative bacterium known for its metabolic versatility, which allows it to grow under many conditions. One facet of this versatility is seen in its ability to grow on a variety of carbon sources (Stanier, Palleroni, and Doudoroff 1966; Ornston 1971; Wargo 2013). The *P. aeruginosa* genome, already considered quite large for that of a bacterium, encodes a noticeably significant amount of membrane transport systems, about two-thirds of which are involved in nutrient uptake (Stover et al. 2000). Once these substrates are transported into the cell, a multitude of potential pathways exists for their catabolism (**Figure 1.1**). A few key pathways of carbon catabolism are summarized below.

Glucose and other hexoses are broken down via the Entner-Doudoroff pathway, an alternative pathway akin to glycolysis. The Entner-Doudoroff pathway is almost completely restricted to prokaryotes (i.e., bacteria and archaea), and is commonly found among aerobic, Gram-negative bacteria (White, Drummond, and Fuqua 2012). While many bacteria can employ both the Entner-Doudoroff and glycolytic pathways depending on environmental factors, pseudomonads are restricted to the Entner-Doudoroff pathway because they lack two key

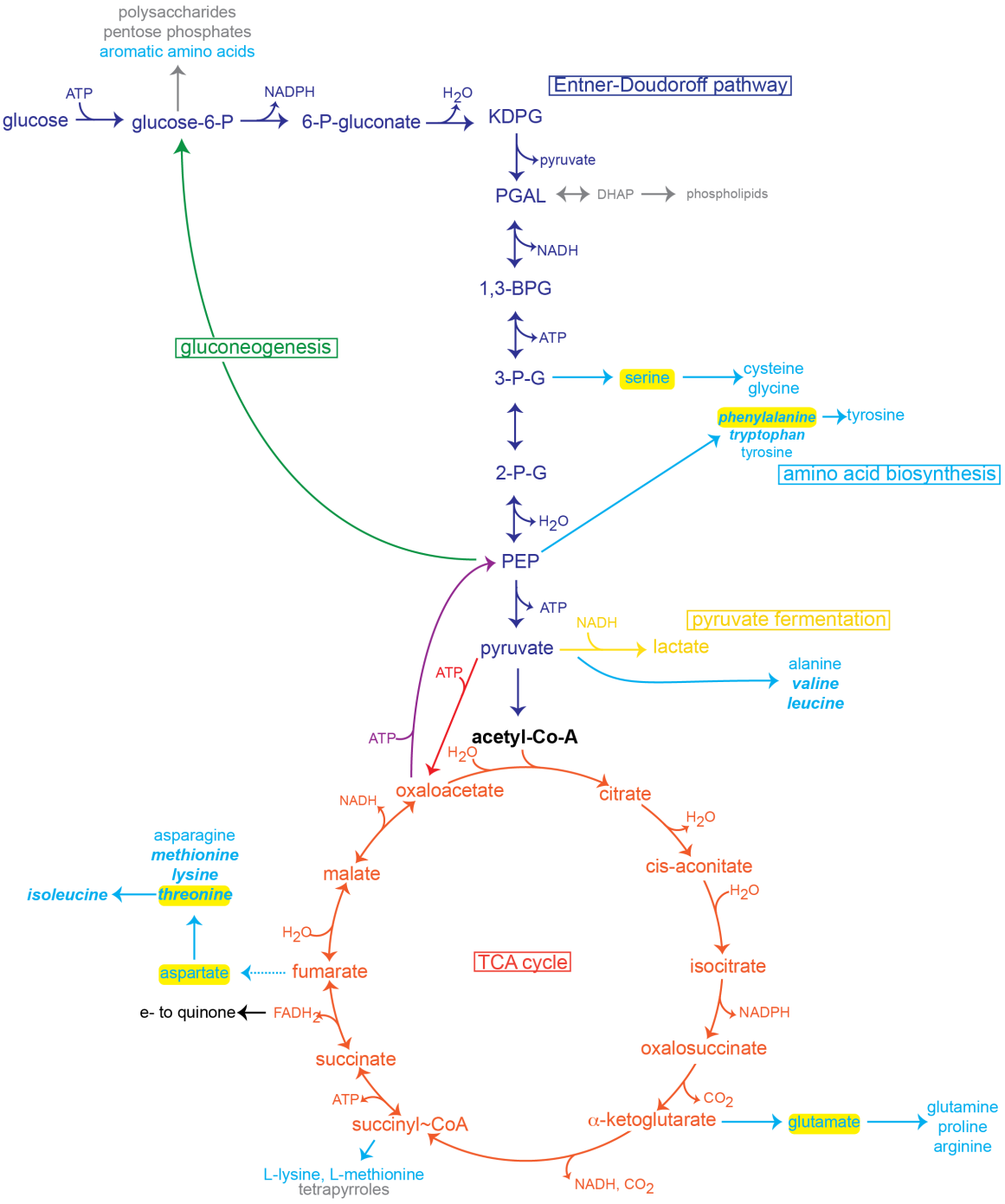

Figure 1.1. An overview of *Pseudomonas aeruginosa* central metabolism. An abridged overview of the central metabolic pathways in *P. aeruginosa*. Dark blue, Entner-Doudoroff pathway; green, gluconeogenesis; orange, tricarboxylic acid (TCA) cycle; purple, generation of phosphoenolpyruvate (PEP); red, pyruvate carboxylation; yellow, pyruvate fermentation; light blue, pathways of amino acid synthesis; gray, anabolic building blocks. Within amino acid synthesis pathways, yellow highlights indicate amino acids that lead to the synthesis of other amino acids while bold and italicized indicate essential amino acids. (Madigan *et al*., 2015, White *et al*., 2012, KEGG Pathway Database (https://www.genome.jp/kegg/pathway.html)).

enzymes necessary to carry out glycolysis. In contrast to glycolysis, which has a net ATP production of two molecules per glucose, the Entner-Doudoroff pathway generates just one net ATP per glucose (White, Drummond, and Fuqua 2012). The enzymes involved in this pathway are produced upon exposure to hexoses, but not in response to three- or four-carbon sugar acids (Ornston 1971) and oxidize glucose to pyruvate. Once pyruvate is generated, it can be oxidized to acetyl-CoA, reduced to lactate, or carboxylated to oxaloacetate (**Figure 1.1**). The fate of pyruvate is determined by the environmental conditions to which the bacterium is exposed.

Under aerobic conditions, pyruvate is usually oxidized to acetyl-CoA, which is further oxidized via the tricarboxylic acid (TCA) cycle (also called the citric acid or Krebs cycle). The TCA cycle begins when acetyl-CoA, together with oxaloacetate, forms the 6-carbon compound citric acid. Through a series of reactions, citric acid is oxidized in a stepwise fashion to ultimately regenerate oxaloacetate, thus fulfilling the "cyclic" nature of the TCA cycle (Madigan et al. 2015; **Figure 1.1**), and producing reduced cofactors and electron carriers such as FADH and NAD(P)H. TCA cycle intermediates serve as precursors for the biosynthesis of amino acids, cytochromes, and fatty acids (Madigan et al. 2015; **Figure 1.1**). It is important that TCA cycle intermediates are constantly replenished so that the cycle can continue to run. This replenishment occurs through a series of anaplerotic reactions, i.e., reactions that generate the intermediates of a metabolic pathway. One of the anaplerotic reactions that replenishes the TCA cycle is mediated by the enzyme pyruvate carboxylase, which is essential for oxaloacetate replenishment when *P. aeruginosa* is growing on a sugar (White, Drummond, and Fuqua 2012; **Figure 1.1**).

As citric acid is oxidized, the electrons released from these reactions are transferred to $NAD(P)^+$ and FAD to generate NAD(P)H and $FADH_2$, respectively. In *P. aeruginosa*, the TCA cycle is the predominant source of reducing power that fuels electron transport (Lee et al. 2015). While various metabolites can influence the cellular redox potential and directly or indirectly donate electrons to the electron transport chain (ETC), NADH participates in numerous

reactions of central metabolism and is the canonical donor to the ETC in textbook models (White, Drummond, and Fuqua 2012; Madigan et al. 2015). It is imperative that NADH is re-oxidized to NAD^+ to enable continual metabolic function. The oxidation of NADH is coupled to ATP synthesis through the ETC, which serves as the major pathway through which NAD^+ is regenerated.

1.3: Dissipating intracellular redox stress: The electron transport chain

1.3.1: Electron carriers

The overall machinery and steps of electron transfer and proton pumping are similar between bacteria and eukaryotes. The respiratory machinery is embedded in the inner membrane of mitochondria in eukaryotes (van der Bliek, Sedensky, and Morgan 2017) and in the cytoplasmic membranes of bacteria (Madigan et al. 2015). Respiratory electron carriers include flavoproteins, quinones, iron-sulfur proteins, and cytochromes, all of which are proteins except for quinones, which are lipids. The protein-based electron carriers contain prosthetic groups, which are the actual sites of electron transfer (White, Drummond, and Fuqua 2012). The prosthetic groups in flavoproteins are flavins, which include flavin adenine dinucleotide (FAD) and flavin mononucleotide (FMN). The prosthetic group in iron-sulfur proteins is the iron-sulfur cluster. The prosthetic group in cytochromes is heme. These electron carriers possess different redox potentials and are arranged such that the electron passes sequentially to carriers with higher potentials until it reaches the molecule with the highest potential, the final electron acceptor.

My main thesis work centered on the physiological role of a cytochrome complex. The heme prosthetic group of cytochromes is made up of four pyrrole rings (hence giving them the classification of tetrapyrroles) joined together through methene bridges (**Figure 1.2**). Each heme contains a centrally-located iron atom that is bound to the nitrogen of each of the four pyrrole rings, and it is this iron that serves as the electron carrier (**Figure 1.2**). Each pyrrole ring can be

modified by a side chain, and the side chains that adorn the pyrrole rings of a heme dictate the heme classification (White, Drummond, and Fuqua 2012).

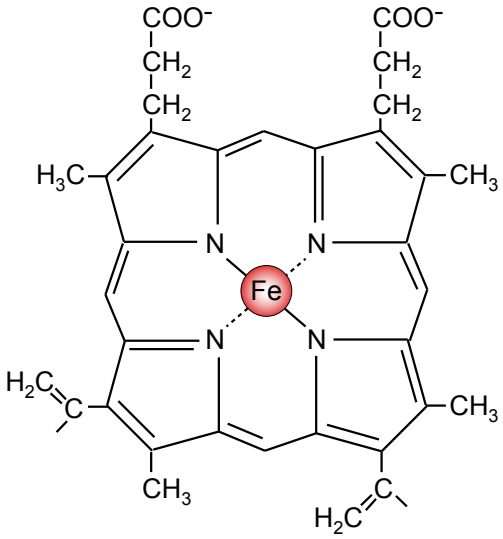

Figure 1.2. General structure of a heme. Heme consists of four pyrrole rings interconnected through methene bridges and a central iron, which is bound to the heme via the nitrogen of each pyrrole ring. The iron atom is the electron carrier; its oxidized form is ferric (Fe(III)) iron while its reduced form is ferrous (Fe(II)) iron.

There are five classes of hemes, and the heme nomenclature is carried over when describing the cytochromes to which they belong: *a*, *b*, *c*, *d*, and *o*. Hemes *d* and *o* have currently only been found in bacterial cytochromes (White, Drummond, and Fuqua 2012). Because hemes are classified by their decorating side chains, they typically show distinguishing spectrophotometric curves. A cytochrome's characteristic peak wavelength is often incorporated into its name, particularly for cytochromes from eukaryotes (i.e., cytochrome b_{556}, which is a cytochrome containing a *b*-type heme that shows a peak at 556 nm). Occasionally, the name of a cytochrome will bear a subscript 3, which indicates the O_2-binding heme (White, Drummond, and Fuqua 2012; Cramer and Kallas 2016). For example, the mitochondrial terminal oxidase (to be discussed further below) is called cytochrome aa_3; the name of this cytochrome tells us that it contains two *a*-type hemes, with the second being the one that binds O_2. Sometimes

cytochrome names contain a prime (‘) annotation, which also denotes the heme that is likely to bind O_2 (Cramer and Kallas 2016).

1.3.2: Electron transfer through the ETC

Here, I will provide a general overview of the steps of the aerobic respiratory chains that function in mitochondria (**Figure 1.3**) and pseudomonads (**Figure 1.4**). Electrons primarily enter the ETC at the NADH dehydrogenase (called Complex I in eukaryotes). The electron released by the oxidation of NADH is transferred to ubiquinone, a molecule in the membrane. This redox reaction is coupled to the translocation of protons across the membrane and contributes to the formation of a proton gradient. Succinate dehydrogenase (Complex II in eukaryotes) also reduces ubiquinone by oxidizing succinate, a TCA cycle intermediate. This electron transfer step serves as a direct link between the TCA cycle and the respiratory chain. The hydrophobic nature of ubiquinone allows it to shuttle electrons from the dehydrogenases to the next electron carrier, the cytochrome bc_1 complex (Complex III) (Madigan et al. 2015; van der Bliek, Sedensky, and Morgan 2017). This complex then passes electrons to another mobile electron carrier, cytochrome *c*, which delivers electrons to O_2 via the activity of the terminal oxidase (Complex IV). The redox reactions catalyzed by the bc_1 complex and the terminal oxidase are both coupled to proton translocation across the membrane. The resulting proton gradient is used to power ATP production by the ATP synthase (ATPase; or Complex V) (Madigan et al. 2015).

1.3.3: The implications of a branched ETC

Eukaryotes have a relatively straightforward electron transport chain (**Figure 1.3**), and the mitochondrial electron transfer pathways are generally invariable across the domain. Bacterial respiratory pathways are often more branched than those of eukaryotes (Poole and Cook 2000; White, Drummond, and Fuqua 2012). Across the bacterial domain, there is more flexibility in terms of the substrates that can be used as electron donors and acceptors in the respiratory chain (White, Drummond, and Fuqua 2012). Furthermore, bacterial respiratory

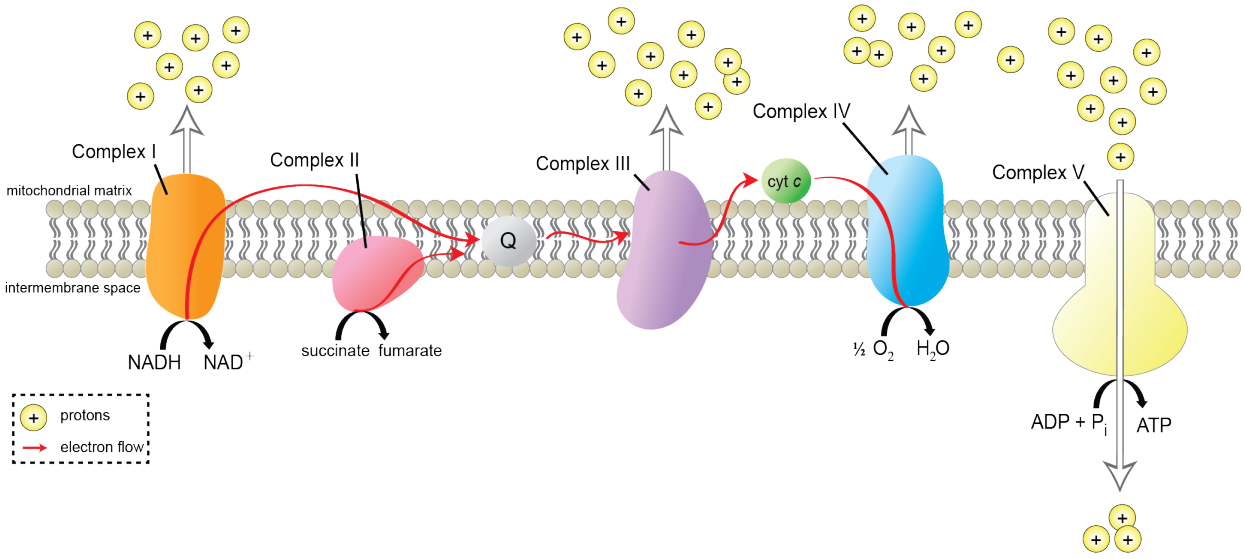

Figure 1.3. Mitochondrial electron transport chain. Electrons enter the electron transport chain (ETC) at Complexes I (orange) or II (pink), the primary dehydrogenases, which then reduce ubiquinone (Q). Q is oxidized by Complex III (the bc_1 complex; purple) which is in turn oxidized by the mobile electron carrier cytochrome *c* (green). Cytochrome *c* donates electrons to Complex IV (the terminal oxidase; blue), which delivers electrons to their final destination, O_2. Complexes I, III, and IV contribute to the generation of a proton gradient (Δp), which is used by Complex V (ATP synthase; yellow) to generate energy in the form of ATP.

chains exhibit more redundancy along various steps of the electron transfer pathways, with multiple iterations of a protein complex existing to catalyze a particular step in the pathway (Poole and Cook 2000; Williams, Zlosnik, and Ryall 2007; Hirai et al. 2016; Jo et al. 2017). These branch points are often influenced by external factors, such that bacterial respiratory chains can be modulated in response to environmental conditions. This provides bacteria with more metabolic versatility, as they are able to adapt their respiratory chains to be the most optimal for specific conditions. For example, the respiratory system of *Escherichia coli* can terminate at one of two terminal oxidases: an energetically favorable but low-O_2-affinity terminal oxidase, "Bo_3", is used when O_2 is abundant while a less energetically favorable but high-O_2-affinity terminal oxidase, "Bd", is used when O_2 is scarce (Williams, Zlosnik, and Ryall 2007).

Our lab's model organism, *P. aeruginosa*, is well-known for its ability to thrive under conditions of low O_2 (Comolli and Donohue 2004; Alvarez-Ortega and Harwood 2007; Williams, Zlosnik, and Ryall 2007; Arai 2011). Not coincidentally, it has even more versatility at the terminal end of the respiratory chain than *E. coli* (Williams, Zlosnik, and Ryall 2007). *P.*

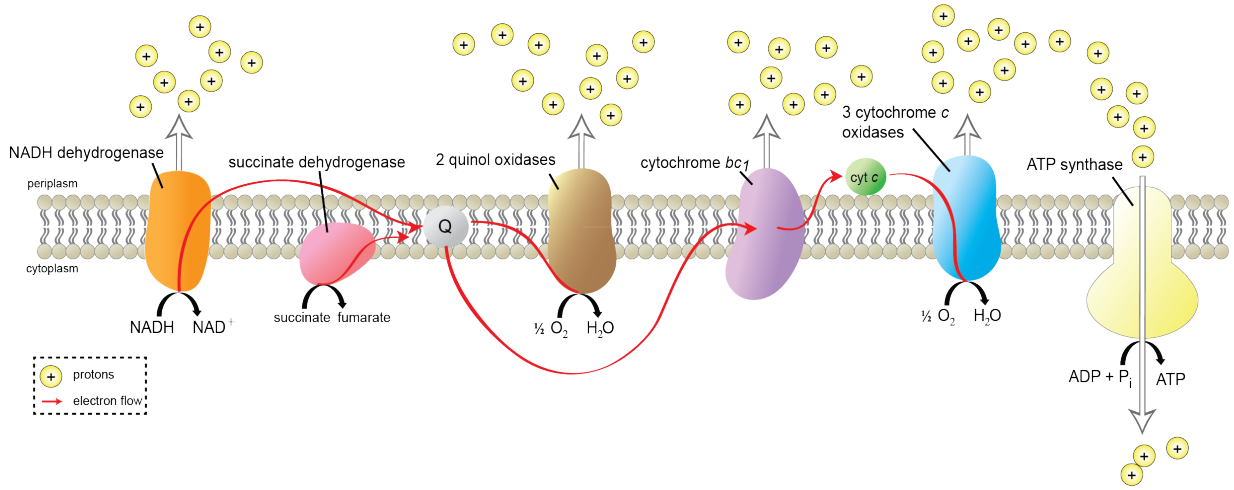

Figure 1.4. *P. aeruginosa* electron transport chain. Electrons enter the electron transport chain (ETC) at the NADH (orange) or succinate (pink) dehydrogenases, which then reduce ubiquinone (Q). Q can be oxidized by quinol oxidases (brown) or the bc_1 complex, the latter of which is oxidized by the mobile electron carrier cytochrome *c* (green). *P. aeruginosa* encodes two quinol oxidases, Bo_3 and Cio. Cytochrome *c* reduces one of three cytochrome *c* oxidases (blue), Aa_3, Cco1, or Cco2. The quinol and cytochrome *c* oxidases are terminal oxidases that deliver electrons to their final destination, O_2. Electron transfer steps mediated by the NADH dehydrogenase, the bc_1 complex, and the terminal oxidases contribute to the generation of a proton gradient (Δp), which is used by ATP synthase (yellow) to generate energy in the form of ATP.

aeruginosa's ability to dominate in microaerobic environments is largely due to its arsenal of five terminal oxidases (**Figure 1.4**), all of which differ in expression patterns, environmental sensitivities, and O_2 affinity (Alvarez-Ortega and Harwood 2007; Kawakami et al. 2010; Hirai et al. 2016)). A more in-depth description of these terminal oxidases will follow in the next section.

1.3.4: P. aeruginosa *colony biofilms as a model system*

We use *P. aeruginosa* colony biofilms as a model to study how resource limitation affects the redox homeostasis of cells in densely-packed aggregates. By placing a 10-µl spot of cells onto an agar plate and monitoring community development, we are able to investigate how *P. aeruginosa* cells coordinate to form elaborate architectures over time. Our lab has shown that O_2 availability plays a crucial role in driving biofilm morphogenesis. While the details of redox balancing in biofilms will be discussed further later in this chapter, it is important to note that as biofilms develop (and grow thicker), O_2 is consumed rather rapidly within the biofilm, with no O_2

detected below a depth of ~75-80 μm from the surface (Dietrich et al. 2013; Jo et al. 2017). Biofilms are fully oxic during early stages of development; however, as they grow thicker, they develop a considerable anoxic zone such that cells positioned further into the colony have less access to O_2 than cells at the periphery (Jo et al. 2017; Chapter 2).

Limited access to O_2, the terminal electron acceptor, poses a problem to the biofilm because this compromises the ETC's ability to dissipate the accumulated reducing power that is created during metabolism. This is quantifiable and manifests as an increased intracellular NADH/NAD^+ ratio as biofilms develop (Dietrich et al. 2013). Once the biofilm's NADH/NAD^+ ratio reaches a tipping point, cells within the biofilm will coordinate and begin to wrinkle their surface, thereby increasing their access to O_2. This wrinkling coincides with a drop in NADH/NAD^+ ratios back down to levels during early development (Dietrich et al. 2013). Therefore, access to O_2 is directly related to intracellular redox state and *P. aeruginosa* has a variety of mechanisms through which they maximize their access to O_2, one of which is a large complement of terminal oxidases.

1.3.5: The terminal oxidases of P. aeruginosa

This section is adapted from:
Jo, J, Price-Whelan, A, Dietrich, LEP (2014). An aerobic exercise: Defining the roles of *Pseudomonas aeruginosa* terminal oxidases. *J Bacteriol* 196, 4203-4205.

In 2014, I co-authored a commentary article in the *Journal of Bacteriology* about the terminal oxidases of *P. aeruginosa*. This commentary was written as a companion piece to a study published in the same issue that elucidated the efficiencies of the respiratory chain terminated by each of these oxidases and determined their affinities for O_2. This section is a modified version of that commentary piece, the published version of which is included as an appendix to my thesis.

P. aeruginosa is an exceptionally metabolically versatile organism, and the presence of an ETC terminating at five different oxidases is but one aspect of this adaptability (**Figure 1.5**). The mitochondrial respiratory chain terminates at the Aa_3 (or Cox) complex, which accepts electrons from cytochrome *c* and is therefore referred to as a cytochrome *c* oxidase. *P. aeruginosa* encodes an Aa_3 oxidase as well as two more cytochrome *c* oxidases, Cco1 and

Cco2. Furthermore, it contains two terminal oxidases, Bo_3 and Cio, that receive their electrons directly from the ubiquinone pool and, as such, are called (ubi)quinol oxidases (Williams, Zlosnik, and Ryall 2007).

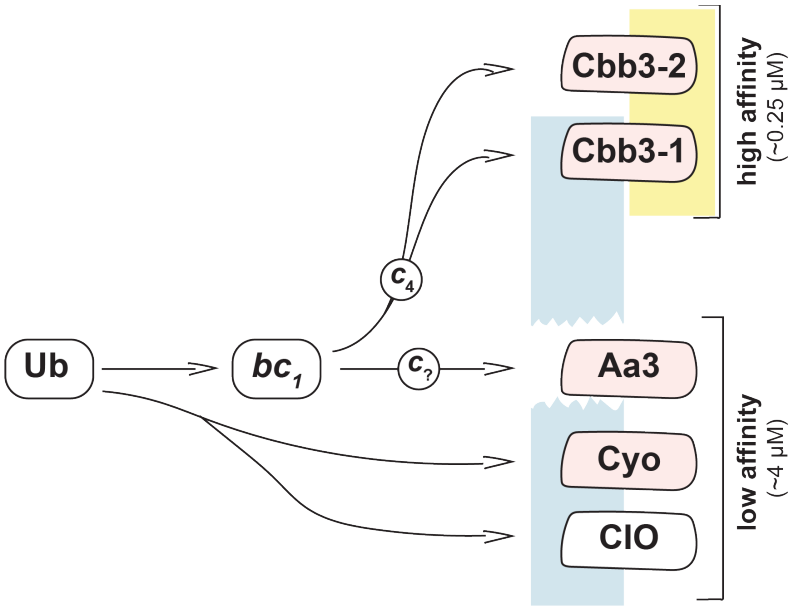

The *P. aeruginosa* membrane-bound electron transport chain can employ five different oxygen reductases. Ubiquinone (Ub) is reduced by a dehydrogenase (not shown) and acts as the electron donor for the cytochrome bc_1 complex, Cyo, or CIO. The cytochrome bc_1 complex reduces a *c*-type cytochrome, which then acts as the electron donor for Aa_3, Cbb_3-1 (or Cco1), or Cbb_3-2 (or Cco2). Heme-copper oxidases are represented by pink shapes. Oxidases that support growth better under microaerobic conditions are shaded yellow, while those that support growth better under typical conditions are shaded blue. These roles are influenced by intrinsic chemical properties and expression levels of the individual complexes. Approximate affinities for oxygen (K_m Values obtained amperometrically) are shown.

A diverse collection of terminal oxidases may be especially important for an organism that has a proficiency for persisting in biofilms, which are characterized by the formation of steep O_2 gradients (Xu et al. 1998; Werner et al. 2004; Wessel et al. 2014) *P. aeruginosa*'s five terminal oxidases have varying proton-pumping efficiencies, affinities for O_2 (Arai et al. 2014), and are expressed in response to different environmental factors (Comolli and Donohue 2004; Alvarez-Ortega and Harwood 2007; Kawakami et al. 2010; Arai et al. 2014). These divergent characteristics allow *P. aeruginosa* to thrive under many different conditions and contribute to its overall success as a ubiquitously-found bacterium.

The Bo_3 terminal oxidase (which is sometimes referred to as Cyo) has mostly been characterized in *E. coli*, which uses this low-O_2-affinity enzyme to grow under highly aerobic conditions (D'Mello, Hill, and Poole 1995). Arai and colleagues confirmed that this enzyme is also a low affinity enzyme in *P. aeruginosa* (K_m = 3.2 μM; Arai et al. 2014) whose expression is upregulated specifically in response to iron starvation (Kawakami et al. 2010). Because its overall expression is very low, Bo_3 is not expected to contribute significantly to *P. aeruginosa* growth under laboratory conditions (Kawakami et al. 2010; Arai 2011).

Cio, or the cyanide insensitive oxidase, is the only copper-free terminal oxidase in *P. aeruginosa*. It is encoded by a two-gene operon bearing high sequence homology (at both the DNA and amino acid levels) to the *E. coli bd* quinol oxidases (Cunningham, Pitt, and Williams 1997) and for this reason the *P. aeruginosa* Cio is often referred to as a *bd*-type quinol oxidase. However, spectral studies have not detected cytochrome *d* in *P. aeruginosa*, so Cio is believed to belong to an atypical subfamily of *bd*-type quinol oxidases with an altered heme composition (Cunningham, Pitt, and Williams 1997). *E. coli*'s *bd* oxidases are known for their high O_2 affinity and expression under microaerobic growth conditions (Cunningham, Pitt, and Williams 1997; Williams, Zlosnik, and Ryall 2007). *P. aeruginosa*'s Cio has also been demonstrated to be important for microaerobic growth in both liquid cultures and biofilms (Alvarez-Ortega and Harwood 2007) and therefore had also been assumed to have a high affinity for O_2. However, more recent work measuring the affinities of *P. aeruginosa*'s terminal oxidases surprisingly showed that Cio is a low-affinity enzyme (K_m = 4 μM; Arai et al. 2014).

As its name implies, Cio is also resistant to cyanide, a virulence factor that *P. aeruginosa* produces during early stationary phase (Blumer and Haas 2000). Micromolar concentrations of cyanide inhibit complexes belonging to the heme copper oxidase (HCO) superfamily (Blumer and Haas 2000), which includes the Aa_3, Bo_3, and Cco oxidases produced by *P. aeruginosa*, and cyanide has been detected in stationary-phase *P. aeruginosa* cultures at 300-500 μM (Lenney and Gilchrist 2011). *P. aeruginosa* mutants lacking the genes encoding Cio are less resistant to cyanide (Comolli and Donohue 2002). Furthermore, transcriptional reporters have

shown *cio* to be upregulated by cyanide (Comolli and Donohue 2002) and low O_2 concentrations (Alvarez-Ortega and Harwood 2007).

The *P. aeruginosa* Aa_3 terminal oxidase, while phylogenetically related to the mitochondrial terminal oxidase, does not seem to play a significant role in supporting *P. aeruginosa* growth under normal laboratory conditions, as it is not expressed at high levels in cultures grown aerobically in a nutrient-rich medium (Kawakami et al. 2010). This is in contrast to many bacteria that *do* utilize Aa_3 for growth, including *Bacillus subtilis* and *P. denitrificans* (Arai 2011). *P. aeruginosa* Aa_3, on the other hand, is upregulated in response to nutrient limitation, specifically carbon, nitrogen, or iron starvation (Kawakami et al. 2010) and has been shown to be regulated by the sigma factor RpoS (Schuster et al. 2004). Bacterial sigma factors are positive regulators of transcription that can have regulons containing dozens to hundreds of genes (Schulz et al. 2015). RpoS is one such regulator that is active at the onset of stationary phase (Potvin, Sanschagrin, and Levesque 2008). That the genes encoding the Aa_3 oxidase are upregulated by RpoS, then, is in line with observations that their expression is increased when nutrients are limited, as is often the case in stationary phase (Madigan et al. 2015).

The final two terminal oxidases, Cco1 and Cco2, are both members of the family of cbb_3 cytochrome *c* oxidases. cbb_3-type oxidases are exclusively found in bacteria and are known for their very high affinities for O_2 (Pitcher and Watmough 2004). Because of their O_2 affinity, these enzymes tend to be induced under hypoxic conditions. The *P. aeruginosa* Cco's indeed are high affinity enzymes, with K_m values that are an order of magnitude lower than those of Bo_3, Cio, and Aa_3 (nanomolar vs. micromolar, respectively; Arai et al. 2014). Consistent with this, Cco2 is regulated by Anr, a transcription factor that regulates gene expression at the shift from aerobic to microaerobic conditions (Ray and Williams 1997; Comolli and Donohue 2004). However, Cco1 is constitutively expressed by *P. aeruginosa*, even under high aeration conditions (Comolli and Donohue 2004). The Cco's have been demonstrated to be the predominant enzymes that support *P. aeruginosa* growth under normal laboratory conditions, with Cco1 being sufficient to support wild-type (WT) levels of growth under aerobic conditions and either Cco1 or Cco2 able

to support WT levels of growth under microaerobic conditions (Arai et al. 2014; Jo et al. 2017). A more detailed look at the functional redundancy of Cco1 and Cco2, as well as their roles in biofilm development, will follow in Chapter 2.

1.4: Other strategies for redox balancing

In addition to its branched aerobic respiratory chain, *P. aeruginosa* possesses alternative metabolic pathways that can function to balance the intracellular redox state and generate ATP. These include anaerobic respiration (through denitrification) and fermentation.

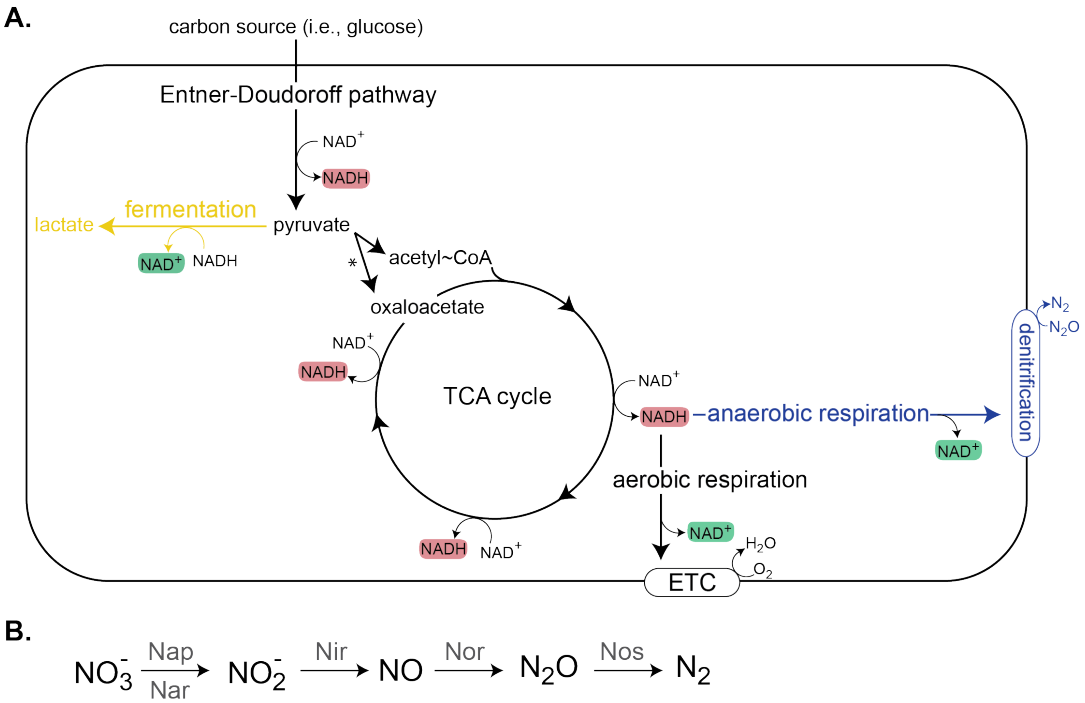

Figure 1.6. *P. aeruginosa* denitrification and pyruvate fermentation pathways. (A) The denitrification (blue) and pyruvate fermentation (yellow) pathways as they fit into overall *P. aeruginosa* metabolism. Red shaded boxes indicate steps in which the reduced intermediate NADH is formed; green shaded boxes indicate steps in which NADH can be re-oxidized to NAD^+. Asterisk (*) refers to the anaplerotic step of pyruvate carboxylation, further discussed in Chapter 4 (section 4.2). **(B)** The stepwise reduction of nitrate (NO_3) to molecular nitrogen (N_2) via denitrification.

1.4.1: Denitrification

Denitrification is the process by which nitrate (NO_3) is reduced to molecular nitrogen (N_2) via the intermediates nitrite, nitric oxide, and nitrous oxide (**Figure 1.6**; Zumft 1997; Williams,

Zlosnik, and Ryall 2007). Most components of the anaerobic respiratory pathway are the same between aerobic respiration and denitrification (Williams, Zlosnik, and Ryall 2007); as such, denitrification is also coupled to the generation of a proton gradient for ATP production. As in aerobic respiration, electrons from NADH pass to the quinone pool, which can then pass electrons directly to terminal reductases or to the bc_1 complex, the latter of which can also donate electrons to terminal reductases. The denitrification pathways of *P. aeruginosa* are physiologically relevant for hypoxic and anoxic environments, which will be touched upon briefly in sections 1.5 and 1.6; however, because denitrification is outside the scope of my thesis, I will not discuss it further here.

1.4.2: Fermentation

Under anoxic conditions, *P. aeruginosa* is able to grow or survive using fermentation of arginine or pyruvate, respectively (Williams, Zlosnik, and Ryall 2007; **Figure 1.6**). Arginine fermentation requires a complex growth medium and yields modest levels of growth. Pyruvate fermentation produces lactate and generates enough energy to support anaerobic survival (Williams, Zlosnik, and Ryall 2007; Glasser, Kern, and Newman 2014; Lin et al. 2018). The contribution of pyruvate fermentation to *P. aeruginosa* physiology will be further discussed in Chapter 4 (section 4.1).

1.4.3: Phenazine reduction: Extracellular electron transfer

The previous sections have described the immense versatility found within central metabolic pathways of *P. aeruginosa*. By modulating flux through these pathways in response to environmental conditions, *P. aeruginosa* can maintain a balanced intracellular redox state. Another strategy that can be employed by this bacterium to deal with redox stress is the production and utilization of phenazines. Phenazines are endogenous secondary metabolites that were traditionally considered to be antibiotics, toxic to competing bacteria in the environment (Chin-A-Woeng and Bloemberg 2003). More recently, the redox-active quality of

phenazines has been credited for helping *P. aeruginosa* thrive in environments in which iron (Wang and Newman 2008) or O_2 (Price-Whelan, Dietrich, and Newman 2007; Wang, Kern, and Newman 2010; Dietrich et al. 2013) are limiting.

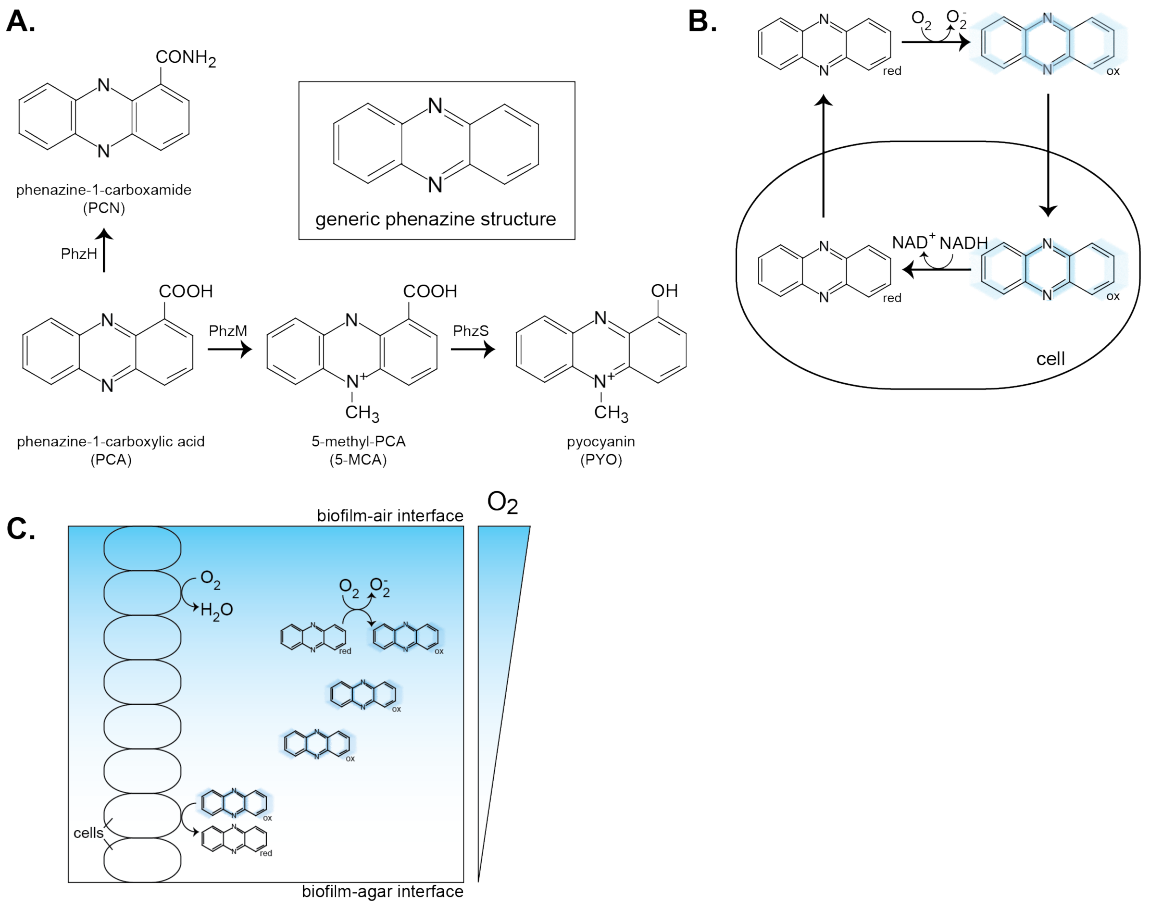

Figure 1.7. Electron shuttling by phenazines. (A) The phenazine biosynthetic pathway starts with the precursor phenazine, phenazine-1-carboxylic acid (PCA). PhzH converts PCA to phenazine-1-carboxamide (PCN), PhzM converts PCA to 5-methyl-PCA (5-Me-PCA), PhzS converts 5-Me-PCA to pyocyanin (PYO). **(B)** Phenazines are reduced (red) intracellularly and are transported out of the cell, where they are oxidized (ox) by extracellular oxidants such as O_2. These oxidized phenazines can then be transported back into cell where they can oxidize NADH to NAD^+. **(C)** A model for phenazine-mediated redox balancing in *P. aeruginosa* colony biofilms. Cells closer to the biofilm-air interface can use O_2 as a terminal electron acceptor while cells near the biofilm-agar interface cannot. Oxidized phenazines originating from the oxic zones of the biofilm are able to accept electrons from cells in the anoxic zones, thereby allowing these cells to dissipate intracellular redox state in the absence of oxygen.

The phenazine biosynthetic pathway in *P. aeruginosa* begins with the conversion of chorismate to phenazine-1-carboxylic acid (PCA), the precursor phenazine, by the redundant operons *phzA1-G1* (*phz1*) and *phzA2-G2* (*phz2*) (Recinos et al. 2012). PCA can then be

modified by several phenazine biosynthetic enzymes to yield the derivatives phenazine-1-carboxamide (PCN), 5-methyl-PCA (5-Me-PCA), and pyocanin (PYO) (**Figure 1.7A**). These phenazine derivatives possess differing redox potentials that contribute to their varying specificities toward different oxidants (Wang and Newman 2008; Wang, Kern, and Newman 2010).

Phenazines, through their redox-activity, play a role in iron acquisition. Iron is often found in the insolube Fe(III) form in aerobic environments (Wang and Newman 2008), posing a problem for organisms needing this substrate for growth. *P. aeruginosa* is able to overcome this obstacle by using phenazines to reduce Fe(III) to the soluble and bioavailable form, Fe(II) (Hernandez, Kappler, and Newman 2004).

Phenazines also support *P. aeruginosa* growth under conditions of O_2 limitation. Previous work from our group has shown that the methylated phenazines, specifically 5-Me-PCA, are the primary contributors to redox balancing in *P. aeruginosa* colony biofilms (Sakhtah et al. 2016), where O_2 availability decreases with depth. A mutant unable to synthesize phenazines, Δ*phz* (in which both *phz1* and *phz2* operons are deleted), displays a significant biofilm phenotype relative to the WT, such that it is unable to maintain an anoxic zone. Intracellular NADH/NAD^+ measurements have shown that the Δ*phz* mutant experiences redox stress, in the form of accumulated reducing equivalents, earlier than the WT. This redox stress correlates with decreased O_2 concentration and is ameliorated by an earlier onset of wrinkling (Price-Whelan, Dietrich, and Newman 2007; Dietrich et al. 2013). In addition to wrinkling earlier, Δ*phz* biofilms are much thinner and form higher ridges (wrinkles) than those formed by the WT, and these features serve to keep Δ*phz* biofilms fully aerobic throughout development. Additionally, phenazines have been shown to support anaerobic survival of *P. aeruginosa* (Wang, Kern, and Newman 2010) and to enhance energy generation during pyruvate fermentation (Glasser, Kern, and Newman 2014). Phenazines are reduced intracellularly and in turn react with oxidants (such as O_2 and Fe(III)) outside the cell (Wang and Newman 2008;

Figure 1.7B). This “electron shuttling” by phenazines helps to alleviate redox stress in cells with limited access to O_2 (**Figure 1.7C**).

Additionally, the production of pyocyanin (PYO), another methylated phenazine, by *P. aeruginosa* has been linked to virulence in mice (Lau et al. 2004). Phenazines have been detected in sputum samples of patients with respiratory illnesses (Wilson et al. 1988), and their presence is negatively correlated with lung function (Hunter et al. 2012). Furthermore, as with most cellular pathways in *P. aeruginosa*, phenazine production has been shown to be sensitive to environmental conditions, including carbon source (van Rij et al. 2004; Huang et al. 2012; Bosire, Blank, and Rosenbaum 2016).

1.5: The implications of metabolic versatility on *P. aeruginosa*’s impact as a clinically-relevant pathogen

P. aeruginosa’s metabolic versatility undoubtedly contributes to the bacterium’s ability to thrive in diverse environments, one being the human host. *P. aeruginosa* is the leading cause of morbidity and mortality in patients with the genetic disease cystic fibrosis (CF), with about 80% of afflicted individuals suffering from chronic infections in their lungs (Williams and Davies 2012). The underlying cause of CF is a mutation in the gene encoding a chloride channel, the CF transmembrane conductance regulator (CFTR), which results in abnormal ion transport across epithelial membranes (Williams, Zlosnik, and Ryall 2007; Conway and Cohen 2015). This leads to the formation of a dehydrated layer on epithelial cells, including those of the gastrointestinal and pulmonary systems, and increased mucus viscosity (Murray, Egan, and Kazmierczak 2007; Williams, Zlosnik, and Ryall 2007). This viscous mucus, or sputum, is resistant to normal bodily clearing and provides a breeding ground for bacteria.

The mucus of the CF lung is a heterogeneous environment, with different metabolites, O_2 availabilities, and antibiotic concentrations present along the airway (Ciofu et al. 2012; Cowley et al. 2015). Normal pulmonary mucus consists of water, salts, mucins, and surfactants; mucins are glycoprotein components of mucus that contribute to its gel-like consistency and

surfactants function in facilitating gas exchange across the mucosal layer (Conway and Cohen 2015). In CF sputum, these components are present at altered levels and additional molecules normally absent in healthy sputum are detected. These points will be elaborated upon in Chapter 4 (section 4.1).

Although the environmental conditions of the CF lung are quite varied, *P. aeruginosa* is consistently one of the most commonly-found pathogenic bacteria colonizing CF sputum. This is perhaps unsurprising given the metabolic versatility described above; its abilities to utilize diverse substrates as energy sources and scavenge small amounts of available O_2 may allow *P. aeruginosa* to flourish in these conditions. Virtually all CF patients are prone to *P. aeruginosa* infections and disease prognosis significantly worsens when these infections become chronic and establish as biofilms (Høiby et al. 2011; Williams and Davies 2012; Ciofu et al. 2012).

In the CF lung environment, *P. aeruginosa* also produces various virulence factors, some of which can at once kill competing cells (including those of the host as well as other invading bacteria) while benefiting their producer. These include phenazines, which have been detected in the sputum of CF patients (Wilson et al. 1988). Another virulence factor released by *P. aeruginosa* is cyanide, which, as previously mentioned, inhibits the activity of heme-copper terminal oxidases and has been detected in CF sputum (Ryall et al. 2008; Sanderson et al. 2008). *P. aeruginosa*'s Cio terminal oxidase allows it to grow even when cyanide is present in its surrounding environment, but any competing cells that do not encode a cyanide-insensitive oxidase will be sensitive to killing by this respiratory toxin. Detection of both phenazines and cyanide in sputum samples has been correlated with the presence of chronic *P. aeruginosa* infection in patients as well as compromised lung function (Hunter et al. 2012; Ryall et al. 2008; Sanderson et al. 2008).

1.6: Biofilms in chronic lung infections

Another major factor contributing to pathogenesis is *P. aeruginosa*'s ability to form robust biofilms. Biofilms are multicellular assemblages of bacteria encased within a self-produced

matrix composed of extracellular DNA, proteins, and polysaccharides (Høiby et al. 2011). As previously mentioned, the formation of an O_2 gradient presents an obstacle for cells growing in biofilms. As a consequence of both O_2 diffusion into the biofilm and O_2 consumption by resident cells, cells found deeper within the biofilm have less access to O_2 than those at the periphery (Werner et al. 2004). This leads to metabolic heterogeneity along the O_2 gradient (Ciofu et al. 2012), with cells in each microenvironment tuned to maximize energy generation/conservation in their specific set of conditions (Williams, Zlosnik, and Ryall 2007; Poole and Cook 2000).

Despite the inherent challenges of the biofilm lifestyle, this is the primary mode of bacterial growth in nature and in a host (Høiby et al. 2011; Penesyan, Gillings, and Paulsen 2015), likely because cells within biofilms are afforded more protection against outside stresses such as antibiotics. Indeed, the biofilm lifestyle is primarily to blame for the failure of antibiotic treatments in CF patients (Ciofu et al. 2012) and the establishment of chronic infections (Høiby et al. 2011). *P. aeruginosa* biofilms in diseased lungs are often characterized by higher mutation rates and exhibit genetic modifications with conferred phenotypes that include increased matrix production and antibiotic resistance (Williams and Davies 2012). Because sublethal concentrations of antibiotics have been shown to increase mutation rates in *P. aeruginosa* (Nair et al. 2013), the fact that biofilm cells are even more resistant to antibiotics poses a major obstacle in the quest to find new drugs that can effectively kill *P. aeruginosa*. Furthermore, the heterogeneous nature of CF lung environments likely contributes to the presence of “persister” cells, which are able to survive in microenvironments of lower antibiotic concentrations while contributing to the establishment of chronic infection (Williams and Davies 2012).

Metabolic versatility and diverse strategies for redox balancing also contribute to *P. aeruginosa*’s ability to form robust biofilms. Its arsenal of terminal oxidases allows it to flourish under a spectrum of O_2 concentrations ranging from atmospheric to microaerobic. Its abilities to denitrify and ferment allow it to survive and grow under anoxic conditions. The production and utilization of redox-active phenazines further support redox balancing and growth under micro- and anaerobic conditions. In the following chapters, I will expand upon these strategies and

demonstrate that *P. aeruginosa* is even more metabolically versatile than previously appreciated. In Chapter 2, I will describe a novel Cco terminal oxidase complex that contributes to biofilm physiology, phenazine utilization, and virulence. In Chapter 3, I will discuss how carbon sources affect the expression and utilization of *P. aeruginosa* aerobic respiratory chain components and phenazine-dependent metabolism, underscoring how this bacterium's physiology is highly dependent on the environmental conditions under which is it grown. Finally, in Chapter 4, I will discuss other metabolic pathways that contribute to *P. aeruginosa* redox balancing and biofilm development as well as a redox-based mechanism of biofilm development in the phylogenetically distinct bacterium *Bacillus subtilis*. Together, these results will allow for a deeper appreciation for the various adaptations used by *P. aeruginosa* to maintain redox homeostasis and flourish in the biofilm lifestyle.

1.7: References

Alvarez-Ortega, Carolina, and Caroline S. Harwood. 2007. “Responses of Pseudomonas Aeruginosato Low Oxygen Indicate That Growth in the Cystic Fibrosis Lung Is by Aerobic Respiration.” *Molecular Microbiology* 65 (1): 153–65.

Arai, Hiroyuki. 2011. “Regulation and Function of Versatile Aerobic and Anaerobic Respiratory Metabolism in Pseudomonas Aeruginosa.” *Frontiers in Microbiology* 2 (May): 103.

Arai, Hiroyuki, Takuro Kawakami, Tatsuya Osamura, Takehiro Hirai, Yoshiaki Sakai, and Masaharu Ishii. 2014. “Enzymatic Characterization and in Vivo Function of Five Terminal Oxidases in Pseudomonas Aeruginosa.” *Journal of Bacteriology* 196 (24): 4206–15.

Bliek, Alexander M. van der, Margaret M. Sedensky, and Phil G. Morgan. 2017. “Cell Biology of the Mitochondrion.” *Genetics* 207 (3): 843–71.

Blumer, C., and D. Haas. 2000. “Mechanism, Regulation, and Ecological Role of Bacterial Cyanide Biosynthesis.” *Archives of Microbiology* 173 (3): 170–77.

Bosire, Erick M., Lars M. Blank, and Miriam A. Rosenbaum. 2016. “Strain- and Substrate-Dependent Redox Mediator and Electricity Production by Pseudomonas Aeruginosa.” *Applied and Environmental Microbiology* 82 (16): 5026–38.

Chin−A−Woeng, T. F. C., and G. V. Bloemberg. 2003. “Phenazines and Their Role in Biocontrol by Pseudomonas Bacteria.” New Phytologist. https://onlinelibrary.wiley.com/doi/abs/10.1046/j.1469-8137.2003.00686.x.

Ciofu, Oana, Lotte F. Mandsberg, Hengzhuang Wang, and Niels Høiby. 2012. “Phenotypes Selected during Chronic Lung Infection in Cystic Fibrosis Patients: Implications for the Treatment of Pseudomonas Aeruginosa Biofilm Infections.” *FEMS Immunology and Medical Microbiology* 65 (2): 215–25.

Comolli, James C., and Timothy J. Donohue. 2002. “Pseudomonas Aeruginosa RoxR, a Response Regulator Related to Rhodobacter Sphaeroides PrrA, Activates Expression of the Cyanide-Insensitive Terminal Oxidase.” *Molecular Microbiology* 45 (3): 755–68.

Comolli, James C. and Tinothy J. Donohue. 2004. “Differences in Two Pseudomonas Aeruginosa cbb3 Cytochrome Oxidases.” Molecular Microbiology 51 (4): 1193–1203.

Conway, Tyrrell, and Paul S. Cohen. 2015. *Metabolism and Bacterial Pathogenesis*. ASM Press.

Cowley, Elise S., Sebastian H. Kopf, Alejandro LaRiviere, Wiebke Ziebis, and Dianne K. Newman. 2015. “Pediatric Cystic Fibrosis Sputum Can Be Chemically Dynamic, Anoxic, and Extremely Reduced Due to Hydrogen Sulfide Formation.” *mBio* 6 (4): e00767.

Cramer, William A., and Toivo Kallas, eds. 2016. *Cytochrome Complexes: Evolution, Structures, Energy Transduction, and Signaling*. Advances in Photosynthesis and Respiration.

Cunningham, L., M. Pitt, and H. D. Williams. 1997. “The cioAB Genes from Pseudomonas Aeruginosa Code for a Novel Cyanide-Insensitive Terminal Oxidase Related to the Cytochrome Bd Quinol Oxidases.” *Molecular Microbiology* 24 (3): 579–91.

Dietrich, Lars E. P., Chinweike Okegbe, Alexa Price-Whelan, Hassan Sakhtah, Ryan C. Hunter, and Dianne K. Newman. 2013. “Bacterial Community Morphogenesis Is Intimately Linked to the Intracellular Redox State.” *Journal of Bacteriology* 195 (7): 1371–80.

D’Mello, Rita, Susan Hill, and Robert K. Poole. 1995. “The Oxygen Affinity of Cytochrome Bo’in Escherichia Coli Determined by the Deoxygenation of Oxyleghemoglobin and Oxymyoglobin: Km Values for Oxygen Are in the Submicromolar Range.” *Journal of Bacteriology* 177 (3): 867–70.

Glasser, Nathaniel R., Suzanne E. Kern, and Dianne K. Newman. 2014. “Phenazine Redox Cycling Enhances Anaerobic Survival in Pseudomonas Aeruginosa by Facilitating Generation of ATP and a Proton-Motive Force.” *Molecular Microbiology* 92 (2): 399–412.

Hall-Stoodley, Luanne, J. William Costerton, and Paul Stoodley. 2004. “Bacterial Biofilms: From the Natural Environment to Infectious Diseases.” *Nature Reviews. Microbiology* 2 (2): 95–108.

Hernandez, Maria E., Andreas Kappler, and Dianne K. Newman. 2004. “Phenazines and Other Redox-Active Antibiotics Promote Microbial Mineral Reduction.” *Applied and Environmental Microbiology* 70 (2): 921–28.

Hirai, Takehiro, Tatsuya Osamura, Masaharu Ishii, and Hiroyuki Arai. 2016. “Expression of Multiple cbb3 Cytochrome c Oxidase Isoforms by Combinations of Multiple Isosubunits in Pseudomonas Aeruginosa.” *Proceedings of the National Academy of Sciences of the United States of America*, October. https://doi.org/10.1073/pnas.1613308113.

Høiby, Niels, Oana Ciofu, Helle Krogh Johansen, Zhi-Jun Song, Claus Moser, Peter Østrup Jensen, Søren Molin, Michael Givskov, Tim Tolker-Nielsen, and Thomas Bjarnsholt. 2011. “The Clinical Impact of Bacterial Biofilms.” *International Journal of Oral Science* 3 (2): 55–65.

Huang, Jiaofang, Elisabeth Sonnleitner, Bin Ren, Yuquan Xu, and Dieter Haas. 2012. “Catabolite Repression Control of Pyocyanin Biosynthesis at an Intersection of Primary and Secondary Metabolism in Pseudomonas Aeruginosa.” *Applied and Environmental Microbiology* 78 (14): 5016–20.

Hunter, Ryan C., Vanja Klepac-Ceraj, Magen M. Lorenzi, Hannah Grotzinger, Thomas R. Martin, and Dianne K. Newman. 2012. “Phenazine Content in the Cystic Fibrosis Respiratory Tract Negatively Correlates with Lung Function and Microbial Complexity.” *American Journal of Respiratory Cell and Molecular Biology* 47 (6): 738–45.

Jo, Jeanyoung, Krista L. Cortez, William Cole Cornell, Alexa Price-Whelan, and Lars Ep Dietrich. 2017. “An Orphan cbb3-Type Cytochrome Oxidase Subunit Supports Pseudomonas Aeruginosa Biofilm Growth and Virulence.” *eLife* 6 (November). https://doi.org/10.7554/eLife.30205.

Kawakami, Takuro, Miho Kuroki, Masaharu Ishii, Yasuo Igarashi, and Hiroyuki Arai. 2010. “Differential Expression of Multiple Terminal Oxidases for Aerobic Respiration in Pseudomonas Aeruginosa.” *Environmental Microbiology* 12 (6): 1399–1412.

Lau, Gee W., Huimin Ran, Fansheng Kong, Daniel J. Hassett, and Dimitri Mavrodi. 2004. “Pseudomonas Aeruginosa Pyocyanin Is Critical for Lung Infection in Mice.” *Infection and Immunity* 72 (7): 4275–78.

Lee, Samuel A., Larry A. Gallagher, Metawee Thongdee, Benjamin J. Staudinger, Soyeon Lippman, Pradeep K. Singh, and Colin Manoil. 2015. “General and Condition-Specific Essential Functions of Pseudomonas Aeruginosa.” *Proceedings of the National Academy of Sciences of the United States of America* 112 (16): 5189–94.

Lenney, W., and F. J. Gilchrist. 2011. “Pseudomonas Aeruginosa and Cyanide Production.” *The European Respiratory Journal: Official Journal of the European Society for Clinical Respiratory Physiology* 37 (3): 482–83.

Lin, Yu-Cheng, William Cole Cornell, Jeanyoung Jo, Alexa Price-Whelan, and Lars E. P. Dietrich. 2018. “The Pseudomonas Aeruginosa Complement of Lactate Dehydrogenases Enables Use of D- and L-Lactate and Metabolic Cross-Feeding.” *mBio* 9 (5). https://doi.org/10.1128/mBio.00961-18.

Madigan, Michael T., John M. Martinko, Kelly S. Bender, Daniel H. Buckley, and David A. Stahl. 2015. *Brock Biology of Microorganisms*. Pearson.

Murray, Thomas S., Marie Egan, and Barbara I. Kazmierczak. 2007. “Pseudomonas Aeruginosa Chronic Colonization in Cystic Fibrosis Patients.” *Current Opinion in Pediatrics* 19 (1): 83–88.

Nair, C. G., C. Chao, B. Ryall, and H. D. Williams. 2013. “Sub-Lethal Concentrations of Antibiotics Increase Mutation Frequency in the Cystic Fibrosis Pathogen Pseudomonas Aeruginosa.” *Letters in Applied Microbiology* 56 (2): 149–54.

Ornston, L. N. 1971. “Regulation of Catabolic Pathways in Pseudomonas.” *Bacteriological Reviews* 35 (2): 87–116.

Penesyan, Anahit, Michael Gillings, and Ian T. Paulsen. 2015. “Antibiotic Discovery: Combatting Bacterial Resistance in Cells and in Biofilm Communities.” *Molecules* 20 (4): 5286–98.

Pitcher, Robert S., and Nicholas J. Watmough. 2004. “The Bacterial Cytochrome cbb3 Oxidases.” *Biochimica et Biophysica Acta* 1655 (1-3): 388–99.

Poole, R. K., and G. M. Cook. 2000. “Redundancy of Aerobic Respiratory Chains in Bacteria? Routes, Reasons and Regulation.” *Advances in Microbial Physiology* 43: 165–224.

Potvin, Eric, François Sanschagrin, and Roger C. Levesque. 2008. “Sigma Factors in Pseudomonas Aeruginosa.” *FEMS Microbiology Reviews* 32 (1): 38–55.

Price-Whelan, Alexa, Lars E. P. Dietrich, and Dianne K. Newman. 2007. “Pyocyanin Alters Redox Homeostasis and Carbon Flux through Central Metabolic Pathways in Pseudomonas Aeruginosa PA14.” *Journal of Bacteriology* 189 (17): 6372–81.

Ray, A., and H. D. Williams. 1997. “The Effects of Mutation of the Anr Gene on the Aerobic Respiratory Chain of Pseudomonas Aeruginosa.” *FEMS Microbiology Letters* 156 (2): 227–32.

Recinos, David A., Matthew D. Sekedat, Adriana Hernandez, Taylor Sitarik Cohen, Hassan Sakhtah, Alice S. Prince, Alexa Price-Whelan, and Lars E. P. Dietrich. 2012. “Redundant Phenazine Operons in Pseudomonas Aeruginosa Exhibit Environment-Dependent Expression and Differential Roles in Pathogenicity.” *Proceedings of the National Academy of Sciences of the United States of America* 109 (47): 19420–25.

Rij, E. Tjeerd van, Monique Wesselink, Thomas F. C. Chin-A-Woeng, Guido V. Bloemberg, and Ben J. J. Lugtenberg. 2004. “Influence of Environmental Conditions on the Production of Phenazine-1-Carboxamide by Pseudomonas Chlororaphis PCL1391.” *Molecular Plant-Microbe Interactions: MPMI* 17 (5): 557–66.

Ryall, B., J. C. Davies, R. Wilson, A. Shoemark, and H. D. Williams. 2008. “Pseudomonas Aeruginosa, Cyanide Accumulation and Lung Function in CF and Non-CF Bronchiectasis Patients.” *The European Respiratory Journal: Official Journal of the European Society for Clinical Respiratory Physiology* 32 (3): 740–47.

Sakhtah, Hassan, Leslie Koyama, Yihan Zhang, Diana K. Morales, Blanche L. Fields, Alexa Price-Whelan, Deborah A. Hogan, Kenneth Shepard, and Lars E. P. Dietrich. 2016. “The Pseudomonas Aeruginosa Efflux Pump MexGHI-OpmD Transports a Natural Phenazine That Controls Gene Expression and Biofilm Development.” *Proceedings of the National Academy of Sciences of the United States of America* 113 (25): E3538–47.

Sanderson, K., L. Wescombe, S. M. Kirov, A. Champion, and D. W. Reid. 2008. “Bacterial Cyanogenesis Occurs in the Cystic Fibrosis Lung.” *The European Respiratory Journal: Official Journal of the European Society for Clinical Respiratory Physiology* 32 (2): 329–33.

Schulz, Sebastian, Denitsa Eckweiler, Agata Bielecka, Tanja Nicolai, Raimo Franke, Andreas Dötsch, Klaus Hornischer, Sebastian Bruchmann, Juliane Düvel, and Susanne Häussler. 2015. “Elucidation of Sigma Factor-Associated Networks in Pseudomonas Aeruginosa Reveals a Modular Architecture with Limited and Function-Specific Crosstalk.” *PLoS Pathogens* 11 (3): e1004744.

Schuster, Martin, Andrew C. Hawkins, Caroline S. Harwood, and E. P. Greenberg. 2004. “The Pseudomonas Aeruginosa RpoS Regulon and Its Relationship to Quorum Sensing.” *Molecular Microbiology* 51 (4): 973–85.

Stanier, R. Y., N. J. Palleroni, and M. Doudoroff. 1966. “The Aerobic Pseudomonads: A Taxonomic Study.” *Journal of General Microbiology* 43 (2): 159–271.

Stover, C. K., X. Q. Pham, A. L. Erwin, S. D. Mizoguchi, P. Warrener, M. J. Hickey, F. S. Brinkman, et al. 2000. “Complete Genome Sequence of Pseudomonas Aeruginosa PAO1, an Opportunistic Pathogen.” *Nature* 406 (6799): 959–64.

Wang, Yun, Suzanne E. Kern, and Dianne K. Newman. 2010. “Endogenous Phenazine Antibiotics Promote Anaerobic Survival of Pseudomonas Aeruginosa via Extracellular Electron Transfer.” *Journal of Bacteriology* 192 (1): 365–69.

Wang, Yun, and Dianne K. Newman. 2008. “Redox Reactions of Phenazine Antibiotics with Ferric (hydr)oxides and Molecular Oxygen.” *Environmental Science & Technology* 42 (7): 2380–86.

Wargo, Matthew J. 2013. “Homeostasis and Catabolism of Choline and Glycine Betaine: Lessons from Pseudomonas Aeruginosa.” *Applied and Environmental Microbiology* 79 (7): 2112–20.

Werner, Erin, Frank Roe, Amandine Bugnicourt, Michael J. Franklin, Arne Heydorn, Søren Molin, Betsey Pitts, and Philip S. Stewart. 2004. “Stratified Growth in Pseudomonas Aeruginosa Biofilms.” *Applied and Environmental Microbiology* 70 (10): 6188–96.

Wessel, Aimee K., Talha A. Arshad, Mignon Fitzpatrick, Jodi L. Connell, Roger T. Bonnecaze, Jason B. Shear, and Marvin Whiteley. 2014. “Oxygen Limitation within a Bacterial Aggregate.” *mBio* 5 (2): e00992.

White, David, James T. Drummond, and Clay Fuqua. 2012. *The Physiology and Biochemistry of Prokaryotes*. Oxford University Press.

Williams, Huw D., and Jane C. Davies. 2012. “Basic Science for the Chest Physician: Pseudomonas Aeruginosa and the Cystic Fibrosis Airway.” *Thorax* 67 (5): 465–67.

Williams, Huw D., James E. A. Zlosnik, and Ben Ryall. 2007. “Oxygen, Cyanide and Energy Generation in the Cystic Fibrosis Pathogen Pseudomonas Aeruginosa.” *Advances in Microbial Physiology* 52: 1–71.

Wilson, R., D. A. Sykes, D. Watson, A. Rutman, G. W. Taylor, and P. J. Cole. 1988. “Measurement of Pseudomonas Aeruginosa Phenazine Pigments in Sputum and Assessment of

Their Contribution to Sputum Sol Toxicity for Respiratory Epithelium." *Infection and Immunity* 56 (9): 2515–17.

Xu, K. D., P. S. Stewart, F. Xia, C. T. Huang, and G. A. McFeters. 1998. "Spatial Physiological Heterogeneity in Pseudomonas Aeruginosa Biofilm Is Determined by Oxygen Availability." *Applied and Environmental Microbiology* 64 (10): 4035–39.

Zumft, W. G. 1997. "Cell Biology and Molecular Basis of Denitrification." *Microbiology and Molecular Biology Reviews: MMBR* 61 (4): 533–616.

Chapter Two

An orphan *cbb*$_3$-type cytochrome oxidase subunit supports *Pseudomonas aeruginosa* biofilm growth and virulence

This chapter is adapted from:
Jo, J, Cortez, KL, Cornell, WC, Price-Whelan, A, Dietrich, LE (2017). An orphan *cbb*$_3$-type cytochrome oxidase subunit supports *Pseudomonas aeruginosa* biofilm growth and virulence. *eLife* 6, e30205.

For this work, I formulated hypotheses, engineered all deletion and reporter constructs, and designed and performed all experiments, except competition assays (**Figures 2.3A** and **2.3B**; performed by Krista L. Cortez) and thin sectioning of biofilms (**Figure 2.3C**, **Figure 2.4**, **Figure 2.5B** (bottom), and **Figure 2.5C**; performed by William Cole Cornell). I contributed to the analysis and interpretation of all generated data and in the writing of this paper.

I thank Rachel Hainline for technical assistance with competition assays, Christopher Beierschmitt for technical assistance with worm pathogenicity assays, and Konstanze Schiessl for help with image analysis and feedback on the manuscript.

2.1: Abstract

Hypoxia is a common challenge faced by bacteria during associations with hosts due in part to the formation of densely packed communities (biofilms). *cbb*$_3$-type cytochrome *c* oxidases, which catalyze the terminal step in respiration and have a high affinity for oxygen, have been linked to bacterial pathogenesis. The pseudomonads are unusual in that they often contain multiple full and partial (i.e., “orphan”) operons for *cbb*$_3$-type oxidases and oxidase subunits. Here, we describe a unique role for the orphan catalytic subunit CcoN4 in colony biofilm development and respiration in the opportunistic pathogen *Pseudomonas aeruginosa* PA14. We also show that CcoN4 contributes to the reduction of phenazines, antibiotics that support redox balancing for cells in biofilms, and to virulence in a *Caenorhabditis elegans* model of infection. These results highlight the relevance of the colony biofilm model to pathogenicity and underscore the potential of *cbb*$_3$-type oxidases as therapeutic targets.

2.2: Introduction

Among the oxidants available for biological reduction, molecular oxygen (O_2) provides the highest free energy yield. Since the accumulation of O_2 in the atmosphere between

~2.4-0.54 billion years ago (Kirschvink and Kopp 2008; Dietrich, Tice, and Newman 2006), organisms that can use it for growth and survival, and tolerate its harmful byproducts, have evolved to exploit this energy and increased in complexity (Knoll and Sperling 2014; Falkowski 2006). At small scales and in crowded environments, rapid consumption of O_2 leads to competition for this resource and has promoted diversification of bacterial and archaeal mechanisms for O_2 reduction that has not occurred in eukaryotes (Brochier-Armanet, Talla, and Gribaldo 2009). The various enzymes that allow bacteria to respire O_2 exhibit a range of affinities and proton-pumping efficiencies and likely contribute to competitive success in hypoxic niches (Morris and Schmidt 2013). Such environments include the tissues of animal and plant hosts that are colonized by bacteria of high agricultural (Preisig et al. 1996) and clinical (Way et al. 1999; Weingarten, Grimes, and Olson 2008) significance.

The opportunistic pathogen *Pseudomonas aeruginosa*, a colonizer of both plant and animal hosts (Rahme et al. 1995), has a branched respiratory chain with the potential to reduce O_2 to water using at least five different terminal oxidase complexes: two quinol oxidases (bo_3 (Cyo) and a *bd*-type cyanide insensitive oxidase (CIO)) and three cytochrome *c* oxidases (aa_3, cbb_3-1, and cbb_3-2) (**Figure 2.1A**). Several key publications have described *P. aeruginosa*'s complement of terminal oxidases and oxidase subunits, revealing features specific to this organism (Williams, Zlosnik, and Ryall 2007; Comolli and Donohue 2004; Alvarez-Ortega and Harwood 2007; Arai et al. 2014; Kawakami et al. 2010; Jo, Price-Whelan, and Dietrich 2014). *P. aeruginosa* is somewhat unusual in that it encodes two oxidases belonging to the cbb_3-type family. These enzymes are notable for their relatively high catalytic activity at low O_2 concentrations and restriction to the bacterial domain (Brochier-Armanet, Talla, and Gribaldo 2009; Pitcher and Watmough 2004). (The *P. aeruginosa* cbb_3-type oxidases are often referred to as cbb_3-1 and cbb_3-2; however, we will use "Cco1" and "Cco2" for these enzymes, consistent with the annotations of their encoding genes.) Most bacterial genomes that encode cbb_3-type oxidases contain only one operon for such a complex, which is induced specifically under conditions of O_2 limitation (Cosseau and Batut 2004). In *P. aeruginosa*, the *cco2* operon is

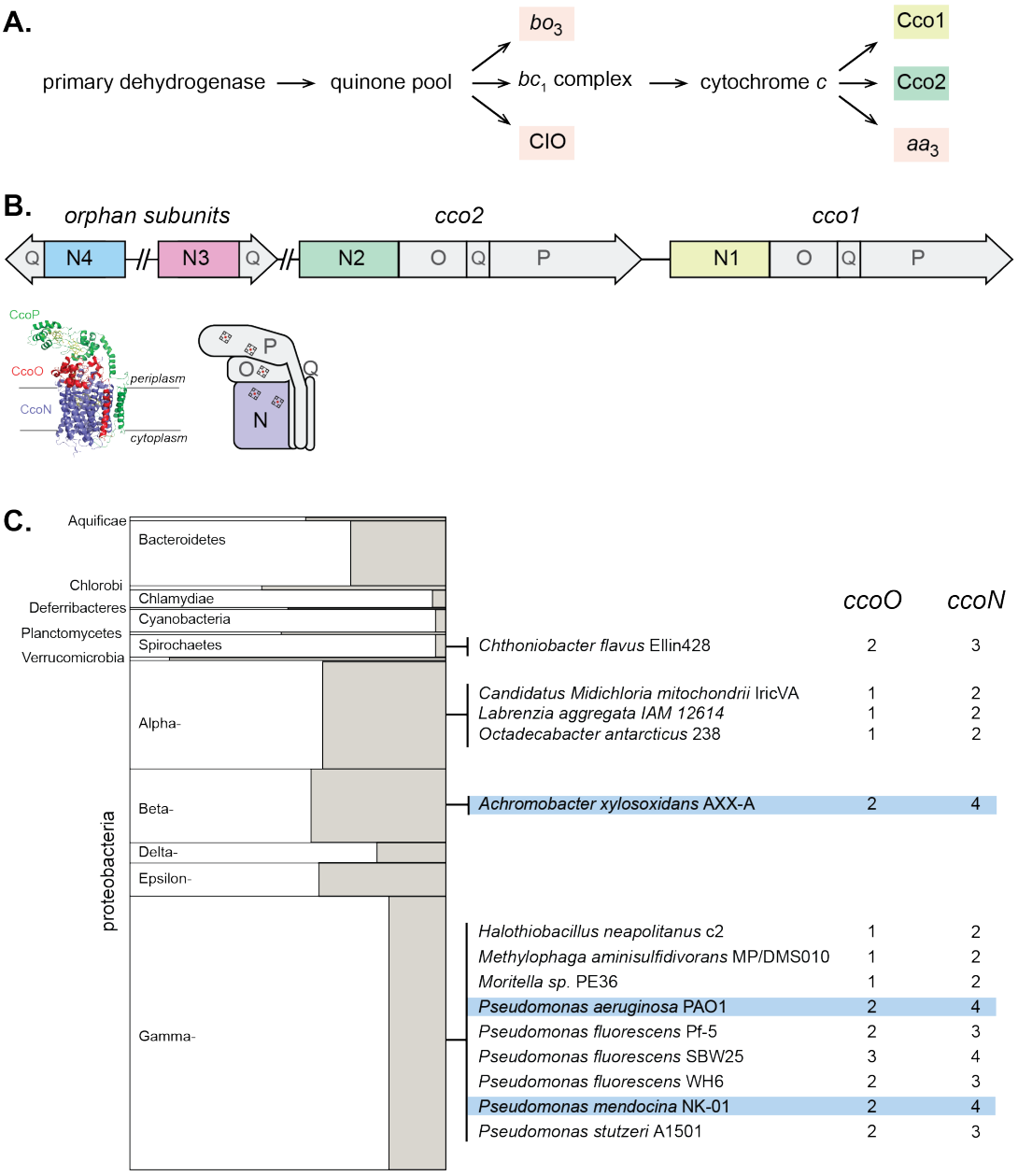

Figure 2.1. The respiratory chain and arrangement of *cco* genes and protein products in *P. aeruginosa*, and the phylogenetic distribution of orphan *ccoN* genes. (A) Branched electron transport chain in *P. aeruginosa*, containing five terminal oxidases. **(B)** Organization of *cco* genes in the *P. aeruginosa* genome. The cartoon of the Cco complex is based on the Cco structure from *P. stutzeri* (PDB: 3mk7) (Buschmann et al. 2010a). **(C)** Left: graphical representation of the portion of genomes in each bacterial phylum that contain *ccoO* and *N* homologs. The clades Chrysiogenetes, Gemmatimonadetes, and Zetaproteobacteria were omitted because they each contain only one species with *ccoO* and *N* homologs. The height of each rectangle indicates the total number of genomes included in the analysis. The width of each shaded rectangle represents the portion of genomes that contain *ccoN* homologs. Middle: genomes that contain more *ccoN* than *ccoO* homologs (indicating the presence of orphan *ccoN* genes) are listed. Right: numbers of *ccoO* and *ccoN* homologs in each genome. Blue highlights genomes containing more than one orphan *ccoN* homolog.

induced during growth at low O_2 concentrations, but the *cco1* operon is expressed constitutively at high levels (Comolli and Donohue 2004; Kawakami et al. 2010).

An additional quirk of the *P. aeruginosa* terminal oxidase complement lies in the presence of genes for "orphan" *cbb*$_3$-type subunits at chromosomal locations distinct from the *cco1* and *cco2* operons. While the *cco1* and *cco2* operons, which are chromosomally adjacent, each contain four genes encoding a functional Cco complex (consisting of subunits N, O, P, and Q), the two additional partial operons *ccoN3Q3* and *ccoN4Q4* each contain homologs coding for only the Q and catalytic N subunits (**Figure 2.1B**). Expression of the *ccoN3Q3* operon is induced under anaerobic denitrification conditions (Alvarez-Ortega and Harwood 2007), and by nitrite exposure during growth under 2% O_2 (Hirai et al. 2016). During aerobic growth in liquid cultures, *ccoN4Q4* is induced by cyanide, which is produced in stationary phase (Hirai et al. 2016). However, additional expression studies indicate that *ccoN4Q4* transcription is influenced by redox conditions, as this operon is induced by O_2 limitation (Alvarez-Ortega and Harwood 2007) and slightly downregulated in response to pyocyanin, a redox-active antibiotic produced by *P. aeruginosa* (Dietrich et al. 2006).

In a recent study, Hirai et al. characterized the biochemical properties and physiological roles of *P. aeruginosa cbb*$_3$ isoforms containing combinations of canonical and orphan subunits (Hirai et al. 2016). In a strain lacking all of the aerobic terminal oxidases, expression of any isoform conferred the ability to grow using O_2, confirming that isoforms containing the orphan N subunits are functional. When preparations from wild-type, stationary-phase *P. aeruginosa* cells were separated on 2D gels and probed with anti-CcoN4 antibody, this subunit was detected at the same position as the assembled CcoNOP complex, showing that CcoN4-containing heterocomplexes form in vivo. Furthermore, the authors found that the products of *ccoN3Q3* and *ccoN4Q4* contributed resistance to nitrite and cyanide, respectively, during growth in liquid cultures under low-O_2 conditions. While these results provide insight into contributions of the *cbb*$_3$ heterocomplexes to growth in liquid cultures, potential roles for N3- and N4-containing isoforms in biofilm growth and pathogenicity have yet to be explored.

The biofilm lifestyle—in which cells grow in a dense community encased in a self-produced matrix—has been linked to the establishment and persistence of infections in diverse systems (Edwards and Kjellerup 2012; Rybtke et al. 2015). Biofilm development promotes the formation of O_2 gradients such that cells at a distance from the biofilm surface are subjected to hypoxic or anoxic conditions (Werner et al. 2004). Using a colony morphology assay to study redox metabolism and its relationship to community behavior, we have shown that O_2 limitation for cells in biofilms leads to an imbalance in the intracellular redox state. This can be relieved by a change in community morphology, which increases the surface area-to-volume ratio of the biofilm and therefore access to O_2 for resident cells (Kempes et al. 2014). For *P. aeruginosa* cells in biofilms, the intracellular accumulation of reducing power can also be prevented by production and reduction of endogenous antibiotics called phenazines, which mediate extracellular electron transfer to oxidants available at a distance (Dietrich et al. 2013). We have found that biofilm-specific phenazine production contributes to pathogenicity in a murine model of acute pulmonary infection (Recinos et al. 2012), further underscoring the importance of phenazine-mediated redox balancing for *P. aeruginosa* cells in communities.

Because of the formation of an O_2 gradient inherent to the biofilm lifestyle, we hypothesized that the differential regulation of the *P. aeruginosa cco* operons affects their contributions to metabolic electron flow in biofilm subzones. We evaluated the roles of various *cbb*$_3$-type oxidase isoforms in multicellular behavior and virulence. Our results indicate that isoforms containing the orphan subunit CcoN4 can support survival in biofilms via O_2 and phenazine reduction and contribute to *P. aeruginosa* pathogenicity in a *Caenorhabditis elegans* “slow killing” model of infection.

2.3: Results

2.3.1: A small minority of bacterial genomes encode cbb$_3$*-type oxidase subunits in partial ("orphan") operons*

Biochemical, genetic, and genomic analyses suggest that the CcoN and CcoO subunits, typically encoded by an operon, form the minimal functional unit of *cbb*$_3$-type oxidases (Ducluzeau, Ouchane, and Nitschke 2008; de Gier et al. 1996; Zufferey et al. 1996). CcoN is the membrane-integrated catalytic subunit and contains two *b*-type hemes and a copper ion. CcoO is membrane-anchored and contains one *c*-type heme. Additional redox subunits and/or subunits implicated in complex assembly, such as CcoQ and CcoP, can be encoded by adjacent genes (**Figure 2.1B**). *ccoNO*-containing clusters are widely distributed across phyla of the bacterial domain (Ducluzeau, Ouchane, and Nitschke 2008). We used the EggNOG database, which contains representative genomes for more than 3000 bacterial species (Huerta-Cepas et al. 2016) to obtain an overview of the presence and frequency of *cco* genes. Out of 3318 queried bacterial genomes we found 467 with full *cco* operons (encoding potentially functional *cbb*$_3$-type oxidases with O and N subunits). Among these, 78 contain more than one full operon. We also used EggNOG to look for orphan *ccoN* genes by examining the relative numbers of *ccoO* and *ccoN* homologs in individual genomes. We found 14 genomes, among which *Pseudomonas* species are overrepresented, that contain orphan *ccoN* genes (**Figure 2.1C**), and our analysis yielded 3 species that contain more than one orphan *ccoN* gene: *Pseudomonas mendocina*, *Pseudomonas aeruginosa*, and *Achromobacter xylosoxidans*. *P. mendocina* is a soil bacterium and occasional nosocomial pathogen that is closely related to *P. aeruginosa*, based on 16S rRNA gene sequence comparison (Anzai et al. 2000). *A. xylosoxidans*, in contrast, is a member of a different proteobacterial class but nevertheless is often mistaken for *P. aeruginosa* (Saiman et al. 2001). Like *P. aeruginosa*, it is an opportunistic pathogen that can cause pulmonary infections in immunocompromised individuals and patients with cystic fibrosis (De Baets et al. 2007; Firmida et al. 2016). Hirai et al. previously reported a ClustalW-based analysis of CcoN homologs specifically from pseudomonads, which indicated

the presence of orphan genes in additional species not represented in the EggNOG database. These include *P. denitrificans*, which contains two orphan genes (Hirai et al. 2016).

2.3.2: CcoN4-containing isoforms function specifically in biofilms to support community morphogenesis and respiration

During growth in a biofilm, subpopulations of cells are subjected to regimes of electron donor and O_2 availability that may create unique metabolic demands and require modulation of the respiratory chain for survival (Alvarez-Ortega and Harwood 2007; Borriello et al. 2004; Werner et al. 2004). We therefore investigated the contributions of individual *cco* genes and gene clusters to *P. aeruginosa* PA14 biofilm development using a colony morphology assay, which has demonstrated sensitivity to electron acceptor availability and utilization (Dietrich et al. 2013). Because the Cco1 and Cco2 complexes are the most important cytochrome oxidases for growth of *P. aeruginosa* in fully aerated and O_2-limited liquid cultures (Alvarez-Ortega and Harwood 2007; Arai et al. 2014), we predicted that mutations disabling the functions of Cco1 and Cco2 would affect colony growth. Indeed, a mutant lacking both the *cco1* and *cco2* operons ("Δ*cco1cco2*") produced thin biofilms with a smaller diameter than the wild type. After five days of development, this mutant displayed a dramatic phenotype consisting of a tall central ring feature surrounded by short ridges that emanate radially (**Figure 2.2A**, **Figure 2.2— figure supplement 1A**). Δ*cco1cco2* colonies were also darker in color, indicating increased uptake of the dye Congo red, which binds to the extracellular matrix produced by biofilms (Friedman and Kolter 2004). Surprisingly, a strain specifically lacking the catalytic subunits of Cco1 and Cco2 ("Δ*N1*Δ*N2*"), while showing a growth defect similar to that of Δ*cco1cco2* when grown in liquid culture (**Figure 2.2C**), showed biofilm development that was similar to that of the wild type (**Figure 2.2A**, **Figure 2.2--figure supplement 1A)**.

As it is known that CcoN3 and CcoN4 can form functional complexes with subunits of the Cco1 and Cco2 oxidases in *P. aeruginosa* PAO1 (Hirai et al. 2016), this led us to hypothesize that Cco isoforms containing the orphan subunits CcoN3 and/or CcoN4 could

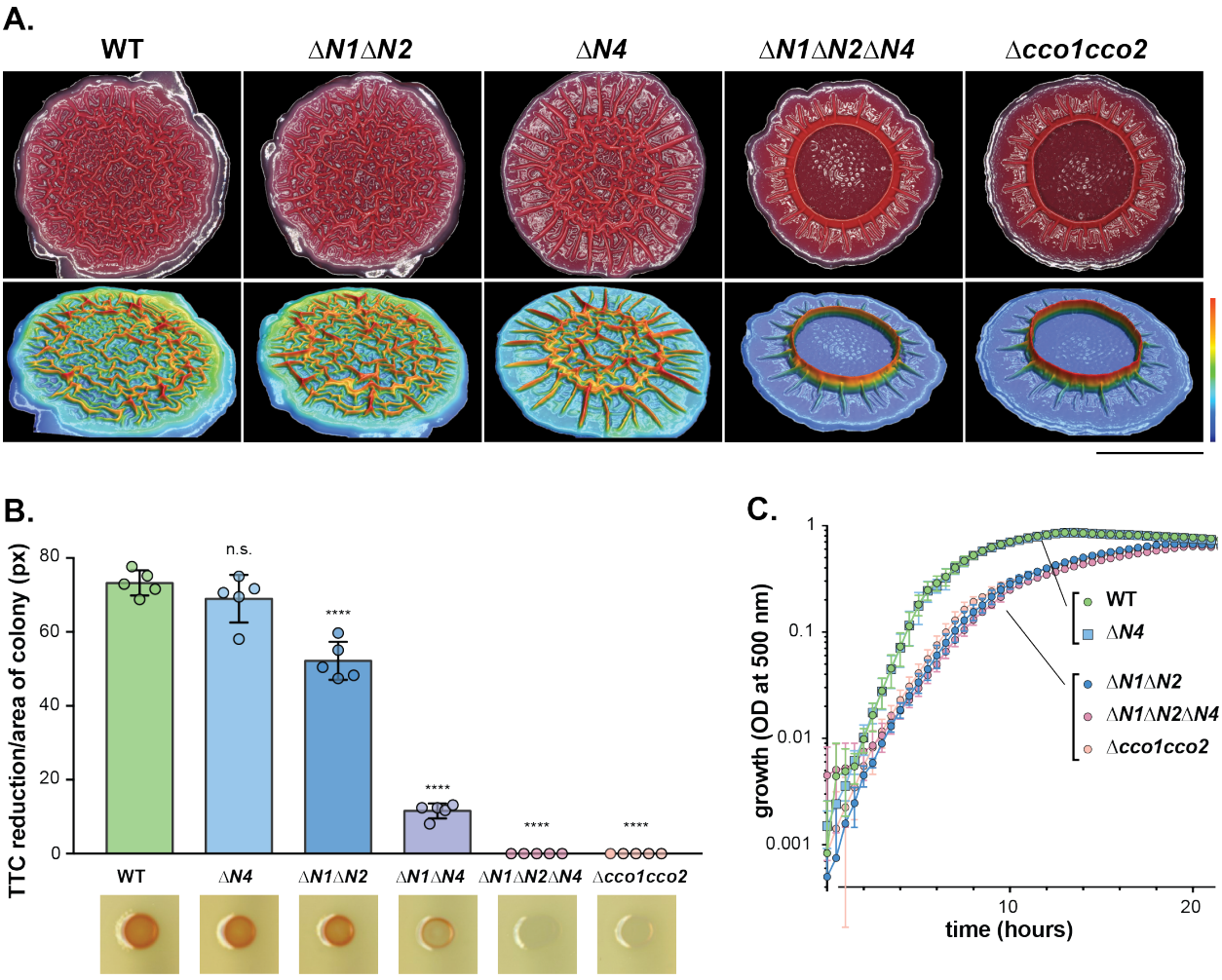

Figure 2.2. CcoN4-containing heterocomplexes make biofilm-specific contributions to morphogenesis and respiration. (A) Top: Five-day-old colony biofilms of PA14 WT and *cco* mutant strains. Biofilm morphologies are representative of more than ten biological replicates. Images were generated using a Keyence digital microscope. Scale bar is 1 cm. Bottom: 3D surface images of the biofilms shown in the top panel. Images were generated using a Keyence wide-area 3D measurement system. Height scale bar: bottom (blue) to top (red) is 0 - 0.7 mm for WT, Δ*N1*Δ*N2*, and Δ*N4*; 0 - 1.5 mm for Δ*N1*Δ*N2*Δ*N4* and Δ*cco1cco2*. **(B)** TTC reduction by *cco* mutant colonies after one day of growth. Upon reduction, TTC undergoes an irreversible color change from colorless to red. Bars represent the average, and error bars represent the standard deviation, of individually-plotted biological replicates (n = 5). P-values were calculated using unpaired, two-tailed t tests comparing each mutant to WT (****, P ≤ 0.0001). For full statistical reporting, refer to Table 4. **(C)** Mean growth of PA14 WT and *cco* mutant strains in MOPS defined medium with 20 mM succinate. Error bars represent the standard deviation of biological triplicates.

substitute for Cco1 and Cco2 in the biofilm context. Deleting *ccoN3* ("Δ*N3*" or "Δ*N1*Δ*N2*Δ*N3*") did not have an observable effect on biofilm development when mutants were compared to respective parent strains (**Figure 2.2— figure supplement 1A**). However, the phenotype of a

"Δ*N1*Δ*N2*Δ*N4*" mutant was consistent with our model, as it mimicked that of the Δ*cco1cco2* mutant in both liquid-culture and biofilm growth (**Figures 2.2A** and **2.2C**, **Figure 2.2— figure supplement 1A)**. Furthermore, we found that a mutant lacking only *ccoN4* ("Δ*N4*") displayed an altered phenotype in that it began to form wrinkle structures earlier than the wild type (**Figure 2.2— figure supplement 1A**), which developed into a disordered region of wrinkles inside a central ring, surrounded by long, radially emanating ridges (**Figure 2.2A**). Reintroduction of the *ccoN4* gene into either of these strains restored the phenotypes of the respective parent strains (**Figure 2.2— figure supplement 1A**). Deletion of either *ccoN2* or *ccoN3* in the Δ*N4* background did not exacerbate the colony phenotype seen in Δ*N4* alone. However, the "Δ*N1*Δ*N4*" double mutant showed an intermediate phenotype relative to Δ*N4* and Δ*N1*Δ*N2*Δ*N4* (**Figure 2.2— figure supplement 1B**), suggesting some functional redundancy for CcoN1 and CcoN4. The developmental pattern of the Δ*N4* colony is reminiscent of those displayed by mutants defective in phenazine production and sensing (**Figure 2.2— figure supplement 1A**) (Dietrich et al. 2008, 2013; Sakhtah et al. 2016; Okegbe et al. 2017). Although Δ*N4* itself showed a unique phenotype in the colony morphology assay, its growth in shaken liquid cultures was indistinguishable from that of the wild type (**Figure 2.2C**). Deleting the three non-cbb_3-type terminal oxidases ("Δ*cox*Δ*cyo*Δ*cio*"), did not affect biofilm morphology (**Figure 2.2— figure supplement 2C**). These results suggest that CcoN4-containing Cco isoform(s) play physiological roles that are specific to the growth conditions encountered in biofilms.

Next, we asked whether CcoN4 contributes to respiration in biofilms. We tested a suite of *cco* mutants for reduction of triphenyl tetrazolium chloride (TTC), an activity that is often associated with cytochrome *c* oxidase-dependent respiration (Rich et al. 2001). The Δ*cco1cco2* mutant showed a severe defect in TTC reduction, which was recapitulated by the Δ*N1*Δ*N2*Δ*N4* mutant. As in the colony morphology assay, this extreme phenotype was not recapitulated in a mutant lacking only CcoN1 and CcoN2, indicating that CcoN4 contributes to respiratory activity in PA14 biofilms. Although we did not detect a defect in TTC reduction for the Δ*N4* mutant, we

saw an intermediate level of TTC reduction for Δ*N1*Δ*N4* compared to Δ*N1*Δ*N2* and Δ*N1*Δ*N2*Δ*N4*, further implicating the CcoN4 subunit in this activity (**Figure 2.2B**).

A recent study implicated CcoN4 in resistance to cyanide, a respiratory toxin that is produced by *P. aeruginosa* (Hirai et al. 2016). The altered biofilm phenotypes of Δ*N4* mutants could therefore be attributed to an increased sensitivity to cyanide produced during biofilm growth. We deleted the *hcn* operon, coding for cyanide biosynthetic enzymes, in the wild-type, phenazine-null, and various *cco* mutant backgrounds. The biofilm morphologies and liquid-culture growth of these strains were unaffected by the Δ*hcnABC* mutation, indicating that the biofilm-specific role of CcoN4 explored in this work is independent of its role in mediating cyanide resistance (**Figure 2.2— figure supplement 2**). Additionally, we examined genomes available in the Pseudomonas Genome Database for the presence of homologs encoding CcoN subunits (*ccoN* genes) and enzymes for cyanide synthesis (*hcnABC*) (Winsor et al. 2016) and did not find a clear correlation between the presence of *hcnABC* and *ccoN4* homologs (**Figure 2.2— figure supplement 3**).

Together, the effects of *cco* gene mutations that we observed in assays for colony morphogenesis and TTC reduction suggest that one or more CcoN4-containing Cco isoform(s) support respiration and redox balancing, and is/are utilized preferentially in comparison to CcoN1- and CcoN2-containing Cco complexes, in biofilms. We performed a sequence alignment of the CcoN subunits encoded by the PA14 genome and identified residues that are unique to CcoN4 or shared uniquely between CcoN4 and CcoN1, which showed the strongest functional redundancy with CcoN4 in our assays (**Figure 2.2— figure supplement 4A**). We also threaded the CcoN4 sequence using the available structure of the CcoN subunit from *P. stutzeri* (Buschmann et al. 2010) and highlighted these residues (**Figure 2.2— figure supplement 4B**). It is noteworthy that most of the highlighted residues are surface-exposed, specifically on one half of the predicted CcoN4 structure, where they may engage in binding an unknown protein partner or specific lipids. In contrast, sites that have been described as points of interaction with CcoO and CcoP are mostly conserved, further supporting the notion that

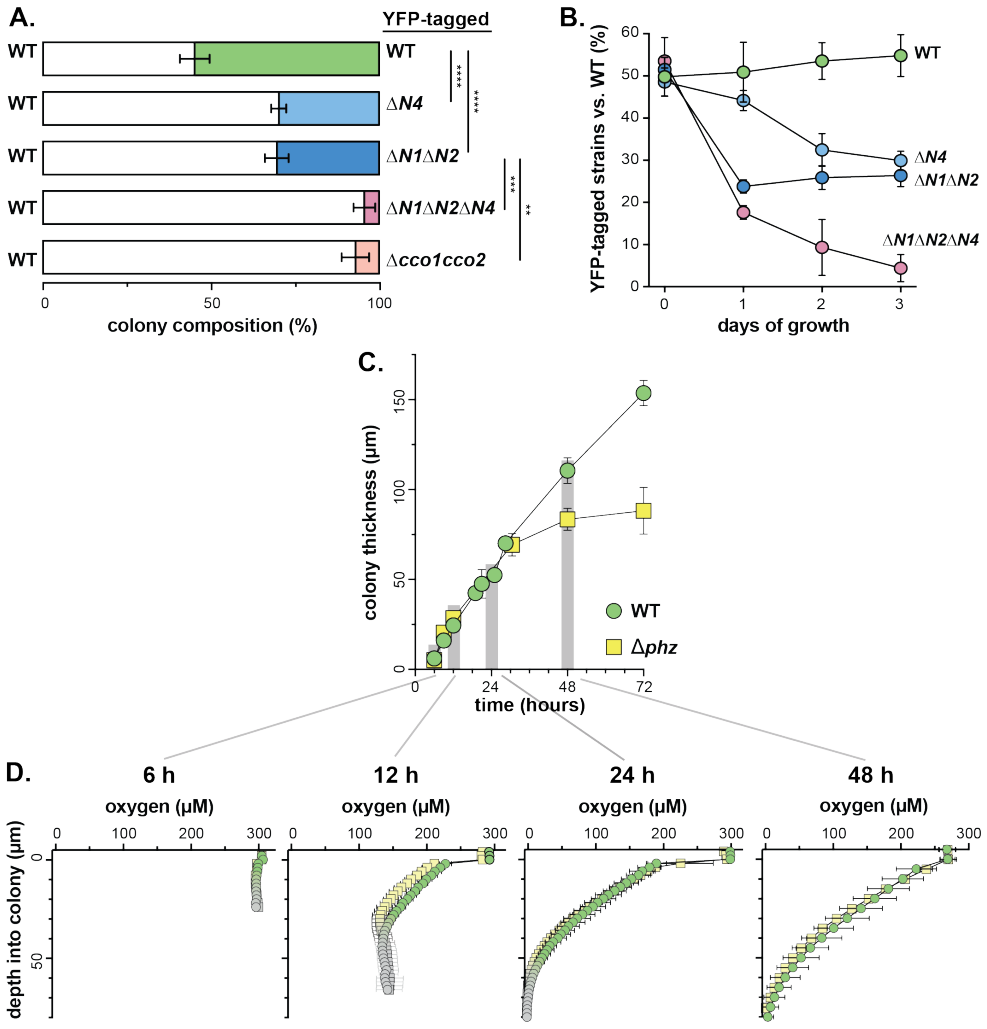

Figure 2.3. CcoN4 confers a competitive advantage in biofilms, particularly when O_2 becomes limiting. (A) Relative fitness of various YFP-labeled *cco* mutants when co-cultured with WT in mixed-strain biofilms for three days. Error bars represent the standard deviation of biological triplicates. P-values were calculated using unpaired, two-tailed t tests (**, $P \leq 0.01$; ***, $P \leq 0.001$; ****, $P \leq 0.0001$). For full statistical reporting, refer to Table 4. **(B)** Time course showing relative fitness, over a period of three days, of various *cco* mutants when co-cultured with WT in mixed-strain biofilms. Results are shown for experiments in which the WT was co-cultured with various "labeled" strains, i.e. those that were engineered to constitutively express YFP. (See Figure 3—figure supplement 1 for results from experiments in which the labeled WT was co-cultured with unlabeled mutants.) Error bars represent the standard deviation of biological triplicates. **(C)** Change in thickness over three days of development for colony biofilms of WT and Δ*phz* as assessed by thin sectioning and DIC microscopy. After the onset of wrinkling, thickness was determined for the base (i.e., the "valley" between wrinkles). Error bars represent the standard deviation of biological triplicates. **(D)** O_2 profiles of colonies at selected timepoints within the first three days of biofilm development. Green, WT; yellow, Δ*phz*; gray, outside the colony (measurements made in the agar directly below the colony). Error bars denote standard deviation of biological triplicates.

CcoN4 can interact with these subunits in Cco complexes.

2.3.3: Different CcoN subunits are required for competitive fitness in early or late colony development

To further test CcoN4's contribution to growth in biofilms, we performed competition assays in which Δ*N4* and other mutants were grown as mixed-strain biofilms with the wild type. In each of these assays, one strain was labeled with constitutively-expressed YFP so that the strains could be distinguished during enumeration of colony forming units (CFUs). Experiments were performed with the label on each strain to confirm that YFP expression did not affect fitness (**Figure 2.3— figure supplement 1A**, **B**). When competitive fitness was assessed after three days of colony growth (**Figure 2.3A**), Δ*N4* cells showed a disadvantage, with the wild type outcompeting Δ*N4* by a factor of two. This was similar to the disadvantage observed for the Δ*N1*Δ*N2* mutant, further suggesting that the orphan subunit CcoN4 plays a significant role in biofilm metabolism. Remarkably, deletion of *ccoN4* in mutants already lacking *ccoN1* and *ccoN2* led to a drastic decrease in fitness, with the wild type outcompeting Δ*N1*Δ*N2*Δ*N4* by a factor of 16. This disadvantage was comparable to that observed for the mutant lacking the full *cco* operons (Δ*cco1cco2*), underscoring the importance of CcoN4-containing isoforms during biofilm growth.

To further explore the temporal dynamics of N subunit utilization, we repeated the competition assay, but sampled each day over the course of three days (**Figure 2.3B**). The fitness disadvantage that we had found for strains lacking CcoN1 and CcoN2 was evident after only one day of growth and did not significantly change after that. In contrast, the Δ*N4*-specific decline in fitness did not occur before the second day. These data suggest that the contributions of the various N subunits to biofilm metabolism differ depending on developmental stage.

DIC imaging of thin sections from wild-type colonies reveals morphological variation over depth that may result from decreasing O_2 availability (**Figure 2.3— figure supplement 1C)**. We have previously reported that three-day-old PA14 colony biofilms are hypoxic at depth (Dietrich

et al. 2013) and that O_2 availability is generally higher in thinner biofilms, such as those formed by a phenazine-null mutant (Δ*phz*). We have proposed that the utilization of phenazines as electron acceptors in wild-type biofilms enables cellular survival in the hypoxic zone and promotes colony growth (Okegbe, Price-Whelan, and Dietrich 2014). The relatively late-onset phenotype of the Δ*N4* mutant in the competition assay suggested to us that CcoN4 may play a role in survival during formation of the hypoxic colony subzone and that this zone could arise at a point between one and two days of colony growth. We measured O_2 concentrations in wild-type and Δ*phz* biofilms at specific time points over development, and found that O_2 declined similarly with depth in both strains (**Figure 2.3D**). The rate of increase in height of Δ*phz* tapered off when a hypoxic zone began to form, consistent with our model that the base does not increase in thickness when electron acceptors (O_2 or phenazines) are not available. Although we cannot pinpoint the exact depth at which the O_2 microsensor leaves the colony base and enters the underlying agar, we can estimate these values based on colony thickness measurements (**Figure 2.3C**). When we measured the thickness of wild-type and Δ*phz* biofilms over three days of incubation, we found that the values began to diverge between 30 and 48 hours of growth, after the colonies reached ~70 μm in height, which coincides with the depth at which O_2 becomes undetectable. Δ*phz* colonies reached a maximum thickness of ~80 μm, while wild-type colonies continued to grow to ~150 μm (**Figure 2.3C**). In this context, it is interesting to note that the point of divergence for the increase in wild-type and Δ*phz* colony thickness corresponds to the point at which CcoN4 becomes important for cell viability in our mixed-strain colony growth experiments (**Figure 2.3B**). We hypothesize that this threshold thickness leads to a level of O_2 limitation that is physiologically relevant for the roles of phenazines and CcoN4 in biofilm metabolism.

2.3.4: cco *genes show differential expression across biofilm subzones*

P. aeruginosa's five canonical terminal oxidases are optimized to function under and in response to distinct environmental conditions, including various levels of O_2 availability (Arai et

al. 2014; Kawakami et al. 2010; Alvarez-Ortega and Harwood 2007; Comolli and Donohue 2004). Furthermore, recent studies, along with our results, suggest that even within the Cco terminal oxidase complexes, the various N subunits may perform different functions (Hirai et al. 2016). We sought to determine whether differential regulation of *cco* genes could lead to uneven expression across biofilm subzones. To test this, we engineered reporter strains in which GFP expression is regulated by the *cco1*, *cco2*, or *ccoN4Q4* promoters. Biofilms of these strains were grown for three days, thin-sectioned, and imaged by fluorescence microscopy. Representative results are shown in the left panel of **Figure 2.4**. The right panel of **Figure 2.4** contains plotted GFP signal intensity and O_2 concentration measurements over depth for PA14 wild-type colonies. *cco1* and *ccoN4* expression patterns indicate that the Cco1 oxidase and the CcoN4 subunit are produced throughout the biofilm (**Figure 2.4**). *cco2* expression, on the other hand, is relatively low in the top portion of the biofilm and shows a sharp induction starting at a depth of ~45 μm. This observation is consistent with previous studies showing that *cco2* expression is regulated by Anr, a global transcription factor that controls gene expression in response to a shift from oxic to anoxic conditions (Comolli and Donohue 2004; Kawakami et al. 2010; Ray and Williams 1997).

Though previous studies have evaluated expression as a function of growth phase in shaken liquid cultures for *cco1* and *cco2*, this property has not been examined for *ccoN4Q4*. We monitored the fluorescence of our engineered *cco* gene reporter strains during growth under this condition in a nutrient-rich medium. As expected based on the known constitutive expression of *cco1* and Anr-dependence of *cco2* induction, we saw *cco1*-associated fluorescence increase before that associated with *cco2*. Induction of *ccoN4Q4* occurred after that of *cco1* and *cco2* (**Figure 2.4— figure supplement 1**), consistent with microarray data showing that this locus is strongly induced by O_2 limitation (Alvarez-Ortega and Harwood 2007). However, our observation that *ccoN4Q4* is expressed in the aerobic zone, where *cco2* is not expressed, in biofilms (**Figure 2.4**) suggests that an Anr-independent mechanism functions to induce this operon during multicellular growth.

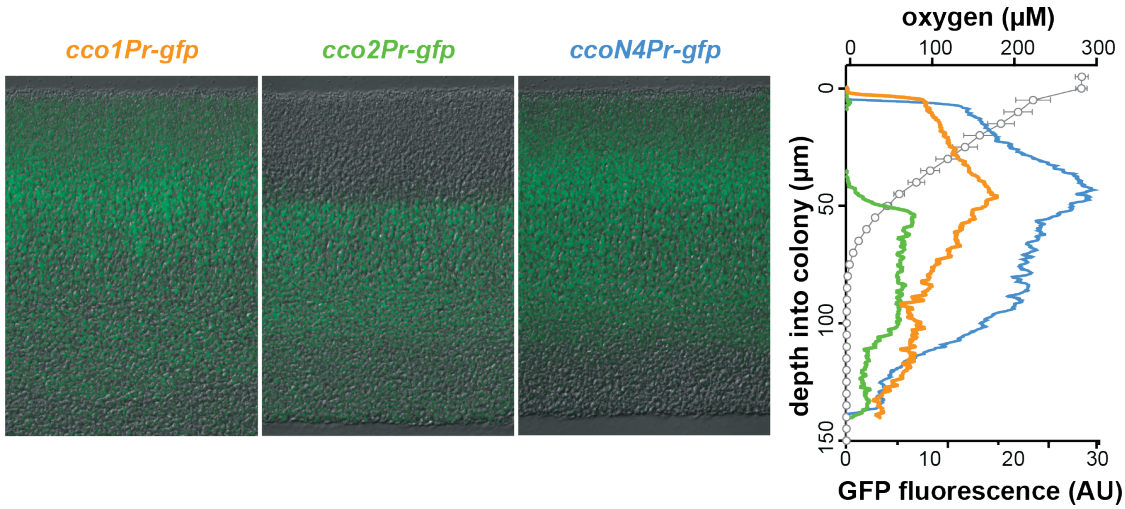

Figure 2.4. *cco* genes are differentially expressed over biofilm depth. Left: Representative images of thin sections prepared from WT biofilms grown for three days. Each biofilm is expressing a translational GFP reporter under the control of the *cco1*, *cco2*, or *ccoQ4N4* promoter. Reporter fluorescence is shown in green and overlain on respective DIC images. Right: Fluorescence values corresponding to images on the left. Fluorescence values for a strain containing the *gfp* gene without a promoter (the empty MCS control) have been subtracted from each respective plot. O_2 concentration over depth (open circles) from three-day-old WT biofilms is also shown. Error bars represent the standard deviation of biological triplicates and are not shown in cases where they would be obscured by the point markers. y-axis in the right panel provides a scale bar for the left panel. Reporter fluorescence images and values are representative of four biological replicates.

Our results indicate that different Cco isoforms may function in specific biofilm subzones, but that CcoN4-containing isoforms could potentially form throughout the biofilm. These data, together with our observation that Δ*N4* biofilms exhibit a fitness disadvantage from day two (**Figure 2.3B**), led us to more closely examine the development and chemical characteristics of the biofilm over depth.

2.3.5: Microelectrode-based redox profiling reveals differential phenazine reduction activity in wild-type and cco *mutant biofilms*

The results shown in **Figure 2.2B** implicate CcoN4-containing isoforms in the reduction of TTC, a small molecule that interacts with the respiratory chain (Rich et al. 2001). Similar activities have been demonstrated for phenazines, including the synthetic compound phenazine methosulfate (PMS) (Nachlas, Margulies, and Seligman 1960) and those produced naturally by *P. aeruginosa* (Armstrong and Stewart-Tull 1971). Given that CcoN4 and phenazines function to

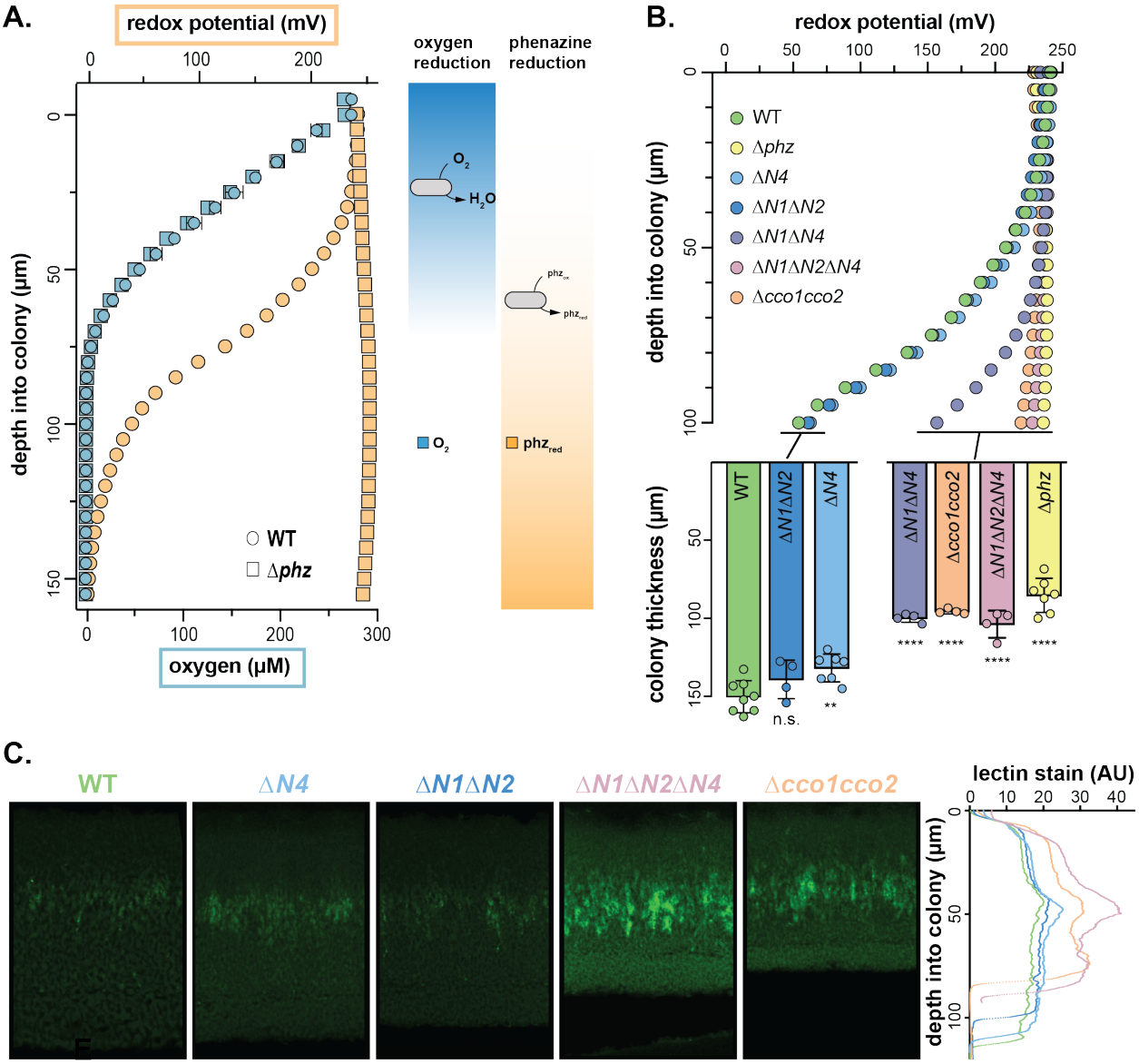

Figure 2.5. Characterization of chemical gradients and matrix distribution in PA14 WT and mutant colony biofilms. (A) Left: Change in O_2 concentration (blue) and redox potential (orange) with depth for WT and Δ*phz* biofilms grown for two days. For O_2 profiles, error bars represent the standard deviation of biological triplicates. For redox profiles, data are representative of at least five biological replicates. Right: model depicting the distribution of O_2 and reduced vs. oxidized phenazines in biofilms. **(B)** Top: Change in redox potential with depth for WT and various mutant biofilms grown for two days. Data are representative of at least five biological replicates. Bottom: Thickness of three-day-old colony biofilms of the indicated strains. Bars represent the average of the plotted data points (each point representing one biological replicate, n ≥ 4), and error bars represent the standard deviation. P-values were calculated using unpaired, two-tailed t tests comparing each mutant to WT (n.s., not significant; **, P ≤ 0.01; ****, P ≤ 0.0001). For full statistical reporting, refer to Table 4. **(C)** Left: Representative thin sections of WT and *cco* mutant biofilms, stained with lectin and imaged by fluorescence microscopy. Biofilms were grown for two days before sampling. Right: Relative quantification of lectin stain signal intensity. Coloration of strain names in the left panel provides a key for the plotted data, and the y-axis in the right panel provides a scale bar for the left panel. Lectin-staining images and values are representative of four biological replicates.

influence morphogenesis at similar stages of biofilm growth (**Figures 2.2A**, **3**, **Figure 2.2— figure supplement 1**, **Figure 2.3— figure supplement 1A**, **B**), we wondered whether the role of CcoN4 in biofilm development was linked to phenazine metabolism. We used a Unisense platinum microelectrode with a 20-30 μm tip to measure the extracellular redox potential in biofilms as a function of depth. This electrode measures the inclination of the sample to donate or accept electrons relative to a Ag/AgCl reference electrode. We found that wild-type colonies showed a decrease in redox potential over depth, indicating an increased ratio of reduced to oxidized phenazines, while the redox potential of Δ*phz* colonies remained unchanged (**Figure 2.5A**). To confirm that phenazines are the primary determinant of the measured redox potential in the wild type, we grew Δ*phz* colonies on medium containing PMS (which resembles the natural phenazines that regulate *P. aeruginosa* colony morphogenesis (Sakhtah et al. 2016)), and found that these colonies yielded redox profiles similar to those of the wild type (**Figure 2.5 — figure supplement 1A**). Therefore, though the microelectrode we employed is capable of interacting with many redox-active substrates, we found that its signal was primarily determined by phenazines in our system. In addition, while wild-type colonies showed rapid decreases in O_2 availability starting at the surface, the strongest decrease in redox potential was detected after ~50 μm (**Figure 2.5A**). These results suggest that the bacteria residing in the biofilm differentially utilize O_2 and phenazines depending on their position and that O_2 is the preferred electron acceptor.

We hypothesized that one or more of the CcoN subunits encoded by the PA14 genome is required for phenazine reduction and tested this by measuring the redox potential over depth for a series of *cco* mutants (**Figure 2.5B**, **top**). We saw very little reduction of phenazines in the Δ*cco1cco2* colony, suggesting that *cbb*$_3$-type oxidases are required for this activity. In contrast, the mutant lacking the catalytic subunits of Cco1 and Cco2, Δ*N1*Δ*N2*, showed a redox profile similar to the wild type, indicating that isoforms containing one or both of the orphan CcoN subunits could support phenazine reduction activity. Indeed, although redox profiles obtained for the Δ*N1*Δ*N2* and Δ*N4* mutants were similar to those obtained for the wild type, the redox profile

of the Δ*N1*Δ*N2*Δ*N4* mutant recapitulated that of Δ*cco1cco2.* These results indicate redundancy in the roles of some of the CcoN subunits. Consistent with this, Δ*N1*Δ*N4* showed an intermediate defect in phenazine reduction. We note that the triple mutant Δ*cox*Δ*cyo*Δ*cio* showed a wild-type-like redox profile, indicating that the cbb_3-type terminal oxidases are sufficient for normal phenazine reduction (**Figure 2.5— figure supplement 1B**). Extraction and measurement of phenazines released from wild-type and *cco* mutant biofilms showed that variations in redox profiles could not be attributed to differences in phenazine production (**Figure 2.5— figure supplement 1C**).

Our group has previously shown that a Δ*phz* mutant compensates for its lack of phenazines by forming thinner colonies, thus limiting the development of the hypoxic subzone seen in the wild type (Dietrich et al. 2013). We therefore hypothesized that mutants unable to reduce phenazines would likewise result in thinner colonies. Indeed, we observed that the *cco* mutants that lacked phenazine reduction profiles in the top panel of **Figure 2.5B** produced biofilms that were significantly thinner than wild-type and comparable to that of the Δ*phz* mutant (**Figure 2.5B**, **bottom**).

Our group has also reported that reduction of nitrate, an alternate electron acceptor for *P. aeruginosa* (Williams, Zlosnik, and Ryall 2007), can serve as an additional redox-balancing strategy for cells in biofilms (Dietrich et al. 2013). Colony wrinkling is stimulated by a reduced cellular redox state; thus, provision of nitrate in the growth medium inhibits colony feature formation. We hypothesized that nitrate reduction could compensate for defects in O_2 and phenazine reduction and inhibit colony wrinkling in the *cco* mutants that are the focus of this study. To test this, we grew strains on medium containing 10 or 40 mM potassium nitrate. We found that 10 mM nitrate was sufficient to inhibit wrinkling for up to 4 days of incubation in the wild type, Δ*N4*, and Δ*N1*Δ*N4*, but that Δ*phz* and Δ*N1*Δ*N2*Δ*N4* had initiated wrinkling at this point (**Figure 2.5— figure supplement 1D)**. When we grew these strains on medium containing 40 mM nitrate, we saw increased inhibition of wrinkling such that the wild type, Δ*phz*, Δ*N4*, and Δ*N1*Δ*N4* remained completely smooth at 4 days of incubation. Though Δ*N1*Δ*N2*Δ*N4* had shown

some feature formation after 4 days on this medium, it was diminished relative to the same point on 10 mM nitrate. These results suggest that O_2 reduction, phenazine reduction, and nitrate reduction can operate in synchrony to oxidize the redox states of cells in biofilms and that provision of nitrate can compensate for defects in O_2 and phenazine reduction to enable maintenance of redox homeostasis.

2.3.6: Wild-type and cco *mutant colony biofilms show increased matrix production at a consistent depth*

We have recently demonstrated that extracellular matrix production, a hallmark of biofilm formation, is regulated by redox state in PA14 colony biofilms. Increased matrix production correlates with the accumulation of reducing power (as indicated by higher cellular NADH/NAD^+ ratios) due to electron acceptor limitation and is visible in the hypoxic region of Δ*phz* colonies (Dietrich et al. 2013; Okegbe et al. 2017). The morphologies of our *cco* mutants (**Figure 2.2A**) suggest that matrix production can also be induced by respiratory chain dysfunction, which may be linked to defects in phenazine utilization (**Figure 2.5B**). To further examine the relationships between Cco isoforms and redox imbalance in biofilms, we prepared thin sections from two day-old colonies and stained with fluorescein-labeled lectin, which binds preferentially to the Pel polysaccharide component of the matrix (Jennings et al. 2015). Consistent with their similar gross morphologies, the wild-type and Δ*N1*Δ*N2* biofilms showed similar patterns of staining, with a faint band of higher intensity at a depth of ~40 μm (**Figure 2.5C**). Δ*N4* also showed a similar pattern, with a slightly higher intensity of staining in this band. Δ*N1*Δ*N2*Δ*N4* and Δ*cco1cco2* showed more staining throughout each sample, with wider bands of greater intensity at the ~40 μm point. These data suggest that deletion of the Cco complexes leads to a more reduced biofilm, which induces production of more matrix, and that CcoN4 contributes significantly to maintaining redox homeostasis when O_2 is limiting.

2.3.7: ccoN4 contributes to P. aeruginosa *virulence in a* C. elegans *slow killing model*

We have previously shown that a mutant defective in biofilm-specific phenazine production, which also shows altered colony morphology (Dietrich et al. 2008, 2013), exhibits decreased virulence (Recinos et al. 2012). We and others have suggested that one way in which phenazines could contribute to virulence is by acting as electron acceptors to balance the intracellular redox state in the hypoxic conditions that are encountered during infection (Price-Whelan, Dietrich, and Newman 2006; Newman 2008; Dietrich et al. 2013). Because CcoN4 is required for wild-type biofilm architecture and respiration (**Figures 2.2A**, **2.2C**, and **2.5C**), we hypothesized that it could also contribute to virulence. To test this, we conducted virulence assays using the nematode *Caenorhabditis elegans* as a host. It has been shown that *P. aeruginosa* is pathogenic to *C. elegans* and that the slow killing assay mimics an infection-like killing of *C. elegans* by the bacterium (Tan, Mahajan-Miklos, and Ausubel 1999). While Δ*N1*Δ*N2* killed with wild type-like kinetics, Δ*N1*Δ*N2*Δ*N4* and Δ*cco1cco2* both showed comparably-impaired killing relative to wild-type PA14 (**Figure 2.6**).

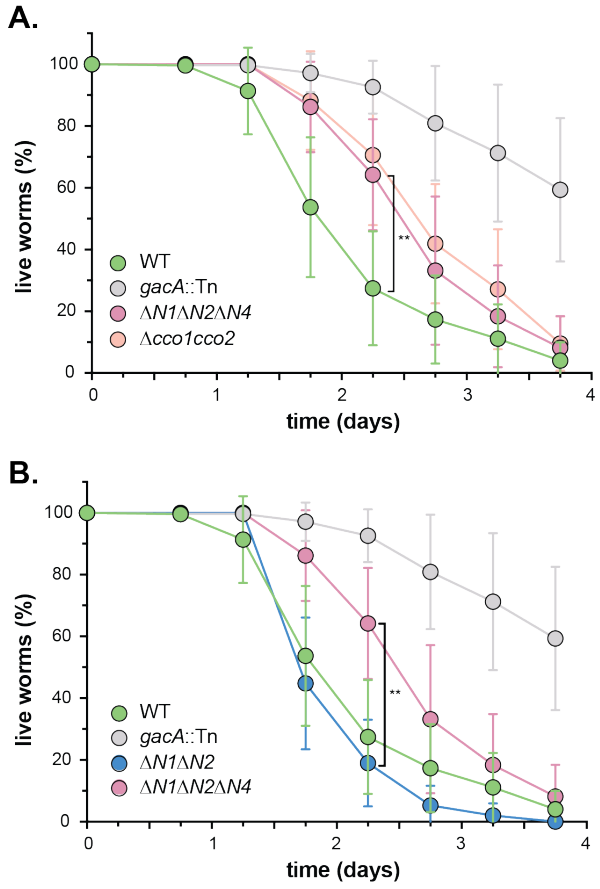

Figure 2.6. CcoN4-containing isoform(s) make unique contributions to PA14 virulence. Slow-killing kinetics of WT, *gacA*, and various *cco* mutant strains in the nematode *Caenorhabditis elegans*. Nearly 100% of the *C. elegans* population exposed to WT PA14 is killed after four days of exposure to the bacterium, while a mutant lacking GacA, a regulator that controls expression of virulence genes in *P. aeruginosa*, shows decreased killing, with ~50% of worms alive four days post-exposure. **(A)** Δ*N1*Δ*N2*Δ*N4* and Δ*cco1cco2* show comparably attenuated pathogenicity relative to WT. Error bars represent the standard deviation of at least six biological replicates. At 2.25 days post-exposure, significantly less *C. elegans* were killed by Δ*N1*Δ*N2*Δ*N4* than by WT (unpaired two-tailed t test; p = 0.0022). **(B)** Δ*N1*Δ*N2* displays only slightly reduced pathogenicity when compared to WT. At 2.25 days post-exposure, significantly more *C. elegans* were killed by Δ*N1*Δ*N2* than by Δ*N1*Δ*N2*Δ*N4* (unpaired two-tailed t test; p = 0.003). For full statistical reporting, refer to Table 4. Error bars represent the standard deviation of at least four biological replicates, each with a starting sample size of 30-35 worms per replicate.

2.4: Discussion

Biofilm formation contributes to *P. aeruginosa* pathogenicity and persistence during different types of infections, including the chronic lung colonizations seen in individuals with cystic fibrosis (Tolker-Nielsen 2014; Rybtke et al. 2015). The conditions found within biofilm microenvironments are distinct from those in well-mixed liquid cultures with respect to availability of electron donors and acceptors. We have previously described the roles of phenazines, electron-shuttling antibiotics produced by *P. aeruginosa*, in biofilm-specific metabolism. In this study, we focused on *P. aeruginosa*'s large complement of genes encoding *cbb*$_3$-type cytochrome oxidase subunits and set out to test their contributions to metabolic electron flow in biofilms.

The *P. aeruginosa* genome contains four different homologs of *ccoN*, encoding the catalytic subunit of *cbb*$_3$-type oxidase. Only two of these (*ccoN1* and *ccoN2*) are co-transcribed with a *ccoO* homolog, encoding the other critical component of an active *cbb*$_3$-type oxidase (**Figure 2.1B**). However, genetic studies have demonstrated that all four versions of CcoN can form functional complexes when expressed with either of the two CcoO homologs (Hirai et al. 2016). In well-mixed liquid cultures, mutants lacking the "orphan" subunits did not show growth defects (**Figure 2.2C**) (Hirai et al. 2016). We were therefore surprised to find that the Δ*N4* mutant showed a unique morphotype in a colony biofilm assay (**Figure 2.2A**, **Figure 2.2—figure supplement 1A**). We have applied this assay extensively in our studies of the mechanisms underlying cellular redox balancing and sensing and noted that the phenotype of Δ*N4* was similar to that of mutants with defects in electron shuttling and redox signaling (Dietrich et al. 2013; Okegbe et al. 2017).

We characterized the effects of a Δ*N4* mutation on biofilm physiology through a series of assays. In well-mixed liquid cultures, Δ*cco1cco2* showed a growth phenotype similar to that of Δ*N1*Δ*N2*. While Hirai et al. have shown that wild-type *P. aeruginosa* cultures grown planktonically do form Cco heterocomplexes containing CcoN4, our observations suggest that such complexes do not contribute significantly to growth under these conditions. Consistent with

this, deleting *ccoN4* in the Δ*N1*Δ*N2* background had no effect on planktonic growth (**Figure 2.2C**). However, in biofilm-based experiments, we found that deleting *N4* alone was sufficient to cause an altered morphology phenotype (**Figure 2.2A** and **Figure 2.2— figure supplement 1A**), and that deleting *N4* in either a Δ*N1* or a Δ*N1*Δ*N2* background profoundly affected biofilm physiology. These experiments included quantification of respiratory activity in colonies, in which deletion of CcoN4 led to a significant decrease (**Figure 2.2B**); biofilm co-culturing, in which CcoN4 was required for competitive fitness (**Figure 2.3A** and **B**, **Figure 2.3— figure supplement 1**); redox profiling, which showed that CcoN4 can contribute to phenazine reduction (**Figure 2.5B, top**); colony thickness measurements, which showed that CcoN4 is required for the formation of the hypoxic and anoxic zones (**Figure 2.5B, bottom**); and matrix profiling, which showed that CcoN4 contributes to the repression of Pel polysaccharide production (**Figure 2.5C**). The overlap in zones of expression between *cco1*, *cco2*, and *ccoN4Q4* seen in colony thin sections (**Figure 2.4**) implies that CcoN4 can form heterocomplexes with Cco1 and Cco2 subunits that span the depth of the colony and function to influence the physiology of *P. aeruginosa* biofilms in these ways.

The mutant phenotypes and gene expression profiles reported in this study suggest roles for CcoN4 in O_2 and phenazine reduction specifically in the biofilm context, and allow us to draw conclusions about the roles of other CcoN subunits. The expression of *ccoN4Q4* throughout the biofilm depth suggests that CcoN4-containing isoforms could contribute to cytochrome *c* oxidation in both oxic and hypoxic zones (**Figure 2.4**). This constitutes a deviation from the previously published observation that these genes are specifically induced in hypoxic liquid cultures when compared to well-aerated ones (Alvarez-Ortega and Harwood 2007). Therefore, the *ccoN4Q4* expression we observed in the relatively oxic, upper portion of the colony may be specific to biofilms.

Δ*N4* displayed a colony morphology indicative of redox stress and had a fitness disadvantage compared to the wild type (**Figures 2.2A**, **2.3A** and **B**, **Figure 2.5B**, **bottom**, **Figure 2.3— figure supplement 1**). However, because it did not show a defect in phenazine

reduction (**Figure 2.5B**, **top**), we attribute its colony morphology and impaired fitness phenotypes to its proposed role in O_2 reduction (Hirai et al. 2016). Similarly, *ΔN1ΔN2* showed reduced fitness compared to the wild type (**Figure 2.3A** and **B**, **Figure 2.3— figure supplement 1**) while showing phenazine reduction comparable to that of the wild type (**Figure 2.5B**), implying that one or both of these subunits contribute to oxygen reduction in biofilms. When CcoN4 was deleted in conjunction with CcoN1 and CcoN2, however, the resulting strain showed a severe phenazine reduction defect, a phenotype recapitulated by deleting both *cco* operons (**Figure 2.5B**). Thus, our observations suggest a role for the cbb_3-type oxidases in phenazine reduction in addition to their established roles in O_2 reduction, thereby expanding our understanding of their overall contributions *P. aeruginosa*'s physiology and viability.

The results described here can inform our model of how cells survive under distinct conditions in the microenvironments within biofilms. Previous work has shown that pyruvate fermentation can support survival of *P. aeruginosa* under anoxic conditions (Eschbach et al. 2004) and that phenazines facilitate this process (Glasser, Kern, and Newman 2014). Additional research suggests that phenazine reduction is catalyzed adventitiously by *P. aeruginosa* flavoproteins and dehydrogenases (Glasser et al. 2017). Our observation that cbb_3-type cytochrome oxidases, particularly those containing the CcoN1 or CcoN4 subunits, were required for phenazine reduction in hypoxic biofilm subzones (**Figure 2.5B**) further implicates the electron transport chain in utilization of these compounds. It is also interesting in light of the historical roles of phenazines acting as mediators in biochemical studies of the cytochrome bc_1 complex and cytochrome oxidases (King 1963; Armstrong and Stewart-Tull 1971; Davidson et al. 1992). Based on this earlier work, we can speculate that different CcoN subunits may indirectly influence phenazine reduction, which could occur at the cytochrome *c* binding site of the CcoO subunit or elsewhere in the electron transport chain, through effects these CcoN subunits have on the overall function or stability of respiratory complexes. Ultimately, various mechanisms of phenazine reduction and phenazine-related metabolisms may be relevant at different biofilm depths or depending on electron donor availability. Our results suggest that, in

the colony biofilm system, enzyme complexes traditionally considered to be specific to oxygen reduction may contribute to anaerobic survival.

Because biofilm formation is often associated with colonization of and persistence in hosts, we tested whether CcoN4 contributes to *P. aeruginosa* pathogenicity in *C. elegans*. Similar to our observations in biofilm assays, we found that the Δ*cco1cco2* mutant displayed a more severe phenotype than the Δ*N1*Δ*N2* mutant, suggesting that an orphan subunit can substitute for those encoded by the *cco1* and *cco2* operons. We also found that deleting *ccoN4* in Δ*N1*Δ*N2* led to a Δ*cco1cco2*-like phenotype, suggesting that CcoN4 is the subunit that can play this role (**Figure 2.6**). In host microenvironments where O_2 is available, CcoN4-containing isoforms could contribute to its reduction. Additionally, in hypoxic zones, CcoN4-containing isoforms could facilitate the reduction of phenazines, enabling cellular redox balancing. Both of these functions would contribute to persistence of the bacterium within the host. The contributions of the *cbb*$_3$-type oxidases to *P. aeruginosa* pathogenicity raise the possibility that compounds interfering with Cco enzyme function could be effective therapies for these infections. Such drugs would be attractive candidates due to their specificity for bacterial respiratory chains and, as such, would not affect the host's endogenous respiratory enzymes.

Our discovery that an orphan *cbb*$_3$-type oxidase subunit contributes to growth in biofilms further expands the picture of *P. aeruginosa*'s remarkable respiratory flexibility. Beyond modularity at the level of the terminal enzyme complex (e.g., utilization of an *aa*$_3$- vs. a *cbb*$_3$-type oxidase), the activity of *P. aeruginosa*'s respiratory chain is further influenced by substitution of orphan *cbb*$_3$-type catalytic subunits for native ones. Utilization of CcoN4-containing isoforms promotes phenazine reduction activity and may influence aerobic respiration in *P. aeruginosa* biofilms. For the exceptional species that contain orphan *cbb*$_3$-type catalytic subunits, this fine level of control could be particularly advantageous during growth and survival in environments covering a wide range of electron acceptor availability (Cowley et al. 2015).

2.5: Materials and methods

2.5.1: Bacterial strains and growth conditions

P. aeruginosa strain UCBPP-PA14 (Rahme et al. 1995) was routinely grown in lysogeny broth (LB; 1% tryptone, 1% NaCl, 0.5% yeast extract) (Bertani 2004) at 37 ˚C with shaking at 250 rpm unless otherwise indicated. Overnight cultures were grown for 12-16 hours. For genetic manipulation, strains were typically grown on LB solidified with 1.5% agar. Strains used in this study are listed in **Table 2.3**. In general, liquid precultures served as inocula for experiments. Overnight precultures for biological replicates were started from separate clonal source colonies on streaked agar plates. For technical replicates, a single preculture served as the source inoculum for subcultures.

2.5.2: Construction of mutant P. aeruginosa *strains*

For making markerless deletion mutants in *P. aeruginosa* PA14 (**Table 2.3**) 1 kb of flanking sequence from each side of the target gene were amplified using the primers listed in **Table 2.1** and inserted into pMQ30 through gap repair cloning in *Saccharomyces cerevisiae* InvSc1 (Shanks et al. 2006). Each plasmid listed in **Table 2.2** was transformed into *Escherichia coli* strain UQ950, verified by restriction digests, and moved into PA14 using biparental conjugation. PA14 single recombinants were selected on LB agar plates containing 100 µg/ml gentamicin. Double recombinants (markerless deletions) were selected on LB without NaCl and modified to contain 10% sucrose. Genotypes of deletion mutants were confirmed by PCR. Combinatorial mutants were constructed by using single mutants as hosts for biparental conjugation, with the exception of ∆*cco1cco2*, which was constructed by deleting the *cco1* and *cco2* operons simultaneously as one fragment. *ccoN4* complementation strains were made in the same manner, using primers LD438 and LD441 listed in **Table 2.1** to amplify the coding sequence of *ccoN4*, which was verified by sequencing and complemented back into the site of the deletion.

2.5.3: Colony biofilm morphology assays

Overnight precultures were diluted 1:100 in LB (Δ*N1*Δ*N2*, Δ*N1*Δ*N2*Δ*N3*, Δ*N1*Δ*N2*Δ*N4*, Δ*N1*Δ*N2*Δ*N4*Δ*N3*, Δ*N1*Δ*N2*Δ*N4::N4*, Δ*cco1cco2*, Δ*N1*Δ*N2*Δ*hcn*, Δ*N1*Δ*N2*Δ*N4*Δ*hcn*, Δ*cco1cco2*Δ*hcn*, and Δ*cox*Δ*cyo*Δ*cio* were diluted 1:50) and grown to mid-exponential phase (OD at 500 nm ≈ 0.5). Ten microliters of subcultures were spotted onto 60 mL of colony morphology medium (1% tryptone, 1% agar [Teknova A7777] containing 40 µg/ml Congo red dye [VWR AAAB24310-14] and 20 µg/ml Coomassie blue dye [Omnipur; VWR EM-3300]) in a 10 cm x 10 cm x 1.5 cm square Petri dish (LDP D210-16). For preparation of biofilms grown on on phenazine methosulfate (PMS), colony morphology medium was supplemented with 200 µM PMS (Amresco 0361) after autoclaving. For nitrate experiments, colony morphology medium was supplemented with 0, 10, or 40 mM potassium nitrate. Plates were incubated for up to five days at 25 ˚C with > 90% humidity (Percival CU-22L) and imaged daily using a Keyence VHX-1000 digital microscope. Images shown are representative of at least ten biological replicates. 3D images of biofilms were taken on day 5 of development using a Keyence VR-3100 wide-area 3D measurement system. Δ*cox*Δ*cyo*Δ*cio*, *hcn* deletion mutants, and strains grown for the nitrate experiment were imaged using a flatbed scanner (Epson E11000XL-GA) and are representative of at least three biological replicates

2.5.4: TTC reduction assay

One microliter of overnight cultures (five biological replicates), grown as described above, was spotted onto a 1% tryptone, 1.5% agar plate containing 0.001% (w/v) TTC (2,3,5-triphenyl-tetrazolium chloride [Sigma-Aldrich T8877]) and incubated in the dark at 25 ˚C for 24 hours. Spots were imaged using a scanner (Epson E11000XL-GA) and TTC reduction, normalized to colony area, was quantified using Adobe Photoshop CS5. Colorless TTC undergoes an irreversible color change to red when reduced. Pixels in the red color range were quantified and normalized to colony area using Photoshop CS5.

2.5.5: Liquid culture growth assays

(i) Overnight precultures were diluted 1:100 (Δ*N1*Δ*N2*, Δ*N1*Δ*N2*Δ*N4*, and Δ*cco1cco2* were diluted 1:50) in 1% tryptone in a clear- flat-bottom polystyrene 96-well plate (VWR 82050-716) and grown for two hours (OD_{500nm} ≈ 0.2). These cultures were then diluted 100-fold in 1% tryptone in a new 96-well plate and incubated at 37 °C with continuous shaking on the medium setting in a Biotek Synergy 4 plate reader. Growth was assessed by taking OD readings at 500 nm every thirty minutes for at least 24 hours.

(ii) *hcn* mutants: Overnight precultures were diluted 1:100 (Δ*N1*Δ*N2*Δ*hcn*, Δ*N1*Δ*N2*Δ*N4*Δ*hcn*, and Δ*cco1cco2*Δ*hcn* were diluted 1:50) in MOPS minimal medium (50 mM 4-morpholinepropanesulfonic acid (pH 7.2), 43 mM NaCl, 93 mM NH_4Cl, 2.2 mM KH_2PO4, 1 mM $MgSO_4•7H_2O$, 1 µg/ml $FeSO_4•7H_2O$, 20 mM sodium succinate hexahydrate) and grown for 2.5 hours until OD at 500 nm ≈ 0.1. These cultures were then diluted 100-fold in MOPS minimal medium in a clear, flat-bottom polystyrene 96-well plate and incubated at 37 °C with continuous shaking on the medium setting in a Biotek Synergy 4 plate reader. Growth was assessed by taking OD readings at 500 nm every thirty minutes for at least 24 hours.

(iii) Terminal oxidase reporters: Overnight precultures were grown in biological triplicate; each biological triplicate was grown in technical duplicate. Overnight precultures were diluted 1:100 in 1% tryptone and grown for 2.5 hours until OD at 500 nm ≈ 0.1. These cultures were then diluted 100-fold in 1% tryptone in a clear, flat-bottom, polystyrene black 96-well plate (VWR 82050-756) and incubated at 37 °C with continuous shaking on the medium setting in a Biotek Synergy 4 plate reader. Expression of GFP was assessed by taking fluorescence readings at excitation and emission wavelengths of 480 nm and 510 nm, respectively, every hour for 24 hours. Growth was assessed by taking OD readings at 500 nm every 30 minutes for 24 hours. Growth and RFU values for technical duplicates were averaged to obtain the respective values for each biological replicate. RFU values for a strain without a promoter inserted upstream of the *gfp* gene (MCS-*gfp*) were considered background and subtracted from the fluorescence values of each reporter.

2.5.6: Competition assays

Overnight precultures of fluorescent (YFP-expressing) and non-fluorescent strains were diluted 1:100 in LB (Δ*N1*Δ*N2*, Δ*N1*Δ*N2*Δ*N4* and Δ*cco1cco2* were diluted 1:50) and grown to mid-exponential phase (OD at 500 nm ≈ 0.5). Exact OD at 500 nm values were read in a Spectronic 20D+ spectrophotometer (Thermo Scientific) and cultures were adjusted to the same OD. Adjusted cultures were then mixed in a 1:1 ratio of fluorescent:non-fluorescent cells and ten µl of this mixture were spotted onto colony morphology plates and grown for three days as described above. At specified time points, biofilms were collected, suspended in one mL of 1% tryptone, and homogenized on the "high" setting in a bead mill homogenizer (Omni Bead Ruptor 12); day one colonies were homogenized for 35 seconds while days two and three colonies were homogenized for 99 seconds. Homogenized cells were serially diluted and 10^{-6}, 10^{-7}, and 10^{-8} dilutions were plated onto 1% tryptone plates and grown overnight at 37 °C. Fluorescent colony counts were determined by imaging plates with a Typhoon FLA7000 fluorescent scanner (GE Healthcare) and percentages of fluorescent vs. non-fluorescent colonies were determined.

2.5.7: Construction of terminal oxidase reporters

Translational reporter constructs for the Cco1, Cco2, and CcoN4Q4 operons were constructed using primers listed in **Table 2.1**. Respective primers were used to amplify promoter regions (500 bp upstream of the operon of interest), adding an SpeI digest site to the 5' end of the promoter and an XhoI digest site to the 3' end of the promoter. Purified PCR products were digested and ligated into the multiple cloning site (MCS) of the pLD2722 vector, upstream of the *gfp* sequence. Plasmids were transformed into *E. coli* strain UQ950, verified by sequencing, and moved into PA14 using biparental conjugation with *E. coli* strain S17-1. PA14 single recombinants were selected on M9 minimal medium agar plates (47.8 mM Na_2HPO_4•$7H_2O$, 22 mM KH_2PO_4, 8.6 mM NaCl, 18.6 mM NH_4Cl, 1 mM $MgSO_4$, 0.1 mM $CaCl_2$, 20 mM sodium citrate dihydrate, 1.5% agar) containing 100 µg/ml gentamicin. The plasmid backbone was resolved out of PA14 using Flp-FRT recombination by introduction of the pFLP2 plasmid (Hoang

et al. 1998) and selected on M9 minimal medium agar plates containing 300 µg/ml carbenicillin and further on LB agar plates without NaCl and modified to contain 10% sucrose. The presence of *gfp* in the final clones was confirmed by PCR.

2.5.8: Thin sectioning analyses

Two layers of 1% tryptone with 1% agar were poured to depths of 4.5 mm (bottom) and 1.5 mm (top). Overnight precultures were diluted 1:100 (Δ*N1*Δ*N2*, Δ*N1*Δ*N4*, Δ*N1*Δ*N2*Δ*N4,* Δ*cco1cco2* were diluted 1:50) in LB and grown for two hours, until early-mid exponential phase. Five to ten µL of subculture were then spotted onto the top agar layer and colonies were incubated in the dark at 25 ˚C with > 90% humidity (Percival CU-22L) and grown for up to three days. At specified time points to be prepared for thin sectioning, colonies were covered by a 1.5-mm-thick 1% agar layer. Colonies sandwiched between two 1.5-mm agar layers were lifted from the bottom layer and soaked for four hours in 50 mM L-lysine in phosphate buffered saline (PBS) (pH 7.4) at 4 ˚C, then fixed in 4% paraformaldehyde, 50 mM L-lysine, PBS (pH 7.4) for four hours at 4˚C, then overnight at 37 °C. Fixed colonies were washed twice in PBS and dehydrated through a series of ethanol washes (25%, 50%, 70%, 95%, 3x 100% ethanol) for 60 minutes each. Colonies were cleared via three 60-minute incubations in Histoclear-II (National Diagnostics HS-202) and infiltrated with wax via two separate washes of 100% Paraplast Xtra paraffin wax (Electron Microscopy Sciences; Fisher Scientific 50-276-89) for two hours each at 55 ˚C, then colonies were allowed to polymerize overnight at 4 ˚C. Tissue processing was performed using an STP120 Tissue Processor (Thermo Fisher Scientific 813150). Trimmed blocks were sectioned in ten µm-thick sections perpendicular to the plane of the colony using an automatic microtome (Thermo Fisher Scientific 905200ER), floated onto water at 45 ˚C, and collected onto slides. Slides were air-dried overnight, heat-fixed on a hotplate for one hour at 45 ˚C, and rehydrated in the reverse order of processing. Rehydrated colonies were immediately mounted in TRIS-Buffered DAPI:Fluorogel (Electron Microscopy Sciences; Fisher Scientific 50-246-93) and overlaid with a coverslip. Differential interference contrast (DIC) and fluorescent

confocal images were captured using an LSM700 confocal microscope (Zeiss). Each strain was prepared in this manner in at least biological triplicates.

2.5.9: Colony thickness measurements

Colonies were prepared for thin sectioning as described above, but growth medium was supplemented with 40 µg/ml Congo Red dye and 20 µg/ml Coomassie Blue dye. Colony height measurements were obtained from confocal DIC images using Fiji image processing software (Schindelin et al. 2012).

2.5.10: Lectin staining

Two-day-old colonies were prepared for thin sectioning as described above. Rehydrated colonies were post-stained in 100 µg/mL fluorescein-labeled *Wisteria floribunda* lectin (Vector Laboratories FL-1351) in PBS before being washed twice in PBS, mounted in TRIS-buffered DAPI and overlaid with a coverslip. Fluorescent confocal images were captured using an LSM700 confocal microscope (Zeiss).

2.5.11: Redox profiling of biofilms

A 25 µm-tip redox microelectrode and external reference (Unisense RD-25 and REF-RM) were used to measure the extracellular redox state of day two (~ 48 h) biofilms (grown as for the colony biofilm morphology assays). The redox microelectrode measures the tendency of a sample to take up or release electrons relative to the reference electrode, which is immersed in the same medium as the one on which the sample is grown. The redox microelectrode was calibrated according to manufacturer's instructions using a two-point calibration to 1% quinhydrone in pH 4 buffer and 1% quinhydrone in pH 7 buffer. Redox measurements were taken every five µm throughout the depth of the biofilm using a micromanipulator (Unisense MM33) with a measurement time of three seconds and a wait time between measurements of

five seconds. Profiles were recorded using a multimeter (Unisense) and the SensorTrace Profiling software (Unisense).

2.5.12: Oxygen profiling of biofilms

A 25 µm-tip oxygen microsensor (Unisense OX-25) was used to measure oxygen concentrations within biofilms during the first two days of development, grown as described above. For oxygen profiling on three-day-old colonies (**Figure 2.4**), biofilms were grown as for the thin sectioning analyses. To calibrate the oxygen microsensor, a two-point calibration was used. The oxygen microsensor was calibrated first to atmospheric oxygen using a calibration chamber (Unisense CAL300) containing water continuously bubbled with air. The microsensor was then calibrated to a "zero" point using an anoxic solution of water thoroughly bubbled with N_2; to ensure complete removal of all oxygen, N_2 was bubbled into the calibration chamber for a minimum of 30 minutes before calibrating the microsensor to the zero calibration point. Oxygen measurements were then taken throughout the depth of the biofilm using a measurement time of three seconds and a wait time between measurements of five seconds. For six-hour-old colonies, a step size of one µm was used to profile through the entire colony; for 12-hour and 24-hour colonies, two µm; for 48-hour colonies, five µm. A micromanipulator (Unisense MM33) was used to move the microsensor within the biofilm and profiles were recorded using a multimeter (Unisense) and the SensorTrace Profiling software (Unisense).

2.5.13: Phenazine quantification

Overnight precultures were diluted 1:10 in LB and spotted onto a 25- mm 0.2 µm filter disk (pore size: 0.2 µm; GE Healthcare 110606) placed into the center of one 35 x 10 mm round Petri dish (Falcon 351008). Colonies were grown for two days in the dark at 25 ˚C with > 90% humidity. After two days of growth, each colony (with filter disk) was lifted off its respective plate and weighed. Excreted phenazines were then extracted from the agar medium overnight in five mL of 100% methanol (in the dark, nutating at room temperature). Three hundred µl of this

overnight phenazine/methanol extraction were then filtered through a 0.22 µm cellulose Spin-X column (Thermo Fisher Scientific 07-200-386) and 200 µl of the flow-through were loaded into an HPLC vial. Phenazines were quantified using high-performance liquid chromatography (Agilent 1100 HPLC System) as described previously (Dietrich et al. 2006; Sakhtah et al. 2016).

2.5.14: C. elegans *pathogenicity (slow killing) assays*

Slow killing assays were performed as described previously (Tan, Mahajan-Miklos, and Ausubel 1999; Powell and Ausubel 2008). Briefly, ten µl of overnight PA14 cultures (grown as described above) were spotted onto slow killing agar plates (0.3% NaCl, 0.35% Bacto-Peptone, 1 mM $CaCl_2$, 1 mM $MgSO_4$, 5 µg/ml cholesterol, 25 mM KPO_4, 50 µg/ml FUDR, 1.7% agar) and plates were incubated for 24 hours at 37 °C followed by 48 hours at room temperature (~23 °C). Larval stage 4 (L4) nematodes were picked onto the PA14-seeded plates and live/dead worms were counted for up to four days. Each plate was considered a biological replicate and had a starting sample size of 30-35 worms.

2.5.15: Statistical analysis

Data analysis was performed using GraphPad Prism version 7 (GraphPad Software, La Jolla California USA). Values are expressed as mean ± SD. Statistical significance of the data presented was assessed with the two-tailed unpaired Student's t-test. Values of $P \leq 0.05$ were considered significant (*, $P \leq 0.05$; **, $P \leq 0.01$; ***, $P \leq 0.001$; ****, $P \leq 0.0001$). A summary of the statistical analyses performed can be found in **Table 2.4**.

2.6: References

Alvarez-Ortega, Carolina, and Caroline S. Harwood. 2007. “Responses of Pseudomonas aeruginosa to Low Oxygen Indicate That Growth in the Cystic Fibrosis Lung Is by Aerobic Respiration.” Molecular Microbiology 65 (1): 153–65.

Anzai, Y., H. Kim, J. Y. Park, H. Wakabayashi, and H. Oyaizu. 2000. “Phylogenetic Affiliation of the Pseudomonads Based on 16S rRNA Sequence.” *International Journal of Systematic and Evolutionary Microbiology* 50 Pt 4 (July): 1563–89.

Arai, Hiroyuki, Takuro Kawakami, Tatsuya Osamura, Takehiro Hirai, Yoshiaki Sakai, and Masaharu Ishii. 2014. “Enzymatic Characterization and in Vivo Function of Five Terminal Oxidases in Pseudomonas Aeruginosa.” *Journal of Bacteriology* 196 (24): 4206–15.

Armstrong, A. V., and D. E. Stewart-Tull. 1971. “The Site of the Activity of Extracellular Products of Pseudomonas Aeruginosa in the Electron-Transport Chain in Mammalian Cell Respiration.” *Journal of Medical Microbiology* 4 (2): 263–70.

Bertani, Giuseppe. 2004. “Lysogeny at Mid-Twentieth Century: P1, P2, and Other Experimental Systems.” *Journal of Bacteriology* 186 (3): 595–600.

Biasini, Marco, Stefan Bienert, Andrew Waterhouse, Konstantin Arnold, Gabriel Studer, Tobias Schmidt, Florian Kiefer, et al. 2014. “SWISS-MODEL: Modelling Protein Tertiary and Quaternary Structure Using Evolutionary Information.” *Nucleic Acids Research* 42 (Web Server issue): W252–58.

Borriello, Giorgia, Erin Werner, Frank Roe, Aana M. Kim, Garth D. Ehrlich, and Philip S. Stewart. 2004. “Oxygen Limitation Contributes to Antibiotic Tolerance of Pseudomonas Aeruginosa in Biofilms.” *Antimicrobial Agents and Chemotherapy* 48 (7): 2659–64.

Brochier-Armanet, Celine, Emmanuel Talla, and Simonetta Gribaldo. 2009. “The Multiple Evolutionary Histories of Dioxygen Reductases: Implications for the Origin and Evolution of Aerobic Respiration.” *Molecular Biology and Evolution* 26 (2): 285–97.

Buschmann, Sabine, Eberhard Warkentin, Hao Xie, Julian D. Langer, Ulrich Ermler, and Hartmut Michel. 2010. “The Structure of cbb3 Cytochrome Oxidase Provides Insights into Proton Pumping.” *Science* 329 (5989): 327–30.

Comolli, James C., and Timothy J. Donohue. 2004. “Differences in Two Pseudomonas Aeruginosa cbb3 Cytochrome Oxidases.” *Molecular Microbiology* 51 (4): 1193–1203.

Cosseau, Céline, and Jacques Batut. 2004. “Genomics of the ccoNOQP-Encoded cbb3 Oxidase Complex in Bacteria.” *Archives of Microbiology* 181 (2): 89–96.

Cowley, Elise S., Sebastian H. Kopf, Alejandro LaRiviere, Wiebke Ziebis, and Dianne K. Newman. 2015. “Pediatric Cystic Fibrosis Sputum Can Be Chemically Dynamic, Anoxic, and Extremely Reduced Due to Hydrogen Sulfide Formation.” *mBio* 6 (4): e00767.

Davidson, E., T. Ohnishi, M. Tokito, and F. Daldal. 1992. “Rhodobacter Capsulatus Mutants Lacking the Rieske FeS Protein Form a Stable Cytochrome bc1 Subcomplex with an Intact Quinone Reduction Site.” *Biochemistry* 31 (13): 3351–58.

De Baets, Frans, Petra Schelstraete, Sabine Van Daele, Filomeen Haerynck, and Mario Vaneechoutte. 2007. “Achromobacter Xylosoxidans in Cystic Fibrosis: Prevalence and Clinical

Relevance.” *Journal of Cystic Fibrosis: Official Journal of the European Cystic Fibrosis Society* 6 (1): 75–78.

Dehio, C., and M. Meyer. 1997. “Maintenance of Broad-Host-Range Incompatibility Group P and Group Q Plasmids and Transposition of Tn5 in Bartonella Henselae Following Conjugal Plasmid Transfer from Escherichia Coli.” *Journal of Bacteriology* 179 (2): 538–40.

Dietrich, Lars E. P., Chinweike Okegbe, Alexa Price-Whelan, Hassan Sakhtah, Ryan C. Hunter, and Dianne K. Newman. 2013. “Bacterial Community Morphogenesis Is Intimately Linked to the Intracellular Redox State.” *Journal of Bacteriology* 195 (7): 1371–80.

Dietrich, Lars E. P., Alexa Price-Whelan, Ashley Petersen, Marvin Whiteley, and Dianne K. Newman. 2006. “The Phenazine Pyocyanin Is a Terminal Signalling Factor in the Quorum Sensing Network of Pseudomonas Aeruginosa.” *Molecular Microbiology* 61 (5): 1308–21.

Dietrich, Lars E. P., Tracy K. Teal, Alexa Price-Whelan, and Dianne K. Newman. 2008. “Redox-Active Antibiotics Control Gene Expression and Community Behavior in Divergent Bacteria.” *Science* 321 (5893): 1203–6.

Dietrich, Lars E. P., Michael M. Tice, and Dianne K. Newman. 2006. “The Co-Evolution of Life and Earth.” *Current Biology: CB* 16 (11): R395–400.

Ducluzeau, Anne-Lise, Soufian Ouchane, and Wolfgang Nitschke. 2008. “The cbb3 Oxidases Are an Ancient Innovation of the Domain Bacteria.” *Molecular Biology and Evolution* 25 (6): 1158–66.

Edwards, Sarah, and Birthe V. Kjellerup. 2012. “Exploring the Applications of Invertebrate Host-Pathogen Models for in Vivo Biofilm Infections.” *FEMS Immunology and Medical Microbiology* 65 (2): 205–14.

Eschbach, Martin, Kerstin Schreiber, Katharina Trunk, Jan Buer, Dieter Jahn, and Max Schobert. 2004. “Long-Term Anaerobic Survival of the Opportunistic Pathogen Pseudomonas Aeruginosa via Pyruvate Fermentation.” *Journal of Bacteriology* 186 (14): 4596–4604.

Falkowski, Paul G. 2006. “Evolution. Tracing Oxygen’s Imprint on Earth's Metabolic Evolution.” *Science* 311 (5768): 1724–25.

Firmida, M. C., R. H. V. Pereira, E. A. S. R. Silva, E. A. Marques, and A. J. Lopes. 2016. “Clinical Impact of Achromobacter Xylosoxidans Colonization/infection in Patients with Cystic Fibrosis.” *Brazilian Journal of Medical and Biological Research = Revista Brasileira de Pesquisas Medicas E Biologicas / Sociedade Brasileira de Biofisica ... [et Al.]* 49 (4): e5097.

Friedman, Lisa, and Roberto Kolter. 2004. “Genes Involved in Matrix Formation in Pseudomonas Aeruginosa PA14 Biofilms.” *Molecular Microbiology* 51 (3): 675–90.

Gier, J. W. de, M. Schepper, W. N. Reijnders, S. J. van Dyck, D. J. Slotboom, A. Warne, M. Saraste, et al. 1996. “Structural and Functional Analysis of aa3-Type and cbb3-Type Cytochrome c Oxidases of Paracoccus Denitrificans Reveals Significant Differences in Proton-Pump Design.” *Molecular Microbiology* 20 (6): 1247–60.

Glasser, Nathaniel R., Suzanne E. Kern, and Dianne K. Newman. 2014. “Phenazine Redox Cycling Enhances Anaerobic Survival in Pseudomonas Aeruginosa by Facilitating Generation of ATP and a Proton-Motive Force.” *Molecular Microbiology* 92 (2). Wiley Online Library: 399–412.

Glasser, Nathaniel R., Benjamin X. Wang, Julie A. Hoy, and Dianne K. Newman. 2017. “The Pyruvate and α-Ketoglutarate Dehydrogenase Complexes of Pseudomonas Aeruginosa Catalyze Pyocyanin and Phenazine-1-Carboxylic Acid Reduction via the Subunit Dihydrolipoamide Dehydrogenase.” *The Journal of Biological Chemistry* 292 (13): 5593–5607.

Hirai, Takehiro, Tatsuya Osamura, Masaharu Ishii, and Hiroyuki Arai. 2016. “Expression of Multiple cbb3 Cytochrome c Oxidase Isoforms by Combinations of Multiple Isosubunits in Pseudomonas Aeruginosa.” *Proceedings of the National Academy of Sciences of the United States of America*, October. doi:10.1073/pnas.1613308113.

Hoang, T. T., R. R. Karkhoff-Schweizer, A. J. Kutchma, and H. P. Schweizer. 1998. “A Broad-Host-Range Flp-FRT Recombination System for Site-Specific Excision of Chromosomally-Located DNA Sequences: Application for Isolation of Unmarked Pseudomonas Aeruginosa Mutants.” *Gene* 212 (1): 77–86.

Huerta-Cepas, Jaime, Damian Szklarczyk, Kristoffer Forslund, Helen Cook, Davide Heller, Mathias C. Walter, Thomas Rattei, et al. 2016. “eggNOG 4.5: A Hierarchical Orthology Framework with Improved Functional Annotations for Eukaryotic, Prokaryotic and Viral Sequences.” *Nucleic Acids Research* 44 (D1): D286–93.

Jennings, Laura K., Kelly M. Storek, Hannah E. Ledvina, Charlène Coulon, Lindsey S. Marmont, Irina Sadovskaya, Patrick R. Secor, et al. 2015. “Pel Is a Cationic Exopolysaccharide That Cross-Links Extracellular DNA in the Pseudomonas Aeruginosa Biofilm Matrix.” *Proceedings of the National Academy of Sciences of the United States of America* 112 (36): 11353–58.

Jo, Jeanyoung, Alexa Price-Whelan, and Lars E. P. Dietrich. 2014. “An Aerobic Exercise: Defining the Roles of Pseudomonas Aeruginosa Terminal Oxidases.” *Journal of Bacteriology* 196 (24): 4203–5.

Kawakami, Takuro, Miho Kuroki, Masaharu Ishii, Yasuo Igarashi, and Hiroyuki Arai. 2010. “Differential Expression of Multiple Terminal Oxidases for Aerobic Respiration in Pseudomonas Aeruginosa.” *Environmental Microbiology* 12 (6): 1399–1412.

Kearse, Matthew, Richard Moir, Amy Wilson, Steven Stones-Havas, Matthew Cheung, Shane Sturrock, Simon Buxton, et al. 2012. “Geneious Basic: An Integrated and Extendable Desktop Software Platform for the Organization and Analysis of Sequence Data.” *Bioinformatics* 28 (12): 1647–49.

Kempes, Christopher P., Chinweike Okegbe, Zwoisaint Mears-Clarke, Michael J. Follows, and Lars E. P. Dietrich. 2014. “Morphological Optimization for Access to Dual Oxidants in Biofilms.” *Proceedings of the National Academy of Sciences of the United States of America* 111 (1): 208–13.

King, T. E. 1963. “Reconstitution of respiratory chain enzyme system. XII. Some observations on the reconstitution of the succinate oxidase system from heart muscle.” The Journal of Biological Chemistry 238 (December): 4037–51.

Kirschvink, Joseph L., and Robert E. Kopp. 2008. “Palaeoproterozoic Ice Houses and the Evolution of Oxygen-Mediating Enzymes: The Case for a Late Origin of Photosystem II.” *Philosophical Transactions of the Royal Society of London. Series B, Biological Sciences* 363 (1504): 2755–65.

Knoll, Andrew H., and Erik A. Sperling. 2014. “Oxygen and Animals in Earth History.” *Proceedings of the National Academy of Sciences of the United States of America* 111 (11): 3907–8.

Lambertsen, Lotte, Claus Sternberg, and Søren Molin. 2004. “Mini-Tn7 Transposons for Site-Specific Tagging of Bacteria with Fluorescent Proteins.” *Environmental Microbiology* 6 (7): 726–32.

Liberati, Nicole T., Jonathan M. Urbach, Sachiko Miyata, Daniel G. Lee, Eliana Drenkard, Gang Wu, Jacinto Villanueva, Tao Wei, and Frederick M. Ausubel. 2006. “An Ordered, Nonredundant Library of *Pseudomonas Aeruginosa* Strain PA14 Transposon Insertion Mutants.” *Proceedings of the National Academy of Sciences of the United States of America* 103 (8): 2833–38.

Morris, Rachel L., and Thomas M. Schmidt. 2013. “Shallow Breathing: Bacterial Life at Low O(2).” *Nature Reviews. Microbiology* 11 (3): 205–12.

Nachlas, M. M., S. I. Margulies, and A. M. Seligman. 1960. “A Colorimetric Method for the Estimation of Succinic Dehydrogenase Activity.” *The Journal of Biological Chemistry* 235 (February): 499–503.

Newman, D. K. 2008. “From Iron Oxides to Infections.” *Geobiology* 6 (3): 196–200.

Okegbe, Chinweike, Blanche L. Fields, Stephanie J. Cole, Christopher Beierschmitt, Chase J. Morgan, Alexa Price-Whelan, Richard C. Stewart, Vincent T. Lee, and Lars E. P. Dietrich. 2017. “Electron-Shuttling Antibiotics Structure Bacterial Communities by Modulating Cellular Levels of c-Di-GMP.” *Proceedings of the National Academy of Sciences of the United States of America* 114 (26): E5236–45.

Okegbe, Chinweike, Alexa Price-Whelan, and Lars E. P. Dietrich. 2014. “Redox-Driven Regulation of Microbial Community Morphogenesis.” *Current Opinion in Microbiology* 18 (April): 39–45.

Pitcher, Robert S., and Nicholas J. Watmough. 2004. “The Bacterial Cytochrome cbb3 Oxidases.” *Biochimica et Biophysica Acta* 1655 (1-3): 388–99.

Powell, Jennifer R., and Frederick M. Ausubel. 2008. “Models of Caenorhabditis Elegans Infection by Bacterial and Fungal Pathogens.” *Methods in Molecular Biology* 415: 403–27.

Preisig, O., R. Zufferey, L. Thöny-Meyer, C. A. Appleby, and H. Hennecke. 1996. “A High-Affinity cbb3-Type Cytochrome Oxidase Terminates the Symbiosis-Specific Respiratory Chain of Bradyrhizobium Japonicum.” *Journal of Bacteriology* 178 (6): 1532–38.

Price-Whelan, Alexa, Lars E. P. Dietrich, and Dianne K. Newman. 2006. “Rethinking ‘Secondary’ Metabolism: Physiological Roles for Phenazine Antibiotics.” *Nature Chemical Biology* 2 (2): 71–78.

Rahme, L. G., E. J. Stevens, S. F. Wolfort, J. Shao, R. G. Tompkins, and F. M. Ausubel. 1995. “Common Virulence Factors for Bacterial Pathogenicity in Plants and Animals.” *Science* 268 (5219): 1899–1902.

Ray, A., and H. D. Williams. 1997. “The Effects of Mutation of the Anr Gene on the Aerobic Respiratory Chain of Pseudomonas Aeruginosa.” *FEMS Microbiology Letters* 156 (2): 227–32.

Recinos, David A., Matthew D. Sekedat, Adriana Hernandez, Taylor Sitarik Cohen, Hassan Sakhtah, Alice S. Prince, Alexa Price-Whelan, and Lars E. P. Dietrich. 2012. “Redundant Phenazine Operons in Pseudomonas Aeruginosa Exhibit Environment-Dependent Expression and Differential Roles in Pathogenicity.” *Proceedings of the National Academy of Sciences of the United States of America* 109 (47): 19420–25.

Rich, P. R., L. A. Mischis, S. Purton, and J. T. Wiskich. 2001. “The Sites of Interaction of Triphenyltetrazolium Chloride with Mitochondrial Respiratory Chains.” *FEMS Microbiology Letters* 202 (2): 181–87.

Rybtke, Morten, Louise Dahl Hultqvist, Michael Givskov, and Tim Tolker-Nielsen. 2015. “Pseudomonas Aeruginosa Biofilm Infections: Community Structure, Antimicrobial Tolerance and Immune Response.” *Journal of Molecular Biology* 427 (23): 3628–45.

Saiman, L., Y. Chen, S. Tabibi, P. San Gabriel, J. Zhou, Z. Liu, L. Lai, and S. Whittier. 2001. “Identification and Antimicrobial Susceptibility of Alcaligenes Xylosoxidans Isolated from Patients with Cystic Fibrosis.” *Journal of Clinical Microbiology* 39 (11): 3942–45.

Sakhtah, Hassan, Leslie Koyama, Yihan Zhang, Diana K. Morales, Blanche L. Fields, Alexa Price-Whelan, Deborah A. Hogan, Kenneth Shepard, and Lars E. P. Dietrich. 2016. “The Pseudomonas Aeruginosa Efflux Pump MexGHI-OpmD Transports a Natural Phenazine That Controls Gene Expression and Biofilm Development.” *Proceedings of the National Academy of Sciences of the United States of America* 113 (25): E3538–47.

Schindelin, Johannes, Ignacio Arganda-Carreras, Erwin Frise, Verena Kaynig, Mark Longair, Tobias Pietzsch, Stephan Preibisch, et al. 2012. “Fiji: An Open-Source Platform for Biological-Image Analysis.” *Nature Methods* 9 (7): 676–82.

Schrödinger, LLC. 2015. “The PyMOL Molecular Graphics System, Version 1.8.”

Shanks, Robert M. Q., Nicky C. Caiazza, Shannon M. Hinsa, Christine M. Toutain, and George A. O’Toole. 2006. “Saccharomyces Cerevisiae-Based Molecular Tool Kit for Manipulation of Genes from Gram-Negative Bacteria.” *Applied and Environmental Microbiology* 72 (7). Am Soc Microbiol: 5027–36.

Simon, R., U. Priefer, and A. Pühler. 1983. “A Broad Host Range Mobilization System for In Vivo Genetic Engineering: Transposon Mutagenesis in Gram Negative Bacteria.” *Nature Biotechnology* 1 (9). Nature Publishing Group: 784–91.

Tan, M. W., S. Mahajan-Miklos, and F. M. Ausubel. 1999. “Killing of Caenorhabditis Elegans by Pseudomonas Aeruginosa Used to Model Mammalian Bacterial Pathogenesis.” *Proceedings of the National Academy of Sciences of the United States of America* 96 (2): 715–20.

Tolker-Nielsen, Tim. 2014. “Pseudomonas Aeruginosa Biofilm Infections: From Molecular Biofilm Biology to New Treatment Possibilities.” *APMIS. Supplementum*, no. 138 (December): 1–51.

Way, S. S., S. Sallustio, R. S. Magliozzo, and M. B. Goldberg. 1999. “Impact of Either Elevated or Decreased Levels of Cytochrome Bd Expression on Shigella Flexneri Virulence.” *Journal of Bacteriology* 181 (4): 1229–37.

Weingarten, Rebecca A., Jesse L. Grimes, and Jonathan W. Olson. 2008. “Role of Campylobacter Jejuni Respiratory Oxidases and Reductases in Host Colonization.” *Applied and Environmental Microbiology* 74 (5): 1367–75.

Werner, Erin, Frank Roe, Amandine Bugnicourt, Michael J. Franklin, Arne Heydorn, Søren Molin, Betsey Pitts, and Philip S. Stewart. 2004. “Stratified Growth in Pseudomonas Aeruginosa Biofilms.” *Applied and Environmental Microbiology* 70 (10): 6188–96.

Williams, Huw D., James E. A. Zlosnik, and Ben Ryall. 2007. “Oxygen, Cyanide and Energy Generation in the Cystic Fibrosis Pathogen Pseudomonas Aeruginosa.” *Advances in Microbial Physiology* 52: 1–71.

Winsor, Geoffrey L., Emma J. Griffiths, Raymond Lo, Bhavjinder K. Dhillon, Julie A. Shay, and Fiona S. L. Brinkman. 2016. “Enhanced Annotations and Features for Comparing Thousands of Pseudomonas Genomes in the Pseudomonas Genome Database.” *Nucleic Acids Research* 44 (D1): D646–53.

Zufferey, Rachel, Oliver Preisig, Hauke Hennecke, and Linda Thöny-Meyer. 1996. “Assembly and Function of the Cytochrome Cbb Oxidase Subunits in Bradyrhizobium Japonicum.” *The Journal of Biological Chemistry* 271 (15): 9114–19.

2.7: Tables

Table 2.1: Primers used in this study.

primer number	sequence	used to make plasmid number
LD717	ccaggcaaattctgttttatcagaccgcttctgcgttctgatCAGGACAAGCAGTGGGAAC	pLD1852
LD718	aggtgttgtaggccatcagcTGGCGGACCACCTTATAGTT	
LD958	aactataaggtggtccgccaCGGTGGTTTCTTCCTCACC	
LD959	ggaattgtgagcggataacaatttcacacaggaaacagctGGTCCAGCCTTTTTCCTTGT	
LD725	ccaggcaaattctgttttatcagaccgcttctgcgttctgatCCCCTCAGAGAAGTCAGTCG	pLD1610
LD726	aggtgttgtaggccatcaggGGCGGACCACCTTGTAGTTA	
LD727	taactacaaggtggtccgccCCTGATGGCCTACAACACCT	
LD728	ggaattgtgagcggataacaatttcacacaggaaacagctCAGCGGGTTGTCATACTCCT	
LD741	ccaggcaaattctgttttatcagaccgcttctgcgttctgatTCGAGGGCTTCGAGAAGAT	pLD1616
LD742	aggtgttgtaggccatcagcCAGGGTCATCAGGGTGAACT	
LD743	agttcaccctgatgaccctgGCTGATGGCCTACAACACCT	
LD744	ggaattgtgagcggataacaatttcacacaggaaacagctCGGGTGATGTCGACGTATTC	
LD438	ggaattgtgagcggataacaatttcacacaggaaacagctCCGTTGATTTCCTTCTGCAT	pLD1264 (LD438 - LD441) pLD1853 (LD438 and LD441)
LD439	ctacaaggtggttcgccagtCGCTGACCTACTCCTTCGTC	
LD440	gacgaaggagtaggtcagcgACTGGCGAACCACCTTGTAG	
LD441	ccaggcaaattctgttttatcagaccgcttctgcgttctgatCATCGACCTGGAAGTGCTC	
LD725	ccaggcaaattctgttttatcagaccgcttctgcgttctgatCCCCTCAGAGAAGTCAGTCG	pLD1929
LD1063	gttgcccaggtgttcctgtGGCGGACCACCTTGTAGTTA	
LD949	ggaattgtgagcggataacaatttcacacaggaaacagctTGTAGTCGAGGGACTTCTTGC	
LD1064	taactacaaggtggtccgccACAGGAACACCTGGGCAAC	

Table 2.1 (continued): Primers used in this study.

primer number	sequence	used to make plasmid number
LD2168	ccaggcaaattctgttttatcagaccgcttctgcgttctgatATGTAGGGATCGAGCGACAG	pLD2791
LD2169	acacgatatccagcccctctTGGACATCGCGCCGTTCCTC	
LD2170	gaggaacggcgcgatgtccaAGAGGGGCTGGATATCGTGT	
LD2171	ggaattgtgagcggataacaatttcacacaggaaacagctAAGAGGTCATAATCGGCGGT	
LD2120	gattcgacatcactagtACGCCCAGCTCCAACAAA	pLD2777
LD2121	gattcgatgccctcgaGCTAGGGGTTCCACGGTTAAT	
LD2122	gattcgactgcactagtCATCGACTTGCCGCCCAG	pLD2778
LD2123	gattcgatgccctcgaGCTATGGGCTTCCATCCAC	
LD2124	gattcgactgcactagtGGCTACTTCCTCTGGCTGG	pLD2779
LD2125	gattcgactgcctcgagCTGTACAGTCCCGAAAGAAATGAAC	
LD1118	ccaggcaaattctgttttatcagaccgcttctgcgttctgatTCTTCAGGTTCTCGCGGTAG	pLD1966
LD1119	aagtgccagtaccaactggcGCAGATCCAGAAGATGGTCA	
LD1120	tgaccatcttctggatctgcGCCAGTTGGTACTGGCACTT	
LD1121	ggaattgtgagcggataacaatttcacacaggaaacagctATCGCGAGACTCATGGTTTT	
LD1134	ccaggcaaattctgttttatcagaccgcttctgcgttctgatCGCTGCTTGTCGATCTGTT	pLD1967
LD1135	gcgacatgaccctgttcaacCTGACCGGCTACTGGACC	
LD1136	ggtccagtagccggtcagGTTGAACAGGGTCATGTCGC	
LD1137	ggaattgtgagcggataacaatttcacacaggaaacagctCCTCGGCGACCATGAATAC	
LD1126	ccaggcaaattctgttttatcagaccgcttctgcgttctgatTTCAGGTTCTTCGGGTTCTC	pLD2044
LD1187	aacagcgcgccgaccagcatCTCTTCGTTCGTTTTCAGCC	
LD1188	ggctgaaaacgaacgaagagATGCTGGTCGGCGCGCTGTT	
LD1189	ggaattgtgagcggataacaatttcacacaggaaacagctGCGTTGATGAAGCGGATAAC	

Table 2.2: Plasmids used in this study

plasmid	description	source
pMQ30	7.5 kb mobilizable vector; oriT, sacB, GmR.	Shanks et al. 2006
pAKN69	Contains mini-Tn7(Gm)PA1/04/03::eyfp fusion.	Lambertsen et al. 2004
pLD2722	GmR, TetR flanked by Flp recombinase target (FRT) sites to resolve out resistance casettes.	this study
pFLP2	Site-specific excision vector with cI857-controlled FLP recombinase encoding sequence, sacB, ApR.	Hoang et al. 1998
pLD1852	ΔccoN1 PCR fragment introduced into pMQ30 by gap repair cloning in yeast strain InvSc1.	this study
pLD1610	ΔccoN2 PCR fragment introduced into pMQ30 by gap repair cloning in yeast strain InvSc1.	this study
pLD1616	ΔccoN3 PCR fragment introduced into pMQ30 by gap repair cloning in yeast strain InvSc1.	this study
pLD1264	ΔccoN4 PCR fragment introduced into pMQ30 by gap repair cloning in yeast strain InvSc1.	this study
pLD1929	Δcco1 cco2 PCR fragment introduced into pMQ30 by gap repair cloning in yeast strain InvSc1.	this study
pLD2791	Δhcn PCR fragment introduced into pMQ30 by gap repair cloning in yeast strain InvSc1.	this study
pLD1853	Full genomic sequence of ccoN4 PCR fragment introduced into pMQ30 by gap repair cloning in yeast strain InvSc1. Verified by sequencing.	this study
pLD1966	Δaa3 PCR fragment introduced into pMQ30 by gap repair cloning in yeast strain IncSc1.	this study
pLD1967	Δbo3 PCR fragment introduced into pMQ30 by gap repair cloning in yeast strain IncSc1.	this study
pLD2044	Δcio PCR fragment introduced into pMQ30 by gap repair cloning in yeast strain IncSc1.	this study
pLD2777	PCR-amplified cco1 promoter ligated into pSEK103 using SpeI and XhoI.	this study
pLD2778	PCR-amplified cco2 promoter ligated into pSEK103 using SpeI and XhoI.	this study
pLD2779	PCR-amplified ccoN4 promoter ligated into pSEK103 using SpeI and XhoI.	this study

Table 2.3: Strains used in this study

strain	number	description	source
Pseudomonas aeruginosa strains			
UCBPP-PA14		Clinical isolate UCBPP-PA14.	Rahme et al. 1995
PA14 ∆phz	LD24	PA14 with deletions in phzA1-G1 and phzA2-G2 operons.	Dietrich et al. 2006
PA14 ∆ccoN1	LD1784	PA14 with deletion in PA14_44370.	this study
PA14 ∆ccoN2	LD1614	PA14 with deletion in PA14_44340.	this study
PA14 ∆ccoN3	LD1620	PA14 with deletion in PA14_40510.	this study
PA14 ∆ccoN4	LD2833	PA14 with deletion in PA14_10500.	this study
PA14 ∆ccoN1 ∆ccoN2	LD1888	PA14 with deletions in PA14_44370 and PA14_44340. Made by mating pLD1610 into LD1784.	this study
PA14 ∆ccoN1 ∆ccoN4	LD1951	PA14 with deletions in PA14_44370 and PA14_10500. Made by mating pLD1264 into LD1784.	this study
PA14 ∆ccoN2 ∆ccoN4	LD1692	PA14 with deletions in PA14_44340 and PA14_10500. Made by mating pLD1264 into LD1614.	this study
PA14 ∆ccoN3 ∆ccoN4	LD1649	PA14 with deletions in PA14_40510 and PA14_10500. Made by mating pLD1264 into LD1620.	this study
PA14 ∆ccoN1 ∆ccoN2 ∆ccoN3	LD1977	PA14 with deletions in PA14_443470, PA14_44340, and PA14_40510. Made by mating pLD1616 into LD1888.	this study
PA14 ∆ccoN1 ∆ccoN2 ∆ccoN4	LD1976	PA14 with deletions in PA14_443470, PA14_44340, and PA14_10500. Made by mating pLD1264 into LD1888.	this study
PA14 ∆ccoN1 ∆ccoN2 ∆ccoN4 ∆ccoN3	LD2020	PA14 with deletions in PA14_443470, PA14_44340, PA14_10500, and PA14_40510. Made by mating pLD1264 into LD1977.	this study
PA14 ∆cco1cco2	LD1933	PA14 with both cco operons (PA14_44340-PA14_44400) deleted simultaneously.	this study
PA14 ∆cox ∆cyo ∆cio	LD2587	PA14 with deletions in PA14_01290-01320 (cox/aa3 operon), PA14_47150-47210 (cyo/bo3 operon), and PA14_13030-13040 (cio operon). Made by mating pLD1966, pLD1967, and pLD2044, in that order, to PA14.	this study
PA14 ∆hcn	LD2827	PA14 with deletion in hcnABC operon (PA14_36310-36330).	this study
PA14 ∆phz ∆hcn	LD2828	PA14 with deletions in phzA1-G1, phzA2-G2, and hcnABC operons. Made by mating pLD2791 into LD24.	this study

Table 2.3 (continued): Strains used in this study

strain	number	description	source
PA14 ΔccoN4 Δhcn	LD2829	PA14 with deletions in PA14_10500 and hcnABC operon. Made by mating pLD2791 into LD2833.	this study
PA14 ΔccoN1 ΔccoN2 Δhcn	LD2830	PA14 with deletions in PA14_44370, PA14_44340, and hcnABC operon. Made by mating pLD2791 into LD1888.	this study
PA14 ΔccoN1 ΔccoN2 ΔccoN4 Δhcn	LD2831	PA14 with deletions in PA14_44370, PA14_44340, PA14_10500 and hcnABC operon. Made by mating pLD2791 into LD1976.	this study
PA14 Δcco1cco2 Δhcn	LD2832	PA14 with deletions in cco1, cco2, and hcnABC operons. Made by mating pLD2791 into LD1933.	this study
PA14 gacA::Tn	LD1560	MAR2xT7 transposon insertion into PA14_30650.	Liberati et al. 2006
PA14 ΔccoN4::ccoN4	LD1867	PA14 ΔccoN4 strain with wild-type ccoN4 complemented back into the site of deletion. Made by mating pLD1853 into LD2833.	this study
PA14 ΔccoN1 ΔccoN2 ΔccoN4::ccoN4	LD2576	PA14 ΔccoN1 ΔccoN2 ΔccoN4 strain with wild-type ccoN4 complemented back into the site of deletion. Made by mating pLD1853 into LD1976.	this study
PA14 MCS-gfp	LD2820	PA14 without a promoter driving gfp expression.	this study
PA14 Pcco1-gfp	LD2784	PA14 with promoter of cco1 operon driving gfp expression.	this study
PA14 Pcco2-gfp	LD2786	PA14 with promoter of cco2 operon driving gfp expression.	this study
PA14 PccoN4-gfp	LD2788	PA14 with promoter of ccoN4Q4 operon driving gfp expression.	this study
PA14-yfp	LD2780	WT PA14 constitutively expressing eyfp.	this study
PA14 ΔccoN1 ΔccoN2-yfp	LD2013	PA14 ΔccoN1 ΔccoN2 constitutively expressing eyfp. Made by mating pAKN69 into LD1888.	this study
PA14 ΔccoN4-yfp	LD2834	PA14 ΔccoN4 constitutively expressing eyfp. Made by mating pAKN69 into LD2833.	this study
PA14 ΔccoN1 ΔccoN2 ΔccoN4-yfp	LD2136	PA14 ΔccoN1 ΔccoN2 ΔccoN4 constitutively expressing eyfp. Made by mating pAKN69 into LD1976.	this study
PA14 Δcco1cco2-yfp	LD2012	PA14 Δcco1cco2 constitutively expressing eyfp. Made by mating pAKN69 into LD1933.	this study
Escherichia coli strains			
UQ950	LD44	E. coli DH5 λpir strain for cloning. F-Δ(argF-lac)169φ80 dlacZ58(ΔM15) glnV44(AS) rfbD1 gyrA96(NalR) recA1 endA1 spoT thi-1 hsdR17 deoR λpir+	D. Lies, Caltech

Table 2.3 (continued): Strains used in this study

strain	number	description	source
BW29427	LD661	Donor strain for conjugation. thrB1004 pro thi rpsL hsdS lacZ ΔM15RP4-1360 Δ(araBAD)567 ΔdapA1314::[erm pir(wt)]	W. Metcalf, University of Illinois
β2155	LD69	Helper strain. thrB1004 pro thi strA hsdsS lacZΔM15 (F'lacZΔM15 lacIq traD36 proA+ proB+) ΔdapA::erm (Ermr)pir::RP4 [::kan (Kmr) from SM10]	Dehio and Meyer, 1997
S17-1	LD2901	StrR , TpR , F− RP4-2-Tc::Mu aphA::Tn7 recA λpir lysogen	Simon et al. 1983
Saccharomyces cerevisiae strains			
InvSc1	LD676	MATa/MATalpha leu2/leu2 trp1-289/trp1-289 ura3-52/ ura3-52 his3-Δ1/his3-Δ1	Invitrogen

Table 2.4: Statistical analyses.

Figure 2.2B	number of values (biological replicates)	mean	median	SD	SEM	lower 95% confidence interval of mean	upper 95% confidence interval of mean
WT	5	73.22	72.94	3.387	1.515	69.02	77.43
Δ*N4*	5	68.97	70.6	6.44	2.88	60.97	76.96
Δ*N1*Δ*N2*	5	52.18	50.46	5.142	2.3	45.79	58.56
Δ*N1*Δ*N4*	5	11.57	12.42	2.011	0.8991	9.074	14.07
Δ*N1*Δ*N2*Δ*N4*	5	0.001958	0.001117	0.001696	0.0007586	-0.0001481	0.004064
Δ*cco1cco2*	5	0.001367	0.0008644	0.001237	0.0005532	-0.0001686	0.002903
t-test	**P value**	**P value summary**					
WT vs. Δ*N4*	0.2273	ns					
WT vs. Δ*N1*Δ*N2*	<0.0001	****					
WT vs. Δ*N1*Δ*N4*	<0.0001	****					
WT vs. Δ*N1*Δ*N2*Δ*N4*	<0.0001	****					
WT vs. Δ*cco1cco2*	<0.0001	****					

Table 2.4 (continued): Statistical analyses

Figure 2.3A	number of values (biological replicates)	mean	median	SD	SEM	lower 95% confidence interval of mean	upper 95% confidence interval of mean
WT-YFP	12	54.95	54.92	4.387	1.266	52.16	57.74
Δ*N4*-YFP	3	29.92	30.83	2.234	1.29	24.37	35.46
Δ*N1*Δ*N2*-YFP	3	30.49	31.91	3.527	2.036	21.73	39.25
Δ*N1*Δ*N2*Δ*N4*-YFP	3	4.408	4.296	3.23	1.865	-3.617	12.43
Δ*cco1cco2*-YFP	3	7.097	5.306	4.093	2.363	-3.072	17.27
t-test	**P value**	**P value summary**					
WT-YFP vs. Δ*N4*- YFP	<0.0001	****					
WT-YFP vs. Δ*N1*Δ*N2*-YFP	<0.0001	****					
Δ*N1*Δ*N2*-YFP vs. Δ*N1*Δ*N2*Δ*N4*-YFP	0.0007	***					
Δ*N1*Δ*N2*-YFP vs. Δ*cco1cco2*-YFP	0.0017	**					

Figure 2.3– figure supplement 1A	number of values (biological replicates)	mean	median	SD	SEM	lower 95% confidence interval of mean	upper 95% confidence interval of mean
WT	12	45.05	45.08	4.387	1.266	42.26	47.84
Δ*N4*	3	28.22	31.31	7.442	4.297	9.731	46.71
Δ*N1*Δ*N2*	3	27.81	28.57	2.514	1.451	21.56	34.05
Δ*N1*Δ*N2*Δ*N4*	3	7.002	6.973	0.7508	0.4335	5.137	8.867
Δ*cco1cco2*	3	5.38	4.183	2.146	1.239	0.05034	10.71
t-test	**P value**	**P value summary**					
WT vs. Δ*N4*	0.0002	***					
WT vs. Δ*N1*Δ*N2*	<0.0001	****					
Δ*N1*Δ*N2* vs. Δ*N1*Δ*N2*Δ*N4*	0.0002	***					
Δ*N1*Δ*N2* vs. Δ*cco1cco2*	0.0003	***					

Table 2.4 (continued): Statistical analyses

Figure 2.5	number of values (biological replicates)	mean	median	SD	SEM	lower 95% confidence interval of mean	upper 95% confidence interval of mean
WT	8	150.3	151.2	10.31	3.644	141.7	158.9
Δ*N1*Δ*N2*	4	139.3	137.6	12.33	6.166	119.6	158.9
Δ*N4*	7	131.9	127.8	8.915	3.369	123.7	140.2
Δ*N1*Δ*N4*	4	99.96	99.34	2.726	1.363	95.62	104.3
Δ*cco1cco2*	4	95.19	95.56	1.559	0.7793	92.71	97.67
Δ*N1*Δ*N2*Δ*N4*	4	102.8	99.79	8.664	4.332	88.98	116.6
Δ*phz*	7	84.98	84.23	10.93	4.131	74.87	95.09
t-test	**P value**	**P value summary**					
WT vs. Δ*N1*Δ*N2*	0.1302	ns					
WT vs. Δ*N4*	0.0028	**					
WT vs. Δ*N1*Δ*N4*	<0.0001	****					
WT vs. Δ*cco1cco2*	<0.0001	****					
WT vs. Δ*N1*Δ*N2*Δ*N4*	<0.0001	****					
WT vs. Δ*phz*	<0.0001	****					

Figure 2.6	number of values (biological replicates)	mean	median	SD	SEM	lower 95% confidence interval of mean	upper 95% confidence interval of mean
WT	9	27.44	39	18.48	6.16	13.24	41.65
gacA::Tn	9	92.56	93	8.546	2.849	85.99	99.12
Δ*N1*Δ*N2*	4	19	21.5	14.07	7.036	-3.39	41.39
Δ*N1*Δ*N2*Δ*N4*	6	64.17	68	18	7.35	45.27	83.06
Δ*cco1cco2*	9	70.56	76	22.69	7.565	53.11	88
t-test	**P value**	**P value summary**					
WT vs. Δ*N1*Δ*N2*Δ*N4*	0.0022	**					
Δ*N1*Δ*N2* vs. Δ*N1*Δ*N2*Δ*N4*	0.0030	**					
WT vs. Δ*N1*Δ*N2*	0.4362	ns					

2.8: Figure supplements

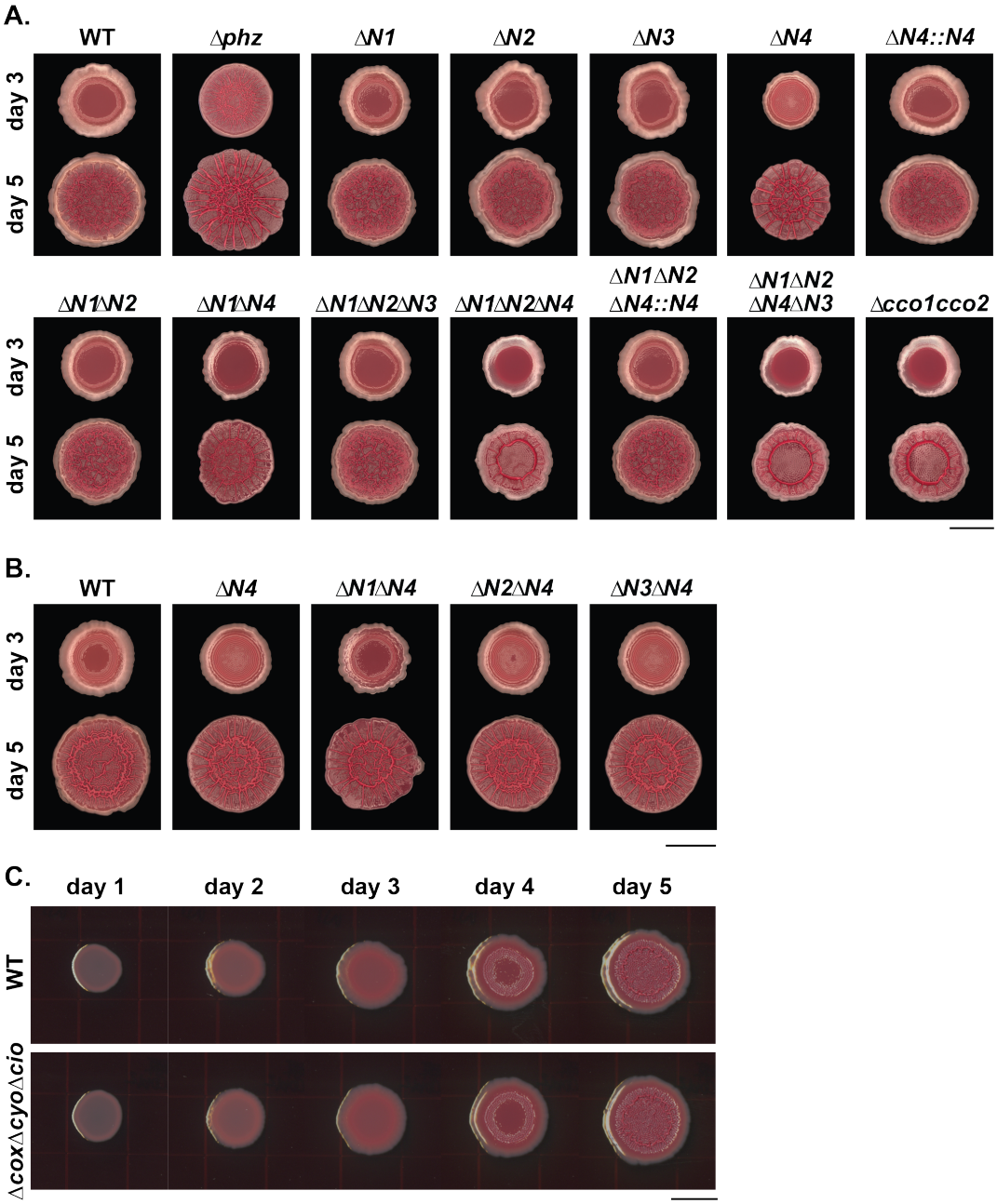

Figure 2.2—figure supplement 1. Effects of individual and combined *cco* gene deletions on colony biofilm morphogenesis. (A) Morphologies of WT, Δ*phz*, and *cco* single, combinatorial, and *ccoN4* complementation strains after 3 and 5 days of incubation. Images shown are representative of at least five biological replicates and were generated using a Keyence digital microscope. Scale bar is 1 cm. **(B)** Development of WT, Δ*N4* and N subunit double mutants containing Δ*N4*. Images shown are representative of at least three biological replicates and were generated using a Keyence digital microscope. Scale bar is 1 cm. **(C)** Development of WT and the triple mutant Δ*cox*Δ*cyo*Δ*cio* in which only the cbb_3-type terminal oxidases are present. Images were generated using a flatbed scanner (Epson Expression 11000XL) and are representative of at least three biological replicates. Scale bar is 1 cm.

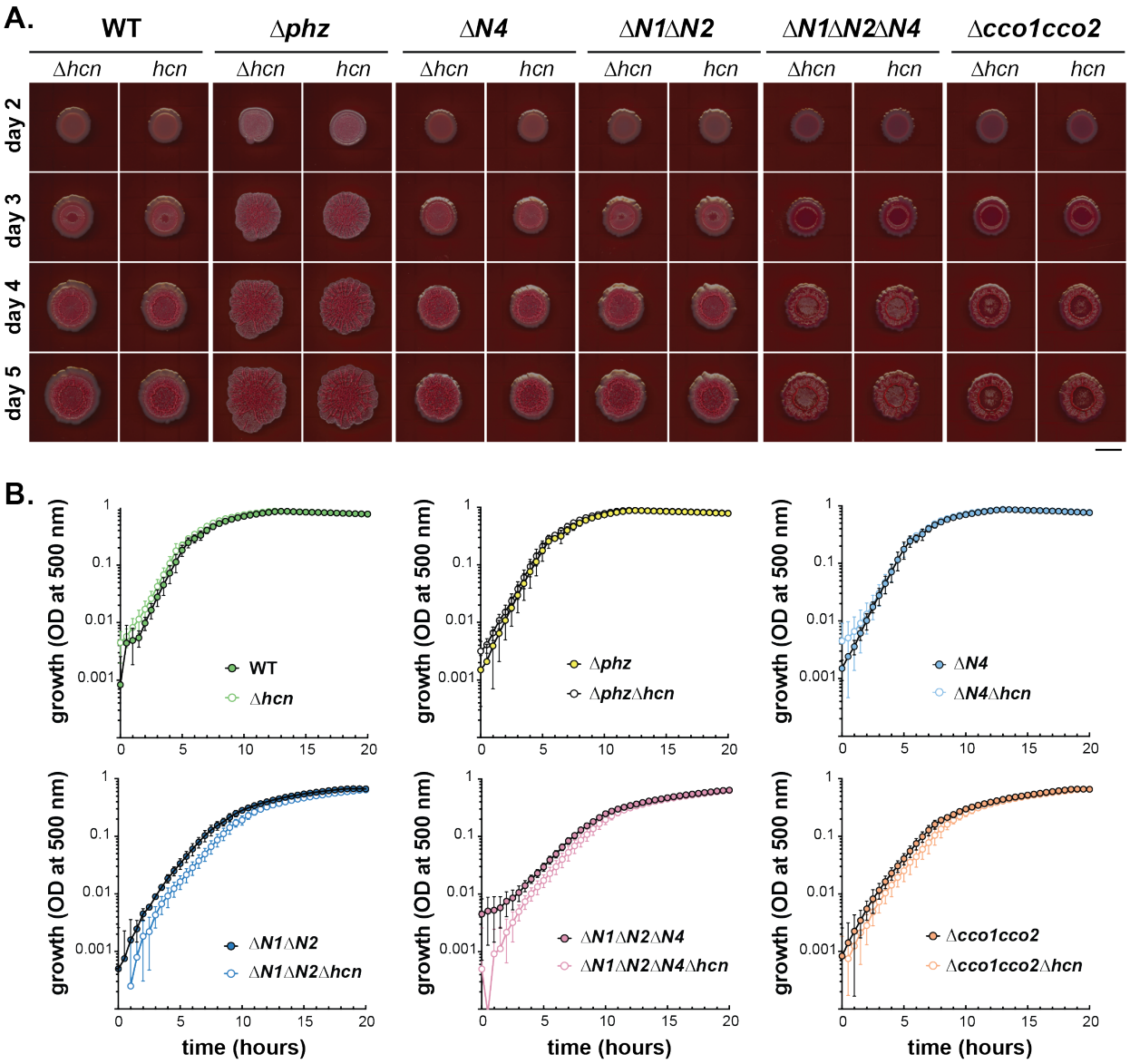

Figure 2.2—figure supplement 2. PA14 WT, Δ*phz*, and *cco* mutant growth phenotypes are unaffected by endogenous cyanide production. (A) Colony development over four days for Δ*phz*, Δ*hcnABC*, and *cco* combinatorial mutants. Images were generated using a flatbed scanner (Epson Expression 11000XL) and are representative of at least three biological replicates. Scale bar is 1 cm. **(B)** Growth of Δ*phz*, Δ*hcnABC*, and *cco* combinatorial mutants in MOPS defined medium with 20 mM succinate. Error bars represent the standard deviation of biological triplicates and are not shown in cases where they would be obscured by the point marker.

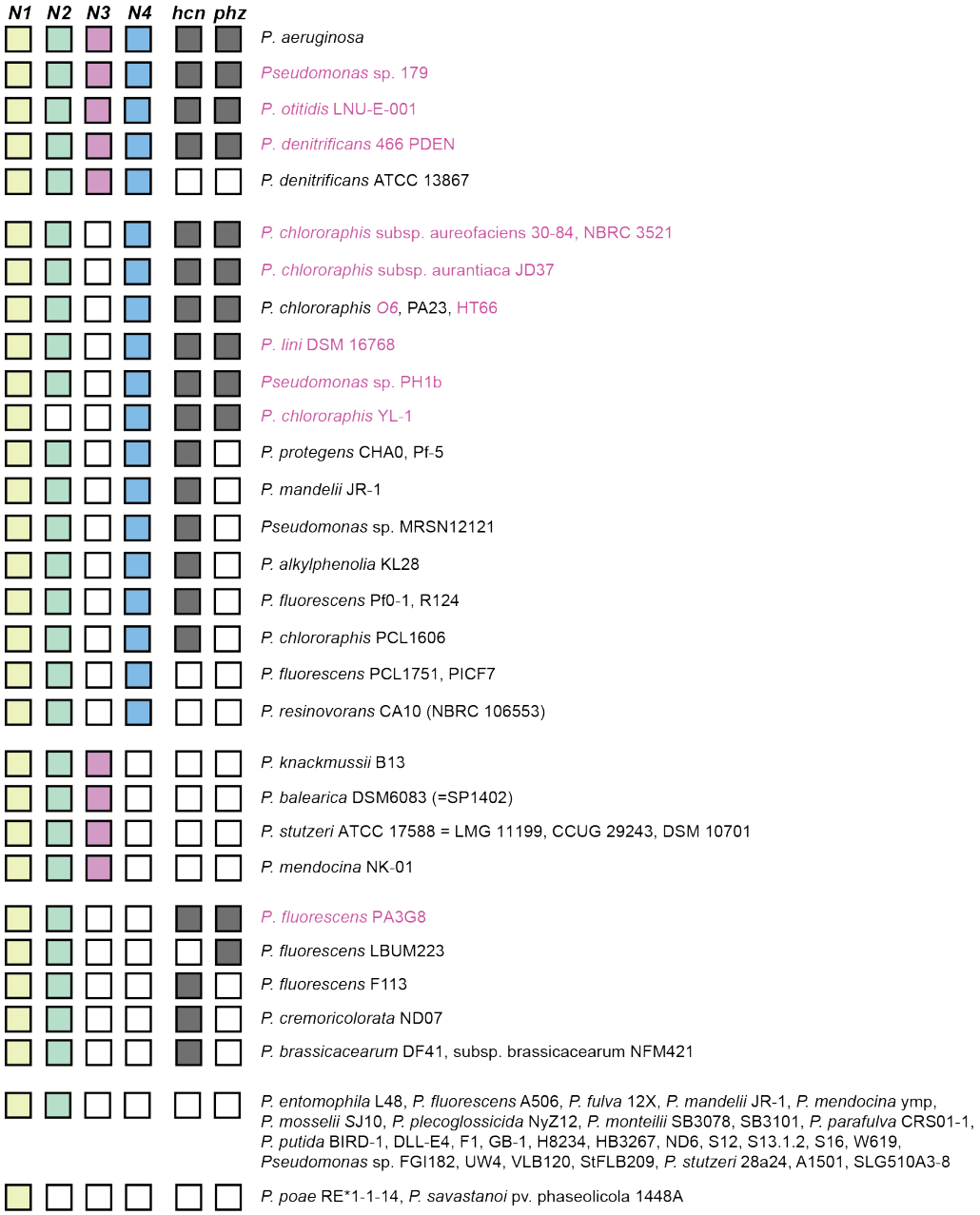

Figure 2.2—figure supplement 3. Pseudomonads with CcoN homologs. We examined genomes available in the Pseudomonas Genome Database (Winsor et al. 2016) for CcoN homologs by performing a protein BLAST search on CcoN1 from *P. aeruginosa* PA14. All hits from full genomes, excluding other *P. aeruginosa* strains, were aligned using ClustalW and a tree was built using the geneious tree builder (Geneious 10 (Kearse et al. 2012)). We also included draft genomes that contained genes involved in phenazine biosynthesis (highlighted in purple). The tree revealed four clusters, each being more closely related to one of the four N subunits from PA14, which allowed us to annotate the N subunits accordingly. We next probed all genomes with N subunits for the presence of genes involved in cyanide synthesis (*hcnABC*) and phenazine biosynthesis (*phzABCDEFG*). We did not find a clear correlation between the presence of CcoN4 and Hcn proteins (Hirai et al. 2016). We note that with the exception of two *P. fluorescens* strains, those containing *phzABCDEFG* operons also contained *ccoN4*.

A.

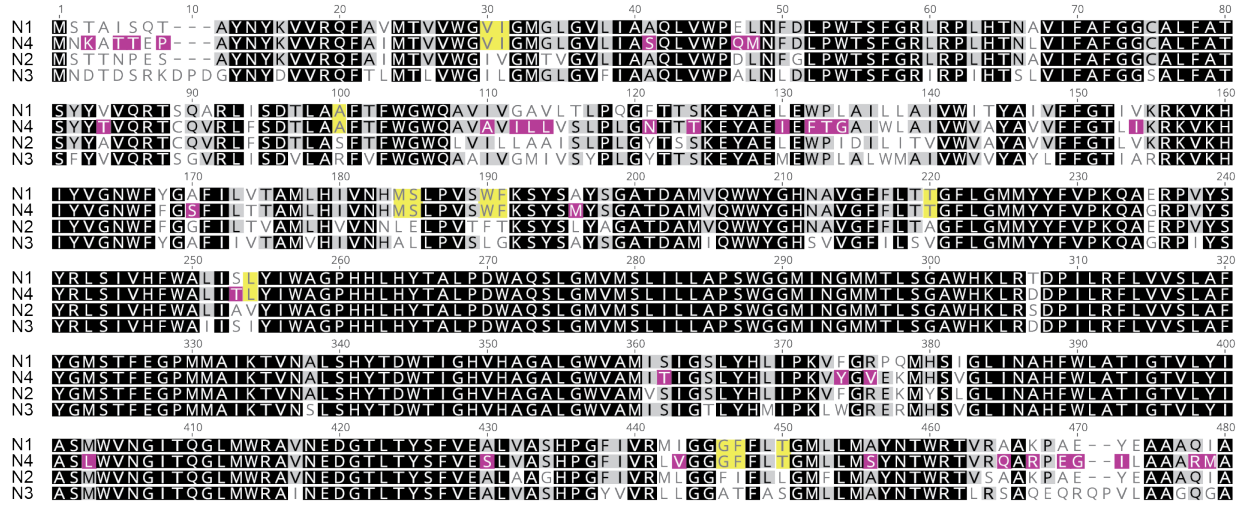

B.

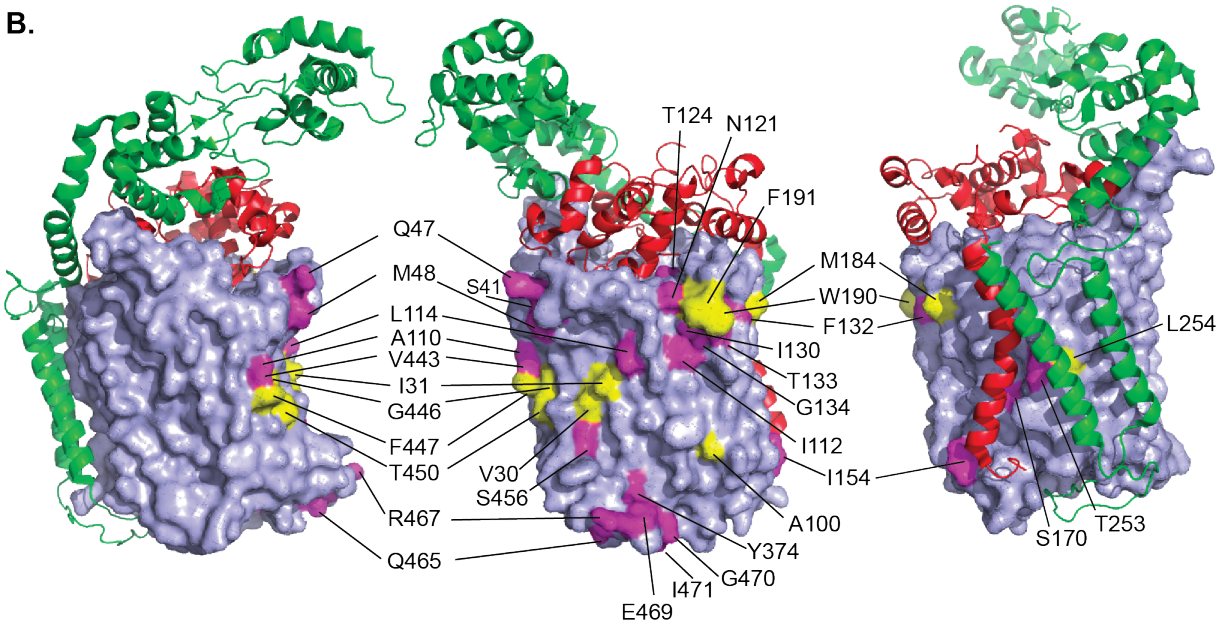

Figure 2.2—figure supplement 4. Comparison of the PA14 CcoN subunit sequences and analysis of the predicted structure of CcoN4. (A) Amino acid alignment (ClustalW) of the four CcoN subunits encoded by the PA14 genome. Residues conserved among all four N subunits are highlighted in black; residues conserved among any three of the four N subunits in gray; residues shared exclusively between CcoN1 and CcoN4 in yellow; and residues unique to CcoN4 in purple. **(B)** Predicted structure of CcoN4 from *P. aeruginosa* PA14, obtained by threading the PA14 sequence through the reported structure for the CcoN subunit of *P. stutzeri* (PDB: 5DJQ; (Buschmann et al. 2010b)) using SWISS-MODELL (Biasini et al. 2014). Surface-exposed residues that are shared exclusively between CcoN1 and CcoN4 are shown in yellow, while residues that are unique to CcoN4 are shown in magenta. Ribbon structures of the CcoO and CcoP subunits from *P. stutzeri* are shown in red and green, respectively. Structures were generated using PyMol (Schrödinger, LLC 2015).

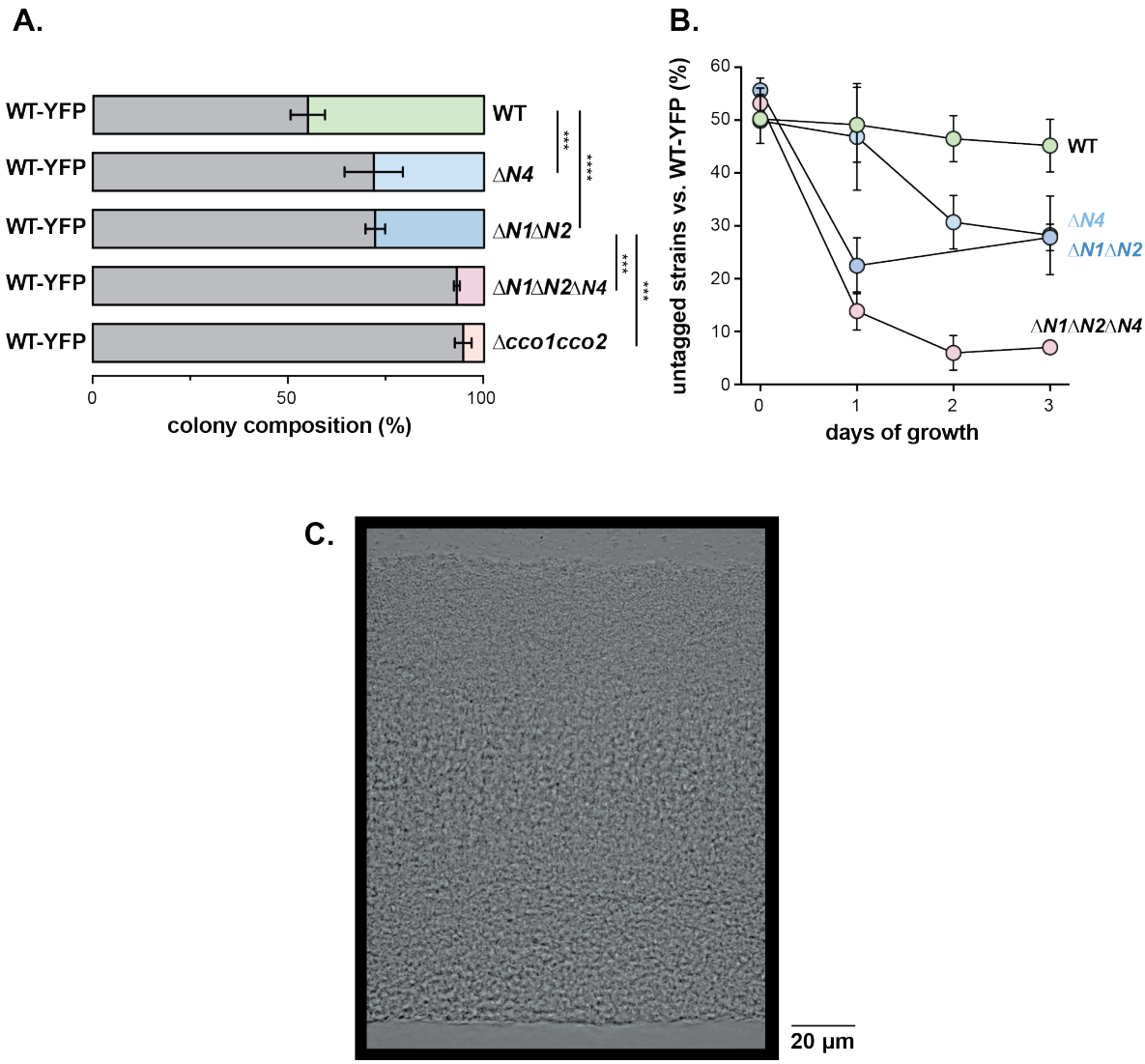

Figure 2.3—figure supplement 1. CcoN4 is necessary for optimal fitness in biofilms, particularly when O_2 becomes limiting. (A) Relative fitness of YFP-labeled WT when co-cultured with various *cco* mutant strains in mixed-strain biofilms for three days. Error bars represent the standard deviation of biological triplicates. P-values were calculated using unpaired, two-tailed t tests (***, P ≤ 0.001; ****, P ≤ 0.0001). For full statistical reporting, refer to Table 4. **(B)** Time course showing relative fitness, over a period of three days, of YFP-labeled WT when co-cultured with various *cco* mutant strains in mixed-strain biofilms. Error bars represent the standard deviation of biological triplicates. **(C)** DIC image of a three-day-old WT biofilm.

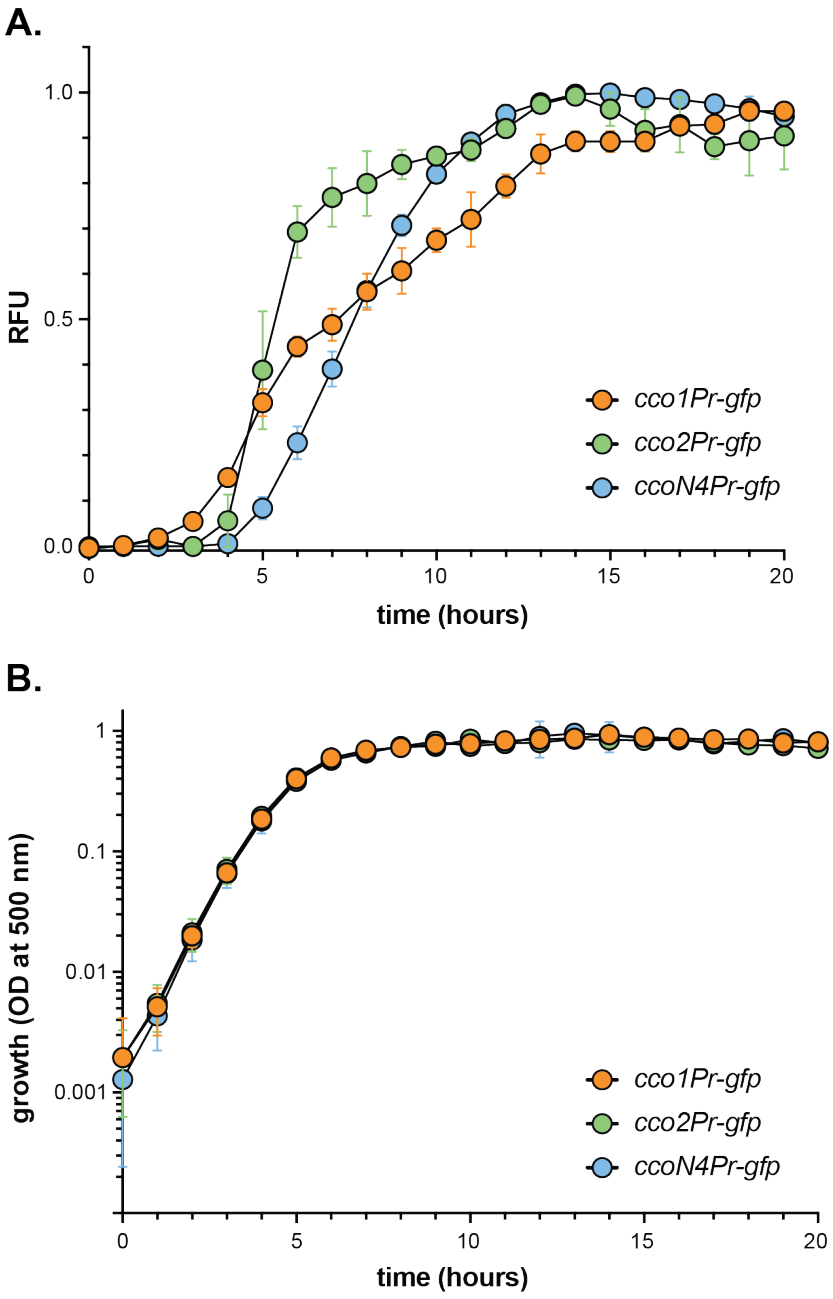

Figure 2.4—figure supplement 1. Expression of *cco* reporters in shaken liquid cultures. **(A)** Fluorescence of translational reporter strains, engineered to express GFP under the control of the *cco1*, *cco2*, or *ccoN4Q4* promoter during growth in 1% tryptone. Fluorescence values for a strain containing the *gfp* gene without a promoter (the MCS control) were treated as background and subtracted from each growth curve. **(B)** Liquid-culture growth of translational reporter strains in 1% tryptone. Error bars in **(A)** and **(B)** represent the standard deviation of biological triplicates and are not drawn in cases where they would be obscured by point markers.

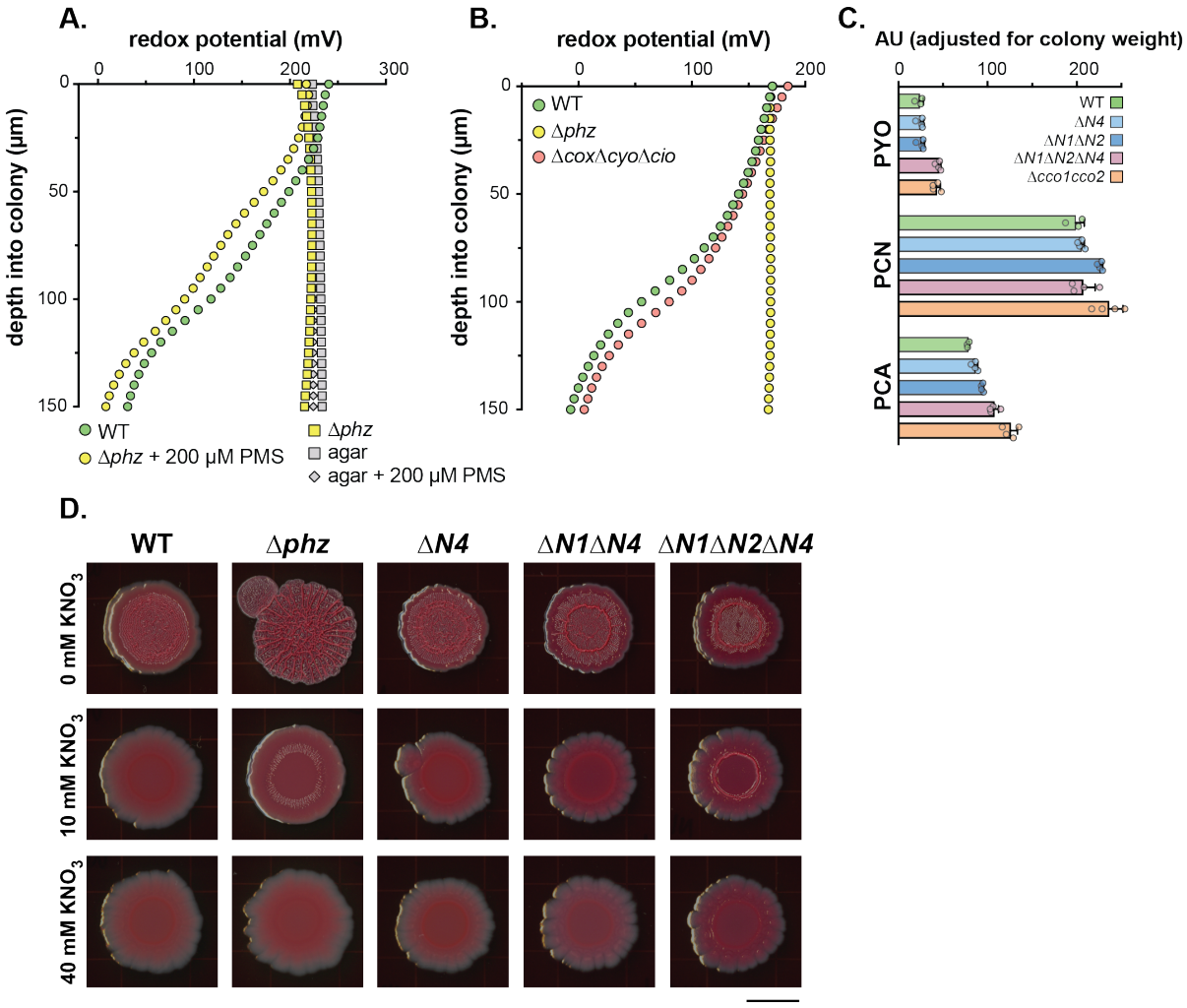

Figure 2.5—figure supplement 1. Use of a redox microelectrode to measure phenazine reduction in colony biofilms. (A) Change in redox potential over depth for two-day-old biofilms of PA14 WT, Δ*phz*, and Δ*phz* grown on 200 μM phenazine methosulfate (PMS). Data are representative of at least three biological replicates. To ensure that addition of PMS did not alter the baseline redox potential, a measurement was also taken of agar only. **(B)** Change in redox potential with depth for WT, Δ*phz*, and Δ*cox*Δ*cyo*Δ*cio* biofilms grown for two days. Data are representative of at least two biological replicates. **(C)** Levels of phenazines extracted from the agar medium underneath the colony and separated by HPLC, adjusted for biomass, for PA14 WT and various *cco* mutant biofilms grown for two days. Data represent the area under each peak in absorbance units for the phenazines indicated, and error bars represent standard deviation of at least three biological replicates. The phenazines pyocyanin (PYO), phenazine-1-carboxamide (PCN), and phenazine-1-carboxylic acid (PCA) were quantified. **(D)** Colony biofilm morphologies on day four of development for WT and various *cco* mutant biofilms grown on colony morphology plates containing 0, 10, and 40 mM potassium nitrate. Images were generated using a flatbed scanner (Epson Expression 11000XL) and are representative of at least three biological replicates. Scale bar is 1 cm.

Chapter 3

Carbon source influences electron flow through the aerobic respiratory chain of *Pseudomonas aeruginosa*

This chapter represents a manuscript that is being prepared for publication. I was responsible for all the work, except for the thin-sectioning of biofilms (**Figure 3.4B**), which was performed by William Cole Cornell. Matthew Greenwald and Brett Colbert assisted in the construction of transcriptional reporters for terminal oxidases. While most of the experiments have been completed, some are still pending; these will be mentioned throughout the text.

3.1: Introduction

A hallmark of the domain Bacteria is metabolic diversity, i.e. the vast variety of pathways and substrates that can be used to generate energy for growth or survival (Madigan et al., 2015). The metabolic diversity of bacteria allows them to persist in conditions that generally do not support eukaryotes, which produce energy almost exclusively by redox transformations of oxygen and water (Poole and Cook, 2000). An additional advantage for many bacteria is metabolic versatility, in which one species is able use multiple substrates and/or pathways for energy generation. Metabolic versatility affords the ability to grow in disparate environments and provides resilience in changing conditions.

A feature of bacteria that contributes to their metabolic versatility is respiratory chain branching (Madigan et al., 2015; Poole and Cook, 2000; White et al., 2012). While the mitochondrial electron transport chain (ETC) has one route for electrons to be delivered to the final electron acceptor, oxygen (O_2), bacterial respiratory chains often have multiple routes (most commonly two or three) (White et al., 2012). Furthermore, many species of bacteria are able to use substrates other than O_2, such as nitrate, as the final electron acceptor. This confers the ability to grow and respire anaerobically.

Work from our group and others has recently uncovered an additional level of branching in the respiratory chain of the Gram-negative, opportunistic pathogen *Pseudomonas aeruginosa*. *P. aeruginosa*'s ETC terminates at one of five canonical terminal oxidases, the enzymes that catalyze the final electron transfer step to reduce O_2 to water (Arai, 2011; Williams et al., 2007). Each of these terminal oxidases possesses unique characteristics, including

different expression patterns and affinities for O_2 (Alvarez-Ortega and Harwood, 2007; Arai et al., 2014; Comolli and Donohue, 2004; Kawakami et al., 2010). Our picture of the diversity at the terminal end of the ETC was further expanded by the discovery that the *P. aeruginosa* "Cco" complexes, which belong to the *cbb*$_3$ family of terminal oxidases, can contain subunits encoded by multiple, redundant operons present at distinct sites in the genome (Hirai et al., 2016). These heterocomplexes (i.e., isoforms) were shown to have specific roles under different conditions (Hirai et al., 2016) and to contribute differentially to biofilm physiology and redox state (Jo et al., 2017).

Another important aspect of *P. aeruginosa* metabolic versatility lies at the opposite, inaugural end of the ETC. This bacterium, being a chemoorganoheterotroph, obtains energy by oxidizing organic compounds, which also serve as source of carbon and electrons. The metabolism of carbon sources generates reducing equivalents, mainly in the form of NADH, which are re-oxidized when they feed electrons to the ETC (Madigan et al., 2015; White et al., 2012). It has long been appreciated that pseudomonads can metabolize a wide range of carbon sources and fine-tune their respiratory chains in response to changing environmental conditions (Poole and Cook, 2000; Stanier et al., 1966; Williams et al., 2007). When the genome of this bacterium was first sequenced, it was the largest of the bacterial genomes sequenced up to that point at ~ 6.3 million base pairs, and its size was attributed to the metabolic versatility of the organism (Stover et al., 2000). Of special note was the large number of membrane transport systems encoded, two thirds of which were annotated to be involved in nutrient uptake. These systems undoubtedly play a role in *P. aeruginosa*'s ability to thrive under diverse environmental conditions.

While *P. aeruginosa* can be found in nutrient-rich environments, such as soil, it is also found in more limited environments, such as water reservoirs (Eichner et al., 2014). Another environment in which *P. aeruginosa* is commonly found is in the lungs of patients with cystic fibrosis (CF) (Ciofu et al., 2012; Eichner et al., 2014; Høiby et al., 2011; Williams and Davies, 2012) where a defect in a chloride channel leads to the accumulation of thick mucus. *P.*

aeruginosa persists in this heterogeneous environment despite the scarcity of its preferred electron acceptor, O_2. Mutations in genes involved in nutrient uptake (Son et al., 2007) and primary metabolic pathways like the tricarboxylic acid (TCA) cycle (Hoboth et al., 2009) have been shown to be selected for in strains adapted to persist in CF lungs.

Metabolism is often conceptualized as a modular process in which the oxidation of diverse carbon sources can be coupled to the respiration of diverse electron acceptors via common, central pathways. However, this is an oversimplification as different carbon sources offer varying degrees of reducing power. As carbon sources are oxidized, electrons released from this process are transferred via dehydrogenases to ubiquinone, a redox-active lipid that ultimately reduces terminal oxidases. The redox state of the ubiquinone pool in the membrane has been shown to affect gene expression in *Escherichia coli* and *Rhodobacter capsulatus*, indicating that the so-called “charging” of the ubiquinone pool is an important regulatory step in bacterial respiration (Aussel et al., 2014). Therefore, it is perhaps unsurprising that different carbon sources have been shown to alter electron flow through central metabolic pathways and the activity of respiratory chain enzymes (Saint-Amans et al., 2001).

Furthermore, nutrient conditions, including carbon source identity and availability, have been shown to affect the development of *P. aeruginosa* biofilms (Shrout et al., 2006; Sriramulu et al., 2005). Biofilms are dense organizations of cells enclosed in a self-produced matrix with important implications for virulence (Elias and Banin, 2012; Høiby et al., 2011). Additionally, the production of phenazines, redox-active secondary metabolites that support redox balancing when O_2 is limiting (Glasser et al., 2014; Wang et al., 2010), is sensitive to environmental conditions (van Rij et al., 2004). Phenazines are necessary for the formation of an anoxic zone in a colony biofilm model (Dietrich et al., 2013) and recent work from our group indicates that they interact with components of the ETC (Jo et al., 2017). While *P. aeruginosa*’s metabolic versatility is well-known, how and whether specific carbon sources affect electron flow to phenazines and through the respiratory chain during biofilm growth has not been studied.

To investigate how electron donor affects downstream metabolic processes, I looked at the influence of carbon source on *P. aeruginosa* PA14 physiology. I began by testing a wide range of carbon sources for respiratory activity, and then chose three representative carbon sources for follow-up experiments: glucose (a fermentable carbon source metabolized via glycolysis [or, in the case of *P. aeruginosa*, the analogous Entner-Doudoroff pathway]), succinate (a TCA cycle intermediate), and tryptone (an undefined medium representative of nutrient-rich conditions (Frimmersdorf et al., 2010) and one that is commonly used to grow *P. aeruginosa* in laboratories).

I was particularly interested in investigating how the presence of specific terminal oxidases and phenazines might influence *P. aeruginosa*'s utilization of different carbon sources. I chose to focus on the Cco and Cio terminal oxidases, as those have been shown to be sufficient for *P. aeruginosa* growth under the microaerobic conditions in which this bacterium thrives (Alvarez-Ortega and Harwood, 2007). These terminal oxidases represent two diverging pathways of electron flow through the *P. aeruginosa* ETC: Cio accepts electrons from the quinone pool while the Cco's accept electrons from cytochrome *c* (**Figure 3.1A**). As work from our group has recently implicated the Cco terminal oxidases in phenazine utilization in biofilms (Jo et al., 2017), I also assessed how specific carbon sources influence phenazine production. My results indicate that the identity of the carbon source has profound effects on PA14 growth, colony biofilm morphogenesis, terminal oxidase expression, and phenazine production and utilization.

3:2: Results

3.2.1: Identification of carbon sources that support reduction of tetrazolium violet

To assess the influence of different carbon sources on *P. aeruginosa* PA14's branched ETC, I measured respiratory activity using a commercially-available "phenotype microarray" (PM). The array is a 96-well plate containing 95 carbon sources and respiration is

quantified by incubating cells in a manufacturer-provided growth medium with the redox indicator dye “tetrazolium violet,” which undergoes an irreversible color change from faint yellow to purple upon reduction. The reduction of tetrazolium dyes is dependent on the ETC (Berridge et al., 2005).

I compared dye reduction by the PA14 strains WT, PaCco, and PaCio in the presence and absence of phenazines to address the question of how different respiratory chain components and phenazines might affect electron flow in *P. aeruginosa*. PaCco (Δ*cox*Δ*cyo*Δ*cio*; the *cox* operon encodes Aa_3, the *cyo* operon encodes Bo_3, and the *cio* operon encodes Cio) is a terminal oxidase mutant that only has the Cco terminal oxidases remaining; PaCio (Δ*cox*Δ*cyo*Δ*cco1cco2*) only has the Cio terminal oxidase remaining (**Figure 3.1A**). The respective phenazine-null strains of these mutants are referred to as PaCcoΔ*phz* and PaCioΔ*phz*. I chose to focus on these terminal oxidases because they have been shown to be most important for aerobic and microaerobic growth in *P. aeruginosa* under laboratory conditions (Alvarez-Ortega and Harwood, 2007; Arai, 2011). Because terminal oxidase gene deletions can result in growth defects (Alvarez-Ortega and Harwood, 2007; Arai et al., 2014; Jo et al., 2017; Chapter 2) I wanted to ensure that any dye reduction phenotype observed in the terminal oxidase mutants was an effect of altered electron flow rather than abrogated growth. Therefore, I performed a separate set of experiments, using the same strains, in which cells were resuspended in a MOPS-buffered medium (with no tetrazolium violet or added carbon source) and measured cell density at 500 nm to assay for growth on the provided carbon source. Carbon sources that did not support growth are listed in **Figure 3.1–figure supplement 1.**

37 of the 95 tested carbon sources supported PA14 growth, and of those, 22 supported dye reduction by PA14 (**Figure 3.1B**). I did not notice any obvious carbon source preference with respect to amino acids, carbohydrates, and carboxylic acids. These results are consistent with previous reports that have shown *P. aeruginosa* to be capable of utilizing a variety of carbon sources (Stanier et al., 1966).

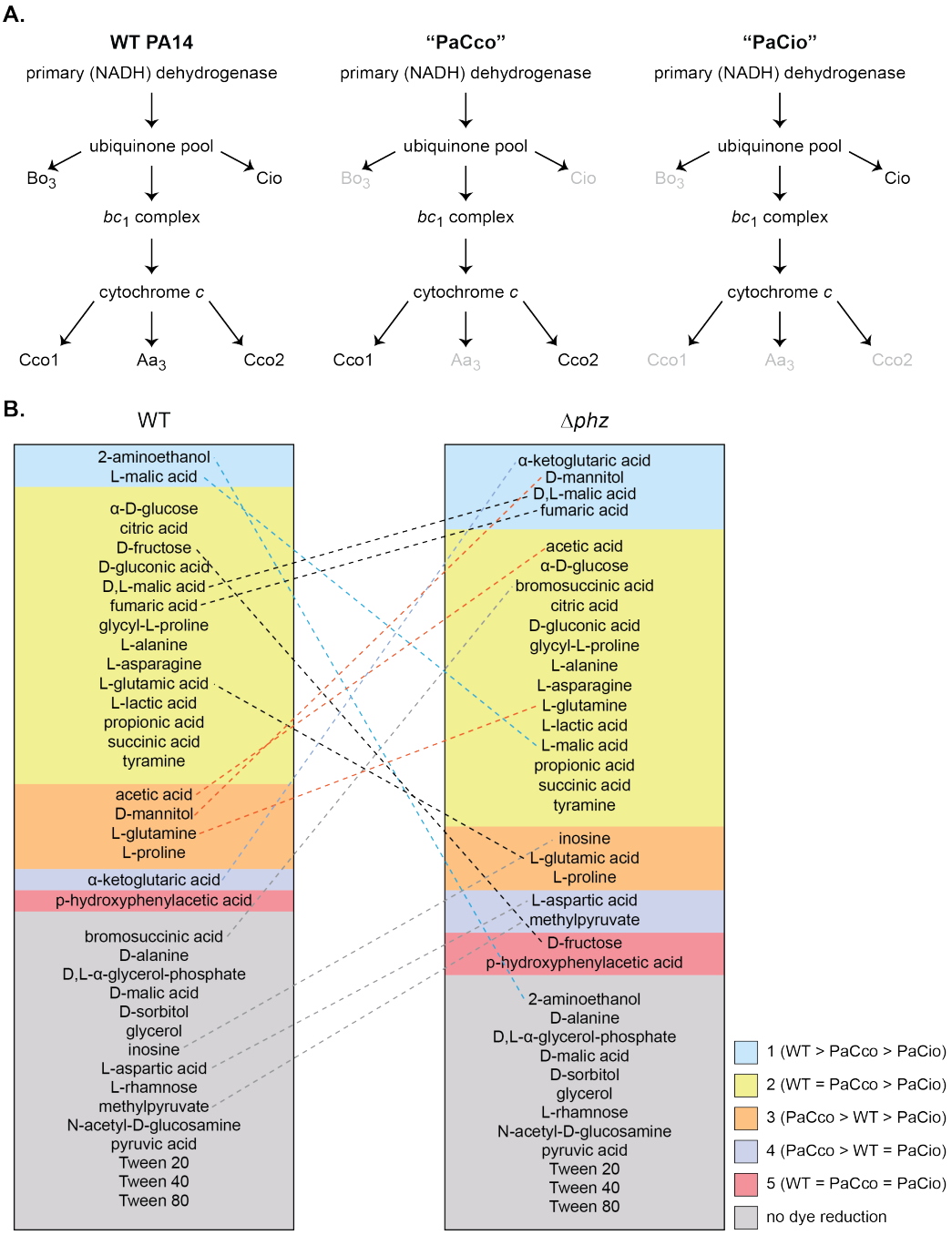

Figure 3.1. Carbon sources that support growth of PA14. (A) A simplified diagram of electron flow through the *P. aeruginosa* electron transport chain, indicating the terminal oxidases remaining in the WT (left), PaCco (middle), and PaCio (right). Terminal oxidases in gray indicate those that have been deleted in respective strains. **(B)** Carbon sources that support growth of PA14 strains (total = 37), classified into groups based on levels of tetrazolium violet reduction in the presence (left) and absence (right) of phenazines. Gray, no reduction in any strains; blue, group 1 (WT > PaCco > PaCio); yellow, group 2 (WT = PaCco > PaCio); orange, group 3 (PaCco > WT > PaCio); lavender, group 4 (PaCco > WT = PaCio); red, group 5 (WT = PaCco = PaCio). Dashed lines interconnecting carbon sources indicate those whose dye reduction patterns were affected by phenazines.

3.2.2: Respiratory chain composition influences tetrazolium dye reduction in P. aeruginosa

For the carbon sources that facilitated tetrazolium violet reduction, I then asked whether this activity was predominantly mediated by the quinol oxidase Cio or the cytochrome *c* oxidase Cco complexes. To assess how availability of the various ETC branches affects carbon source utilization with respect to dye reduction and growth, I tested the terminal oxidase mutants PaCco and PaCio. I grouped the carbon sources into five categories according to their relative levels of dye reduction: (1) WT > PaCco > PaCio, (2) WT = PaCco > PaCio, (3) PaCco > WT > PaCio, (4) PaCco > WT = PaCio, and (5) WT = PaCco = PaCio (**Figure 3.1B**). I have encountered some discrepancies between trials of the same strain, and more trials are planned to elucidate which trends are reproducible. However, I have been able to preliminarily group the carbon sources into the aforementioned categories and make some general observations.

Carbon sources that fell into groups 1 and 2 (i.e., WT or WT and PaCco exhibited the most dye reduction) were consistent with previous observations that the Cco terminal oxidases support WT-like physiology in liquid cultures and biofilms (Arai et al., 2014; Jo et al., 2017). In contrast, carbon sources in the remaining groups resulted in altered electron flow, with PaCco displaying most dye reduction (groups 3 and 4) or WT, PaCco, and PaCio contributing equally to dye reduction (group 5). While the latter does represent an interesting deviation from expected dye reduction kinetics (i.e., those seen in groups 1 and 2), I was particularly intrigued by groups 3 and 4 as we recently showed that the Cco terminal oxidases are required for WT biofilm development and phenazine utilization on tryptone (Jo et al., 2017).

Carbon sources in group 3 resulted in the most dye reduction by PaCco, followed by WT, then PaCio. The carbon sources that fell into this group were acetic acid, D-mannitol, L-proline, and L-glutamine (**Figure 3.2A**). The lower levels of dye reduction in these carbon sources by PaCio could be attributed to this strain's significant growth defect (**Figure 3.2–figure supplement 1A**). However, the dye reduction phenotype of PaCco relative to the WT in group 3

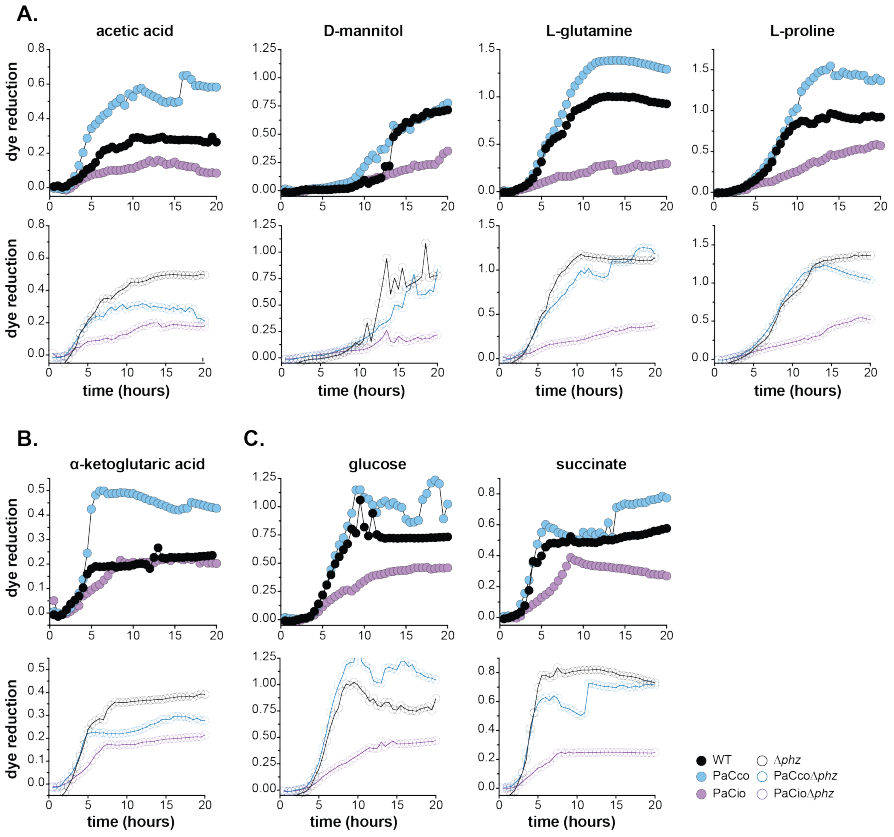

Figure 3.2. Dye reduction kinetics of carbon sources of interest. Dye reduction (absorbance at 590 nm) over time of carbon sources in group 3 **(A)** and group 4 **(B)**. Initial designations into groups were based on dye reduction with phenazines, and dye reduction curves are shown in the presence (top, closed circles) and absence (bottom, open circles) of phenazines. Data represent the average of two biological replicates. **(C)** Dye reduction over time for glucose, a representative glycolytic carbon source, and succinate, a representative TCA cycle carbon source, in the presence (top, closed circles) and absence (bottom, open circles) of phenazines.

carbon sources cannot be attributed to differential growth, as I observed similar growth yields for these two strains (**Figure 3.2–figure supplement 1A**).

Group 4 represented carbon sources that again lead to the most dye reduction by PaCco, but in which dye reduction by WT is comparable to that by PaCio (**Figure 3.2B**). Only one carbon source was in this group: α-ketoglutaric acid, a TCA cycle intermediate that serves as a branchpoint from central metabolism to the synthesis of various amino acids including proline and glutamine, two carbon sources identified in group 3 (**Figure 1.1B**).

3.2.3: Phenazines have differential effects on tetrazolium dye reduction depending on respiratory chain composition

Recently we found that the Cco terminal oxidases are required for phenazine reduction in tryptone-grown colonies (Jo et al., 2017). Because phenazines have been shown to receive electrons from the mitochondrial ETC (Armstrong and Stewart-Tull, 1971), I studied dye reduction patterns of the aforementioned strains in the phenazine-null (Δ*phz*) background as well. Indeed, by comparing dye reduction kinetics of WT, PaCco, and PaCio with the equivalent strains in a phenazine-null (Δ*phz*) background, I found that the group assignment changed for 14 out of the 37 carbon sources that support WT growth (**Figure 3.1B**), indicating that the presence of phenazines had significant effects on dye reduction and, by extension, electron flow in PA14. For example, when phenazines are present, PaCco reduces tetrazolium violet more than WT when grown in L-glutamine or L-proline (**Figure 3.2A**, top). However, when phenazines are absent, Δ*phz* and PaCcoΔ*phz* exhibit similar levels of dye reduction (**Figure 3.2A**, bottom); in other words, carbon sources that were categorized into group 3 with phenazines could now be classified into group 2 (**Figures 3.1B** and **3.2A**). A similar switching of groupings was observed for acetic acid and α-ketoglutaric acid (**Figures 3.1A** and **3.2A**, **B**).

Of the five carbon sources in groups 3 and 4, three (L-proline, L-glutamine, and α-ketoglutaric acid) are intermediates or direct branchpoints off of the TCA cycle (**Figure 1.1**). Therefore, I wondered what dye reduction patterns would be observed for the standard glycolytic and TCA cycle carbon sources glucose and succinate. When I compared dye reduction patterns of PA14 in glucose and succinate, I found that glucose fell into carbon-source group 3 while succinate fell into group 2 (**Figure 3.2C**). When comparing growth profiles of WT and PaCco, I found similar levels of growth (**Figure 3.2–figure supplement 1C**), again indicating that any dye reduction phenotypes observed are independent of growth differences.

While the PM-based dye reduction and growth assays provided insights into factors that alter electron flow through the *P. aeruginosa* ETC (the presence of certain terminal oxidases and phenazines), I chose to focus subsequent experiments on the following carbon sources: α-

ketoglutaric acid, glutamine, glucose, succinate, and tryptone. All of these carbon sources, with the exception of tryptone, are directly or closely linked to central metabolic pathways. Glucose and succinate represent *P. aeruginosa*'s two main pathways for carbon source oxidation, the Entner-Doudoroff pathway and the TCA cycle, respectively. Additionally, while many previous studies have been carried out using these two carbon sources in liquid culture, less has been done exploring how they alter biofilm growth and physiology. α-ketoglutaric acid is another TCA cycle intermediate and the precursor for glutamine synthesis. The α-ketoglutaric acid-glutamine branchpoint also represents an important hub between carbon and nitrogen metabolism (Doucette et al., 2011). The experiments using α-ketoglutaric acid and glutamine have not yet been completed and, as such will not be discussed further here. Finally, I included tryptone as an additional carbon source because it is commonly used to culture *P. aeruginosa* in laboratory settings and may more closely mimic the nutrient-rich conditions in which *P. aeruginosa* is sometimes found in nature (Frimmersdorf et al., 2010).

3.2.4: Effects of phenazines and carbon sources on planktonic and biofilm growth in PA14

To confirm the growth trends for glucose and succinate that I observed in the PM plates (**Figure 3.2),** I grew the same six strains (WT, PaCco, PaCio, Δ*phz*, PaCcoΔ*phz*, PaCioΔ*phz*) using the following media: a MOPS-buffered defined medium with either 20 mM glucose or succinate as the sole carbon source or a broth made with tryptone, an undefined tryptic protein digest that is a popular ingredient in bacterial growth media. Consistent with the data shown in **Figure 3.2**, PaCio had a growth defect relative to WT and PaCco in all media tested (**Figure 3.3A**). Cells grew fastest in 1% tryptone, followed by MOPS-succinate, then MOPS-glucose (**Figure 3.3A**). Because glucose is a 6-carbon compound while succinate is a 4-carbon compound, I wanted to ensure that these growth trends were not a byproduct of discrepancies in molar availabilities of carbon source. When I grew PA14 in MOPS medium with 30 mM

succinate, I found that the trends observed in **Figure 3A** persisted (**Figure 3–figure supplement 1**).

WT and PaCco exhibited similar growth patterns in 1% tryptone and MOPS-succinate (**Figure 3.3A**). However, PaCco had an exponential-phase growth defect relative to the WT when grown in MOPS-glucose (**Figure 3.3A**). Also specifically in glucose, the lack of phenazines resulted in an exponential phase growth defect for all strains tested (**Figure 3.3A**), suggesting that phenazines promote optimal planktonic growth when glucose is the sole carbon source. Phenazines have been implicated in redox balancing during anaerobic survival via pyruvate fermentation (Glasser et al., 2014); their contribution to growth on glucose suggests that phenazines may also help to offset a redox imbalance that occurs during metabolism of this carbon source.

While liquid culture represents one mode of bacterial growth, in nature bacteria often grow as biofilms, multicellular aggregates of cells encased in a self-produced matrix (Hall-Stoodley et al., 2004; Toyofuku et al., 2016), which affords protection from external assaults. The increased resistance of biofilms to chemicals such as antibiotics presents a formidable challenge to eradicating biofilm-based bacterial infections (Høiby et al., 2011; Murray et al., 2007). To test whether the growth phenotypes I saw in liquid culture would be recapitulated in biofilms, I next grew PA14 colony biofilms on agar plates containing tryptone, glucose, or succinate and monitored their development.

Growth on tryptone yielded the largest and thickest WT biofilms (**Figure 3.3B**, **Figure 3.4B**). The colonies also exhibited the most wrinkling and Congo red binding, two features that are indicative of matrix production as a result of redox stress (Dietrich et al., 2013; Friedman and Kolter, 2004; Jennings et al., 2015; Okegbe et al., 2014). On glucose, WT colonies were smaller and paler than those grown on tryptone, while biofilms on succinate were thin (**Figure 3.4B**) and translucent, indicative of poor growth (**Figure 3.3B**). In contrast, Δ*phz* biofilms grown on succinate were thicker and more robust (**Figure 3.3B**), indicating that phenazines negatively affect growth on succinate. I did not notice any obvious differences between WT and Δ*phz*

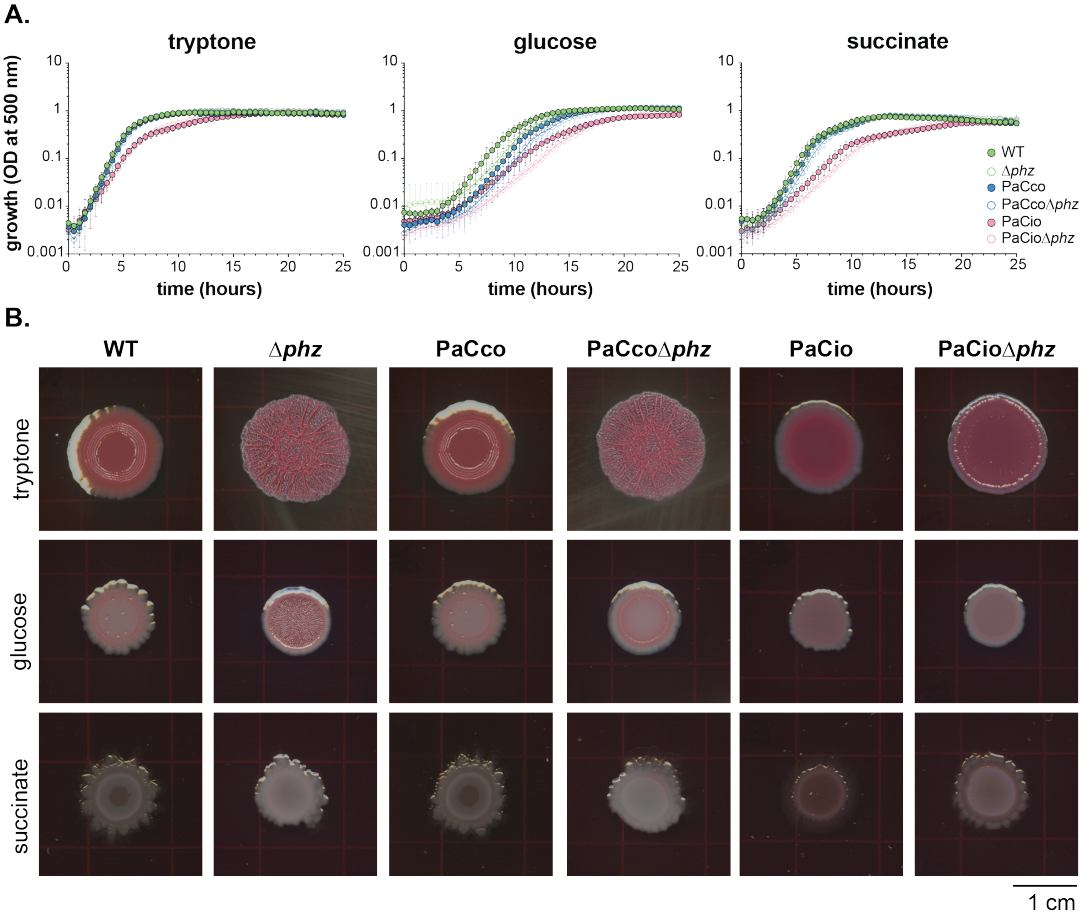

Figure 3.3. Carbon source affects PA14 growth in liquid culture and biofilms. (A) Growth of *P. aeruginosa* PA14 strains in 1% tryptone (left), MOPS defined medium with 20 mM glucose (middle), and MOPS defined medium with 20 mM succinate (right). Data represent the mean values of at least six biological replicates. Error bars denote standard deviation. **(B)** Colony biofilms of *P. aeruginosa* strains on day three of development on varying carbon sources. Colony morphologies are representative of at least three biological replicates.

colonies on glucose and tryptone. I observed the same trends for strains containing only the Cio terminal oxidases (PaCio), although they generally formed thinner and smaller colonies (**Figure 3.3B**).

PaCco phenocopied WT biofilms on all three carbon sources (**Figure 3.3B**; Jo et al., 2017). PaCcoΔ*phz* biofilms were indistinguishable from those formed by Δ*phz* on tryptone and succinate, but they showed delayed wrinkling and less Congo red binding on glucose (**Figure 3.3B**). Taken together, these results suggest a role for phenazines in modulating the efficiency of terminal oxidases in a carbon source-dependent manner, both in liquid culture (**Figures 3.2 and 3.3A**) and in biofilms (**Figure 3.3B**).

3.2.5: Carbon source influences expression of terminal oxidases

The growth data suggested that the presence (or absence) of specific terminal oxidases affects carbon source utilization. To test if carbon sources themselves influence terminal oxidase expression, I created reporters by fusing the promoters of the five terminal oxidases to *gfp* and monitored their expression in tryptone, glucose, and succinate.

I found that in liquid culture, both *cco* operons were most highly expressed on tryptone, with *cco2-gfp* sharply induced upon entry into stationary phase (**Figure 3.4A**). *cco2*'s expression is consistent with previous studies demonstrating that *cco2* is regulated by Anr, a global transcription factor that regulates gene expression during the shift from oxic to anoxic conditions (Ray and Williams, 1997). While aa_3 was equally well-expressed on tryptone and glucose, it was barely detectable on succinate. bo_3 expression was slightly elevated in glucose over tryptone, while I did not detect a significant signal on succinate. Finally, the expression of *cio* was comparable on all three carbon sources. These results illustrate the importance of carbon source on the relative expression pattern for terminal oxidases in liquid culture (**Figure 3.4A**).

Shaking liquid cultures are characterized by a constant influx of O_2 and a homogeneous environment. This is in stark contrast to biofilms which form nutrient gradients that are likely to affect the expression of terminal oxidases. We previously showed that a three-day-old colony biofilm contains O_2 concentrations ranging from atmospheric levels at the top to undetectable levels at the bottom (Jo et al., 2017), making it an intriguing system in which to study terminal oxidase expression. I grew the reporter strains for three days on agar plates with tryptone, glucose, or succinate as the sole carbon sources, then fixed and thin-sectioned the biofilms to visualize terminal oxidase expression along the oxygen gradient (**Figure 3.4B**).

bo_3-*gfp* expression was not observed in biofilms grown on any carbon source (**Figure 3.4B**), indicating that Bo_3 is not highly expressed in the biofilm under these conditions. That I detected bo_3-*gfp* expression in tryptone and glucose when cells were grown planktonically (**Figure 3.4A**) suggests differential regulation of bo_3 in the liquid versus biofilm context. Aa_3,

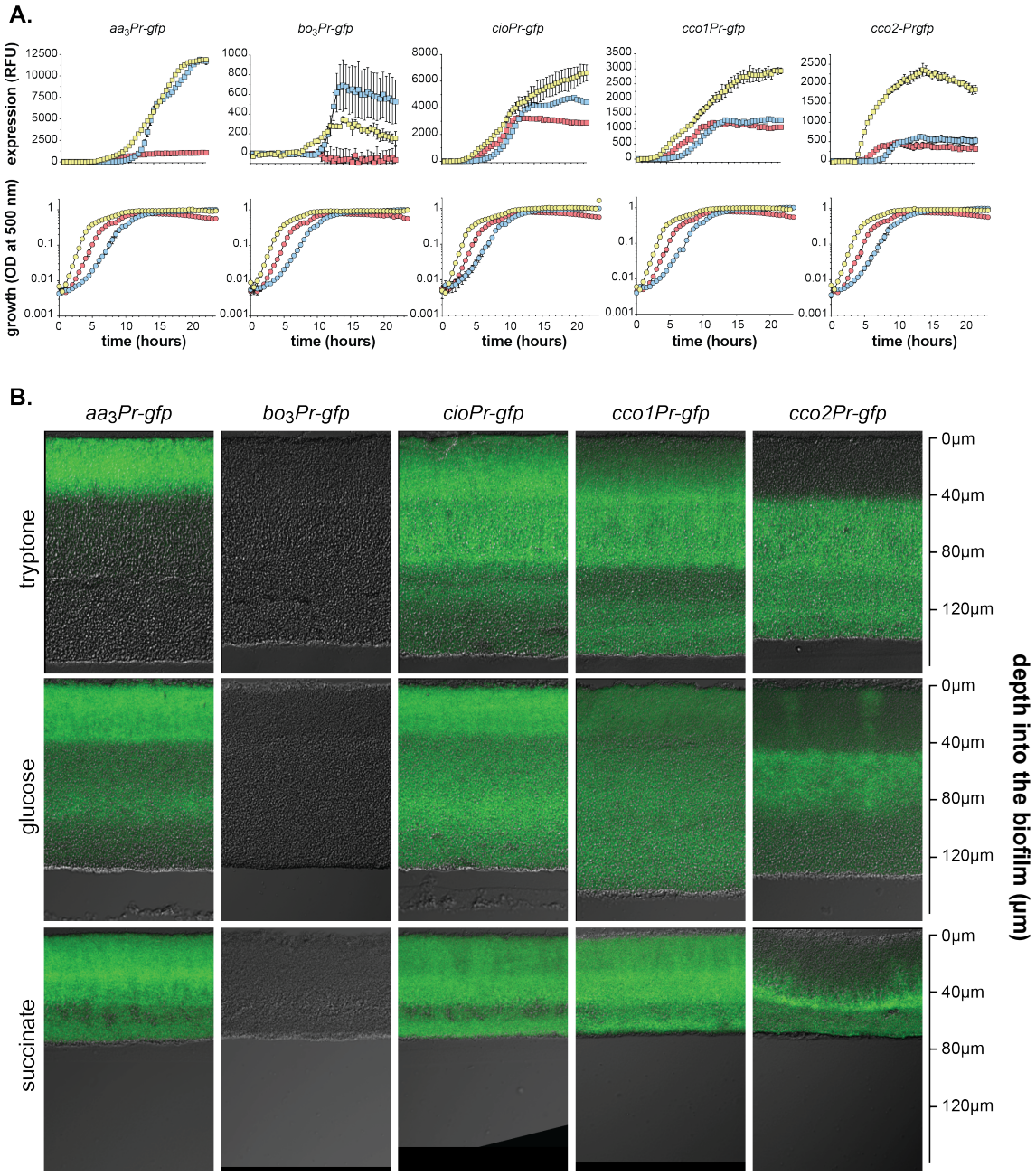

Figure 3.4. Differential expression of terminal oxidases in tryptone, glucose, and succinate. (A) Expression profiles of *P. aeruginosa*'s five terminal oxidases (*aa*$_3$, *bo*$_3$, *cio*, *cco1*, *cco2*) during liquid-culture growth. Strains expressing GFP under the control of terminal oxidase promoters were grown in tryptone (yellow), MOPS-glucose (blue), and MOPS-succinate (red). Top graphs show expression of terminal oxidases (RFU) while bottom graphs show growth curves of corresponding strains. Data represent the average of at least three biological replicates, and error bars denote standard deviation. **(B)** Representative images of thin sections prepared from WT biofilms grown for 3 days on tryptone, MOPS-glucose, or MOPS-succinate agar plates. Each biofilm is expressing GFP under the control of the *aa*$_3$, *bo*$_3$, *cio*, *cco1*, or *cco2* promoter. Reporter fluorescence (green) is overlain on respective DIC images. Scale bars indicate depth (μm) into the biofilm, with "0" representing the biofilm-air interface. Images are representative of at least six biological replicates.

while the predominant terminal oxidase enzyme in many bacteria (Arai, 2011) and the one most closely-related to the mitochondrial terminal oxidase, is expected to play a minor role under normal laboratory conditions in *P. aeruginosa* (Arai et al., 2014). In tryptone and glucose, I observed the highest level of *aa*$_3$-*gfp* expression in the top ~ 40 μm of the biofilm (**Figure 3.4B**). As the biofilm-agar interface is at the bottom of the biofilm, the top of the biofilm represents the region that would be the most nutrient-starved, and this is the location where I saw *aa*$_3$ expressed.

We have previously shown that *cco1* is expressed throughout biofilms grown on tryptone, while *cco2* expression is sharply induced at ~ 40 μm (Jo et al., 2017; **Figure 3.4B**). *cco2-gfp* expression coincides with the biofilm depth at which O_2 becomes limiting (Jo et al., 2017; **Figure 3.4B**) again consistent with its regulation by Anr. *cio-gfp* expression on tryptone was similar to that of *cco1* with two exceptions: *cco1-gfp* showed a bright, thin band of high expression at ~ 45 μm coinciding with a void in *cio-gfp* expression and *cio-gfp* showed a discrete thin band of expression at ~ 100 μm, coinciding with a void in *cco1-gfp* expression. *aa*$_3$-*gfp* had an almost inverse expression profile as that of *cco2-gfp*: it was highly expressed only in the top ~ 40 μm of the biofilm.

When biofilms were grown on glucose (**Figure 3.4B**, middle row), *cco1-gfp* was again seen throughout the biofilm; however, expression was more homogeneous and relatively lower than on tryptone (**Figure 3.4B**, top row). *cco2-gfp* again showed brightest expression in parts of the biofilm that were microaerobic, with expression between 45-90 μm into the biofilm. In contrast to tryptone, where *cco2-gfp* was seen to the bottom of the biofilm, *cco2-gfp* on glucose was only expressed at background levels past 90 μm into the colony. The expression profiles of *cio-gfp* and *aa*$_3$-*gfp* were intriguingly similar on glucose, with both having the highest expression at the top ~ 40 μm of the biofilm, and another (slightly less bright) band of high expression between 80-100 μm.

When biofilms were grown on succinate (**Figure 3.4B**, bottom row), colonies were thinner (only ~ 80 μm as opposed to the 120-150 μm thickness of colonies grown on tryptone

and glucose). *cco1-gfp* and *cio-gfp* showed similar expression on succinate: both were expressed throughout the biofilm, excepting a small void at ~ 60-70 μm, with a band of highest expression seen between ~ 30-50 μm. *aa*$_3$*-gfp* expression was similar, but its highest expression was in a very thin strip at ~ 35 μm. *cco2-gfp* expression on succinate again peaked at ~ 45 μm, as it did on tryptone and glucose, but was restricted to one thin ~ 10 μm strip.

3.2.6: Carbon source affects phenazine production in P. aeruginosa

Given that both carbon source and phenazines affected tetrazolium violet reduction (**Figures 3.1** and **3.2**), I next asked if carbon source itself affects phenazine production. *P. aeruginosa* produces a diverse set of phenazines that have different chemical properties (varying redox potentials, hydrophobicity, and colors) (Price-Whelan et al., 2006; Wang and Newman, 2008). The precursor phenazine, phenazine-1-carboxylic acid (PCA), can be modified into derivatives, such as phenazine-1-carboxamide (PCN) and pyocyanin (PYO) (**Figure 1.7A**). I grew WT PA14 in liquid cultures and biofilms on tryptone, glucose, and succinate and quantified phenazines produced under each condition using high performance liquid chromatography (HPLC).

In agreement with a previous report (Recinos et al., 2012), PCN was produced in biofilms grown on all three carbon sources (**Figure 3.5B**), but it was barely detectable in liquid cultures (**Figure 3.5A**). Conversely, PYO, which was amply produced in liquid culture, was detectable in only trace amounts in biofilms, or not at all in the case of glucose (**Figure 3.5B** and **C**). This indicates a biofilm-specific but carbon source-independent switch from PYO to PCN production between the planktonic and biofilm growth states (**Figure 3.5A**). I note that most of the phenazines produced in biofilms were released into the agar (**Figures 3.5B** and **3.5–figure supplement 1**) and, as such, I will only consider phenazines detected in the agar when discussing phenazines produced in biofilms.

PCA is the precursor for PCN and PYO (**Figure 1.7A**). Intriguingly, while the conversion of PCA to PYO (liquid culture) or PCN (biofilm) occurred in a 10:1 ratio on tryptone and

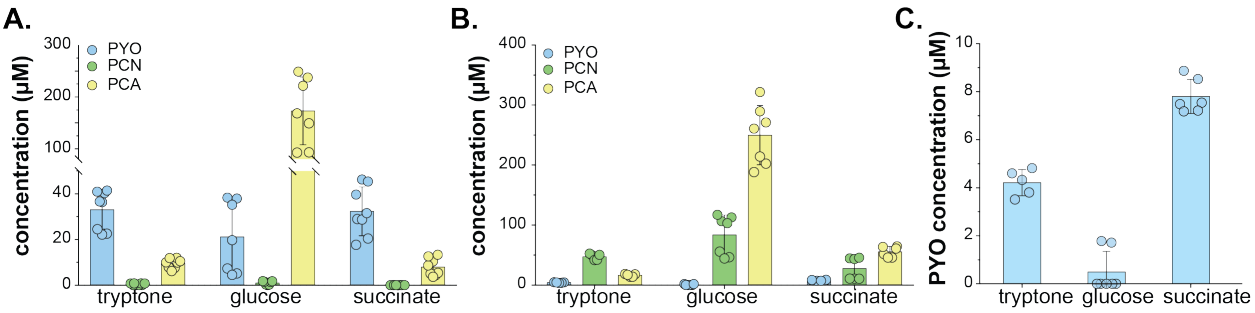

Figure 3.5. Phenazine production is altered in response to carbon source. (A) Quantification of phenazines produced by planktonic WT PA14 cells in late stationary phase of growth. **(B)** Quantification of phenazines secreted into the agar beneath three-day-old WT biofilms. **(C)** Close-up of pyocyanin concentrations shown in panel **(B)**. For all panels, individual data points represent biological replicates, and bars indicate the mean. Error bars denote standard deviation. The phenazines quantified were phenazine-1-carboxylic acid (PCA), phenazine-1-carboxamide (PCN), and pyocyanin (PYO).

succinate, only ~ 20% of PCA was converted when grown on glucose. These dynamics in phenazine production indicate that the carbon source influences the kind and amount of phenazine(s) produced by PA14 and highlights the plasticity of phenazine production in response to environment.

3.2.7: Phenazine reduction patterns are altered by carbon source

Since the redox activity of phenazines is crucial for their functionality (Price-Whelan et al., 2007, 2006; Wang and Newman, 2008) I next asked if carbon sources not only affect their production (**Figure 3.5**) but also their electrochemical reduction. To address this question, I directly measured phenazine reduction throughout the depth of three-day-old biofilms using redox microelectrodes. We have previously shown that WT colonies grown on tryptone show a gradient of increasingly-reduced extracellular redox state as depth into the colony increases and that this reduction gradient is phenazine-dependent (**Figures 2.5A** and **3.6A**; Jo et al., 2017). We have also shown that the Cco terminal oxidases are necessary for phenazine reduction through tryptone-grown colonies (**Figures 2.5B** and **3.6A**; Jo et al., 2017).

When colonies were grown on glucose, phenazines were reduced in the topmost, aerobic zone of the biofilm (**Figure 3.6B**), displaying different reduction patterns than those

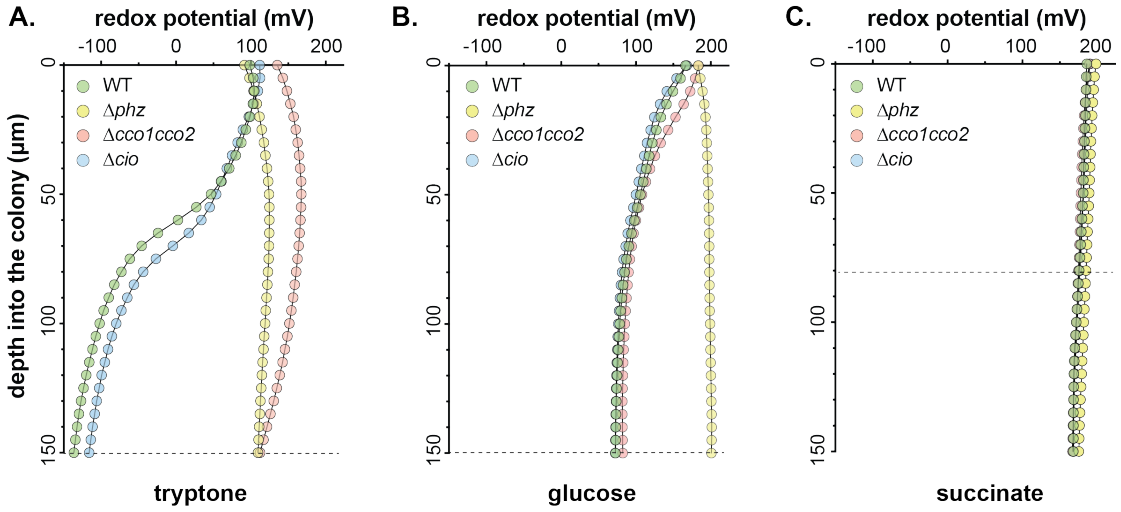

Figure 3.6. Phenazine reduction is influenced by carbon source. Change in redox potential (mV) with depth in three-day-old PA14 biofilms grown on tryptone **(A)**, MOPS-glucose **(B)**, or MOPS-succinate **(C)**. Data shown are representative of at least six biological replicates. Dashed lines indicate approximate colony thickness.

observed on tryptone (**Figure 3.6A**). Furthermore, the Cco oxidases no longer appeared to be required for phenazine reduction on glucose. On succinate, phenazine reduction was not detectable, in spite of the fact that colonies produced similar amounts of phenazine on succinate as they did on tryptone (**Figure 3.5B**). Together, these results support the hypothesis that electron flux through the respiratory chain is altered significantly in response to different carbon sources.

Because PA14 synthesizes multiple different phenazine compounds, all with differing chemical structures, redox potentials, and likely physiological function, I created a "clean" background in which I would be able to measure the reduction of individual phenazines. To this end, I made a mutant unable to produce or modify any of PA14's phenazines, Δ*phzH*Δ*phzM*Δ*phzS* Δ*phzA1-G1*Δ*phzA2-G2* (referred to as "Δ*HMS*Δ*phz*"; **Figure 1.7A**). I then grew this mutant on agar plates containing one of the pure phenazine compounds (PCA, PCN, PMS, or PYO) and measured their reduction on glucose and tryptone. I did not include succinate in this analysis because I did not detect any phenazine reduction in biofilms grown on succinate (**Figure 3.6C**). Because the endogenous PCA derivative 5-methyl-PCA (5-Me-PCA) is

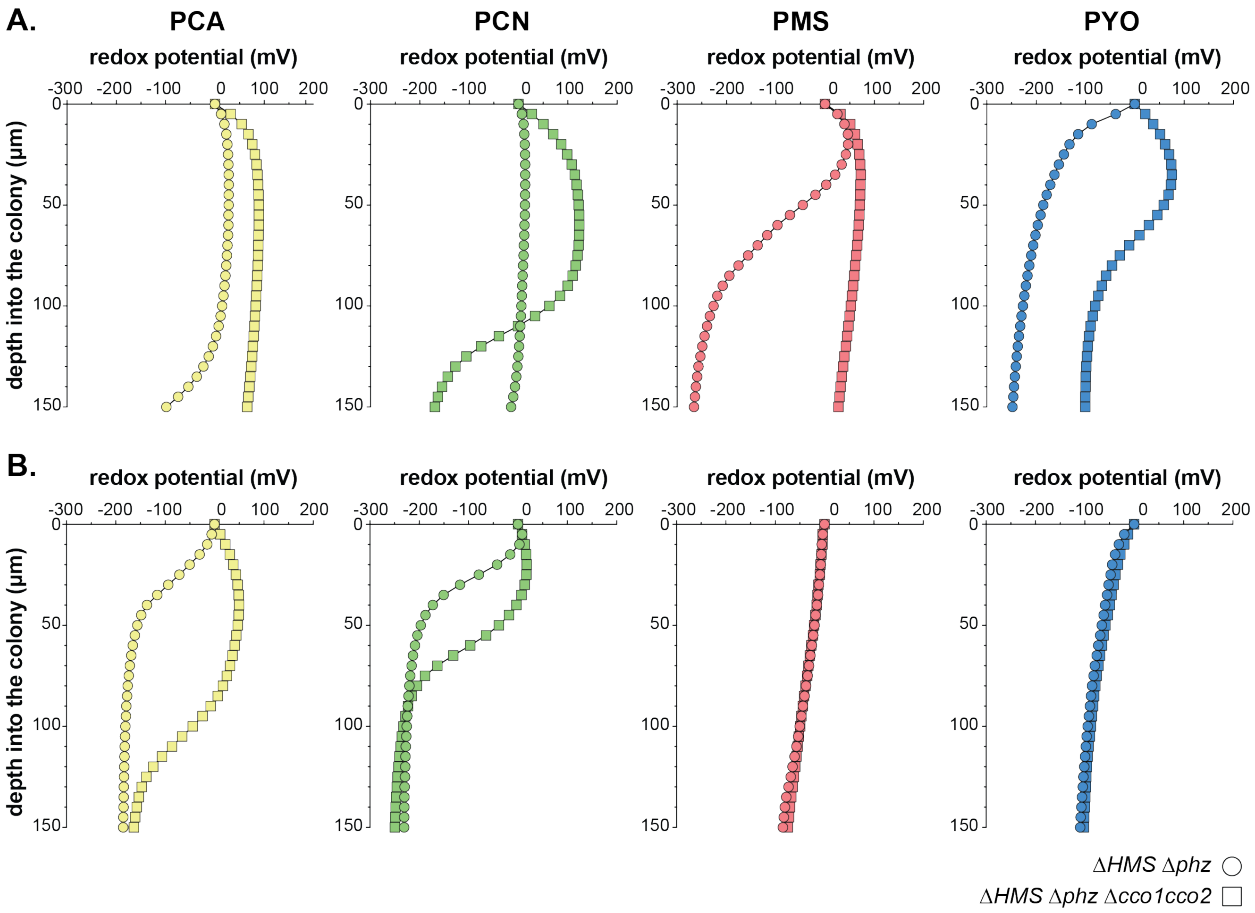

Figure 3.7. Cco terminal oxidases contribute differently to phenazine reduction on tryptone and glucose. Change in redox potential (mV) with depth in three-day-old PA14 biofilms grown on tryptone **(A)** or MOPS-glucose **(B)** supplemented with 200 µM of PCA (yellow), PCN (green), PMS (red), or PYO (blue) by Δ*HMS*Δ*phz* (circles) or Δ*HMS*Δ*phz*Δ*cco1cco2* (squares). Data shown are representative of at least six biological replicates.

highly reactive and unstable (Hansford et al., 1972), I used its synthetic analog, phenazine methosulfate (PMS), as a proxy to study 5-Me-PCA reduction.

Δ*HMS*Δ*phz* biofilms grown on tryptone did not significantly reduce PCA or PCN (**Figure 3.7A**, circles). Both PMS and PYO, on the other hand, were reduced substantially, with differing patterns of reduction. The majority of PYO reduction occurred within the top 50 µm of the biofilm, while PMS showed more gradual reduction until ~ 100 µm into the colony. The PMS reduction curve most resembled that seen in WT colonies grown on tryptone (**Figure 3.6A**). When reduction of exogenously-added phenazines was measured in glucose-grown colonies, I again saw drastically different redox profiles than those observed on tryptone. Here, neither

PMS nor PYO were reduced significantly, while PCA and PCN were; in essence, the reverse of what I observed on tryptone (**Figure 3.7B**).

Because on tryptone phenazine reduction is dependent on the Cco terminal oxidases (Jo et al., 2017), I wondered whether these enzymes were required for phenazine reduction in general or whether they are involved in the reduction of distinct phenazines. To address this question, I created a Δ*HMS*Δ*phz*Δ*cco1cco2* deletion mutant and investigated its ability to reduce exogenously-added phenazines. On tryptone, I found that deleting the Cco's in the Δ*HMS*Δ*phz* background compromised the reduction of all four phenazines tested (**Figure 3.7A**, squares). The most striking phenotype, however, was seen with PMS, one of the two phenazines that are most potent with respect to affecting colony morphogenesis on tryptone (Sakhtah et al., 2016). While the parent strain was able to reduce PMS substantially, the Δ*cco1cco2* mutant showed no PMS reduction.

On glucose, deleting the Cco terminal oxidases did not change the redox profiles seen for Δ*HMS*Δ*phz* grown on PMS or PYO (**Figure 3.7B**), not entirely unexpectedly since these two phenazines were barely, if at all, reduced in the parent strain. However, I was surprised to see that the Δ*HMS*Δ*phz*Δ*cco1cco2* mutant showed reduction defects for both PCA and PCN, because redox profiles of endogenously-produced phenazines indicated that the Cco terminal oxidases were not required for phenazine reduction on glucose (**Figure 3.6**). These results indicate that singly-provided, exogenously-added phenazines may not have the same physiological roles as their endogenously-produced counterparts, which are synthesized in concert with other phenazine derivatives.

3.3: Discussion

Pseudomonas aeruginosa is an important clinical pathogen, notoriously forming chronic infections in nosocomial settings. These infections are hard to eradicate due to characteristics associated with the biofilm lifestyle, in which cells arrange themselves into a multicellular consortium encased in an extracellular matrix. In the cystic fibrosis lung, *P. aeruginosa* is well-

known for causing chronic, biofilm-based infections that ultimately lead to the mortality of patients. In this environment, mutations associated with changes in nutrient uptake and metabolism have been found to be associated with growth in the CF lung environment (Hoboth et al., 2009; Son et al., 2007). Furthermore, ETC genes, including those encoding dehydrogenases and the high-O_2-affinity terminal oxidases Ccos, are upregulated in conditions that mimic those found in the CF lung (Eichner et al., 2014). Therefore, a deeper understanding of the interplay of nutrient availability and respiratory activity may yield new strategies for the treatment of *P. aeruginosa* infections. In this chapter, I describe how carbon sources affect *P. aeruginosa* growth and characterized how a subset of these carbon sources (tryptone, glucose, and succinate) affect biofilm development, expression of terminal oxidase genes, and phenazine production and utilization.

3.3.1: Electron flux through the respiratory chain is modulated in response to terminal oxidase and phenazine availability

I began by screening for carbon sources that support growth and electron flow through the aerobic respiratory chain of *P. aeruginosa*. Strikingly, phenazines or altering the complement of terminal oxidases affected electron flow through the respiratory chain, as indicated by PA14's ability to reduce the redox indicator dye tetrazolium violet (**Figures 3.1B** and **3.2**).

Based on dye reduction kinetics, I classified carbon sources into five groups (**Figure 3.1B**). For all carbon sources that supported growth, tetrazolium violet dye reduction by PaCco was comparable or greater than WT (**Figure 3.1B**). This is in agreement with previous work from our group indicating that the Cco terminal oxidases are mostly responsible for the reduction of another tetrazolium dye, triphenyl-tetrazolium chloride (Jo et al., 2017). Groups 3 and 4 contained carbon sources in which PaCco (where only the Cco terminal oxidases remain) was able to reduce tetrazolium violet even more efficiently than the WT and PaCio, despite the fact that growth levels were comparable between PaCco and WT (**Figures 3.2A** and **B**; **3.2–figure supplement 1A** and **B**). On these carbon sources, the other terminal oxidases (Aa_3, Bo_3,

and Cio) may contribute to growth and divert electrons away from the Cco's. In PaCco, electrons are directly routed to the Cco's, leading to enhanced dye reduction and possibly more efficient electron flow through the respiratory chain, resulting in elevated dye reduction.

I was particularly intrigued by carbon sources in groups 3 and 4 as α-ketoglutaric acid and glutamine represent a node between carbon and nitrogen metabolism where the TCA cycle branches off into the synthesis of glutamate and then glutamine (**Figure 1.1**). Furthermore, glutamine is directly linked to phenazine biosynthesis with one glutamine being required for the production of PCA and another one for its derivatization to PCN (Culbertson and Toney, 2013; Pierson and Thomashow, 1992), **Figure 1.7**). These carbon sources will be the focus of future studies and I expect them to give us new insights with respect to the regulation of phenazine production and reduction (**Figures 3.5**, **3.6**, and **3.7)**. The current study was focused on establishing benchmarks for the various assays utilizing some of the most commonly-used carbon sources for growth of *P. aeruginosa*, i.e. tryptone, a complex, undefined medium composed of peptides resulting from the digest of casein; glucose, a fermentable sugar and precursor of the glycolytic pathway; and succinate, a TCA cycle intermediate (**Figure 1.1**).

On tryptone and succinate, Cco terminal oxidases were necessary and sufficient for WT-like planktonic growth (**Figure 3.3**). On glucose, however, the Cco terminal oxidases were not sufficient for WT-like growth (**Figure 3.3A**), suggesting that other terminal oxidases are more required on glucose. Consistent with this, *cco1* and *cco2* expression are lower while bo_3 expression was more than 2-fold higher in glucose relative to tryptone (**Figure 3.4A**). Because Bo_3 is upregulated under iron limitation (Arai, 2011; Arai et al., 2014), growth on glucose may yield a higher demand for iron, possibly due to changes in the respiratory chain since cytochrome biosynthesis may lead to a high demand for this metal.

3.3.2: Gradients formed within the biofilm inform expression of respiratory complexes

Biofilms and liquid cultures are physiologically quite distinct. An important characteristic of biofilms is the formation of gradients (Werner et al., 2004). As biofilms develop, they increase

in thickness (**Figure 2.3C**; Jo et al., 2017), leading to a carbon source gradient originating at the bottom of the colony and an O_2 gradient originating at the top. In this study I observed biofilm-specific characteristics with respect to the expression and utilization of terminal oxidases. The *bo*$_3$ terminal oxidase is expressed in liquid culture but not in biofilms, irrespective of the carbon source. In glucose, Cco's are not sufficient for WT levels of liquid culture growth (**Figure 3.3A**), but are for WT-like biofilm development (**Figure 3.3B**). In succinate, the lack of phenazines confers more robust growth in biofilms (**Figure 3.3B**) that is not seen in liquid (**Figure 3.3A**).

I found that the biofilm-specific gradients inform expression of different terminal oxidases (**Figure 3.4B)**. The switch from free-living to biofilm growth is also accompanied by altered phenazine production, which is further impacted by growth medium (**Figure 3.5**). Differential phenazine production then contributes to different phenazine utilization throughout biofilm depths, as observed through redox microprofiling (**Figure 3.6**). These results demonstrate the differences that exist between the liquid culture and biofilm modes of growth. This has important implications in the quest for discovery of new antibiotics that are able to fight biofilm-based infections in clinical settings, as the majority of that research is done in liquid culture (Penesyan et al., 2015). However, my results presented here and in Chapter 2 highlight the need for more biofilm-based research during the process of new drug discovery.

3.3.3: Phenazine utilization is not determined solely by phenazine availability

While overall phenazine production levels were similar in PA14 biofilms grown on tryptone and succinate (**Figure 3.5)**, I did not detect any phenazine reduction in succinate-grown biofilms (**Figure 3.6**), suggesting that phenazine reduction is dependent upon more than just availability and/or amount of phenazines produced. Δ*phz* colonies grown on succinate formed more robust biofilms than their phenazine-producing counterparts (**Figure 3.3B**), indicating that phenazines may have a negative effect on biofilm growth on succinate. As succinate-grown biofilms do not reduce phenazines, the redox-active role of phenazines is likely rendered irrelevant on this carbon source and their accumulation may become harmful. This is

supported by the fact that phenazines have been shown to become toxic at high concentrations (Meirelles and Newman, 2018; Sakhtah et al., 2016).

We have previously shown reduction of phenazines on tryptone to be mediated by the Cco terminal oxidases (Jo et al., 2017). Here, I expanded upon these findings by measuring reduction of individual phenazines (**Figure 3.7**). On tryptone, I saw that phenazine methosulfate (PMS, a synthetic analog of the endogenous but highly reactive 5-methyl-PCA [5-Me-PCA]) and pyocyanin (PYO) contributed the majority of redox-active behavior in biofilms (**Figure 3.7A**, circles), indicating that these phenazines are predominantly used on this carbon source. The Δ*cco1cco2* mutant showed reduction defects when grown on PMS and PYO (**Figure 3.7A**, squares), consistent with the Cco-dependent phenazine reduction profiles observed in **Figure 3.6** and reported previously (Jo et al., 2017). As PMS/5-Me-PCA is important for WT colony biofilm morphogenesis and redox balancing (Sakhtah et al., 2016) and PYO has been shown to play a role in virulence in a mouse model (Lau et al., 2004), their successful utilization could have important implications for *P. aeruginosa* growth and virulence.

In contrast to tryptone, here I found that phenazine reduction is Cco-independent on glucose-grown biofilms that endogenously produce phenazines (**Figure 3.6**). These biofilms almost exclusively produce (**Figure 3.5**) and most efficiently reduce (**Figure 3.7**) phenazine-1-carboxamide (PCN) and phenazine-1-carboxylic acid (PCA). Intriguingly, when single phenazines were provided exogenously, Cco's *were* required for the reduction of both PCN and PCA on glucose (**Figure 3.7B**). This discrepancy between endogenous and exogenous phenazine reduction suggests that phenazines, when produced in mixtures, may have synergistic or antagonistic effects that remain to be elucidated.

3.3.4: Conclusion

Together, these results inform our understanding of how *P. aeruginosa* metabolism is influenced by carbon source and mode of growth. Our biofilm results are especially illuminating, as biofilm growth is associated with the formation and persistence of chronic infections in

various host environments. This includes the heterogeneous environment found in the lungs of CF patients, in which varying oxygen concentrations, nutrient availabilities, and antibiotic concentrations are found along airways (Winstanley et al., 2016). *P. aeruginosa*'s adaptable metabolism contributes to its ability to colonize nearly all of these microenvironments and, by extension, its virulence. Phenazines are also involved in mediating virulence, as they have been detected at high concentrations in CF sputum samples (Wilson et al., 1988) and influence immune response in human airway epithelial cells by increasing oxidant production (Price-Whelan et al., 2006). This in turn can affect gene expression patterns in the host (Look et al., 2005) while also having negative repercussions on host tissue. Therefore, the identification of the mechanisms that underlie *P. aeruginosa* persistence in heterogeneous environments, including mediators of phenazine production and/or utilization, would have the potential to vastly improve how chronic *P. aeruginosa* infections are treated.

3:4: Materials and methods

3.4.1: Strains and growth conditions

Pseudomonas aeruginosa strain UCBPP-PA14 (Mathee, 2018; Rahme et al., 1995) overnight precultures were routinely grown for 12-16 hours in lysogeny broth (LB; 1% tryptone, 1% NaCl, 0.5% yeast extract) (Bertani, 2004) at 37˚C with shaking at 250 rpm. Overnight precultures serving as biological replicates were inoculated from separate clonal source colonies grown on streaked LB + 1.5% agar plates. Liquid subcultures were made from diluting overnight precultures 1:100 (1:50 for PaCio and PaCioΔ*phz*) in LB and grown at 37˚C with shaking at 250 rpm until mid-exponential phase (OD at 500 nm ~ 0.5). Liquid subcultures were used for experiments unless otherwise noted. Strains used in this study are listed in **Table 3.1**.

The growth media used in this study were 1% tryptone and MOPS minimal medium (50 mM 4-morpholinepropanesulfonic acid (pH 7.2), 43 mM NaCl, 93 mM NH_4Cl, 2.2 mM KH_2PO_4, 1 mM $MgSO_4 \cdot 7H_2O$, 1 µg/ml $FeSO_4 \cdot 7H_2O$). MOPS minimal medium contained either 20 mM D-glucose (MOPS-glucose) or 20 mM sodium succinate hexahydrate (MOPS-succinate) as a

carbon source unless otherwise noted. Agar-containing versions of each growth medium contained 1% agar (Teknova A7777).

3.4.2: Construction of P. aeruginosa *deletion mutant strains*

Markerless deletions mutants were created by amplifying ~ 1 kb of flanking DNA sequence from each side of the gene(s) to be deleted using the primers listed in **Table 3.2**. These flanking sequences were inserted into pMQ30 via gap repair cloning in *Saccharomyces cerevisiae* strain InvSc1 (Shanks et al., 2006). The resulting plasmids, listed in **Table 3.3**, were then transformed into *Escherichia coli* strain UQ950, verified by restriction digests and/or sequencing, and moved into PA14 using biparental conjugation. Single recombinants in PA14 were selected using LB agar plates containing 100 µg/ml gentamicin. Markerless deletions (double recombinants) were selected on LB without NaCl containing 10% sucrose and confirmed by PCR. Combinatorial mutants were constructed by using single mutants as hosts for biparental conjugation as described in **Table 3.1**.

3.4.3: Construction of reporter strains

Reporter constructs for *P. aeruginosa*'s five terminal oxidases (Aa_3, Bo_3, Cio, Cco1, and Cco2) were constructed using the primers listed in **Table 3.2** to amplify respective promoter regions (500 bp upstream of the respective terminal oxidase operon), adding an SpeI and an XhoI digest site to the 5' and 3' ends of the promoter, respectively. Purified PCR products were digested and ligated into the pLD2722 vector at the multiple cloning site (MCS), upstream of the *gfp* sequence. The resulting plasmids (listed in **Table 3.3**) were transformed into *E. coli* strain UQ950, verified by sequencing, moved into PA14 using biparental conjugation with *E. coli* strain S17-1. Recombinants were selected for as described previously (Jo et al., 2017).

3.4.4: Growth assays and determination of carbon sources that support PA14 growth

One ml of liquid subculture was washed two times in sterile 1x phosphate-buffered saline (PBS; 137 mM NaCl, 2.7 mM KCl, 10 mM Na_2HPO_4, 1.8 mM KH_2PO_4), resuspended in 1 ml MOPS minimal medium without a carbon source, and diluted 1:100 in MOPS minimal medium without a carbon source. One hundred microliters of this cell suspension were dispensed into each well of a phenotype microarray carbon microplate PM1 (Biolog 12111) and incubated at 37˚C with continuous shaking on the medium setting in a Synergy 4 plate reader (BioTek). Growth was measured by taking OD readings at 500 nm every 30 min for 20-24 hr. Each strain was assayed twice in Biolog plate PM1.

Carbon sources that support growth of PA14 strains producing phenazines were then determined by monitoring growth over 20 hours for two biological replicates of each phenazine-producing PA14 strain, and a cutoff of 0.15 was applied to cell density (OD at 500 nm) values. Anything falling below this cutoff was designated as background. Carbon sources with OD_{500nm} readings that exceeded the cutoff of 0.15 were manually inspected to verify growth. I found that 37 carbon sources supported growth (**Figure 3.1B**) while 58 did not (**Figure 3.1–figure supplement 1**).

3.4.5: Biolog phenotype microarrays (i.e., dye reduction assays) and determination of carbon sources that support reduction of tetrazolium violet

For dye reduction assays, PBS-washed cells were resuspended in 1x IF-0 (IF-0a GN/GP Base Inoculating Fluid, Biolog 72268) to a percent transmittance of 42. The 42 %T cell suspension was diluted 1:5 in 1x IF-0 + 1x Redox Dye A (tetrazolium violet; Biolog 74221). One hundred microliters of this cell + dye suspension were dispensed into each well of a PM1 microplate and incubated at 37˚C with continuous shaking on the medium setting in a Synergy 4 plate reader. Growth and dye reduction were measured by taking absorbance readings at 500 nm and 590 nm, respectively, every 30 min for 20-24 hr. After the run was completed, an endpoint spectral scan of the plate was taken, reading absorbance of each well at wavelengths

between (and including) 300 to 800 nm in 10 nm steps. As tetrazolium dye reduction is irreversible, the endpoint scan at 590 nm should represent the maximal dye reduction value.

To determine which carbon sources yield tetrazolium dye reduction, only carbon sources that supported PA14 growth (**Figure 1B**) were considered. Endpoint, maximal dye reduction values for each of these 37 carbon sources for each strain were determined by subtracting the absorbance value at 800 nm (which I considered as background) from the absorbance value at 590 nm. These values were then subjected to a cutoff of 0.25, and anything lower than this value was considered background dye reduction. Values meeting the cutoff were then compared for each carbon source across strains, with phenazine-producing strains compared to each other and phenazine-null strains being compared to each other. Finally, each carbon source was then classified into one of the following six groups based on dye reduction levels: group 1, WT or Δ*phz* > PaCco or PaCcoΔ*phz* > PaCio or PaCioΔ*phz*; group 2, WT or Δ*phz* = PaCco or PaCcoΔ*phz* > PaCio or PaCioΔ*phz*; group 3, PaCco or PaCcoΔ*phz* > WT or Δ*phz* > PaCio or PaCioΔ*phz*; group 4, PaCco or PaCcoΔ*phz* > WT or Δ*phz* = PaCio or PaCioΔ*phz*; group 5, WT or Δ*phz* = PaCco or PaCcoΔ*phz* = PaCio or PaCioΔ*phz*; or no reduction.

3.4.6: Liquid culture growth and terminal oxidase reporter expression assays

For growth assays, one ml of liquid subculture cells was washed two times in sterile 1x PBS and resuspended in one ml sterile 1x PBS. These cells were then diluted 1:100 in respective growth medium (1% tryptone, MOPS-glucose, or MOPS-succinate) in either a clear, flat-bottom polystyrene 96-well plate (VWR 82050-716; for growth assays) or a clear, flat-bottom polystyrene black 96-well plate (VWR 82050-756; for reporter expression assays) and incubated at 37˚C with continuous shaking on the medium setting in a Synergy 4 plate reader. Growth was monitored by taking OD readings at 500 nm every 30 minutes for 20-24 hr.

For reporter expression assays, expression of GFP was also assessed by taking fluorescence readings at excitation and emission wavelengths of 480 nm and 510 nm, respectively, for the duration of the experiment. RFU values for a strain lacking a promoter

upstream of the *gfp* gene (MCS-*gfp*) were subtracted from the fluorescence values of each reporter. Fluorescence and absorbance readings were taken simultaneously.

3.4.7: Colony biofilm morphology assays

Ten microliters of liquid subcultures were spotted onto 60 ml of colony morphology medium in a 10 cm x 10 cm x 1.5 cm square Petri dish (LDP D210-16). Colony morphology medium was 1% tryptone agar, MOPS-glucose agar, or MOPS-succinate agar supplemented with 40 µg/ml Congo red dye (VWR AAAB24310-14) and 20 µg/ml Coomassie blue dye (VWR EM-3300). Colony biofilms were incubated for up to five days in the dark at 25˚C with >90% humidity (Percival CU-22L) and imaged daily using a VHX-1000 digital microscope (Keyence). Images shown are representative of at least four biological replicates.

3.4.8: Thin sectioning assays

Two layers of 1% tryptone with 1% agar were poured to depths of 4.5 mm (bottom) and 1.5 mm (top) and left to solidify overnight. Overnight precultures were diluted 1:100 in LB and grown for ~ 2 h, until early-mid exponential phase. Five microliters of subculture were then spotted onto the top agar layer and colonies were incubated in the dark at 25˚C with > 90% humidity (Percival CU-22L) and grown for three days. After three days, colonies were covered by a 1.5-mm-thick 1% agar layer. Colonies sandwiched between two 1.5-mm agar layers were lifted from the bottom layer, washed for 10 min in 1x PBS (pH 7.4) at room temperature in the dark, and fixed in 4% paraformaldehyde in PBS overnight at room temperature in the dark. Fixed colonies were washed twice in PBS and dehydrated through a series of ethanol washes (25%, 50%, 70%, 95%, 3 × 100% ethanol) for 60 min each. Colonies were cleared via three 60-min incubations in Histoclear-II (National Diagnostics HS-202) and infiltrated with wax via two separate washes of 100% Paraplast Xtra paraffin wax (Thermo Fisher Scientific 50-276-89) for 2 hr each at 55˚C, then colonies were allowed to polymerize overnight at 4˚C. Tissue processing was performed using an STP120 Tissue Processor (Thermo Fisher Scientific 813150). Trimmed

blocks were sectioned in 10-µm-thick sections perpendicular to the plane of the colony using an automatic microtome (Thermo Fisher Scientific 905200ER), floated onto water at 45˚C, and collected onto slides. Slides were air-dried overnight, heat-fixed on a hotplate for 1 hr at 45˚C, and rehydrated in the reverse order of processing. Rehydrated colonies were immediately mounted in TRIS-Buffered DAPI:Fluorogel (Thermo Fisher Scientific 50-246-93) and overlaid with a coverslip. Differential interference contrast (DIC) and fluorescent confocal images were captured using an LSM800 confocal microscope (Zeiss, Germany). Each strain was prepared in this manner in at least biological triplicates.

3.4.9: Phenazine detection and quantification

(i) For phenazine extraction from liquid cultures, overnight cultures of WT PA14 were inoculated in 2 ml of respective growth medium (1% tryptone, MOPS-glucose, or MOPS-succinate) in 13 x 100 mm culture tubes (VWR 10545-936) in at least biological triplicate and incubated at 37˚C with shaking at 250 rpm for 14-16 hr. One milliliter of each overnight culture was dispensed into a microfuge tube and centrifuged for two minutes at 14,000 rpm to pellet cells. Three hundred microliters of the supernatant were applied to a 0.22 µm Spin-X column (VWR 29442-754), centrifuged for two minutes at 14,000 rpm, and 200 µl of the resulting cell-free flow-through were loaded into an HPLC vial for analysis.

(ii) For phenazine extraction from biofilms, 1 ml of liquid subcultures was washed twice in 1x PBS and resuspended in 1 ml of 1x PBS. A 25 mm filter disk with a pore size of 0.2 µm (GE Healthcare 110606) was placed into the center of one 35 x 10 mm round Petri dish (VWR 25373-041) filled with 4 ml of 1% tryptone agar, MOPS-glucose agar, or MOPS-succinate agar and 10 µl of the washed cells were spotted onto the filter disk. Colony biofilms were grown for 3 days in the dark at 25˚C with >90% humidity, after which point each colony and filter were lifted off their plate. The colony biofilm and filter were placed into one 5-ml aliquot of 100% methanol while the agar upon which the biofilm had developed was placed into another 5-ml aliquot of 100% methanol, and phenazines were extracted from the biofilms or agar overnight at room

temperature in the dark. Three hundred microliters of the phenazine extraction were filtered through a 0.22 µm Spin-X column as described above and 200 µl of the cell-free flow-through were loaded into an HPLC vial for analysis.

(iii) Phenazines were identified using high-performance liquid chromatography (Agilent 1100 HPLC System) as described previously (Dietrich et al., 2006; Sakhtah et al., 2016) and comparing sample peaks to peaks of pure phenazine standards run as controls. The area under each peak (mAU*s) was used to determine the concentrations of each phenazine. For phenazines extracted from liquid culture, the area under each peak was first normalized to cell density at the time of phenazine extraction and concentration was determined using the extinction coefficient for each phenazine. Dilution standards of purified PYO, PCA, and PCN were prepared at known concentrations and extinction coefficients (ε) were generated for each based on seven biological replicates. ε_{PYO} = 0.0253 µM/mAU*s, ε_{PCA} = 0.0104 µM/mAU*s, ε_{PCN} = 0.0099 µM/mAU*s.

3.4.10: Redox microprofiling

(i) Extracellular redox states of day 3 (~ 72 hr) phenazine-producing biofilms (**Figure 3.6**) were measured using a 25 µm-tip redox microelectrode and external reference (Unisense RD25 and REF-RM). Colony biofilms were grown as for the colony biofilm morphology assays, except that Congo red and Coomassie blue dyes were omitted. Calibration and redox measurements were performed using the SensorTrace Profiling software (Unisense) as described previously (Jo et al., 2017).

(ii) For measuring extracellular redox states of biofilms grown on exogenously-added phenazines, the respective growth medium (tryptone agar, MOPS-glucose agar, or MOPS-succinate agar) was autoclaved and allowed to cool to ~ 55˚C in a water bath. Purified phenazine compounds were added to final concentrations of 200 µM for all phenazines tested. The phenazines tested were PCA (Apexmol), PCN (Apexmol), PMS (Thermo Fisher Scientific AC130160010), and PYO (Cayman Chemicals); PCA and PCN stock solutions were 25 mM in

DMSO while PMS and PYO stock solutions were 200 mM in DMSO. Extracellular redox states of biofilms were measured on DMSO-only plates to ensure that the solvent did not alter extracellular redox state. Extracellular redox states of day 3 (~ 72 hr) Δ*HMS*Δ*phz* biofilms grown on exogenously-added phenazines were measured as above.

3.5: References

Alvarez-Ortega C, Harwood CS. 2007. Responses of Pseudomonas aeruginosa to low oxygen indicate that growth in the cystic fibrosis lung is by aerobic respiration. *Mol Microbiol* **65**:153–165.

Arai H. 2011. Regulation and Function of Versatile Aerobic and Anaerobic Respiratory Metabolism in Pseudomonas aeruginosa. *Front Microbiol* **2**:103.
Arai H, Kawakami T, Osamura T, Hirai T, Sakai Y, Ishii M. 2014. Enzymatic characterization and in vivo function of five terminal oxidases in Pseudomonas aeruginosa. *J Bacteriol* **196**:4206–4215.

Aussel L, Pierrel F, Loiseau L, Lombard M, Fontecave M, Barras F. 2014. Biosynthesis and physiology of coenzyme Q in bacteria. *Biochim Biophys Acta* **1837**:1004–1011.

Berridge MV, Herst PM, Tan AS. 2005. Tetrazolium dyes as tools in cell biology: new insights into their cellular reduction. *Biotechnol Annu Rev* **11**:127–152.

Bertani G. 2004. Lysogeny at mid-twentieth century: P1, P2, and other experimental systems. *J Bacteriol* **186**:595–600.

Ciofu O, Mandsberg LF, Wang H, Høiby N. 2012. Phenotypes selected during chronic lung infection in cystic fibrosis patients: implications for the treatment of Pseudomonas aeruginosa biofilm infections. *FEMS Immunol Med Microbiol* **65**:215–225.

Comolli JC, Donohue TJ. 2004. Differences in two Pseudomonas aeruginosa cbb3 cytochrome oxidases. *Mol Microbiol* **51**:1193–1203.

Culbertson JE, Toney MD. 2013. Expression and characterization of PhzE from P. aeruginosa PAO1: aminodeoxyisochorismate synthase involved in pyocyanin and phenazine-1-carboxylate production. *Biochim Biophys Acta* **1834**:240–246.

Dietrich LEP, Okegbe C, Price-Whelan A, Sakhtah H, Hunter RC, Newman DK. 2013. Bacterial community morphogenesis is intimately linked to the intracellular redox state. *J Bacteriol* **195**:1371–1380.

Doucette CD, Schwab DJ, Wingreen NS, Rabinowitz JD. 2011. α-Ketoglutarate coordinates carbon and nitrogen utilization via enzyme I inhibition. *Nat Chem Biol* **7**:894–901.

Eichner A, Günther N, Arnold M, Schobert M, Heesemann J, Hogardt M. 2014. Marker genes for the metabolic adaptation of Pseudomonas aeruginosa to the hypoxic cystic fibrosis lung environment. *Int J Med Microbiol* **304**:1050–1061.

Elias S, Banin E. 2012. Multi-species biofilms: living with friendly neighbors. *FEMS Microbiol Rev* **36**:990–1004.

Friedman L, Kolter R. 2004. Genes involved in matrix formation in Pseudomonas aeruginosa PA14 biofilms. *Mol Microbiol* **51**:675–690.

Frimmersdorf E, Horatzek S, Pelnikevich A, Wiehlmann L, Schomburg D. 2010. How Pseudomonas aeruginosa adapts to various environments: a metabolomic approach. *Environ Microbiol* **12**:1734–1747.

Glasser NR, Kern SE, Newman DK. 2014. Phenazine redox cycling enhances anaerobic survival in Pseudomonas aeruginosa by facilitating generation of ATP and a proton-motive force. *Mol Microbiol* **92**:399–412.

Hall-Stoodley L, Costerton JW, Stoodley P. 2004. Bacterial biofilms: from the natural environment to infectious diseases. *Nat Rev Microbiol* **2**:95–108.

Hansford GS, Holliman FG, Herbert RB. 1972. Pigments of Pseudomonas species. IV. In vitro and in vivo conversion of 5-methylphenazinium-1-carboxylate into aeruginosin A. *J Chem Soc Perkin 1* **1**:103–105.

Hirai T, Osamura T, Ishii M, Arai H. 2016. Expression of multiple cbb3 cytochrome c oxidase isoforms by combinations of multiple isosubunits in Pseudomonas aeruginosa. *Proc Natl Acad Sci U S A*. doi:10.1073/pnas.1613308113

Hoboth C, Hoffmann R, Eichner A, Henke C, Schmoldt S, Imhof A, Heesemann J, Hogardt M. 2009. Dynamics of adaptive microevolution of hypermutable Pseudomonas aeruginosa during chronic pulmonary infection in patients with cystic fibrosis. *J Infect Dis* **200**:118–130.

Høiby N, Ciofu O, Johansen HK, Song Z-J, Moser C, Jensen PØ, Molin S, Givskov M, Tolker-Nielsen T, Bjarnsholt T. 2011. The clinical impact of bacterial biofilms. *Int J Oral Sci* **3**:55–65.

Jennings LK, Storek KM, Ledvina HE, Coulon C, Marmont LS, Sadovskaya I, Secor PR, Tseng BS, Scian M, Filloux A, Wozniak DJ, Howell PL, Parsek MR. 2015. Pel is a cationic exopolysaccharide that cross-links extracellular DNA in the Pseudomonas aeruginosa biofilm matrix. *Proc Natl Acad Sci U S A* **112**:11353–11358.

Jo J, Cortez KL, Cornell WC, Price-Whelan A, Dietrich LE. 2017. An orphan cbb3-type cytochrome oxidase subunit supports Pseudomonas aeruginosa biofilm growth and virulence. *Elife* **6**. doi:10.7554/eLife.30205

Kawakami T, Kuroki M, Ishii M, Igarashi Y, Arai H. 2010. Differential expression of multiple terminal oxidases for aerobic respiration in Pseudomonas aeruginosa. *Environ Microbiol* **12**:1399–1412.

Lau GW, Ran H, Kong F, Hassett DJ, Mavrodi D. 2004. Pseudomonas aeruginosa pyocyanin is critical for lung infection in mice. *Infect Immun* **72**:4275–4278.

Look DC, Stoll LL, Romig SA, Humlicek A, Britigan BE, Denning GM. 2005. Pyocyanin and its precursor phenazine-1-carboxylic acid increase IL-8 and intercellular adhesion molecule-1 expression in human airway epithelial cells by oxidant-dependent mechanisms. *J Immunol* **175**:4017–4023.

Madigan MT, Martinko JM, Bender KS, Buckley DH, Stahl DA. 2015. Brock Biology of Microorganisms. Pearson.

Mathee K. 2018. Forensic investigation into the origin of Pseudomonas aeruginosa PA14 - old but not lost. *J Med Microbiol* **67**:1019–1021.

Meirelles LA, Newman DK. 2018. Both toxic and beneficial effects of pyocyanin contribute to the lifecycle of Pseudomonas aeruginosa. *Mol Microbiol*. doi:10.1111/mmi.14132

Murray TS, Egan M, Kazmierczak BI. 2007. Pseudomonas aeruginosa chronic colonization in cystic fibrosis patients. *Curr Opin Pediatr* **19**:83–88.

Okegbe C, Price-Whelan A, Dietrich LEP. 2014. Redox-driven regulation of microbial community morphogenesis. *Curr Opin Microbiol* **18**:39–45.

Penesyan A, Gillings M, Paulsen IT. 2015. Antibiotic discovery: combatting bacterial resistance in cells and in biofilm communities. *Molecules* **20**:5286–5298.

Pierson LS 3rd, Thomashow LS. 1992. Cloning and heterologous expression of the phenazine biosynthetic locus from Pseudomonas aureofaciens 30-84. *Mol Plant Microbe Interact* **5**:330–339.

Poole RK, Cook GM. 2000. Redundancy of aerobic respiratory chains in bacteria? Routes, reasons and regulation. *Adv Microb Physiol* **43**:165–224.

Price-Whelan A, Dietrich LEP, Newman DK. 2007. Pyocyanin alters redox homeostasis and carbon flux through central metabolic pathways in Pseudomonas aeruginosa PA14. *J Bacteriol* **189**:6372–6381.

Price-Whelan A, Dietrich LEP, Newman DK. 2006. Rethinking “secondary” metabolism: physiological roles for phenazine antibiotics. *Nat Chem Biol* **2**:71–78.

Rahme LG, Stevens EJ, Wolfort SF, Shao J, Tompkins RG, Ausubel FM. 1995. Common virulence factors for bacterial pathogenicity in plants and animals. *Science* **268**:1899–1902.

Ray A, Williams HD. 1997. The effects of mutation of the anr gene on the aerobic respiratory chain of Pseudomonas aeruginosa. *FEMS Microbiol Lett* **156**:227–232.

Recinos DA, Sekedat MD, Hernandez A, Cohen TS, Sakhtah H, Prince AS, Price-Whelan A, Dietrich LEP. 2012. Redundant phenazine operons in Pseudomonas aeruginosa exhibit environment-dependent expression and differential roles in pathogenicity. *Proc Natl Acad Sci U S A* **109**:19420–19425.

Saint-Amans S, Girbal L, Andrade J, Ahrens K, Soucaille P. 2001. Regulation of carbon and electron flow in Clostridium butyricum VPI 3266 grown on glucose-glycerol mixtures. *J Bacteriol* **183**:1748–1754.

Sakhtah H, Koyama L, Zhang Y, Morales DK, Fields BL, Price-Whelan A, Hogan DA, Shepard K, Dietrich LEP. 2016. The Pseudomonas aeruginosa efflux pump MexGHI-OpmD transports a natural phenazine that controls gene expression and biofilm development. *Proc Natl Acad Sci U S A* **113**:E3538–47.

Shanks RMQ, Caiazza NC, Hinsa SM, Toutain CM, O’Toole GA. 2006. Saccharomyces cerevisiae-based molecular tool kit for manipulation of genes from gram-negative bacteria. *Appl Environ Microbiol* **72**:5027–5036.

Shrout JD, Chopp DL, Just CL, Hentzer M, Givskov M, Parsek MR. 2006. The impact of quorum sensing and swarming motility on Pseudomonas aeruginosa biofilm formation is nutritionally conditional. *Mol Microbiol* **62**:1264–1277.

Son MS, Matthews WJ Jr, Kang Y, Nguyen DT, Hoang TT. 2007. In vivo evidence of Pseudomonas aeruginosa nutrient acquisition and pathogenesis in the lungs of cystic fibrosis patients. *Infect Immun* **75**:5313–5324.

Sriramulu DD, Lünsdorf H, Lam JS, Römling U. 2005. Microcolony formation: a novel biofilm model of Pseudomonas aeruginosa for the cystic fibrosis lung. *J Med Microbiol* **54**:667–676.
Stanier RY, Palleroni NJ, Doudoroff M. 1966. The aerobic pseudomonads: a taxonomic study. *J Gen Microbiol* **43**:159–271.

Stover CK, Pham XQ, Erwin AL, Mizoguchi SD, Warrener P, Hickey MJ, Brinkman FS, Hufnagle WO, Kowalik DJ, Lagrou M, Garber RL, Goltry L, Tolentino E, Westbrock-Wadman S, Yuan Y, Brody LL, Coulter SN, Folger KR, Kas A, Larbig K, Lim R, Smith K, Spencer D, Wong GK, Wu Z, Paulsen IT, Reizer J, Saier MH, Hancock RE, Lory S, Olson MV. 2000. Complete genome sequence of Pseudomonas aeruginosa PAO1, an opportunistic pathogen. *Nature* **406**:959–964.
Toyofuku M, Inaba T, Kiyokawa T, Obana N, Yawata Y, Nomura N. 2016. Environmental factors that shape biofilm formation. *Biosci Biotechnol Biochem* **80**:7–12.

van Rij ET, Wesselink M, Chin-A-Woeng TFC, Bloemberg GV, Lugtenberg BJJ. 2004. Influence of environmental conditions on the production of phenazine-1-carboxamide by Pseudomonas chlororaphis PCL1391. *Mol Plant Microbe Interact* **17**:557–566.

Wang Y, Kern SE, Newman DK. 2010. Endogenous phenazine antibiotics promote anaerobic survival of Pseudomonas aeruginosa via extracellular electron transfer. *J Bacteriol* **192**:365–369.

Wang Y, Newman DK. 2008. Redox reactions of phenazine antibiotics with ferric (hydr)oxides and molecular oxygen. *Environ Sci Technol* **42**:2380–2386.

Werner E, Roe F, Bugnicourt A, Franklin MJ, Heydorn A, Molin S, Pitts B, Stewart PS. 2004. Stratified growth in Pseudomonas aeruginosa biofilms. *Appl Environ Microbiol* **70**:6188–6196.

White D, Drummond JT, Fuqua C. 2012. The Physiology and Biochemistry of Prokaryotes. Oxford University Press.

Williams HD, Davies JC. 2012. Basic science for the chest physician: Pseudomonas aeruginosa and the cystic fibrosis airway. *Thorax* **67**:465–467.

Williams HD, Zlosnik JEA, Ryall B. 2007. Oxygen, cyanide and energy generation in the cystic fibrosis pathogen Pseudomonas aeruginosa. *Adv Microb Physiol* **52**:1–71.

Wilson R, Sykes DA, Watson D, Rutman A, Taylor GW, Cole PJ. 1988. Measurement of Pseudomonas aeruginosa phenazine pigments in sputum and assessment of their contribution to sputum sol toxicity for respiratory epithelium. *Infect Immun* **56**:2515–2517.

Winstanley C, O'Brien S, Brockhurst MA. 2016. Pseudomonas aeruginosa Evolutionary Adaptation and Diversification in Cystic Fibrosis Chronic Lung Infections. *Trends Microbiol* **24**:327–337.

3.6: Tables

Table 1: Strains used in this study

strain	number	description	source
Pseudomonas aeruginosa strains			
UCBPP-PA14		Clinical isolate UCBPP-PA14.	Rahme et al., 1995
PA14 Δphz	LD24	PA14 with deletions in phzA1-G1 and phzA2-G2 operons.	Dietrich et al., 2006
PA14 Δcco1cco2	LD1933	PA14 with both cco operons (cbb3-1, cbb3-2; PA14_44340-PA14_44400) deleted simultaneously.	Jo et al., 2017
PA14 Δcio	LD2076	PA14 with a deletion in the cio operon (PA14_13030-13040)	this study
PA14 PaCco	LD2587	PA14 with deletions in PA14_01290-01320 (cox/aa3 operon), PA14_47150-47210 (cyo/bo3 operon), and PA14_13030-13040 (cio operon).	Jo et al., 2017
PA14 PaCcoΔphz	LD2588	PA14 with only the Cco terminal oxidases remaining in the phenazine-null background; deletions in the phzA1-G1, phzA2-G2, aa3, bo3, and cio operons.	this study
PA14 PaCio	LD1989	PA14 with only the Cio terminal oxidase remaining; deletions in the aa3, bo3, cco1, and cco2 operons.	this study
PA14 PaCioΔphz	LD1990	PA14 with only the Cio terminal oxidase remaining in the phenazine-null background; deletions in the phzA1-G1, phzA2-G2, aa3, bo3, cco1, and cco2 operons.	this study
PA14 ΔphzH ΔphzM ΔphzS ΔphzA1-G1 ΔphzA2-G2	LD3122	PA14 with deletions in the phenazine biosynthetic genes phzH (PA14_00640), phzM (PA14_09490), phzS (PA14_09400), phzA1-G1, and phzA2-G2.	this study
PA14 ΔphzH ΔphzM ΔphzS ΔphzA1-G1 ΔphzA2-G2 Δcco1cco2	LD3140	PA14 with deletions in the phenazine biosynthetic genes phzH, phzM, phzS, phzA1-G1, phzA2-G2, and the terminal oxidase operons of cco1 and cco2. Made by mating LD1933 to LD3122.	this study
PA14 Paa3-gfp	LD2962	PA14 with promoter of aa3 operon driving gfp expression.	this study
PA14 Pbo3-gfp	LD2966	PA14 with promoter of bo3 operon driving gfp expression.	this study
PA14Pcio-gfp	LD2969	PA14 with promoter of cio operon driving gfp expression.	this study
PA14 Pcco-1-gfp	LD2784	PA14 with promoter of cco1 operon driving gfp expression.	Jo et al., 2017

Table 3.1 (continued): Strains used in this study

strain	number	description	source
PA14 Pcco-2-gfp	LD2786	PA14 with promoter of cco2 operon driving gfp expression.	Jo et al., 2017
Escherichia coli strains			
UQ950	LD44	E. coli DH5 λpir strain for cloning. F-Δ(argF-lac)169φ80 dlacZ58(ΔM15) glnV44(AS) rfbD1 gyrA96(NalR) recA1 endA1 spoT thi-1 hsdR17 deoR λpir+	D. Lies, Caltech
BW29427	LD661	Donor strain for conjugation. thrB1004 pro thi rpsL hsdS lacZ ΔM15RP4-1360 Δ(araBAD)567 ΔdapA1314::[erm pir(wt)]	W. Metcalf, University of Illinois
β2155	LD69	Helper strain. thrB1004 pro thi strA hsdsS lacZΔM15 (F'lacZΔM15 lacIq traD36 proA+ proB+) ΔdapA::erm (Ermr)pir::RP4 [::kan (Kmr) from SM10]	Dehio and Meyer, 1997.
S17-1	LD2901	StrR , TpR , F− RP4-2-Tc::Mu aphA::Tn7 recA λpir lysogen	Teng et al., 1998
Saccharomyces cerevisiae strains			
InvSc1	LD676	MATa/MATalpha leu2/leu2 trp1-289/trp1-289 ura3-52/ura3-52 his3-Δ1/his3-Δ1	Invitrogen

Table 3.2: Primers used in this study

primer number	sequence	used to make plasmid number
LD725	ccaggcaaattctgttttatcagaccgcttctgcgttctgatCCCCTCAGAGAAGTCAGTCG	pLD1929
LD1063	gttgcccaggtgttcctgtGGCGGACCACCTTGTAGTTA	
LD949	ggaattgtgagcggataacaatttcacacaggaaacagctTGTAGTCGAGGGACTTCTTGC	
LD1064	taactacaaggtggtccgccACAGGAACACCTGGGCAAC	
LD1118	ccaggcaaattctgttttatcagaccgcttctgcgttctgatTCTTCAGGTTCTCGCGGTAG	pLD1966
LD1119	aagtgccagtaccaactggcGCAGATCCAGAAGATGGTCA	
LD1120	tgaccatcttctggatctgcGCCAGTTGGTACTGGCACTT	
LD1121	ggaattgtgagcggataacaatttcacacaggaaacagctATCGCGAGACTCATGGTTTT	

Table 3.2 (continued): Primers used in this study

primer number	sequence	used to make plasmid number
LD1134	ccaggcaaattctgttttatcagaccgcttctgcgttctgatCGCTGCTTGTCGATCTGTT	pLD1967
LD1135	gcgacatgaccctgttcaacCTGACCGGCTACTGGACC	
LD1136	ggtccagtagccggtcagGTTGAACAGGGTCATGTCGC	
LD1137	ggaattgtgagcggataacaatttcacacaggaaacagctCCTCGGCGACCATGAATAC	
LD1126	ccaggcaaattctgttttatcagaccgcttctgcgttctgatTTCAGGTTCTTCGGGTTCTC	pLD2044
LD1187	aacagcgcgccgaccagcatCTCTTCGTTCGTTTTCAGCC	
LD1188	ggctgaaaacgaacgaagagATGCTGGTCGGCGCGCTGTT	
LD1189	ggaattgtgagcggataacaatttcacacaggaaacagctGCGTTGATGAAGCGGATAAC	
LD2247	gattcgactgcactagtCTCGCCTTGCGGCTGGATGG	pLD2958
LD2248	gattcgactgcctcgagTCGGGTTCCCCTTATCGTTG	
LD2249	gattcgactgcactagtAAGCCCTACTTTATCTATG	pLD2959
LD2250	gattcgactatctcgagCTTCCGGCCTTAATCGATG	
LD2251	gattcgactgcactagtCGCGGCGCTGGCGGAAACG	pLD2960
LD2252	gattcgactgcctcgaGGCAACTCCTCTTCAGGTTC	
LD2120	gattcgacatcactagtACGCCCAGCTCCAACAAA	pLD2777
LD2121	gattcgatgccctcgaGCTAGGGGTTCCACGGTTAAT	
LD2122	gattcgactgcactagtCATCGACTTGCCGCCCAG	pLD2778
LD2123	gattcgatgccctcgaGCTATGGGCTTCCATCCAC	

Table 3.3: Plasmids used in this study

plasmid	description	source
pMQ30	7.5 kb mobilizable vector; oriT, sacB, GmR.	Shanks et al., 2006
pLD2722	GmR, TetR flanked by Flp recombinase target (FRT) sites to resolve out resistance casettes.	Jo et al., 2017
pFLP2	Flp recombinase-producing plasmid	Hoang et al., 1998.
pLD1929	Δcco1 cco2 PCR fragment introduced into pMQ30 by gap repair cloning in yeast strain InvSc1.	Jo et al., 2017
pLD1966	Δaa3 PCR fragment introduced into pMQ30 by gap repair cloning in yeast strain InvSc1.	this study
pLD1967	Δbo3 PCR fragment introduced into pMQ30 by gap repair cloning in yeast strain InvSc1.	this study
pLD2044	Δcio PCR fragment introduced into pMQ30 by gap repair cloning in yeast strain InvSc1.	this study
pLD2958	PCR-amplified aa3 promoter ligated into pLD2722 using SpeI and XhoI.	this study
pLD2959	PCR-amplified bo3 promoter ligated into pLD2722 using SpeI and XhoI.	this study
pLD2960	PCR-amplified cio promoter ligated into pLD2722 using SpeI and XhoI.	this study
pLD2777	PCR-amplified cco1 promoter ligated into pLD2722 using SpeI and XhoI.	Jo et al., 2017
pLD2778	PCR-amplified cco2 promoter ligated into pLD2722 using SpeI and XhoI.	Jo et al., 2017

3.7: Figure supplements

carbon source	mode of action
1,2-propanediol	C-Source, alcohol
2-deoxyadenosine	C-Source, carbohydrate
acetoacetic acid	C-Source, carboxylic acid
adenosine	C-Source, carbohydrate
adonitol	C-Source, carbohydrate
D-aspartic acid	C-Source, amino acid
D-cellobiose	C-Source, carbohydrate
D-fructose-6-phosphate	C-Source, carbohydrate
D-galactonic acid-γ-lactone	C-Source, carboxylic acid
D-galactose	C-Source, carbohydrate
D-galacturonic acid	C-Source, carboxylic acid
D-glucosaminic acid	C-Source, carboxylic acid
D-glucose-1-phosphate	C-Source, carbohydrate
D-glucose-6-phosphate	C-Source, carbohydrate
D-glucuronic acid	C-Source, carboxylic acid
D-mannose	C-Source, carbohydrate
D-melibiose	C-Source, carbohydrate
D-psicose	C-Source, carbohydrate
D-ribose	C-Source, carbohydrate
D-saccharinic acid	C-Source, carboxylic acid
D-serine	C-Source, amino acid
D-threonine	C-Source, amino acid
D-trehalose	C-Source, carbohydrate
D-xylose	C-Source, carbohydrate
dulcitol	C-Source, carbohydrate
formic acid	C-Source, carboxylic acid
glucuronamide	C-Source, amide
glycolic acid	C-Source, carboxylic acid
glycyl-L-aspartic acid	C-Source, amino acid
glycyl-L-glutamic acid	C-Source, amino acid
glyoxylic acid	C-Source, carboxylic acid
L-alanyl-glycine	C-Source, amino acid
L-arabinose	C-Source, carbohydrate
L-fucose	C-Source, carbohydrate
L-galactonic acid-γ-lactone	C-Source, carboxylic acid
L-lyxose	C-Source, carbohydrate
L-serine	C-Source, amino acid
L-threonine	C-Source, amino acid
lactulose	C-Source, carbohydrate
m-hydroxyphenyl-acetic acid	C-Source, carboxylic acid
m-inositol	C-Source, carbohydrate
m-tartaric acid	C-Source, carboxylic acid
maltose	C-Source, carbohydrate
maltotriose	C-Source, carbohydrate
monomethylsuccinate	C-Source, carboxylic acid
mucic acid	C-Source, carboxylic acid
N-acetyl-β-D-mannosamine	C-Source, carbohydrate
phenylethylamine	C-Source, amine
sucrose	C-Source, carbohydrate
thymidine	C-Source, carbohydrate
tricarballylic acid	C-Source, carboxylic acid
uridine	C-Source, carbohydrate
α-D-lactose	C-Source, carbohydrate
α-hydroxy-butyric acid	C-Source, carboxylic acid
α-hydroxy-glutaric acid-γ-lactone	C-Source, carboxylic acid
α-ketobutyric acid	C-Source, carboxylic acid
α-methyl-D-galactoside	C-Source, carbohydrate
β-methyl-D-glucoside	C-Source, carbohydrate

Figure 3.1–figure supplement 1. Carbon sources that do not support growth of PA14. The 58 carbon sources (and their modes of action as designated by Biolog, Inc.) in the phenotype microarray plate that did not support growth of PA14 strains.

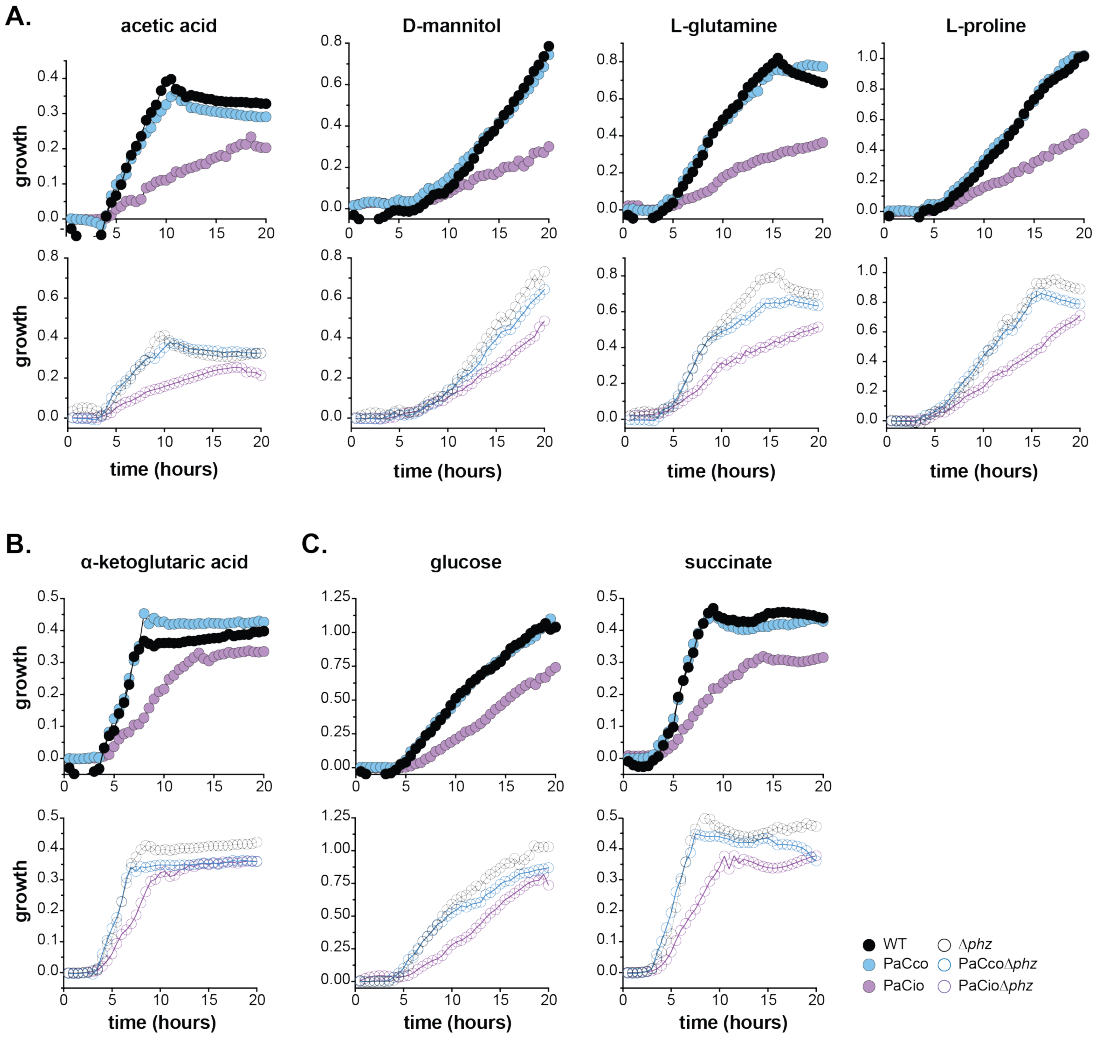

Figure 3.2–figure supplement 1. Growth profiles of carbon sources of interest. Growth curves (absorbance at 500 nm) over time of carbon sources in group 3 **(A),** group 4 **(B)**, and glucose and succinate **(C)** in the presence (top, closed circles) and absence (bottom, open circles) of phenazines. Data represent the average of two biological replicates.

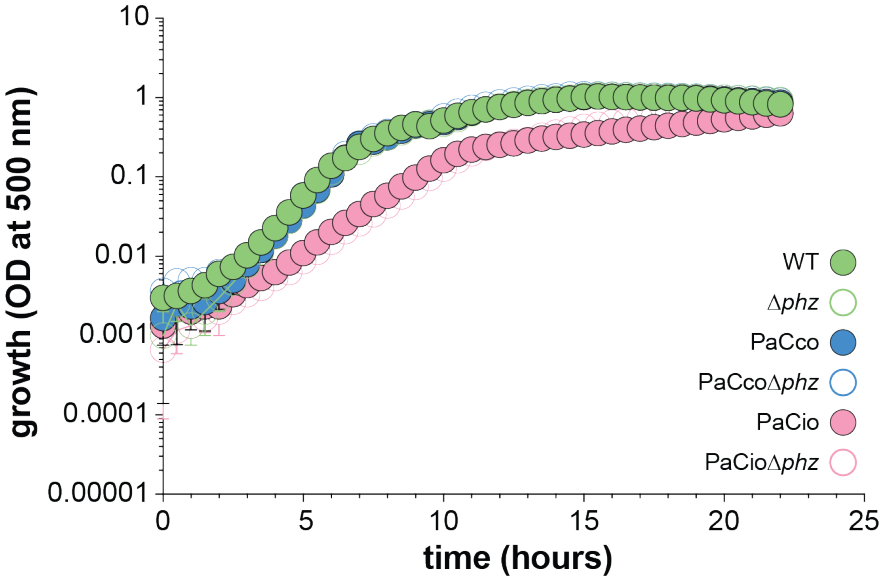

Figure 3.3–figure supplement 1. PA14 growth in MOPS + 30 mM succinate. Growth curves of PA14 strains in MOPS defined medium with 30 mM succinate. Data represent the mean values of at least three biological replicates, and error bars denote standard deviation.

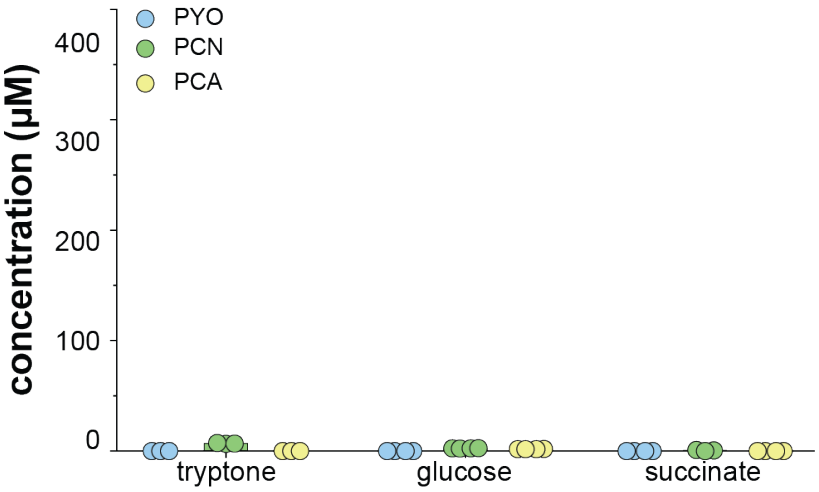

Figure 3.5–figure supplement 1. Phenazine production in three-day-old biofilms. Quantification of phenazines retained in three-day old WT biofilms. Individual data points represent biological replicates, and bars indicate the mean. Error bars denote standard deviation. PCA, phenazine-1-carboxylic acid; PCN, phenazine-1-carboxamide; PYO, pyocyanin.

Chapter 4

Other pathways of energy generation in *Pseudomonas aeruginosa* and the contribution of redox state to biofilm formation in *Bacillus subtilis*

In the preceding chapters, I have discussed projects for which I was the primary contributor. The main metabolic pathways considered in those chapters involved the oxidation of a carbon source via aerobic respiration. This chapter represents a collection of papers to which I contributed as a co-author through various collaborations. I have distilled each paper into its main points, including experiments that I performed.

Here, I will discuss some alternative pathways of energy generation carried out by *P. aeruginosa*, starting with two alternative fates of pyruvate. During aerobic respiration, pyruvate is oxidized to acetyl-CoA at the end of the Entner-Doudoroff pathway. At this point, it will enter the TCA cycle and its oxidation (ultimately to CO_2) will be coupled to energy generation via the ETC. However, under different environmental conditions and nutrient availabilities, pyruvate can be reduced to lactate or carboxylated to oxaloacetate. I will discuss each of these fates, in the context of my collaborations, in turn. I will then discuss research elucidating the role of a metabolic enzyme originally believed to mediate the carboxylation of pyruvate to oxaloacetate. Finally, I will conclude with a project that demonstrates a role for redox state in driving biofilm development in another bacterium, *Bacillus subtilis*.

The figures presented in this chapter were modified from their respective articles with the exception of **Figures 4.11** (modified from Okegbe *et al*., 2014) and **4.12** (my unpublished data). Materials and methods relevant to the points discussed in this chapter are adapted from their respective articles, with minor revisions.

4:1: The *Pseudomonas aeruginosa* complement of lactate dehydrogenases contributes to growth in CF lung-like environments

This section is adapted from:

Lin, YC, Cornell, WC, **Jo, J**, Price-Whelan, A, Dietrich, LEP (2018). The *Pseudomonas aeruginosa* complement of lactate dehydrogenases enables use of D- and L-lactate and metabolic cross-feeding. *mBio* 9, e00961-18.

I performed the growth assays in the various synthetic CF media (**Figure 4.4**) and the data analysis and interpretation for those experiments.

In addition to being able to produce energy via oxygen or nitrate respiration, *P. aeruginosa* is also capable of fermenting arginine or pyruvate when it encounters anoxic conditions (**Figure 1.6**). Arginine fermentation provides enough ATP to allow for growth while pyruvate fermentation is less efficient, allowing for anaerobic survival but not growth (Shoesmith and Sherris 1960; Vander Wauven et al. 1984; Williams, Zlosnik, and Ryall 2007). The *P. aeruginosa* genome encodes four enzymes annotated to be involved in the conversion between lactate and pyruvate. LdhA reduces pyruvate to the D-enantiomer of lactate (D-lactate) while

LldE mediates the reverse reaction (conversion of D-lactate to pyruvate). *P. aeruginosa* also encodes LldD, an enzyme that converts L-lactate to pyruvate, as well as an additional, less-characterized enzyme LldA, which is 44% identical to LldD. *lldD* and *lldE* are co-transcribed in the same operon along with another gene encoding a lactate permease (*lldP*) while *lldA* is found elsewhere in the genome, not in an operon (**Figure 4.1**). That *P. aeruginosa* has two enzymes for L-lactate metabolism is interesting in light of the facts that (1) this bacterium does not produce L-lactate and (2) L-lactate is mostly a byproduct of plant and mammalian metabolism (Petersen 2005; Maurino and Engqvist 2015). We therefore hypothesized that LldA functions redundantly with LldD as an L-lactate dehydrogenase, and that together these enzymes would contribute to *P. aeruginosa* survival in a host.

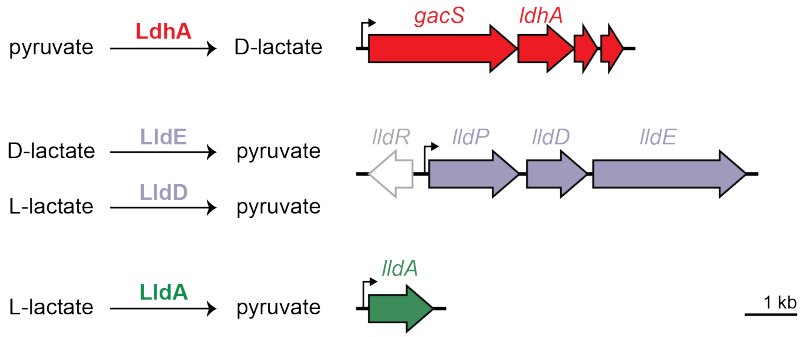

Figure 4.1. The *P. aeruginosa* genome encodes several enzymes that interconvert pyruvate and lactate. (Left) Reactions catalyzed by *P. aeruginosa*'s lactate dehydrogenases; (right) chromosomal loci encoding each of the corresponding enzymes. LdhA catalyzes the reduction of pyruvate during anaerobic survival. LldE catalyzes the oxidation of D-lactate during aerobic growth. Unlike *E. coli*, which contains only one gene encoding an L-lactate dehydrogenase, *P. aeruginosa* contains two orthologues for this enzyme. LldD catalyzes the oxidation of L-lactate during aerobic growth. This study describes a role for LldA in catalyzing the oxidation of L-lactate during aerobic growth.

In order to characterize the conditions under which the different lactate metabolism genes are expressed, we created reporter constructs that fused the promoters of *lldPDE* and *lldA* to *gfp*. We then grew these reporters planktonically in a defined MOPS-buffered medium with D-glucose, L-lactate, or D-lactate as the sole carbon source (**Figure 4.2**). We saw a quick and strong expression of *lldPDE-gfp* in both D- and L-lactate starting from early stages of growth, as expected, and a low level of expression in D-glucose starting later in growth. The latter was most likely *lldPDE-gfp* expression in response to production of D-lactate at later

stages of growth (**Figure 4.2**). *lldA-gfp* expression, on the other hand, was more gradual and only seen in response to L-lactate, consistent with the hypothesis that LldA specifically oxidizes L-lactate to pyruvate.

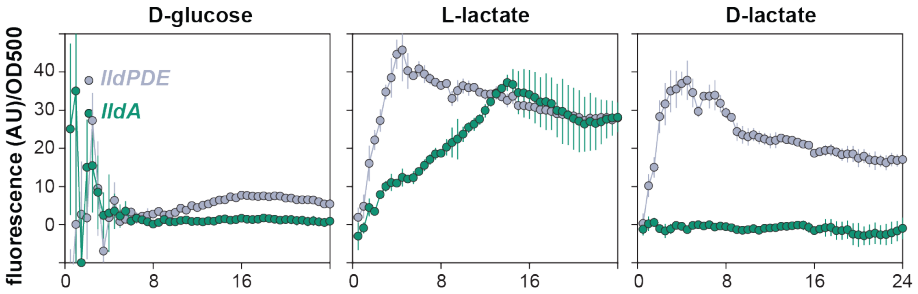

Figure 4.2. Expression of loci associated with pyruvate and lactate metabolism during aerobic, liquid-culture growth. Strains engineered to express GFP under the control of promoters upstream of *lldP* (which is cotranscribed with *lldD* and *lldE*) or *lldA* were grown in MOPS medium, with the indicated compounds provided as sole carbon sources. Background fluorescence from a strain with a promoterless reporter (MCS-*gfp*) was subtracted before normalization to the OD at 500 nm. Error bars, which are often obscured by the point markers, represent the standard deviations from biological triplicates. AU, arbitrary units.

To then assess the physiological contributions of *lldD*, *lldE*, and *lldA* to *P. aeruginosa* growth, we generated deletion mutants of *lldDE* and *lldA* and characterized the development of the resulting colony biofilms on different carbon sources. Mutants grown with D-glucose as the sole carbon source showed biofilm development indistinguishable from that of the WT (**Figure 4.3**). Indeed, Δ*lldA* showed WT-like growth in all carbon sources tested, including L- and D-lactate, indicating that LldA alone is not necessary for metabolism of either lactate enantiomer. When Δ*lldDE* was grown on D-lactate, colony biofilms exhibited a severe growth defect with almost no growth, consistent with previous reports that LldE is likely solely responsible for D-lactate metabolism (Gao et al. 2012). When Δ*lldDE* was grown on L-lactate, the resulting colonies were able to grow robustly, but displayed more wrinkled biofilms that bound more Congo red dye relative to the WT (**Figure 4.3**), features we have previously shown to be indicative of redox stress in biofilms (Dietrich et al. 2008, 2013). This phenotype indicated that LldD participates in L-lactate utilization, but that it is likely working in conjunction with another enzyme whose presence allows Δ*lldDE* to grow on L-lactate. Strikingly, while Δ*lldA* showed WT-like biofilm development on L-lactate, the Δ*lldDE*Δ*lldA* double mutant produced biofilms that

were unable to grow on this carbon source **(Figure 4.3**). These results suggest that LldA functions redundantly with LldD in L-lactate metabolism.

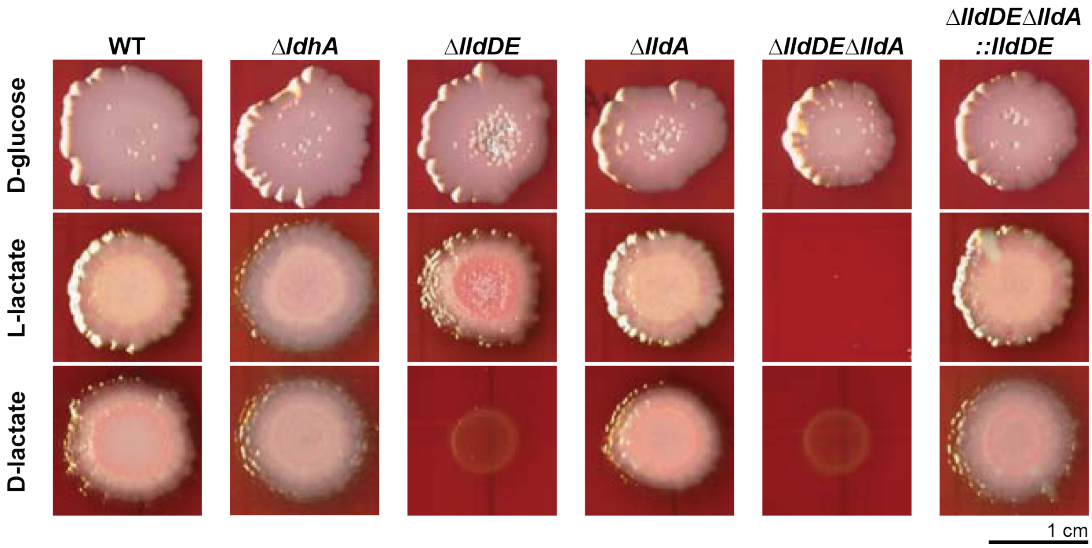

Figure 4.3. Physiological roles of enzymes that interconvert pyruvate and lactate during biofilm growth. Growth and morphological development of the indicated strains under an oxic atmosphere on MOPS medium containing the dyes Congo red and Coomassie blue and amended with D-glucose, L-lactate, or D-lactate. Images were taken after 4 days of incubation. WT, wild type.

As previously mentioned, it is noteworthy that *P. aeruginosa* has two enzymes for the conversion of L-lactate to pyruvate when it itself does not produce L-lactate as a metabolic byproduct. Furthermore, the redundant role we described for LldA in biofilm formation on L-lactate was in contrast to previous reports in another pseudomonad, *P. stutzeri*, which showed that the *lldDE* operon alone is required for growth on L-lactate (Gao et al. 2012). These observations led us to hypothesize that the presence of a redundant gene for L-lactate utilization in *P. aeruginosa* contributes to its success as a human pathogen.

To further explore the possibility that *lldA* contributes to *P. aeruginosa* growth in a pathogenic context, we grew our mutants in a variety of synthetic CF media designed to mimic sputum from CF patients (Palmer, Aye, and Whiteley 2007; Fung et al. 2010; Turner et al. 2015). Nutrient conditions found in CF sputum are markedly different from those found in sputum from healthy individuals. Healthy sputum is a mixture of water, salts, mucins, and surfactants; in CF patients, the levels of these ingredients are altered, and additional molecules not found in healthy sputum are detected. Specifically, CF sputum contains higher amounts of free amino

acids, DNA, iron, and lactate. Lactate has been measured in millimolar concentrations ranging from 3-14.1 mM and the presence of it in CF sputum correlates to lung inflammation (Conway and Cohen 2015). We tested the growth of Δ*lldDE*Δ*lldA* in three kinds of synthetic CF media: (1) synthetic CF medium (SCFM, a defined mixture of ions, amino acids, iron, and carbon sources; (Palmer, Aye, and Whiteley 2007)), (2) ASMDM (modified artificial sputum medium, similar to SCFM but also containing bovine serum albumin, mucin, and herring sperm DNA; (Fung et al. 2010)), and (3) SCFM2, which is similar to ASMDM but also contains the large molecules N-acetyl-D-glucosamine and dipalmitoylphosphatidylcholine (Turner et al. 2015).

Compared to WT *P. aeruginosa*, the Δ*lldDE*Δ*lldA* mutant had about 10% less growth in SCFM, with the growth defect starting after cells were in stationary phase (**Figure 4.4A**). The mutant also had a stationary growth defect compared to the WT in ASMDM (**Figure 4.4B**) and SCFM2 (**Figure 4.4C**), but in the former, Δ*lldDE*Δ*lldA* showed slower growth starting in exponential phase. Together, these data indicate that the lactate dehydrogenases contribute to growth in media that are similar in makeup to the sputum found in CF patients. That the Δ*lldDE*Δ*lldA* mutant displayed growth defects relative to the WT in all three synthetic media tested also suggests that these enzymes may contribute to the virulence of *P. aeruginosa* in the CF lung.

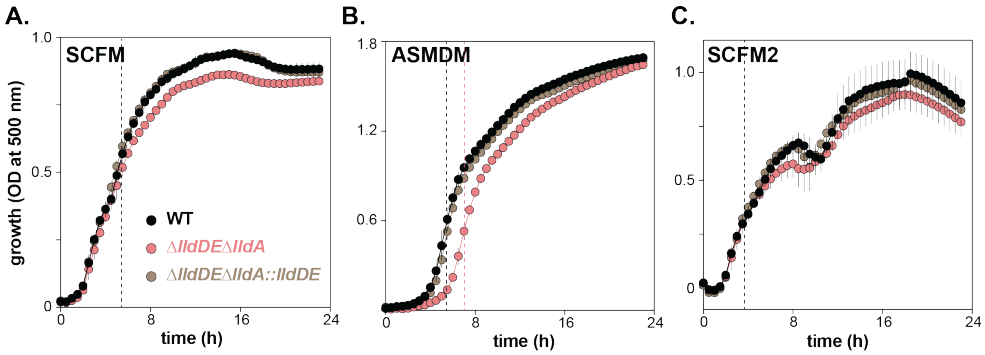

Figure 4.4. PA14 utilizes the L-lactate in various synthetic cystic fibrosis sputum media for growth. Growth of the indicated strains in SCFM **(A)**, ASMDM **(B)**, and SCFM2 **(C)**. Error bars represent the standard deviations from at least four biological replicates and are omitted in cases where they would be obscured by point markers. Dashed lines indicate onset of stationary phase. In panel **(B)**, Δ*lldDE* Δ*lldA* reaches stationary phase at a later time point than the other two strains; its onset of stationary phase is delineated by the red dashed line while the onset of stationary phase for the other two strains is indicated by the black dashed line.

Lactate is a major component of the CF sputum (Palmer, Aye, and Whiteley 2007), and while *P. aeruginosa* can convert pyruvate into D-lactate, the L-enantiomer is produced by eukaryotes rather than bacteria (Starkey and Rahme 2009; Lorenz et al. 2016; Winsor et al. 2016). Therefore, the presence of a gene for L-lactate utilization is likely tied to *P. aeruginosa*'s prevalence as a plant and human pathogen. Furthermore, the presence of *lldA*, a redundant gene for L-lactate utilization, may allow this bacterium to more efficiently metabolize this carbon source when colonizing a eukaryotic host. In support of this hypothesis are our results in **Figure 4.4**, which demonstrate that LldD and LldA cooperatively contribute to optimal growth in media that mimic the nutrient conditions of CF sputum. While the majority of pseudomonad species contain either the LldD or LldA enzymes for L-lactate utilization, *P. aeruginosa* contains both (Lin et al. 2018); together, these two enzymes may endow this bacterium to more successfully colonize and persist in CF lung environments.

4:2: Pyruvate carboxylation affects *Pseudomonas aeruginosa* biofilm morphogenesis

This section is adapted from:

Choi, PH, **Jo, J**, Lin, YC, Lin, MH, Chou, CY, Dietrich, LE, Tong, L (2016). A distinct holoenzyme organization for two-subunit pyruvate carboxylase. *Nat Commun* 7, 12713.

The work presented in this section resulted from a collaboration with the Tong lab at Columbia University. I generated all of the *Pseudomonas aeruginosa* mutant and complementation strains discussed in this section and conducted initial liquid culture and colony biofilm growth assays. I also contributed to the data analysis and interpretation of the work pertaining to *P. aeruginosa* and the role of pyruvate carboxylase in biofilm morphogenesis and redox balancing.

Pyruvate, in addition to being oxidized to acetyl-CoA and reduced to lactate, can be carboxylated to oxaloacetate, an intermediate of the TCA cycle. **P**yruvate **c**arboxylase (PC) is the enzyme that catalyzes the carboxylation of pyruvate to oxaloacetate, thereby functioning in anaplerosis of the TCA cycle. When *P. aeruginosa* grows on organic acids (such as succinate) or amino acids (which are plentiful in a complex carbon source like tryptone), it is able to

synthesize oxaloacetate easily from these compounds. However, when it is grown on a sugar (i.e., glucose), PC activity is necessary for oxaloacetate replenishment.

Through a collaboration with the Tong lab at Columbia University, we were able to gain more insight into the structure and function of PC (*PA14_71720-71740*), a member of the biotin-dependent carboxylase family, which also includes **a**cetyl-**C**oA **c**arboxylase (ACC) and **p**ropionyl-**C**oA **c**arboxylase (PCC) (Tong 2013). Reactions mediated by biotin-dependent carboxylases function in two steps: first, the enzyme carboxylates its biotin cofactor and then this carboxyl group is transferred from the biotin to the substrate (Tong 2013; Tran et al. 2015). These enzymes contain three core domains: the **b**iotin **c**arboxylase (BC) domain, the **c**arboxyl**t**ransferase (CT) domain, and the **b**iotin **c**arboxyl **c**arrier **p**rotein (BCCP) domain. The biotin cofactor interacts with the carboxylase enzyme at the BCCP domain and is carboxylated by the BC domain. The CT domain mediates the transfer of the carboxyl group to the enzyme's substrate.

In pyruvate carboxylases of eukaryotes and most bacteria, these domains are found within one polypeptide chain and are therefore called "single-chain" PCs. However, in a subset of Gram-negative bacteria, including *Methylobacillus flagellatus* and *P. aeruginosa*, the domains are encoded by two genes, the α and β subunits (**Figure 4.5A**), and are accordingly classified as two-subunit enzymes. In these enzymes, the α subunit contains the BC domain while the β subunit contains the CT and BCCP domains.

The structures of single-chain PCs had been previously reported and showed that the holoenzyme consists of four PC monomers forming a two-layered homotetramer (St Maurice et al. 2007; Xiang and Tong 2008); **Figure 4.5B**). Each layer contains two PC monomers and previous structural insights have indicated that PC will only be catalytically active in the tetrameric form; the tetramerization of PC is mediated by the **P**C **t**etramerization (PT) domain (Tong 2013). This is because the BCCP-biotin is carboxylated by the BC domain of one monomer and then transfers the CO_2 to a pyruvate molecule in the CT domain of another monomer in the same layer, hence making both monomers necessary for pyruvate

carboxylation. However, the conformation of these two monomers is only stable when the enzyme forms a tetramer, as two monomers in the same layer have minimal interactions with one another.

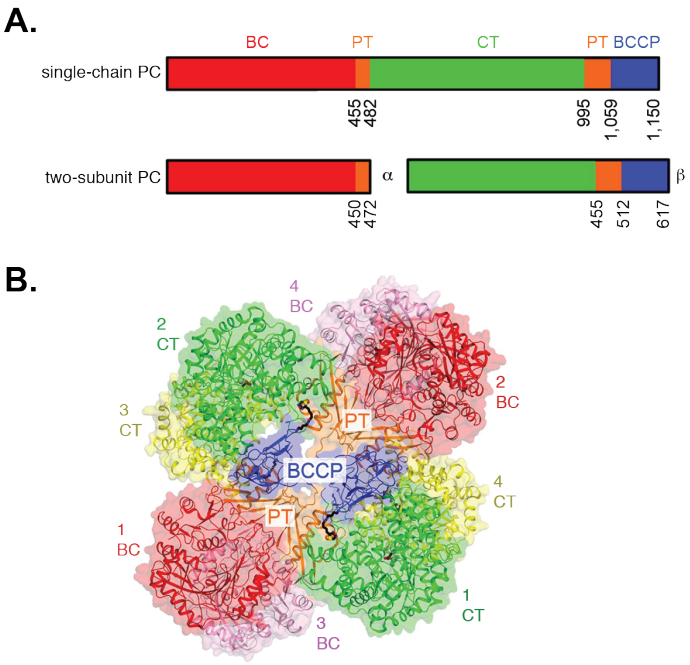

Figure 4.5. Organization of single-chain and two-subunit pyruvate carboxylases. **(A)** Domain organization of *Staphylococcus aureus* pyruvate carboxylase (SaPC), a representative single-chain PC, and *Methylobacillus flagellatus* PC, a representative two-subunit PC. **(B)** Schematic drawing of the structure of the single-chain SaPC holoenzyme (Xiang and Tong, 2008). The domains in the four monomers are labeled and colored according to **(A)**.

Based on these details, the structure of the two-subunit PCs were expected to show an $\alpha_4\beta_4$ stoichiometry, which would correspond to the homotetrameric organization of single-chain PCs previously shown to be important for catalytic activity. Surprisingly, the structure of *M. flagellatus* PC (MfPC), the first reported for a holoenzyme of a two-subunit PC, revealed an $\alpha_2\beta_4$ stoichiometry and an overall divergent structure from the single-chain PCs (**Figure 4.6**).

The region corresponding to the PT domain of MfPC showed a less than 10% sequence identity to the PT domain of single-chain PCs. The α and β subunits of MfPC interact through a helix at the C terminal end of an α subunit making contact with a region in the CT-BCCP linker

of a β subunit (**Figure 4.6**); this interaction corresponds to that mediated through the PT domain of single-chain PCs. Furthermore, the structure of the two-subunit MfPC revealed novel interactions between a CT domain (in a β subunit) and the aforementioned helix (in an α subunit). This interaction led to the formation of a new, "BT-like" domain (**Figure 4.6**, "BT-L" in orange) that resembles the BT domains (which mediate the interaction between **B**C and C**T** domains) found in ACCs and PCCs. This BT-like domain is very likely the driving force behind the $\alpha_2\beta_4$ stoichiometry seen in the two-subunit PCs, which, based on sequence homologies, is expected to be conserved among all bacterial two-subunit PCs.

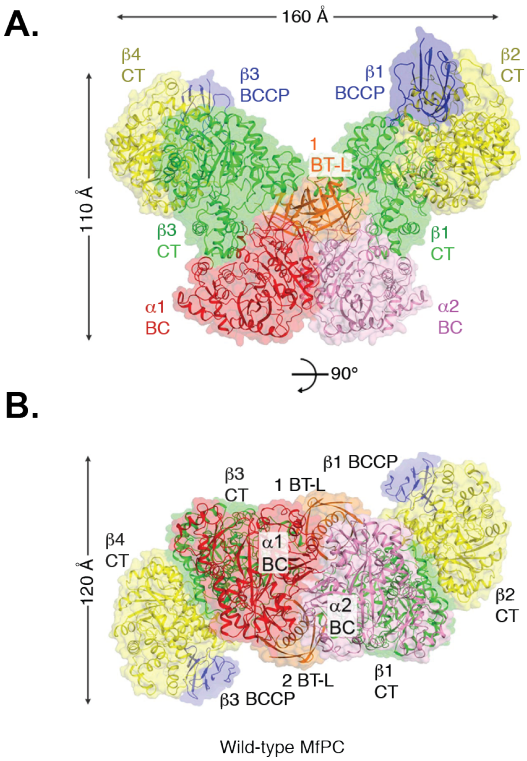

Figure 4.6. Structure of MfPC holoenzyme. (A) Structure of the wild-type MfPC holoenzyme, having the shape of a butterfly in this view. The domains are colored according to **Figure 4.5A**, except that the BC domain of the second subunit is colored in pink. BT-L, BT-like domain. **(B)** Structure of the wild-type MfPC holoenzyme viewed down the BC domain dimer, along the arrow of A.

ACCs also contain BC, CT, and BCCP domains; however, this helix domain is not found in the BC subunit. The presence of this domain has been the source of some confusion, leading to *P. aeruginosa*'s ACC and PC to originally be misannotated (Stover et al. 2000). Through the *in vivo* studies described next and another collaboration with the Tong Lab (to be discussed in section 4.3 below), we were able to clarify the functions of these two enzymes in *P. aeruginosa*.

Because the identity of *P. aeruginosa*'s ACC and PC were somewhat nebulous, and because *P. aeruginosa* PC (PaPC) represents another two-subunit PC, we then conducted

functional studies to investigate the physiological role of PaPC. PaPC has high sequence identity with MfPC, and *in vitro* biochemical assays predict it to also have an $\alpha_2\beta_4$ stoichiometry. In order to study the contribution of this enzyme to *P. aeruginosa* growth, we generated a mutant lacking this enzyme (Δ*PC*) as well as point mutants for some key residues identified through the MfPC structure. The point mutants generated were: K451stop (K451*) in the α subunit, which would disrupt holoenzyme formation, K572A in the β subunit, which would eliminate biotinylation, and A55T in the β subunit, which would interfere with biotin binding to the CT domain and predicted to reduce PC activity by ~50-fold. We also generated a complementation strain that complemented WT PC back into the site of deletion.

In agreement with known contributions of PaPC to *P. aeruginosa* growth on specific carbon sources, Δ*PC* and all point mutants grew comparably to the WT when grown on succinate as a sole carbon source. However, when glucose or pyruvate was the sole carbon source, Δ*PC* showed a significant growth defect in liquid culture relative to the WT (**Figure 4.7A**), indicative of a stalled TCA cycle resulting from a depletion of oxaloacetate. In glucose, growth of K451* and K572A recapitulated that of Δ*PC*, while A55T showed a less severe growth defect than the full deletion. In pyruvate, K451* and K572A again phenocopied Δ*PC*, while A55T displayed WT-like growth. These results confirmed that the A55T point mutation was not as deleterious to enzyme activity as the other two point mutations as expected.

We then extended these physiological studies to biofilms by looking at pellicle and colony formation. Pellicles are biofilms that form from static liquid cultures at the liquid-air interface. When pellicles or colonies were grown on succinate, the Δ*PC* mutant, as expected, looked like the WT. However, when biofilms were grown on either glucose or pyruvate as the sole carbon source, the Δ*PC* mutant conferred a strong growth defect, reflective of what was observed in liquid culture (**Figure 4.7B**, **C**).

After assessing the contribution of PC to biofilm growth on a single carbon source, we next tested 1% tryptone, a complex, rich medium. When WT biofilms are grown on tryptone, they remain relatively smooth until day three of development, when they begin to wrinkle

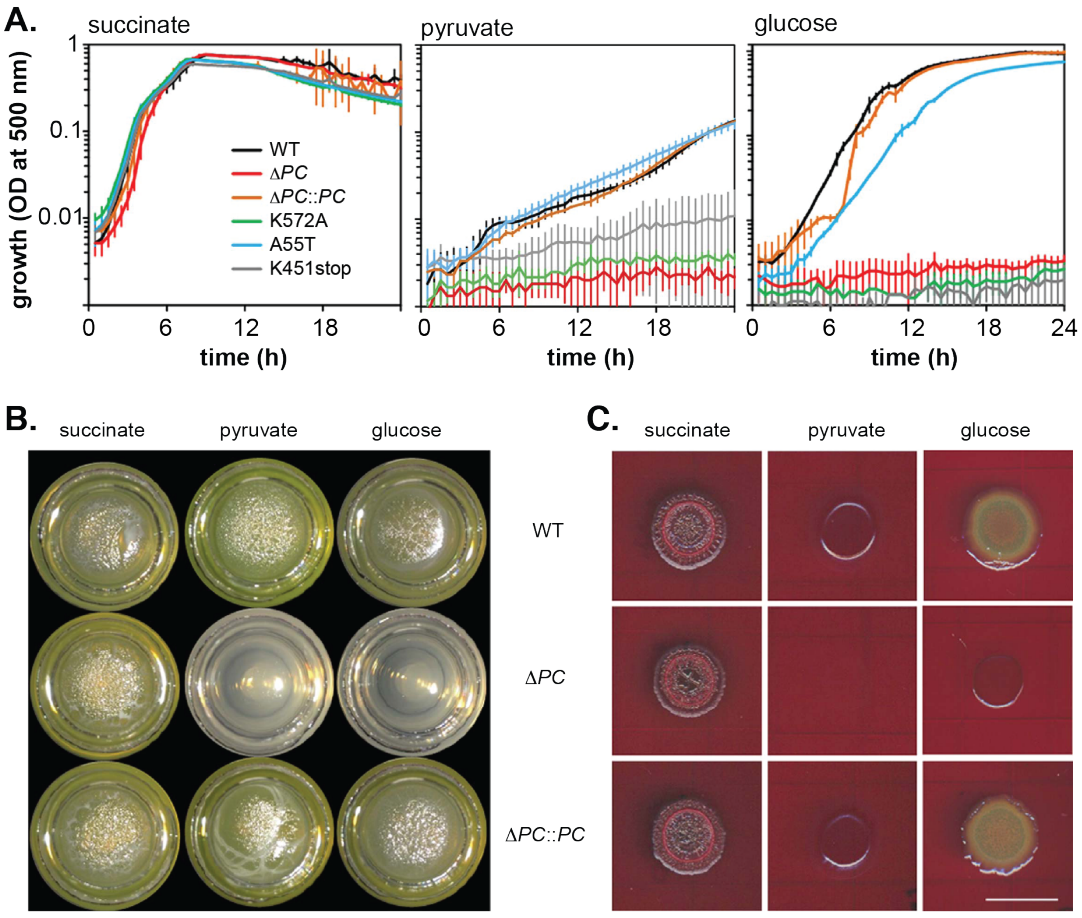

Figure 4.7. The two-subunit PaPC is required for growth on selected carbon sources. (A) Shaken liquid-culture growth of wild-type *P. aeruginosa* PA14, Δ*PC*, the PC-complemented strain and various site-specific mutants in a defined medium containing 20 mM succinate, pyruvate, or glucose as the sole carbon source. Each growth curve represents the average of three biological replicates. Error bars denote standard deviation. **(B)** Pellicles formed by *P. aeruginosa* PA14, Δ*PC*, and the PC-complemented strain on a defined medium containing succinate, pyruvate, or glucose as the sole carbon source. **(C)** Colony morphology of *P. aeruginosa* PA14, Δ*PC*, and the PC-complemented strain on a defined medium (supplemented with 1% agar, Congo red, and Coomassie blue) containing succinate, pyruvate, or glucose as the sole carbon source. Images depict day three of colony development. Scale bar is 1 cm.

(**Figure 4.8A**). The onset of wrinkling has previously been shown to correspond to an increase in intracellular redox stress, which is alleviated by increased surface exposure to O_2 (Dietrich et al. 2013). Compared to the WT, Δ*PC* mutant biofilms displayed morphologies indicative of increased redox stress: they wrinkled earlier and formed thinner biofilms with higher wrinkle structures (**Figure 4.8A**). Of the point mutants generated, only the K572A mutant phenocopied the Δ*PC* mutant.

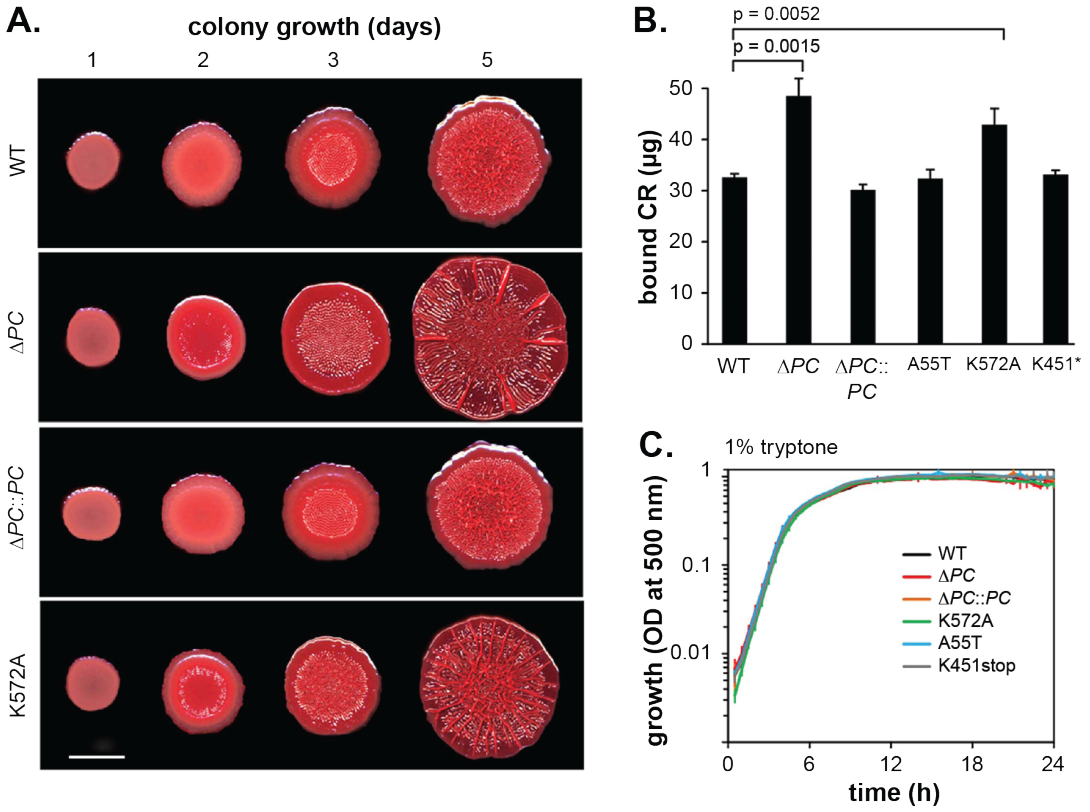

Figure 4.8. PaPC dysfunction leads to increased matrix production and altered colony morphology. (A) Colony morphology of wild-type *P. aeruginosa* PA14, Δ*PC*, the PC-complemented strain, and the K572A mutant on 1% tryptone, 1% agar (supplemented with Congo red and Coomassie blue). Scale bar is 1 cm. **(B)** Quantification of Congo red binding, a proxy for matrix production, for *P. aeruginosa* PA14, Δ*PC*, the PC-complemented strain, and various site-specific mutants grown on 1% tryptone, 1% agar with no added dyes. Colonies were grown for 3 days before they were collected for the Congo red binding assay. **(C)** Shaken liquid-culture growth of *P. aeruginosa* PA14, Δ*PC*, the PC-complemented strain, and various site-specific mutants in 1% tryptone. Each growth curve represents the average of three biological replicates. Error bars denote standard deviation.

As matrix production is necessary for the formation of biofilms structures, we hypothesized that the Δ*PC* mutant would have increased matrix production relative to the WT. To this end, we measured matrix production by quantifying Pel, a major component of PA14 matrix. Pel is a cationic polysaccharide that binds to the anionic dye Congo red, so the proportion of bound Congo red dye is directly proportional to matrix production. We found that Δ*PC* biofilms formed on tryptone bound significantly higher levels of Congo red than the WT (**Figure 4.8B**). Consistent with our tryptone biofilm morphology results, we saw that only the

K572A point mutant showed increased matrix production relative to the WT, while A55T and K451* produced WT levels of matrix.

Surprisingly, we found that the Δ*PC*-mediated growth phenotypes on tryptone were biofilm-specific: when we grew all strains planktonically, we saw that Δ*PC* and all of the point mutants grew like the WT (**Figure 4.8C**). This indicates that the function of PC on a complex medium is more linked to growth in a biofilm context than it is in liquid culture, another indication that growth in the liquid and biofilm contexts are quite divergent and illustrating how *P. aeruginosa* may switch its metabolism in response to its mode of growth. The biofilm-specific phenotype of the PC deletion mutant on a complex medium corresponds to increased redox stress as indicated by colony morphology and Congo red binding assays. Additionally, Δ*PC* showed abrogated growth on glucose and no growth on pyruvate, two carbon sources that are found in CF sputum (Palmer, Aye, and Whiteley 2007; Bensel et al. 2011). Together, these results indicate that PC's expected anaplerotic role does indeed sustain TCA cycle function and participates in redox balancing in biofilms; both of these functions may have important contributions to *P. aeruginosa* as a clinically-relevant pathogen.

4.3: Structure and function of a single-chain, multi-domain long-chain acyl-CoA carboxylase

This section is adapted from:

Tran, TH, Hsiao, YS, **Jo, J**, Chou, CY, Dietrich, LE, Walz, T, Tong, L (2015). Structure and function of a single-chain, multi-domain long-chain acyl-CoA carboxylase. *Nature* 518, 120-124.

The work presented in this section resulted from another collaboration with the Tong Lab at Columbia University. I generated the *Pseudomonas aeruginosa* Δ*LCC* mutant strain and contributed to data analysis and interpretation of the experiments performed in *P. aeruginosa*.

In collaboration with the Tong lab, we studied the function of *P. aeruginosa*'s acetyl-CoA-carboxylase, or ACC. While eukaryotic ACCs are single-chain, multi-domain enzymes, those found in bacteria have been shown to be multi-subunit enzymes. ACCs catalyze the carboxylation of acetyl-CoA to malonyl-CoA, which is then used as a precursor of fatty acid

biosynthesis (Kutchma, Hoang, and Schweizer 1999). In Tran *et al*., 2015, the structure of ACC from *Mycobacterium avium* subspecies *paratuberculosis* was solved and shown to be a single-chain, multi-domain enzyme (**Figure 4.9A**). A homolog of this enzyme is found in *P. aeruginosa* but had been previously mis-annotated to be a pyruvate carboxylase (Stover et al. 2000) and later shown to be an acetyl-CoA carboxylase (Lai et al. 2006). Biochemical assays performed within the scope of our study confirmed that this enzyme did not possess PC activity but instead showed activity toward a variety of acyl-CoAs, including acetyl-CoA and propionyl-CoA, but showed a preference for long-chain substrates, leading this group of enzymes to be named long-chain acyl-CoA carboxylases (or LCCs) (Tran et al. 2015).

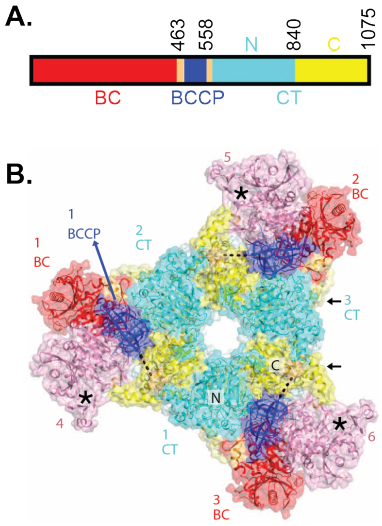

Figure 4.9. Structure of LCC from *M. avium* subspecies *paratuberculosis*. (A) Domain organization of MapLCC, with the domains labeled. **(B)** Overall structure of the 720 kDa hexameric holoenzyme of MapLCC. The six monomers are labeled. The domains in the three monomers in the top layer (numbered 1, 2, 3) are colored as in A. The BC, BCCP, N, and C CT domains in the three monomers in the bottom layer (numbered 4, 5, and 6) are colored pink, pale blue, and pale cyan, and pale yellow, respectively. The disordered region of the BCCP-CT linker is indicated with a dashed line.The BC active sites are indicated with asterisks. The CT active sites are on the side of the CT domain core and indicated with black arrows.

The structure of ACC from *M. avium* subspecies *paratuberculosis* (MapLCC) showed its holoenzyme to be a homohexamer (**Figure 4.9B**). Each monomer contained BC, BCCP, and CT domains as expected and the monomers within the holoenzyme have significant interactions with each other (these interactions include van der Waals and ionic interactions and hydrogen bonding). In contrast to other ACCs, the BC-CT (BT) interaction domain is not found in MapLCC and the BCCP domain of LCC is found in the middle of the peptide rather than at the end of the polypeptide chain (**Figure 4.9A**). As a result, there are two linkers from the BCCP domain to the rest of the protein, making this region very flexible during catalysis, allowing for optimal contact between the biotin and the BC and CT domains, resulting in good catalytic activity (Tong 2013).

To further study the physiological role of this enzyme, we generated a deletion mutant for its ortholog in *P. aeruginosa* (*PA14_46320*; the resulting deletion strain will be referred to as Δ*LCC*) and evaluated its growth under ~ 2,000 conditions using Biolog phenotype microarrays. Some of the conditions tested included growth on various carbon and nitrogen sources and exposure to different antibiotics. Growth was measured as a function of the chemical reduction of a tetrazolium dye that undergoes a color change upon a change in redox state. Overall, Δ*LCC* in *P. aeruginosa* was similar to the reference WT PA14 strain in most conditions tested. Only a few conditions elicited different growth profiles between WT and Δ*LCC*. These were growth in the carbon sources fumarate and gly-pro (a dipeptide) and in the dipeptide nitrogen sources asp-phe, glu-val, met-asp, and met-val (**Figure 4.10**). Only the results on fumarate and met-val were considered significant. On met-val, the Δ*LCC* mutant had a growth defect relative to the WT while on fumarate, the mutant grew significantly better than the WT.

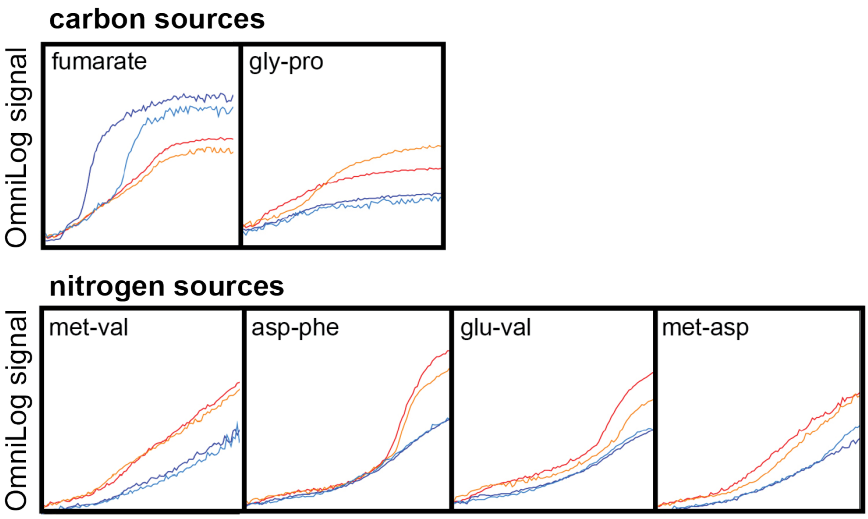

Figure 4.10. *In vivo* function of *P. aeruginosa* LCC. Phenotypic differences between wild type and LCC knockout (Δ*PA14_46320*) *P. aeruginosa* PA14 strains, revealed by a colorimetric assay that monitors the reduction of a tetrazolium dye. Assays were performed twice in each medium for the wild-type (red and orange) and mutant (blue and cyan) strains. For each panel, the horizontal axis is time (24 h) and the vertical axis is OmniLog signal, indicating levels of dye reduction (Shea *et al*., 2012).

The metabolism of methionine and valine both lead to the production of propionyl-CoA (Tran et al. 2015). It is possible that the activity of LCC toward propionyl-CoA, which was demonstrated in this work, contributes to further degradation of propionyl-CoA, a hypothesis

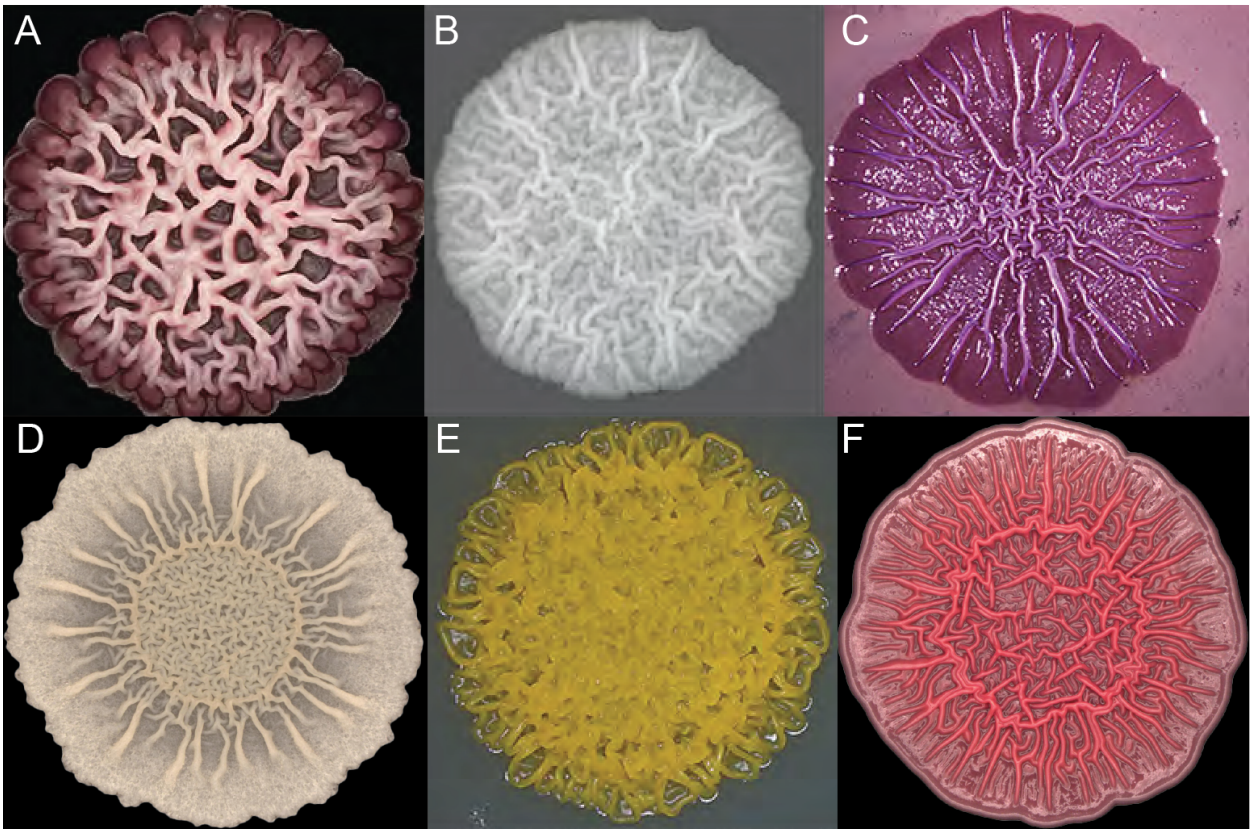

Figure 4.11. Architecturally complex biofilms are formed by diverse microbial species. (A) *Candida albicans*, a eukaryotic fungus (D. Morales and D. Hogan). (B) *Saccharomyces cerevisiae* SK1 (C. Sison, B. Miller, L. Dietrich). (C) *Escherichia coli* K-12 derivative AR3110 (S. Herbst and R. Hengge). (D) *Bacillus subtilis* NCIB3610 (J. Jo and L. Dietrich). (E) *Pseudomonas oryzihabitans*, isolated from a bench in Riverside Park, NY (S. Jordan and L. Dietrich). (F) *Pseudomonas aeruginosa* PA14 (J. Jo and L. Dietrich).

supported by the fact that *P. aeruginosa* does not encode a dedicated PCC (Tran et al. 2015). Propionyl-CoA can also be converted to succinyl-CoA, an important TCA cycle intermediate whose oxidation is linked directly to the reduction of the quinone pool (Williams, Zlosnik, and Ryall 2007). Therefore, met-val metabolism may ultimately lead to anaplerosis of succinate in the TCA cycle and the growth defect of Δ*LCC* seen on met-val may be indicative of succinate depletion, leading to a stalled TCA cycle. Interestingly, the oxidation of succinate leads to the production of fumarate, the only other nutrient source in which the Δ*LCC* showed a significant phenotype. In the case of fumarate, the mutant grows better than WT, which would be consistent with the provision of fumarate allowing the mutant to bypass its succinate deficiency and thus restoring growth to levels surpassing those of WT.

4:4: Redox state contributes to biofilm physiology in *Bacillus subtilis*

This section is adapted from:

Arnaouteli, S, Ferreira AS, Schorb, M, Morris, RJ, Bromley, KM, **Jo, J**, Cortez, KL, Sukhodub, T, Prescott, AR, Dietrich LEP, MacPhee, CE, Stanley-Wall, NR (2017). Binfunctionality of a biofilm matrix protein controlled by redox state. *PNAS* 114, E6184-6191.

The work presented in this section resulted from a collaboration with the Stanley-Wall Lab at the University of Dundee. I generated the oxygen and redox microprofiling data (**Figure 4.15**) and contributed to the data analysis and interpretation of those results.

My thesis work has been focused on studying the mechanisms that underlie biofilm formation in *P. aeruginosa*. However, the ability to form biofilms is a quality shared by many divergent bacteria and even single-celled eukaryotes such as *Saccharomyces cerevisiae* (**Figure 4.11**; Okegbe *et al*., 2014). All these biofilms share key characteristics: they are multicellular assemblages encased within a self-produced matrix that face challenges arising from the formation of nutrient gradients. Here, I will discuss the work I did in collaboration with the Stanley-Wall Lab at the University of Dundee to further elucidate how redox state drives biofilm formation in *Bacillus subtilis*.

B. subtilis is a motile, spore-forming, Gram-positive bacterium commonly found in diverse habitats. It, like *P. aeruginosa*, is a facultative anaerobe with fermentative and denitrification capabilities and possesses a branched respiratory chain whose terminal oxidases can oxidize both the quinone pool and cytochrome *c* (García Montes de Oca et al. 2012). *B. subtilis* is capable of forming highly-structured, rugose biofilms and wrinkle formation appears to be at least partially driven by O_2 availability (Kolodkin-Gal *et al*., 2013). The matrix of these biofilms is composed of an exopolysaccharide whose components are the products of the *epsA-O* operon, protein fibers encoded by the *tapA-sipW-tasA* operon, and *bslA*, which encodes a small secreted protein (Arnaouteli et al. 2017). A distinct feature of *B. subtilis* biofilms is their hydrophobicity, which renders the biofilm impermeable to water, gases, and solvents (**Figure 4.12**; Epstein et al. 2011). As this hydrophobic nature also prevents entry of some biocides into the biofilm, it is thought that this feature affords *B. subtilis* biofilms an added layer of protection against external assault (Arnaouteli et al. 2017). Previous work has attributed the formation of

this so-called hydrophobic “raincoat” to the matrix component BslA (**B**iofilm **S**urface **L**ayer Protein A).

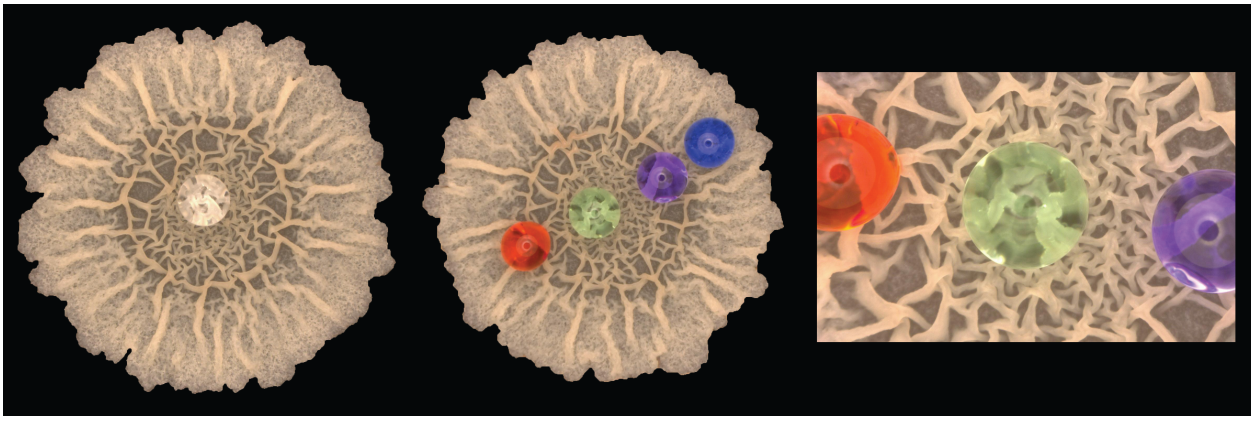

Figure 4.12. Colony biofilms of *B. subtilis* form a hydrophobic coat at the biofilm-air interface. Colored droplets of water placed onto the surface of two-day-old colony biofilms of *B. subtilis* strain NCIB3610 grown on MSgg agar.

BslA is a ~19 kDa amphipathic protein with structural features reminiscent of the immunoglobulin (Ig) superfamily (Arnaouteli et al. 2017). A key feature of BslA is the presence of a series of hydrophobic amino acids that form a “cap” (Hobley et al. 2013). When BslA is in an aqueous environment, its structure is configured in the “cap in” formation wherein the hydrophobic cap is tucked into the protein. When BslA encounters a hydrophobic interface, such as the biofilm-air interface, it will switch to the “cap out” conformation, exposing its hydrophobic residues to form the biofilm raincoat.

Previous work has shown that the Δ*bslA* deletion mutant forms featureless biofilms that do not have hydrophobic coats but instead a “wetting,” hydrophilic surface (Kobayashi and Iwano 2012). Hydrophobicity was determined by a simple assay in which a droplet of water was dispensed onto the surface of the biofilm. In WT biofilms, which possess the hydrophobic coat, the water droplet is retained in a sphere, but in Δ*bslA* biofilms, the water droplet spreads out across the surface of the biofilm. An outstanding question remains in the field as to how *B. subtilis* biofilms access nutrients if they are surrounded by a protective shield of sorts formed by BslA (Hobley et al. 2013; Arnaouteli et al. 2017). An additional feature of BslA, also found among BslA variants in other *Bacillus* species, is the presence of two conserved cysteine residues in the C-terminus, forming a “CxC” motif. Because of the importance of cysteine

residues in stabilizing protein structure, we set out to determine the contribution of the CxC motif to biofilm development.

Preliminary biochemical results indicated that recombinant BslA forms monomers, dimers, and tetramers *in vitro*. To see if oligomerization is also observed *in vivo*, we purified BslA from wild-type (3610) *B. subtilis* biofilms in the presence of Cu(II)-(*o*-phenanthroline)$_3$, which cross-links disulfide bonds. Western blotting results showed that the monomeric, dimeric, and tetrameric forms of BslA are indeed found in WT biofilms (**Figure 4.13A**). When either of the two cysteine residues of the C-terminus was mutated to an alanine ("CxA" or "AxC"), dimerization, but not tetramerization, of BslA was retained. When both cysteine residues were abolished ("AxA"), only monomeric BslA was detected. As expected, the Δ*bslA* deletion mutant showed no BslA in any form. When DTT, a reducing agent that would break disulfide bonds, was added during protein purification, only monomeric BslA was observed in all strains (**Figure 4.13B**). Together, these results indicate that dimerization and tetramerization of BslA are dependent on disulfide bonds formed between the CxC motifs of BslA.

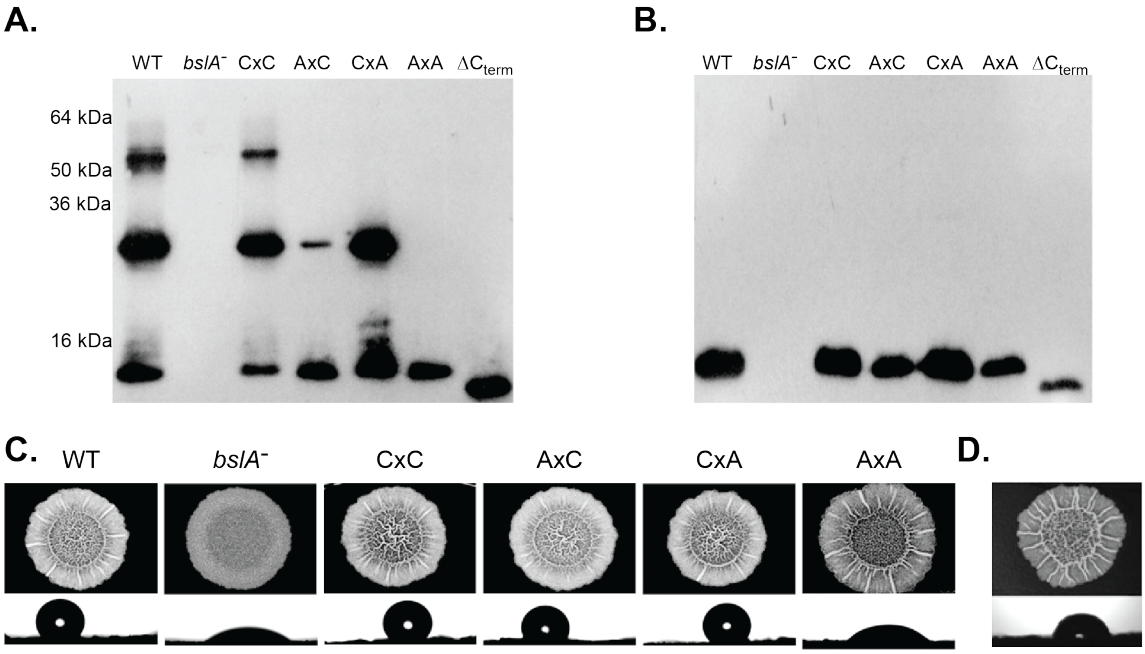

Figure 4.13. BslA is a bifunctional protein. Western blot analysis of BslA in a native **(A)** and reduced **(B)** state using proteins extracted from biofilms. **(C)** Architecture and hydrophobicity of various BslA mutant biofilms. For panels **(A)**, **(B)**, and **(C)**, strains used were WT (NCIB3610), *bslA*⁻ (NRS2097), CxC (NRS2299), AxC (NR5177, CxA (NRS5178), AxA (NRS5179), ΔC_{term} (NRS2957). **(D)** Architecture and hydrophobicity of the Δ*bdbA*Δ*bdbCD* biofilm. For all panels, under each biofilm is an image of a water droplet on the upper surface of the biofilm, illustrating surface hydrophobicity.

We next investigated the physiological contribution of disulfide bonds in *B. subtilis* biofilm development. While the AxA mutant was unable to oligomerize BslA, it was able to form architecturally complex biofilms similar to those formed by the WT (**Figure 4.13C**). However, the surface of the AxA biofilms were hydrophilic (**Figure 4.13C**), suggesting that monomeric BslA contributes to the formation of complex biofilm structures but not surface hydrophobicity. The AxC and CxA mutants, in which tetrameric BslA was not detected, formed complex biofilms whose surfaces were hydrophobic (**Figure 4.13C**), indicating that tetramerization is not required for surface hydrophobicity. These results indicated that at least dimerization is required for the production of the hydrophobic coat.

Because dimerization of BslA is likely mediated by the formation of disulfide bonds, we then explored the mechanisms of disulfide bond formation in *B. subtilis*. Disulfide bond formation, which can be spontaneous in the presence of O_2 (Bardwell 2002), is catalyzed by thiol-disulfide oxidoreductases. In *B. subtilis*, disulfide bond formation is carried out by two such enzymes, BdbA and BdbD. If these enzymes mediate disulfide bond formation, deleting them should result in structured biofilms with a hydrophilic surface. To test this, we generated a deletion mutant lacking the genes encoding both of these enzymes, Δ*bdbA*Δ*bdbCD* (*bdbD* is encoded in an operon with *bdbC*). Δ*bdbA*Δ*bdbCD* produced biofilms whose surfaces were more hydrophilic than that of WT but not to the same degree as the Δ*bslA* mutant (**Figure 4.13D**). This result suggests that there may either be (1) a redundant, yet-undiscovered mechanism of active disulfide bond formation in *B. subtilis* or (2) spontaneous, in conjunction with TDOR-mediated, disulfide bond formation occurring that contributes to BslA dimerization. This in turn would lead to the presence of the hydrophobic coat on the biofilm surface.

To test if the conditions within the biofilm are amenable to spontaneous disulfide bond formation at the surface of the biofilm, we measured O_2 concentrations throughout the depth of WT *B. subtilis* biofilms. We observed a steep O_2 gradient within the biofilm, with no detectable O_2 after ~ 50μm into the biofilm (**Figure 4.14**). The presence of O_2 at the top of the biofilm is in

agreement with the hypothesis that spontaneous disulfide bond formation could be contributing to BslA dimerization.

In *P. aeruginosa* biofilms, O_2 depletion correlates with a more reduced extracellular state in the deeper portions of the biofilm relative to the top (Jo et al. 2017). To confirm that the same is true in *B. subtilis* biofilms, we then measured extracellular redox state using a redox microelectrode and found that the upper portions of the biofilm were more oxidized relative to the bottom (**Figure 4.14**). Together with the O_2 data, which show that the bottom of the biofilm is anoxic, the redox profiling results indicate that there is a lack of electron acceptors in this region, leading to a more reduced environment.

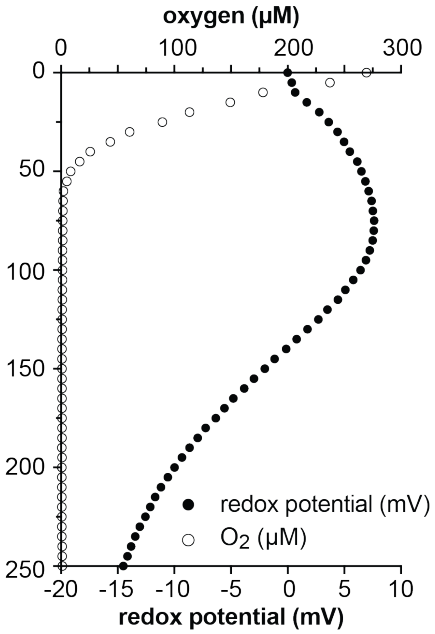

Figure 4.14. Quantification of chemical gradients formed in a *B. subtilis* biofilm. Measurement of the oxygen concentration (μM) and redox potential (mV) as a function of the depth of a three-day-old WT biofilm, with 0 mV being set at the biofilm surface.

As shown previously, a reduced environment abolishes BslA dimerization and tetramerization (**Figure 4.13B**), so it is likely that BslA exists in its monomeric form in the lower biofilm. This would mean that the bottom of the biofilm would be hydrophilic rather than hydrophobic. We tested this by flooding the agar on which a mature WT biofilm had developed with pigmented water. We saw that, rather than being pushed back by a hydrophobic layer, the dye moved outward-in under the biofilm (**Figure 4.15**). Furthermore, when a mature biofilm was turned upside-down, a hydrophilic surface was revealed. Therefore, we concluded that BslA only forms a hydrophobic coat at the biofilm-air interface while the bottom remains hydrophilic,

thus explaining how *B. subtilis* biofilms access nutrients in the presence of a hydrophobic BslA layer.

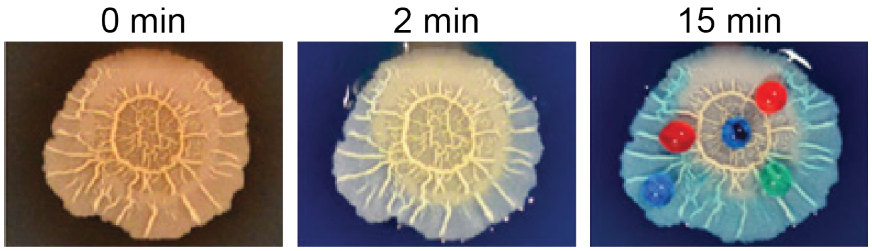

Figure 4.15. The biofilm surface at the biofilm-agar interface is hydrophilic. Time course of water uptake by a mature biofilm visualized by using pigmented water: before treatment (0 min), 2 min after exposure; and 15 min after exposure. At 15 min, 5-µL colored water droplets demonstrate retention of upper biofilm hydrophobicity.

While it is thought that hydrophobic coat formation protects *B. subtilis* biofilms from environmental stressors such as antimicrobial agents, this had not been directly tested. Because we were able to genetically separate the mechanisms of biofilm architectural complexity (sufficiently mediated by presence of monomeric BslA) and hydrophobic coat formation (via disulfide bonding and dimeric BslA), we were able to elucidate which feature is necessary for protection against external assault. To do this, we used three strains: WT, which forms structured biofilms with a hydrophobic coat, Δ*bslA*, which forms featureless, hydrophilic biofilms and the AxA mutant, which forms structured, hydrophilic biofilms. Previous studies have shown that the BslA coat prevents certain biocides from entering *B. subtilis* biofilms (Epstein et al. 2011). One of the common active ingredients in these biocides is the antiseptic chlorhexidine gluconate (CHG), which we used to test whether hydrophobicity or structural complexity (or both) was required to protect the biofilm.

We exposed biofilms to this reagent by placing a 5 µl droplet of 1% CHG onto a mature biofilm. We confirmed that the surface of WT biofilms was hydrophobic to 1% CHG and that the surface of both Δ*bslA* and AxA were hydrophilic (**Figure 4.16A**). We then measured cell survival after a five-minute exposure to 1% CHG relative to that after a five-minute saline exposure. WT biofilms saw a ~ 75% survival rate after exposure to CHG (**Figure 4.16B**). In contrast, we saw that Δ*bslA* biofilms had a nearly 0% survival rate after exposure to CHG, the equivalent of a ~ 38-fold decrease in surviving cells relative to the WT. The AxA mutant, which morphologically

resembles the WT, also had a drastic decrease in survival (~ 15%), indicating that architectural complexity, while affording limited protection, is not sufficient for WT levels of survival against CHG. Taken together, these data suggest that the hydrophobic coat formed by dimeric BslA is mainly responsible for protecting cells growing in biofilms.

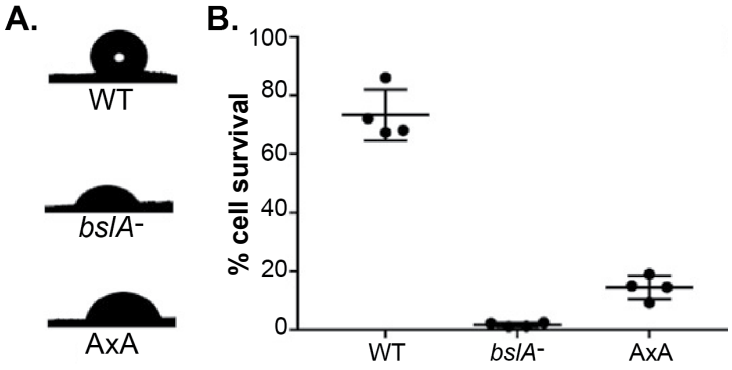

Figure 4.16. Cell survival after exposure to chlorhexidine gluconate. **(A)** An image of a 1% (vol/vol) chlorhexidine gluconate droplet on the upper surface of the biofilm for strain WT (NRS5132), *bslA*⁻ mutant (NRS5131), and the *bslA*⁻ mutant complemented with $BslA_{C178A\ C180A}$ (AxA; NRS5136). **(B)** The strains described above were exposed to 1% (vol/vol) chlorhexidine gluconate, and the percentage survival was calculated.

The results from this study expand our knowledge of how O_2 contributes to biofilm formation. As I and others from our lab have shown, O_2 plays a critical role in driving morphological and gene expression changes in *P. aeruginosa* biofilms (Dietrich et al. 2013; Okegbe, Price-Whelan, and Dietrich 2014; Jo et al. 2017). Similarly, the presence of O_2 at the top of a *B. subtilis* biofilm allows for dimerization of BslA, thus allowing for the formation of a protective hydrophobic coat at the surface of the biofilm.

Hydrophobic coat formation may also play a larger role than protecting just resident *B. subtilis* biofilm cells. In nature, *B. subtilis* often forms populated communities in the upper layers of the soil. Here, it forms mutualistic relationships with plant rhizospheres, preemptively colonizing plant roots thereby protecting plants from pathogenic bacterial colonization while taking advantage of the nutrients released by the plant roots (Arnaouteli et al. 2017). For example, *B. subtilis* colonization and biofilm formation in the roots of *Arabidopsis thaliana* have been shown to protect the plant from infection by a competing, pathogenic bacterium, *P. syringae* (Bais, Fall, and Vivanco 2004). It is possible that the hydrophobic coats of *B. subtilis* biofilms could extend their protective capabilities to offer limited protection to their host from potentially harmful compounds it may encounter.

4.5: Concluding remarks

Together, the research presented in this chapter convey the eclectic mechanisms used by bacteria to maintain redox homeostasis and an efficient metabolism regardless of external environment. The work described in sections 4.1-4.3 add further evidence of *P. aeruginosa*'s astounding metabolic versatility, which renders it a formidable pathogen in clinical settings. The more we understand about this bacterium's fundamental pathways of energy generation and survival, the better equipped we will be at eradicating infections caused by it. The research presented in section 4.4 demonstrates how bacteria can use a principle as foundational as redox state to coordinate complex, multicellular behaviors and illustrates how common this principle is in driving biofilm formation across genera.

4.6: Materials and methods

4.6.1: Methods pertaining to section 4.1

Bacterial strains and growth conditions

Unless otherwise indicated, P. aeruginosa strain UCBPP-PA14 and mutants thereof were routinely grown in lysogeny broth (LB; 1% tryptone, 1% NaCl, 0.5% yeast extract) (Bertani, 2004) at 37˚C with shaking at 250 rpm. Overnight cultures were grown for 16 ± 1 h. For genetic manipulation, strains were typically grown on LB solidified with 1.5% agar. Strains used in this study are listed in **Table 4.1**. In general, liquid precultures served as inocula for experiments. Overnight precultures for biological replicates were started from separate clonal colonies on streak plates.

Construction of mutant P. aeruginosa *strains*

For making markerless deletion mutants in *P. aeruginosa* PA14 (Table 1), 1-kb flanking sequences from each side of the target gene were amplified using the primers listed in **Table 4.2** and inserted into the allelic-replacement vector pMQ30 through gap repair cloning in *Saccharomyces cerevisiae* InvSc1 (Shanks *et al*., 2006). Each plasmid listed in Table 1 was

transformed into *Escherichia coli* strain UQ950, verified by sequencing, and moved into PA14 using biparental conjugation. PA14 single recombinants were selected on LB agar plates containing 100 µg/ml gentamicin. Double recombinants (markerless deletions) were selected on sucrose plates (1% tryptone, 0.5% yeast extract, 10% sucrose, and 1.5% agar). Genotypes of deletion mutants were verified by PCR. Combinatorial mutants were constructed by using single mutants as parent strains.

Construction of GFP reporter strains

Transcriptional reporter constructs for the genes *gacS*, *lldP*, and *lldA* were made by fusing their promoter sequences with *gfp* using primers listed in Table 2. Respective primers were used to amplify promoter regions (as indicated in Table 1) and to add an SpeI digest site to the 5' end of the promoter and an XhoI digest site to its 3' end. For the reporter, an EcoRI site was used instead of XhoI. Purified PCR products were digested and ligated into the multiple cloning site (MCS) upstream of the *gfp* sequence of pLD2722, which is a derivative of pYL122 (Lequette and Greenberg, 2005) and contains a ribosome-binding site between the MCS and *gfp*. Plasmids were transformed into *E. coli* strain UQ950, verified by sequencing, and moved into PA14 using biparental conjugation. Conjugative transfer of pLD2722 was conducted with the *E. coli* strain S17-1 (Lequette and Greenberg, 2005). PA14 single recombinants were selected on M9 minimal medium agar plates (47.8 mM Na_2HPO_4, 22 mM KH_2PO_4, 8.6 mM NaCl, 18.6 mM NH_4Cl, 1 mM $MgSO_4$, 0.1 mM $CaCl_2$, 20 mM sodium citrate dihydrate, 1.5% agar) containing 70 µg/ml gentamicin. The plasmid backbone of pLD2722 was resolved from PA14 using Flp-Flp recombination target (FRT) recombination by introduction of the pFLP2 plasmid (Hoang *et al*., 1998) and selected on M9 minimal medium agar plates containing 300 µg/ml carbenicillin and further on sucrose plates (1% tryptone, 0.5% yeast extract, 10% sucrose, 1.5% agar). The presence of *gfp* in the final clones was confirmed by PCR.

Liquid-culture growth assays

Overnight (16-h) precultures were diluted 1:100 in a clear-bottom, polystyrene black 96-well plate (VWR 82050-756), with each well containing 200 µl of medium. Cultures were then incubated at 37˚C with continuous shaking at medium speed in a BioTek Synergy 4 plate reader. Reporter strains were grown in MOPS medium (50 mM MOPS, 43 mM NaCl, 93 mM NH_4Cl, 2.2 mM KH_2PO_4, 1 mM $MgSO_4$, 1g/ml $FeSO_4$ at pH 7.0) amended with one of the following carbon sources: 20 mM D-glucose, 40 mM L-lactate, or 40 mM D-lactate (Sigma-Aldrich). Expression of GFP was assessed by taking fluorescence readings at excitation and emission wavelengths of 480 nm and 510 nm, respectively, every 30 min for up to 24 h. Growth was assessed by taking readings of optical density at 500 nm simultaneously with the fluorescence readings.

Colony growth assays

Overnight (16-h) precultures were diluted 1:10 in phosphate-buffered saline (PBS). Five microliters of diluted cultures was spotted onto MOPS medium amended with one of the following carbon sources: 20 mM D-glucose, 40 mM L-lactate, or 40 mM D-lactate (Sigma-Aldrich). The culture medium was then solidified with 1% agar (Teknova). Colonies were incubated at 25˚C for up to 4 days and imaged with an Epson Expression 11000XL scanner.

Preparation of synthetic SCFM and derivatives

Cystic fibrosis sputum medium (SCFM) was prepared as described previously (Palmer *et al*., 2007). SCFM contains the following ingredients: 2.28 mM NH_4Cl, 14.94 mM KCl, 51.85 mM NaCl, 10 mM MOPS, 1.3 mM NaH_2PO_4, 1.25 mM Na_2HPO_4, 0.348 mM KNO_3, 0.271 mM K_2SO_4, 1.754 mM $CaCl_2$, 0.606 mM $MgCl_2$, 0.0036 mM $FeSO_4$, 3mM D-glucose, 9.3 mM sodium L-lactate, 0.827 mM L-aspartate, 1.072 mM L-threonine, 1.446 mM L-serine, 1.549 mM L-glutamate•HCl, 1.661 mM L-proline, 1.203 mM glycine, 1.78 mM L-alanine, 0.16 mM L-cysteine•HCl, 1.117 mM L-valine, 0.633 mM L-methionine, 1.12 mM L-isoleucine, 1.609 mM L-

leucine, 0.802 mM L-tyrosine, 0.53 mM L-phenylalanine, 0.676 mM L-ornithine•HCl, 2.128 mM L-lysine•HCl, 0.519 mM L-histidine•HCl, 0.013 mM L-tryptophan, and 0.306 mM L-arginine•HCl. Depending on the solubility of the various salts, concentrations of their stock solutions ranged from 0.2 M to 1 M. Stock concentrations for D-glucose and sodium L-lactate were 1 M and 0.1 M for amino acids. No stock solution was prepared for L-tyrosine or L-tryptophan due to poor solubility. The pH of SCFM was adjusted to 6.5 with KOH and sterilized by filtration (Thermo Scientific Nalgene Rapid-Flow). ASMDM was prepared as previously described (Fung *et al*., 2010) by supplementing SCFM with 10 mg/ml bovine serum albumin, 10 mg/ml mucin from porcine stomach, and 1.4 mg/ml herring sperm DNA. SCFM2 was prepared by supplementing SCFM with 5 mg/ml mucin from porcine stomach, 100 µg/ml 1,2-dioleoyl-sn-glycero-3-phosphocholine (DOPC), 300 µM N-acetyl-D-glucosamine, 600 µg/ml herring sperm DNA as previously described (Turner *et al*., 2015).

4.6.2: Methods pertaining to section 4.2

Protein expression and purification

The α and β subunits for PC from several bacterial species, including *M. flagellatus*, *P. aeruginosa*, *P. fluorescens* and *Thiobacillus denitrificans* were amplified from genomic DNA (American Type Culture Collection) and sub-cloned into the pCDFduet vector (Novagen). The α subunit was sub-cloned into MCS1 with an N-terminal hexa-histidine tag, and the β subunit was sub-cloned into MCS2 with no tag. The internal B-domain deletion was made using overlapping PCR. Surface entropy reduction mutations were chosen based on the UCLA SerP server (Goldschmidt *et al*., 2007). The individual α and β subunits for MfPC were sub-cloned into pET28a with an N-terminal hexa-histidine tag. All expression constructs were co-transformed into BL21 Star (DE3) cells along with a plasmid encoding the *E. coli* biotin ligase (BirA) gene. The cells were cultured in Luria–Bertani (LB) medium with 50 mg/ml streptomycin and 35 mg/ml chloramphenicol, and were induced for 14 h with 1mM isopropyl-β-D-thiogalactoside at 20˚C. Before induction, 20 mg/L biotin and 10mM $MnCl_2$ were added to the growth medium. The

protein was purified through nickel-agarose affinity chromatography (Qiagen) followed by gel filtration chromatography (Sephacryl S-300, GE Healthcare). The purified protein was concentrated to 15 mg/ml in a buffer containing 20 mM Tris (pH 8.0), 150 mM NaCl, 5% (v/v) glycerol and 5 mM dithiothreitol, flash-frozen in liquid nitrogen and stored at -80˚C. The protein was confirmed to be fully biotinylated by a streptavidin gel-shift assay. The N-terminal hexa-histidine tag was not removed for crystallization.

Protein crystallization

Crystals were grown by the sitting-drop vapour diffusion method at 20˚C. For MfPC with B-domain deletion, the protein was incubated with 2.5 mM pyruvate for 30 min at 4 C before crystallization set-up. The reservoir solution contained 19% (w/v) PEG3350, 2% tacsimate (pH 6.0) (Hampton) and 3% (v/v) ethanol. The crystals appeared within 1 week and grew to full size after an additional week. The crystals were cryo-protected in the reservoir solution supplemented with 10% (v/v) ethylene glycol and 5% (w/v) sucrose and were flash-frozen in liquid nitrogen for data collection at 100 K. For wild-type MfPC, the protein at 15 mg/ml was incubated with 2.5 mM ATP and 2.5 mM pyruvate for 30 min at 4˚C before crystallization set-up. The reservoir solution contained 1.3 M ammonium sulfate and 0.1 M sodium citrate (pH 6.0). The crystals appeared after 1 day and grew to full size within a week. They were cryo-protected in the reservoir solution supplemented with 15% (v/v) ethylene glycol and flash-frozen in liquid nitrogen for data collection at 100 K

Data collection and structure determination

X-ray diffraction data were collected at the Advanced Photon Source beamline NE-CAT 24-ID-E using an ADSC Q315r detector and at the X25 beamline at the National Synchrotron Light Source at Brookhaven National Laboratory using a Pilatus 6M detector. The diffraction images were processed using HKL2000 (Otwinowski and Minor, 1997). Crystals of the mutant MfPC belong to space group *R*32 with unit cell parameters of $a = b = 285.8$ Å and $c = 274.9$ Å.

With an $\alpha_2\beta_4$ oligomer in the asymmetric unit, the V_m is 2.9 Å^3 Da–1 and the solvent content is 58%. The structure was solved by the molecular replacement method with the programme Phaser (McCoy *et al*., 2007), using the BC, CT and BCCP domains of the *S. aureus* PC structure (Xiang and Tong, 2008) as the search models. Manual rebuilding was carried out with Coot (Emsley and Cowtan, 2004) and refinement with the programme Refmac (Murshudov *et al*., 1997).

Crystals of wild-type MfPC belong to space group $P3_121$ with unit cell parameters of a = b = 160.8 Å and c = 227.7 Å. A molecular replacement solution for this structure was found with the programme Phaser using the individual BC and CT domains of the refined mutant MfPC structure as the search models. There is one α subunit and two β subunits in the asymmetric unit, and the full $\alpha_2\beta_4$ complex can be generated by a crystallographic two-fold axis. On the basis of this molecular replacement solution, the solvent content of the crystal is 73% and the Matthews coefficient is 4.6Å^3 Da–1. After one round of refinement, electron density was observed indicating the positions of the B domain of BC and the BT-like domain. There was also density indicating a BCCP domain in the active site of the distal CT domain, which itself adopts a conformation that is consistent with an interaction with BCCP. In addition, the MfPC molecules in the crystal do not have direct contacts without this BCCP domain, further supporting its placement in the model. After inclusion of these additional domains, we observed a decrease in the *R* values and clear density for these domains on refinement.

Construction of PC mutant and complementation strains

PC mutant and complementation strains were made for the two-gene operon encoding PC (*PA14_71720-PA14_71740*) in *P. aeruginosa* PA14 as follows. Relevant genomic sequences were amplified, with point mutations introduced where noted in **Table 4.3**, and recombined into the allelic replacement vector pMQ30 through gap repair cloning in the *Saccharomyces cerevisiae* strain InvSc1. The deletion construct contained two fused ~ 1-kb sequences representing regions upstream and downstream of the *PA14_71720-PA14_71740* operon. Point

mutant and complementation constructs contained the full operon sequence, with mutations where appropriate, plus these two flanking regions. Each plasmid was transformed into *E. coli* strain DH5α, verified by sequencing, and put into *P. aeruginosa* using biparental conjugation. PA14 single recombinants were selected on LB plates containing 100 µg/ml gentamicin. Double recombinants (with the final genotype of interest) were selected on agar plates containing 10% (w/v) sucrose, and their genotypes were confirmed by PCR. For point mutant strains, genotypes were confirmed by sequencing.

P. aeruginosa *PA14 growth conditions*

For genetic manipulation and pre-culturing, PA14 was routinely grown in LB (unless otherwise noted) at 37˚C with shaking at 250 rpm. For growth curve analyses, overnight pre-cultures of PA14 strains were diluted 100-fold in either 1% tryptone or a defined medium (50 mM MOPS (4-morpholinepropanesulfonic acid), 43 mM NaCl, 93.5 mM NH_4Cl, 2.2 mM KH_2PO_4, 1 mM $MgSO_4$ and 1 µg/ml $FeSO_4$) amended with 20 mM sodium succinate, sodium pyruvate, or glucose as the carbon source and grown to the following approximate OD_{500nm} values: 0.6 for succinate; 0.1 for pyruvate; and 0.1 for glucose. These cultures were diluted to OD_{500nm} ~ 0.01 and dispensed into 96-well plates, then incubated at 37˚C with continuous shaking on the medium setting in a Biotek Synergy 4 plate reader.

P. aeruginosa *PA14 colony morphology assay*

For the standard assay, PA14 was grown overnight in LB and diluted to OD_{500nm} = 0.5. A volume of 10 µl of these normalized cell suspensions were spotted on colony morphology assay medium (1% tryptone, 1% agar, 40 µg/m Congo red and 20 µg/ml Coomassie blue; 60 ml in each 9 cm x 9 cm square plate) and incubated in a humidified chamber at 25˚C for up to 5 days. When defined media were used for the colony morphology assay, PA14 pre-cultures were grown overnight in MOPS liquid medium with 20mM succinate. Pre-cultures were centrifuged for 1 min at 12, 396 x g and resuspended in defined medium without a carbon source to OD_{500nm} =

0.25. A volume of 10 µl of washed and resuspended cells was spotted onto solidified defined medium (25 mM HEPES (4-(2-hydroxyethyl)-1-piperazineethanesulfonic acid), 7.6 mM $(NH_4)_2SO_4$, 0.8 mM $MgSO_4 \cdot 7H_2O$, 10 mM K_2HPO_4, 20 mM of carbon source (succinate, pyruvate or glucose), 40 µg/ml Congo red, 20 µg/ml Coomassie blue and 1% agar; 60 ml in each 9 cm x 9 cm square plate) and incubated in a humidified chamber at 25˚C for up to 5 days. Images were taken with a CanoScan 5600F scanner (Canon).

P. aeruginosa *PA14 Congo red binding assay*

PA14 colonies were grown for 3 days (76 h) according to the standard colony morphology assay, with the modification that dyes were omitted from the 1% tryptone, 1% agar medium. Each colony was scraped from the agar using a 1-ml pipette tip and resuspended in 1.5 ml phosphate-buffered saline (136 mM NaCl, 2.68 mM KCl, 10.1 mM Na_2HPO_4, 1.76 mM KH_2PO_4 at pH 7.4) supplemented with 60 µg of Congo red. Each colony suspension was briefly vortexed and shaken at 250 rpm at 37˚C for 1 h to allow the matrix to bind the Congo red dye. The colony biomass was then pelleted by centrifugation at 16,873 x g for 2 min. A volume of 200 µl of supernatant was dispensed into 96-well plates and the absorbance at 490 nm, representing unbound Congo red, was measured using a Biotek Synergy 4 plate reader. Bound Congo red was calculated by subtracting the absorbance of the unbound Congo red from that of the control solution containing 60 µg Congo red per 1.5 ml PBS.

P. aeruginosa *PA14 pellicle assay*

Overnight LB pre-cultures of PA14 strains were diluted 100-fold in MOPS liquid medium amended with 20 mM sodium succinate as the carbon source and grown to OD_{500nm} ~ 0.7. A sample (4.6 ml) of each subculture was centrifuged at 10,000 x g for 1 min, and the pellet was resuspended in 23 ml of the defined medium amended with 20 mM sodium succinate, D-glucose, or sodium pyruvate in a scintillation vial, with a starting OD_{500nm} at 0.14 for pellicle

growth. Scintillation vials were incubated without shaking or disturbance at 37˚C for up to 4 days and photographed under side illumination using an iPhone 5S.

Data availability

Atomic coordinates and structure factors for the two reported structures of M. flagellatus PC have been deposited in the Protein Data Bank under the primary accession code 5KS8. The authors declare that all other relevant data supporting the findings of this study are available on request.

4.6.3: Methods pertaining to section 4.3

Protein expression and purification

Full-length LCCs from several different bacterial organisms, including *R. palustris*, *M. avium* subspecies *paratuberculosis* and *P. aeruginosa*, were amplified from genomic DNA by PCR and cloned into pET28a, pET26b and/or pET24d vectors (Novagen). The plasmids were transformed into BL21Star (DE3) cells (Invitrogen). Protein expression was induced with the addition of 1 mM isopropyl β-D-thiogalactoside, and the cells were grown at 16˚C for 16–20 h. To facilitate biotinylation, the recombinant enzyme was co-expressed with the *E. coli* biotin ligase BirA, and 15 mg/l biotin was added to the medium. An avidin shift assay of the purified enzymes showed that *R. palustris* LCC was completely biotinylated. However, purified MapLCC did not show any biotinylation, possibly indicating some degree of selectivity of the BirA enzyme. Expression of *P. aeruginosa* LCC did not produce any soluble protein and was not pursued further.

Cells were lysed by sonication in a buffer containing 20 mM Tris-HCl pH8.0, 250 mM NaCl, 5% (v/v) glycerol, 10 mM 2-mercaptoethanol, and 1 mM phenylmethylsulphonyl fluoride. Soluble enzyme was purified by Ni^{2+}-nitrilotriacetate (Qiagen), anion-exchange and gel-filtration (Sephacryl S-300; GE Healthcare) chromatography. The S-300 running buffer for MapLCC contained 25 mM HEPES pH 7.4, 250 mM NaCl and 2.5 mM dithiothreitol. The purified protein

was concentrated to 6 mg/ml, and the solution was supplemented with 5% (v/v) glycerol before being flash-frozen in liquid nitrogen and stored at -80˚C. The selenomethionyl MapLCC protein was produced in B834 (DE3) cells (Novagen) that were grown in defined LeMaster medium supplemented with selenomethionine (Hendrickson *et al*., 1990). The protein was purified with the same protocol as that for the native enzyme.

Protein crystallization

MapLCC was crystallized at 4˚C using the microbatch method under paraffin oil. The protein solution was mixed with a precipitant solution containing 0.1 M Bis-Tris propane pH 7.5–8.5 and 1.5–2.0 M ammonium sulphate. Crystals took 4–6 weeks to grow to full size, and larger crystals were obtained by microseeding. They were cryoprotected with reservoir solution supplemented with 12–15% (v/v) glycerol and flash-frozen in liquid nitrogen for data collection at 100 K. The C-terminal His tag on the protein was not removed before crystallization.

Data collection and structure determination

X-ray diffraction data for the native (wavelength 1.075 Å) and selenomethionyl (0.979 Å) crystals were collected with a Q315 charge-coupled device (Area Detector Systems Corporation) at the X29A beamline of the National Synchrotron Light Source. The diffraction images were processed with the HKL package (Otwinowski and Minor, 1997). The crystals belong to space group $P2_13$, with cell dimensions of $a = b = c = 220.9$ Å. There are two MapLCC monomers in the crystallographic asymmetric unit.

The structure of MapLCC was solved by a combination of molecular replacement and selenomethionyl SAD phasing. The orientation and position of the BC, CT and BCCP domains were located with the program Phaser (McCoy *et al*., 2007). The Se sites were located with the program SHELX (Sheldrick, 2008), and SOLVE/RESOLVE was used for phasing the reflections and automated model building (Terwilliger, 2003). The atomic model was built with the program Coot (Emsley and Cowtan, 2004). The structure refinement was performed with the program

CNS (Brunger *et al*., 1998). The crystallographic information is summarized in **Table 4.4**. We also obtained a second crystal form of MapLCC, with an entire hexamer in the asymmetric unit, and were able to collect an X-ray diffraction data set to 4.3 Å resolution (space group $P2_12_12_1$, *a* = 102Å, *b* = 292 Å, *c* = 314Å). The structure of this crystal form was readily solved by the molecular replacement method, and it revealed essentially the same holoenzyme architecture (data not shown).

Enzymatic assays

The kinetic assays monitored the hydrolysis of ATP by *R. palustris* LCC in the presence of various acyl-CoA substrates, using coupling enzymes to convert the ADP product to NADH oxidation (Blanchard *et al*., 1999). The reaction mixture contained 100 mM HEPES pH7.5, 40 mM $KHCO_3$, 1.5 mM ATP, 0.4 mM NADH, 200 mM KCl, 10 mM $MgCl_2$, 0.5 mM phosphoenolpyruvate, 3.5/3.7U of lactate dehydrogenase/pyruvate kinase (Sigma), 0.25 μM enzyme (except for MCC, which was at 1.2 μM) and various concentrations of acyl-CoA. The absorbance at 340 nm was monitored for 1.5 min. The initial velocities were fitted to the Michaelis–Menten equation using the program Origin (OriginLab).

Construction of an LCC deletion mutant in P. aeruginosa

A markerless deletion was generated for the gene *PA14_46320* in *P. aeruginosa* PA14, using previously described methods (Recinos *et al*., 2012). In brief, ~ 1-kilobase flanking regions for *PA14_46320* were amplified with primers listed in **Table 4.5** and recombined into the allelic-replacement vector pMQ30 through gap repair cloning in the yeast strain InvSc1 (Shanks *et al*., 2006). This plasmid was transformed into *E. coli* BW29427 and moved into PA14 using biparental conjugation. Luria–Bertani (LB) agar containing 100 μg/ml gentamicin was used to select for *P. aeruginosa* single recombinants. Markerless deletions in *PA14_46320* (double recombinants) were then selected with the use of LB agar plates devoid of NaCl and containing 10% (w/v) sucrose as a counterselection, and their genotypes were confirmed by PCR.

Phenotype microarrays

Phenotype microarray screening was performed by Biolog, Inc., as described (Shea *et al*., 2012).

4.6.4: Methods pertaining to section 4.4

General growth conditions and strain construction

The *B. subtilis* and *E. coli* strains used and constructed in this study are detailed in **Table 4.6**. *E. coli* strain MC1061 was used for the construction and maintenance of plasmids. *B. subtilis* 168 derivatives were obtained by transformation of competent cells with plasmids using standard protocols (Harwood and Cutting, 1990). SPP1 phage transductions were used to introduce DNA into *B. subtilis* strain NCIB3610 (Verhamme *et al*., 2007). Both *E. coli* and *B. subtilis* strains were routinely grown in Lysogeny Broth (LB) medium (10 g of NaCl, 5 g of yeast extract, and 10 g of tryptone per liter) at 37 °C for 16 h. For complex colony formation, *B. subtilis* strains were grown on MSgg medium (5 mM potassium phosphate and 100 mM MOPS at pH 7.0 supplemented with 2 mM $MgCl_2$, 700 µM $CaCl_2$, 50 µM $MnCl_2$, 50 µM $FeCl_3$, 1 µM $ZnCl_2$, 2 µM thiamine, 0.5% glycerol, and 0.5% glutamate) (Branda *et al*., 2001) solidified with 1.5% Select Agar (Invitrogen) at 30°C for 48 h (Branda *et al*., 2001) and imaged as described (Verhamme *et al*., 2007). Ectopic gene expression was induced by medium supplementation with 25 µM isopropyl β-D-1-thiogalactopyranoside (IPTG) as indicated. When appropriate, antibiotics were used at the following concentrations: ampicillin 100 µg/ml, chloramphenicol 5 µg/ml , erythromycin 1 µg/ml with lincomycin 25 µg/ml, kanamycin 25 µg/ml, and spectinomycin 100 µg/ml. Δ*bdbA*, Δ*bdbCD*, and Δ*bdbACD* mutant strains were constructed as described in **Table 4.6** by using standard methodologies.

Plasmid construction and site-directed mutagenesis

All strains, plasmids, and primers used in this study are presented in **Tables 4.6, 4.7, and 4.8** and were constructed by using standard methods. The plasmids for $BslA_{42–181}$ overproduction were obtained by site directed mutagenesis using the plasmid pNW1128 as template, which is a pGEX-6P-1 derivative used previously to overexpress $BslA_{42–181}$ (Hobley *et al*., 2013). Primers for the codon substitutions are included in Table 8, and mutagenesis was achieved following the Stratagene QuikChange kit recommendations.

Protein purification

$BslA_{41–181}$ protein and its derivatives were overexpressed and purified as described (Hobley *et al*., 2013). Briefly, the pGEX1–6P derivative plasmids were introduced into *E. coli* BL21 (DE3). After growth and overexpression, the protein was purified in HEPES buffer. To achieve this purification, the *E. coli* cells were lysed in an Emulsiflex cell disruptor, and the solubilized protein extracts, cleared of cell debris, were incubated with Glutathione Sepharose 4B (GE Healthcare), allowing the fused protein to bind to the GST binding beads. After incubation, the beads containing the BslA-fusion were recovered by using a gravity flow column (Bio-Rad) and suspended into new buffer containing DTT and TEV–His-tagged protease. TEV removed the GST tag from BslA protein, which remained soluble in the purification buffer. The protease and unbound GST were then separated from BslA by incubating the mixture with Ninitrilotriacetic acid (Ni-NTA) agarose (Qiagen) and glutathione beads, followed by a new passage in a gravity flow column. The flow-through recovered contained the purified protein, which was then concentrated by using VivaSpin concentrator. Protein quality was confirmed by size exclusion chromatography analysis.

Size exclusion chromatography (SEC

To evaluate the presence or absence of dimers in the purified proteins, 500 ng of purified protein was analyzed by SEC using a Superdex 75 10/300GL column with a low rate of 0.5 ml/

min in the original purification buffer. Protein samples were also analyzed by using 14% SDS/ PAGE, with and without the addition of a reducing agent (β-mercaptoethanol) as the loading dye and stained with Instant Blue before photography.

Oxidative cross-linking of cysteines in colony biofilms

B. subtilis 48-h grown complex colonies were collected from the agar plate by using a sterile loop and suspended in 250 µl of LB. The biomass was disrupted by passage through a 23 x 1 needle 10 times. The cell suspension obtained was incubated for 15 min at 37°C with 1.8 mM Cu(II)-(o-phenanthroline)3 (hereafter CuPhe) or 10 mM DTT, followed by centrifugation and wash of the pellet with 250 µl of PBS. After centrifugation, the pellet was suspended in 250 µl of PBS, followed by a 15 min incubation with 8 mM N-ethylmaleimide/10 mM EDTA to stop the reaction (Lee *et al*., 1995; Lee *et al*, 1994). Samples were then centrifuged, and the pellet was washed with 250 µl of PBS. The cell pellet was suspended in 250 µl of BugBuster Master Mix (Novagen), followed by gentle sonication to promote the release of the proteins from the biofilm matrix. The samples were then incubated at room temperature with agitation for 20 min, and the insoluble cell debris was removed by centrifugation at 17,000 x g for 10 min at 4°C. The proteins samples were then analyzed by Western blot.

Western blot analysis

The 1.5 µg of total protein extract (see above) was separated on a 14% SDS/PAGE before transfer onto PVDF membrane (Millipore) by electroblotting at 25 V for 2 h. The membrane was incubated for 16 h in 3% (wt/vol) powdered milk in TBS [20 mM Tris·HCl (pH 8.0) and 0.15 M NaCl] at 4°C with shaking. This step was followed by 2-h incubation with purified anti-BslA antibody at a dilution of 1:500 (vol/vol) in TBS in 3% powdered milk wash buffer (TBS + 0.05% Tween 20). The membrane was washed by using wash buffer (TBS + 0.05% Tween 20) and incubated for 45 min with the secondary antibody conjugated to

horseradish peroxidize [goat anti-rabbit (Pierce)] at a dilution of 1:5,000. The membrane was washed, developed, and exposed to X-ray film.

Oxygen profiling of biofilms

Overnight cultures of *B. subtilis* strain 3610 were inoculated from a streaked plate and subsequently grown in LB at 37°C with shaking at 250 rpm for 12–16 h. Precultures were diluted 10-fold in LB and grown at 37°C with shaking at 250 rpm until OD600nm ~ 1.0. Five microliters of the culture were spotted onto an MSgg agar plate and grown at 30 °C for 2 d before analysis. A 25-μm-tip Clark-type oxygen microsensor (Unisense OX-25) was used to measure the oxygen concentrations. The oxygen microsensor was calibrated according to manufacturer's instructions, and measurements were taken throughout the depth of the biofilm (step size = 5 μm, measurement period = 3 s, wait time between measurements = 3 s). Four different colonies were probed, and representative data are shown.

Redox profiling of biofilms

Biofilms were grown as described above, and a 25-μm-tip redox microelectrode with an external reference (Unisense RD-25 and REF-RM) was used to measure the extracellular redox potential. After calibrating the redox microelectrode according to the manufacturer's instructions, redox measurements were taken throughout the depth of the biofilm (step size = 5 μm, measurement period = 3 s, wait time between measurements = 5 s). The redox potential was set to zero at the surface of the colony, and relative values are plotted. Three different colonies were probed, and representative data are shown.

Cell survival upon chlorhexidine gluconate exposure

To test biofilm resistance to chlorhexidine gluconate, colony biofilms were grown for 48 h at 30°C. Droplets of 5 μl of 1% (vol/vol) chlorhexidine gluconate were placed on the biofilm surface (near the periphery) for 5 min at room temperature. The solution was removed, and a

punch biopsy of 5 mm in diameter was recovered (this area encompassed the entire exposed region). This sample was transferred immediately into 500 µl of saline solution, thus diluting any remaining chlorhexidine gluconate, disrupted by passage through a 23 × 1 needle 10 times and washed once with saline solution. The sample was subsequently subjected to mild sonication (20% amplitude, 1 s on, 1 s off, for 5 s total) to liberate bacterial cells from the matrix. Serial dilutions of the cell suspension were made, and 100 µl were plated onto LB agar supplemented with 100 µg/ml spectinomycin; saline solution was used as a control for the process. The percentage survival was evaluated by colony forming unit counting, and results are presented as the percentage of colony forming units obtained after exposure to 1% (vol/vol) chlorhexidine gluconate, divided by the number of colony forming units recovered on the control spots.

4.7: References

Arnaouteli, Sofia, Ana Sofia Ferreira, Marieke Schor, Ryan J. Morris, Keith M. Bromley, Jeanyoung Jo, Krista L. Cortez, et al. 2017. “Bifunctionality of a Biofilm Matrix Protein Controlled by Redox State.” *Proceedings of the National Academy of Sciences of the United States of America* 114 (30): E6184–91.

Bais, Harsh Pal, Ray Fall, and Jorge M. Vivanco. 2004. “Biocontrol of Bacillus Subtilis against Infection of Arabidopsis Roots by Pseudomonas Syringae Is Facilitated by Biofilm Formation and Surfactin Production.” *Plant Physiology* 134 (1): 307–19.

Bardwell, James C. A. 2002. “Disulfide Bond Formation, a Race between FAD and Oxygen.” *Developmental Cell* 3 (6): 758–60.

Bensel, Tobias, Martin Stotz, Marianne Borneff-Lipp, Bettina Wollschläger, Andreas Wienke, Giovanni Taccetti, Silvia Campana, et al. 2011. “Lactate in Cystic Fibrosis Sputum.” *Journal of Cystic Fibrosis: Official Journal of the European Cystic Fibrosis Society* 10 (1): 37–44.

Conway, Tyrrell, and Paul S. Cohen. 2015. *Metabolism and Bacterial Pathogenesis*. ASM Press.
Dietrich, Lars E. P., Chinweike Okegbe, Alexa Price-Whelan, Hassan Sakhtah, Ryan C. Hunter, and Dianne K. Newman. 2013. “Bacterial Community Morphogenesis Is Intimately Linked to the Intracellular Redox State.” *Journal of Bacteriology* 195 (7): 1371–80.

Dietrich, Lars E. P., Tracy K. Teal, Alexa Price-Whelan, and Dianne K. Newman. 2008. “Redox-Active Antibiotics Control Gene Expression and Community Behavior in Divergent Bacteria.” *Science* 321 (5893): 1203–6.

Epstein, Alexander K., Boaz Pokroy, Agnese Seminara, and Joanna Aizenberg. 2011. “Bacterial Biofilm Shows Persistent Resistance to Liquid Wetting and Gas Penetration.” *Proceedings of the National Academy of Sciences of the United States of America* 108 (3): 995–1000.

Fung, Carina, Sharna Naughton, Lynne Turnbull, Pholawat Tingpej, Barbara Rose, Jonathan Arthur, Honghua Hu, et al. 2010. “Gene Expression of Pseudomonas Aeruginosa in a Mucin-Containing Synthetic Growth Medium Mimicking Cystic Fibrosis Lung Sputum.” *Journal of Medical Microbiology* 59 (Pt 9): 1089–1100.

Gao, Chao, Chunhui Hu, Zhaojuan Zheng, Cuiqing Ma, Tianyi Jiang, Peipei Dou, Wen Zhang, et al. 2012. “Lactate Utilization Is Regulated by the FadR-Type Regulator LldR in Pseudomonas Aeruginosa.” *Journal of Bacteriology* 194 (10): 2687–92.

García Montes de Oca, Led Yered Jafet, Alicia Chagolla-López, Luis González de la Vara, Tecilli Cabellos-Avelar, Carlos Gómez-Lojero, and Emma Berta Gutiérrez Cirlos. 2012. “The Composition of the Bacillus Subtilis Aerobic Respiratory Chain Supercomplexes.” *Journal of Bioenergetics and Biomembranes* 44 (4): 473–86.

Hobley, Laura, Adam Ostrowski, Francesco V. Rao, Keith M. Bromley, Michael Porter, Alan R. Prescott, Cait E. MacPhee, Daan M. F. van Aalten, and Nicola R. Stanley-Wall. 2013. “BslA Is a Self-Assembling Bacterial Hydrophobin That Coats the Bacillus Subtilis Biofilm.” *Proceedings of the National Academy of Sciences of the United States of America* 110 (33): 13600–605.

Jo, Jeanyoung, Krista L. Cortez, William Cole Cornell, Alexa Price-Whelan, and Lars Ep Dietrich. 2017. “An Orphan cbb3-Type Cytochrome Oxidase Subunit Supports Pseudomonas Aeruginosa Biofilm Growth and Virulence.” *eLife* 6 (November). https://doi.org/10.7554/eLife.30205.

Kobayashi, Kazuo, and Megumi Iwano. 2012. “BslA(YuaB) Forms a Hydrophobic Layer on the Surface of Bacillus Subtilis Biofilms.” *Molecular Microbiology* 85 (1): 51–66.

Kutchma, A. J., T. T. Hoang, and H. P. Schweizer. 1999. “Characterization of a Pseudomonas Aeruginosa Fatty Acid Biosynthetic Gene Cluster: Purification of Acyl Carrier Protein (ACP) and Malonyl-Coenzyme A:ACP Transacylase (FabD).” *Journal of Bacteriology* 181 (17): 5498–5504.
Lai, Huafang, Jessica L. Kraszewski, Endang Purwantini, and Biswarup Mukhopadhyay. 2006. “Identification of Pyruvate Carboxylase Genes in Pseudomonas Aeruginosa PAO1 and Development of a P. Aeruginosa-Based Overexpression System for alpha4- and alpha4beta4-Type Pyruvate Carboxylases.” *Applied and Environmental Microbiology* 72 (12): 7785–92.

Lin, Yu-Cheng, William Cole Cornell, Jeanyoung Jo, Alexa Price-Whelan, and Lars E. P. Dietrich. 2018. “The Pseudomonas Aeruginosa Complement of Lactate Dehydrogenases Enables Use of D- and L-Lactate and Metabolic Cross-Feeding.” *mBio* 9 (5). https://doi.org/10.1128/mBio.00961-18.

Lorenz, Anne, Vinay Pawar, Susanne Häussler, and Siegfried Weiss. 2016. “Insights into Host-Pathogen Interactions from State-of-the-Art Animal Models of Respiratory Pseudomonas Aeruginosa Infections.” *FEBS Letters* 590 (21): 3941–59.

Maurino, Veronica G., and Martin K. M. Engqvist. 2015. “2-Hydroxy Acids in Plant Metabolism.” *The Arabidopsis Book / American Society of Plant Biologists* 13 (September): e0182.

Okegbe, Chinweike, Alexa Price-Whelan, and Lars E. P. Dietrich. 2014. “Redox-Driven Regulation of Microbial Community Morphogenesis.” *Current Opinion in Microbiology* 18 (April): 39–45.

Palmer, Kelli L., Lindsay M. Aye, and Marvin Whiteley. 2007. “Nutritional Cues Control Pseudomonas Aeruginosa Multicellular Behavior in Cystic Fibrosis Sputum.” *Journal of Bacteriology* 189 (22): 8079–87.

Petersen, Craig. 2005. “D-Lactic Acidosis.” *Nutrition in Clinical Practice: Official Publication of the American Society for Parenteral and Enteral Nutrition* 20 (6): 634–45.

Shoesmith, J. H., and J. C. Sherris. 1960. “Studies on the Mechanism of Arginine-Activated Motility in a Pseudomonas Strain.” *Journal of General Microbiology* 22 (February): 10–24.

Starkey, Melissa, and Laurence G. Rahme. 2009. “Modeling Pseudomonas Aeruginosa Pathogenesis in Plant Hosts.” *Nature Protocols* 4 (2): 117–24.

St Maurice, Martin, Laurie Reinhardt, Kathy H. Surinya, Paul V. Attwood, John C. Wallace, W. Wallace Cleland, and Ivan Rayment. 2007. “Domain Architecture of Pyruvate Carboxylase, a Biotin-Dependent Multifunctional Enzyme.” *Science* 317 (5841): 1076–79.

Stover, C. K., X. Q. Pham, A. L. Erwin, S. D. Mizoguchi, P. Warrener, M. J. Hickey, F. S. Brinkman, et al. 2000. “Complete Genome Sequence of Pseudomonas Aeruginosa PAO1, an Opportunistic Pathogen.” *Nature* 406 (6799): 959–64.

Tong, Liang. 2013. “Structure and Function of Biotin-Dependent Carboxylases.” *Cellular and Molecular Life Sciences: CMLS* 70 (5): 863–91.

Tran, Timothy H., Yu-Shan Hsiao, Jeanyoung Jo, Chi-Yuan Chou, Lars E. P. Dietrich, Thomas Walz, and Liang Tong. 2015. “Structure and Function of a Single-Chain, Multi-Domain Long-Chain Acyl-CoA Carboxylase.” *Nature* 518 (7537): 120–24.

Turner, Keith H., Aimee K. Wessel, Gregory C. Palmer, Justine L. Murray, and Marvin Whiteley. 2015. “Essential Genome of Pseudomonas Aeruginosa in Cystic Fibrosis Sputum.” *Proceedings of the National Academy of Sciences of the United States of America* 112 (13): 4110–15.

Vander Wauven, C., A. Piérard, M. Kley-Raymann, and D. Haas. 1984. “Pseudomonas Aeruginosa Mutants Affected in Anaerobic Growth on Arginine: Evidence for a Four-Gene Cluster Encoding the Arginine Deiminase Pathway.” *Journal of Bacteriology* 160 (3): 928–34.

Williams, Huw D., James E. A. Zlosnik, and Ben Ryall. 2007. “Oxygen, Cyanide and Energy Generation in the Cystic Fibrosis Pathogen Pseudomonas Aeruginosa.” *Advances in Microbial Physiology* 52: 1–71.

Winsor, Geoffrey L., Emma J. Griffiths, Raymond Lo, Bhavjinder K. Dhillon, Julie A. Shay, and Fiona S. L. Brinkman. 2016. “Enhanced Annotations and Features for Comparing Thousands of Pseudomonas Genomes in the Pseudomonas Genome Database.” *Nucleic Acids Research* 44 (D1): D646–53.

Xiang, Song, and Liang Tong. 2008. “Crystal Structures of Human and Staphylococcus Aureus Pyruvate Carboxylase and Molecular Insights into the Carboxyltransfer Reaction.” *Nature Structural & Molecular Biology* 15 (3): 295–302.

4.8: Tables

Table 4.1: Strains and plasmids used in section 4.1

strain/plasmid	number	description	source or reference
Pseudomonas aeruginosa strains			
UCBPP-PA14		Clinical isolate UCBPP-PA14.	Rahme et al., 1995
PA14 ΔlldDE	LD2735	PA14 with deletion in lldDE	Lin et al., 2018
PA14 ΔlldA	LD2844	PA14 with deletion in lldA	Lin et al., 2018
PA14 ΔlldDE ΔlldA	LD2759	PA14 with deletion in lldDE and lldA	Lin et al., 2018

Table 4.1 (continued): Strains and plasmids used in section 4.1

strain/plasmid	number	description	source or reference
PA14 ΔlldDE ΔlldA::lldDE	LD2904	PA14 ΔldDE ΔlldA with complementation of lldDE	Lin et al., 2018
PA14 attB::MCS-gfp	LD2820	PA14 with MCS-gfp inserted at the attB site using pLD2722	Lin et al., 2018
PA14 attB::lldPp-gfp	LD2798	PA14 with lldPp-gfp inserted at the attB site using pLD2797	Lin et al., 2018
PA14 attB::lldAp-gfp	LD2868	PA14 with lldAp-gfp inserted at the attB site using pLD2867	Lin et al., 2018
Escherichia coli strains			
UQ950	LD44	E. coli DH5 λpir strain for cloning. F-Δ(argF-lac)169ϕ80 dlacZ58(ΔM15) glnV44(AS) rfbD1 gyrA96(NalR) recA1 endA1 spoT thi-1 hsdR17 deoR λpir+	D. Lies, Caltech
BW29427	LD661	Donor strain for conjugation. thrB1004 pro thi rpsL hsdS lacZ ΔM15RP4-1360 Δ(araBAD)567 ΔdapA1314::[erm pir(wt)]	W. Metcalfe, University of Illinois
S17-1	LD2901	StrR , TpR , F– RP4-2-Tc::Mu aphA::Tn7 recA λpir lysogen	Teng et al., 1998
Saccharomyces cerevisiae strains			
InvSc1	LD622	MATa/MATalpha leu2/leu2 trp1-289/trp1-289 ura3-52/ura3-52 his3-Δ1/his3-Δ1	Invitrogen
Plasmids			
pMQ30	LD621	Yeast-based allelic-exchange vector; sacB+ , CEN/ARSH, URA3+ , GmR	

Table 4.1 (continued): Strains and plasmids used in section 4.1

strain/plasmid	number	description	source or reference
pLD2734 (pMQ30-ΔlldDE)		ΔlldDE flanking fragments introduced into pMQ30 by gap repair cloning in yeast strain InvSc1	Lin et al., 2018
pLD2758 (pMQ30-ΔlldA)		ΔlldA flanking fragments introduced into pMQ30 by gap repair cloning in yeast strain InvSc1	Lin et al., 2018
pLD2903 (pMQ30-lldDE-comp)		lldDE complementation flanking fragments introduced into pMQ30 by gap repair cloning in yeast strain InvSc1	Lin et al., 2018
pYL122		AmpR rhlA-gfp transcription fusion in mini-CTXlacZ	Lequette and Greenberg, 2005
pUC18-mini-Tn7		AmpR ColE1 replicon mini-Tn7 base vector	Choi et al., 2005
pLD844 (pSEK101)		rhlA promoter of pYL122 was removed (XhoI and EcoRI) and replaced with a multiple cloning site (MCS) from pUC18-mini-Tn7	Lin et al., 2018b
pLD2722 (pSEK103)		aacC1 (gentamicin resistance cassette) from pMQ30 was inserted at the BspDI site of pLD844	Lin et al., 2018b
pLD2797 (pSEK103-lldPp)		324 bp of lldP promoter sequence inserted at the MCS (SpeI and XhoI) of pLD2722	Lin et al., 2018
pLD2867 (pSEK103-lldAp)		356 bp of lldA promoter sequence inserted at the MCS (SpeI and XhoI) of pLD2722	Lin et al., 2018
pFLP2		Site-specific excision vector with cI857-controlled FLP recombinase; sacB+, AmpR	Hoang et al., 1998

Table 4.2: Primers used in section 4.1

primer number	name	sequence	description
1087	attB::gfp-inCheck1	AGGGCCAATCGATAGAGTTT	To verify the genotype of gfp reporter strains
1088	attB::gfp-inCheck2	TCTTCGTGATCTGAAGCCATT	To verify the genotype of gfp reporter strains
1089	attB::gfp-outCheck1	TAGAAGAACAGGCGGACGAT	To verify the genotype of gfp reporter strains
1090	attB::gfp-outCheck2	AGCATCATCGGTACCCAGTC	To verify the genotype of gfp reporter strains
2088	ΔlldDE-yeast1	ggaattgtgagcggataacaatttcacacaggaaacagct CCTACAGCTTCGGCGAGAT	To make pLD2734 (pMQ30-ΔlldDE) by gap repair cloning in yeast strain InvSc1

Table 4.2 (continued): Primers used in section 4.1

primer number	name	sequence	description
2089	ΔlldDE-yeast2	caccaggtagaccacccc GTAGTCGGTGGAAGCGGAAAT	To make pLD2734 (pMQ30-ΔlldDE) by gap repair cloning in yeast strain InvSc1
2090	ΔlldDE-yeast3	atttccgcttccaccgactac GGGGTGGTCTACCTGGTG	To make pLD2734 (pMQ30-ΔlldDE) by gap repair cloning in yeast strain InvSc1
2091	ΔlldDE-yeast4	aggcaaattctgttttatcagaccgcttctgcgttct gat TCCGGCGGATAGAAATAGAA	To make pLD2734 (pMQ30-ΔlldDE) by gap repair cloning in yeast strain InvSc1
2092	ΔlldDE-check1	ACCCTGTTCCTCAAGGTCTG	To verify the genotype of ΔlldDE strains
2093	ΔlldDE-check2	GTCGTGACGTAGGGCGAATA	To verify the genotype of ΔlldDE strains
2094	ΔlldDE-check3	GCATGCTGGTGCACTGAC	To verify the genotype of ΔlldDE strains
2095	ΔlldDE-check4	CAGGCGGTAGACGTACTGGT	To verify the genotype of ΔlldDE strains
2100	ΔlldA-yeast1	ggaattgtgagcggataacaatttcacacagga aacagct ATTTCCGTTTTCCTTCCATC	To make pLD2758 (pMQ30-ΔlldA) by gap repair cloning in yeast strain InvSc1
2101	ΔlldA-yeast2	tatcgcgggtagcttcccgg GTCTTCGATATCGGTGATGACG	To make pLD2758 (pMQ30-ΔlldA) by gap repair cloning in yeast strain InvSc1
2102	ΔlldA-yeast3	cgtcatcaccgatatcgaagac CCGGGAAGCTACCCGCGATA	To make pLD2758 (pMQ30-ΔlldA) by gap repair cloning in yeast strain InvSc1
2103	ΔlldA-yeast4	aggcaaattctgttttatcagaccgcttctgcgttct gat TAACCTGGCAGAACTGAACG	To make pLD2758 (pMQ30-ΔlldA) by gap repair cloning in yeast strain InvSc1
2104	ΔlldA-check1	GACGCGGTATCCCTGATCT	To verify the genotype of ΔlldA strains
2105	ΔlldA-check2	ACCTGCTGGAAAGCTTCGAC	To verify the genotype of ΔlldA strains
2106	ΔlldA-check3	GACTGAAACGGCGGAATTT	To verify the genotype of ΔlldA strains

Table 4.2 (continued): Primers used in section 4.1

primer number	name	sequence	description
2107	ΔlldA-check4	CTCATCGGACTGAAGGGAGA	To verify the genotype of ΔlldA strains
2146	PlldP-F	acgtacgtacactagtCGACACCCTTACCCGAAGT	To make pLD2797 (pSEK103-lldPp) by restriction-ligation
2147	PlldP-R	acgtacgtacctcgaGGGTTGGCTCCCTAATTGTT	To make pLD2797 (pSEK103-lldPp) by restriction-ligation
2203	PlldA-F	acgtacgtacactagtTGCTCGATTTGGGCATGA	To make pLD2867 (pSEK103-lldAp) by restriction-ligation
2204	plldA-R	acgtacgtacctcgagGCAGTCCACTCCTTCGGG	To make pLD2867 (pSEK103-lldAp) by restriction-ligation
2213	lldDE-comp-yeast1	ggaattgtgagcggataacaatttcacacaggaaacagctCCTACAGCTTCGGCGAGAT	To make pLD2903 (pMQ30-lldDE-comp) by gap repair cloning in yeast strain InvSc1
2214	lldDE-comp-yeast2	ACGGTCTCGAGAAAGGGAAT	To make pLD2903 (pMQ30-lldDE-comp) by gap repair cloning in yeast strain InvSc2
2215	lldDE-comp-yeast3	CGCCAGAAAAGCCTGAAA	To make pLD2903 (pMQ30-lldDE-comp) by gap repair cloning in yeast strain InvSc3
2216	lldDE-comp-yeast4	CGGCCTTTTCCAGCAGAC	To make pLD2903 (pMQ30-lldDE-comp) by gap repair cloning in yeast strain InvSc4
2217	lldDE-comp-yeast5	GGCCACGGGTGGTCTATC	To make pLD2903 (pMQ30-lldDE-comp) by gap repair cloning in yeast strain InvSc5
2218	lldDE-comp-yeast6	aggcaaattctgttttatcagaccgcttctgcgttctgatTCCGGCGGATAGAA ATAGAA	To make pLD2903 (pMQ30-lldDE-comp) by gap repair cloning in yeast strain InvSc6

Table 4.3: Primers used in section 4.2

primer name	sequence	description
ΔPA14_71720-71740 1F	ccaggcaaattctgttttatcagaccgcttctgcgttctgatGATGATGCCCTTGAACTGCT	To make the in-frame markerless deletion of PA14_71720-PA14_71740
ΔPA14_71720-71740 1R	gtctactccgaggccgatcAGGCGATGAAGATGGAAACC	To make the in-frame markerless deletion of PA14_71720-PA14_71740
ΔPA14_71720-71740 2F	ggtttccatcttcatcgcctGATCGGCCTCGGAGTAGAC	To make the in-frame markerless deletion of PA14_71720-PA14_71740
ΔPA14_71720-71740 2R	ggaattgtgagcggataacaatttcacacaggaaacagctCAATTCCTCCACCGGTAGTT	To make the in-frame markerless deletion of PA14_71720-PA14_71740
PA14_71720-71740c 1F	ccaggcaaattctgttttatcagaccgcttctgcgttctgatGATGATGCCCTTGAACTGCT	To make the PA14_71720-PA14_71740 complementation strain
PA14_71720-71740c 1R	cggcgagcgctacaagaccaTCACCAACGAAGTGAAGCTG	To make the PA14_71720-PA14_71740 complementation strain
PA14_71720-71740c 2F	cagcttcacttcgttggtgaTGGTCTTGTAGCGCTCGCCG	To make the PA14_71720-PA14_71740 complementation strain
PA14_71720-71740c 2R	tggagttcctgctcgccgacGGCGAGGTGTACTTCATGG	To make the PA14_71720-PA14_71740 complementation strain
PA14_71720-71740c 3F	ccatgaagtacacctcgccGTCGGCGAGCAGGAACTCCA	To make the PA14_71720-PA14_71740 complementation strain
PA14_71720-71740c 3R	ggaattgtgagcggataacaatttcacacaggaaacagctCAATTCCTCCACCGGTAGTT	To make the PA14_71720-PA14_71740 complementation strain
PA14_71740-K451* 1F	ccaggcaaattctgttttatcagaccgcttctgcgttctgatGACGAAGCCCACAGCATC	To make the K451stop point mutation in PA14_71740 (α subunit)
PA14_71740-K451* 1R	gccaggtgcgacgggttgcgttaGATCGAGTACTGGGTCAGTT	To make the K451stop point mutation in PA14_71740 (α subunit)
PA14_71740-K451* 2F	aactgacccagtactcgatctaaCGCAACCCGTCGCACCTGGC	To make the K451stop point mutation in PA14_71740 (α subunit)
PA14_71740-K451* 2R	ggaattgtgagcggataacaatttcacacaggaaacagctCCAGGCCATGCTGGAGAT	To make the K451stop point mutation in PA14_71740 (α subunit)

Table 4.3 (continued): Primers used in section 4.2

primer name	sequence	description
PA14_71720-A55T 1F	ccaggcaaattctgttttatcagaccgcttctgcgttctgatCTCGAGAAGTGCATCGTCAA	To make the A55T point mutation in PA14_71720 (β subunit)
PA14_71720-A55T 1R	cgcacgcaggcgtcgaaggtagtGCCGCCCCAGACTTCCAGCG	To make the A55T point mutation in PA14_71720 (β subunit)
PA14_71720-A55T 2F	cgctggaagtctggggcggcactACCTTCGACGCCTGCGTGCG	To make the A55T point mutation in PA14_71720 (β subunit)
PA14_71720-A55T 2R	ggaattgtgagcggataacaatttcacacaggaaacagctCGCACGTCGATGACTTCCT	To make the A55T point mutation in PA14_71720 (β subunit)
PA14_71720-K572A 1F	ccaggcaaattctgttttatcagaccgcttctgcgttctgatCTGAAGGCCGTGGAAAAC	To make the K572A point mutation in PA14_71720 (β subunit)
PA14_71720-K572A 1R	gcctggacctcggtttccatggcCATCGCCTCGGTGATCAACA	To make the K572A point mutation in PA14_71720 (β subunit)
PA14_71720-K572A 2F	tgttgatcaccgaggcgatggccATGGAAACCGAGGTCCAGGC	To make the K572A point mutation in PA14_71720 (β subunit)
PA14_71720-K572A 2R	ggaattgtgagcggataacaatttcacacaggaaacagctATGATGCCCTTGAACTGCTC	To make the K572A point mutation in PA14_71720 (β subunit)

Table 4.4: Crystallographic information and refinement statistics for section 4.3

	MapLCC
Data collection	
Space group	P213
Cell dimensions	
a, b, c (Å)	220.9, 220.9, 220.9
α, β, γ (˚)	90, 90, 90
Resolution (Å)	50-3.0 (3.1-3.0)*
Rmerge	9.6 (44.6)
I/σI	10.3 (1.9)
Completeness (%)	91 (72)
Redundancy	3.3 (2.1)
Refinement	
Resolution (Å)	50-3.0
No. reflections	64,953
Rwork/Rfree	20.9/26.2
No. atoms	
Protein	14632
Ligand/ion	0
Water	0
B-factors	
Protein	66.4
Ligand/ion	–
Water	–
R.m.s. deviations	
Bond lengths (Å)	0.007
Bond angles (˚)	1.4
Two crystals were used for data collection	
* the highest-resolution shell is shown in parenthesis	

Table 4.5. Primers used in section 4.3

primer name	sequence	description
ΔPA14_46320 flank 1F	ccaggcaaattctgttttatcagaccgcttctgcgttctgat GCTGCCTGCTCTACATGCT	To make the in-frame markerless deletion of PA14_46320
ΔPA14_46320 flank 1R	ccttcaacgccttgctgat CCAGCTACCTGGAGATCGAC	To make the in-frame markerless deletion of PA14_46320
ΔPA14_46320 flank 2F	gtcgatctccaggtagctgg ATCAGCAAGGCGTTGAAGG	To make the in-frame markerless deletion of PA14_46320
ΔPA14_46320 flank 2R	ggaattgtgagcggataacaatttcacacaggaaacagct GGCGCGACCAGTAGAGATT	To make the in-frame markerless deletion of PA14_46320

Table 4.6. Strains used in section 4.4

strain	relevant genotype/description*	source/construction†
Bacillus subtilis strains		
NCIB3610	phototroph	BGSC
NRS2097	NCIB3610 bslA::cml	Verhamme et al., 2009
NRS2299	NCIB3610 bslA:: cml amyE::Phy-spank-bslA-lacI (spc)	Verhamme et al., 2009
NRS5177	NCIB3610 bslA:: cml amyE::Phy-spank-bslAC178A-lacI (spc)	SPP1 NRS5165 → NRS2097
NRS5178	NCIB3610 bslA:: cml amyE::Phy-spank-bslAC180A-lacI (spc)	SPP1 NRS5166 → NRS2097
NRS5179	NCIB3610 bslA:: cml amyE::Phy-spank-bslA C178AC180A-lacI (spc)	SPP1 NRS5167 → NRS2097
NRS2957	NCIB3610 bslA:: cml amyE::Phy-spank-bslA Δ172–181-lacI (spc)	SPP1 NRS2953 → NRS2097
NRS5553	NCIB3610 bdbCD::spc bdbA::erm	SPP1 NRS5139→ NRS5552
NRS5132	NCIB3610 bslA::cml amyE-Pspac-hy-gfpmut2 (spc) sacA::PbslA-bslA (kan)	SSP1 NRS1113→ NRS2978
NRS5136	NCIB3610 bslA::cml amyE-Pspac-hy-gfpmut2 (spc) sacA::PbslA-bslA C178A C180A (kan)	SSP1 NRS5149→ NRS5131
Escherichia coli strains		
MC1061	E. coli F'lacIQ lacZM15 Tn10 (tet)	E. coli Genetic Stock Center
BL21 (DE3)	F– ompT hsdSB(rB–, mB–) gal dcm (DE3)	Studier and Moffatt, 1986

*Drug resistance cassettes are indicated as follows: cml, chloramphenicol resistance; kan, kanamycin resistance; mls, lincomycin and erythromycin resistance; and spc, spectinomycin resistance. BSGC represents the Bacillus genetic stock center.

†The direction of strain construction is indicated with DNA or phage (SPP1) (→) recipient strain.

Table 4.7. Plasmids used in section 4.4

plasmid	description *	source†
pDR111	B. subtilis amyE integration vector for IPTG-induced expression	Britton et al., 2002
pGEX-6P-1	Vector for production of GST-fused proteins	GE Healthcare
pQE70	Cloning vector for His-tag fusions	Qiagen
pET15b-TEV	Vector for production of His tag-fused proteins	Lab sources
pSac-Kan	B. subtilis sacA integration vector	Middleton et al., 2004
pNW1500	pDR111-bslAC178A	this study
pNW1501	pDR111-bslAC180A	this study
pNW1502	pDR111-bslAC178A C180A	this study
pNW1128	pGEX-6P-1-TEV-bslA42–181	Hobley et al., 2013
pNW1503	pGEX-6P-1-TEV-bslA42–181 C178A	this study
pNW1504	pGEX-6P-1-TEV-bslA42–181 C180A	this study
pNW1505	pGEX-6P-1-TEV-bslA42–181 C178A C180A	this study
pNW1510	pGEX-6P-1-TEV-bslA42–171 (Δ172–181)	this study
pNW518	pSac-Kan-PbslA-bslA	this study (coding region amplified with primers NSW646 and NSW645 cloned into pSac-Kan)
pNW1231	pSac-Kan-PbslA-bslAC178A C180A	this study(C178A and C180A mutations introduced into pNW518 with primers NSW1124 and NSW1125)
pNW1079	pDR111- bslAss- yweA-bslA171–181	this study (coding region from pNW1075 cloned into pDR111 using HinDIII and SphI)
pNW611	pQE70-bslA signal sequence (hereafter bslAss)	Ostrowski et al., 2011
pNW1075	pQE70-bslAss-yweA-bslA171–181	This work (synthetic gene amplified with primers NSW2026 and NSW645 and cloned into pNW611)
pNW512	pDR111-bslA	Ostrowski et al., 2011
pNW621	pDR111-bslAΔ172–181-	This work (coding region amplified with primers NSW626 and NSW838)

Table 4.8. Primers used in section 4.4

primer name	sequence	description
NSW12	CGATTCAAAACCTCTTTACTG	amyE locus for assessing double crossovers
NSW13	GCTTAAGCCCGAGTC	amyE locus for assessing double crossovers
NSW1900	TCCTCCGACTCAGCCTgcaGGTTGCAACTAAGCAT	Site-directed mutagenesis (SDM) on pNW512 to convert C178 to Ala (AxC)
NSW1901	ATGCTTAGTTGCAACCtgcAGGCTGAGTCGGAGGA	SDM on pNW512 to convert C178 to Ala (AxC)
NSW1902	GACTCAGCCTTGCGGTgcaAACTAAGCATGCAAGC	SDM on pNW512 to convert C180 to Ala (CxA)
NSW1903	GCTTGCATGCTTAGTTtgcACCGCAAGGCTGAGTC	SDM on pNW512 to convert C180 to Ala (CxA)
NSW1904	TCCGACTCAGCCTgcaGGTgcaAACTAAGCATGCA	SDM on pNW512/pNW1079 to convert C178 and C180 to Ala (AxA)

Chapter 5: Conclusion

5:1: Thesis summary and implications

This thesis presents data that enhance our understanding of *Pseudomonas aeruginosa*'s impressive metabolic flexibility. Specifically, this work has explored the modularity of *P. aeruginosa*'s aerobic respiratory chain and the distinct physiological roles of its terminal oxidases, particularly as they pertain to growth in multicellular communities called biofilms. The research discussed in this thesis has also considered the effects that phenazines, redox-active secondary metabolites, have on electron flow through the *P. aeruginosa* respiratory chain and explored other pathways of energy generation/conservation in *P. aeruginosa*. Because biofilm formation and respiratory flexibility contribute to *P. aeruginosa*'s potential to colonize and persist in hosts, a more detailed understanding of these features will support efforts to treat infections caused by this bacterium.

5:2: An orphan *cbb*$_3$-type cytochrome oxidase subunit supports *Pseudomonas aeruginosa* biofilm growth and virulence

The research presented in Chapter 2 focused on one type of *P. aeruginosa*'s five terminal oxidases, the Cco's, which can contain subunits encoded by redundant genes located at distinct sites on the chromosome (Arai et al. 2014; Hirai et al. 2016; Jo et al. 2017). I identified a biofilm-specific role for the so-called "orphan" Cco terminal oxidase subunit CcoN4. Through genetic analyses, I demonstrated that CcoN4 functions redundantly with the canonical CcoN catalytic subunits CcoN1 and CcoN2 to support WT biofilm development. I showed that CcoN1 and CcoN2 function predominantly in liquid culture and during early stages of biofilm development, conditions where O_2 is abundant. In contrast, CcoN4 does not contribute to growth in liquid culture but rather supports later stages of biofilm development, when the thickness of the community leads to the formation of an anoxic zone at depth. I also demonstrated that CcoN4-containing complexes are important for mediating reduction of phenazines, whose presence is necessary for the formation and maintenance of an anoxic

zone. These results broadened the scope of terminal oxidase function to include phenazine utilization in addition to the reduction of O_2.

Because biofilm formation and survival in O_2-limited environments are important for *P. aeruginosa*'s success as a pathogen, I then asked whether CcoN4-containing heterocomplexes are involved in virulence using a nematode infection model. The results showed that CcoN4-containing complexes do indeed contribute to *P. aeruginosa* pathogenicity and uncovered a potential target for novel drugs.

5:3: Carbon source influences electron flow through the aerobic respiratory chain of *Pseudomonas aeruginosa*

Experiments described in Chapter 3 characterized *P. aeruginosa* growth on different carbon sources and examined how the presence of a subset of terminal oxidases and the production of phenazines affect electron flow through the respiratory chain. I found *P. aeruginosa* respiration and metabolism in liquid cultures to be highly adaptable to different carbon sources. In contrast, I found that carbon sources contribute differentially to biofilm development, underscoring the physiological differences between planktonic and biofilm growth.

I identified carbon sources that support reduction of a redox dye that is typically used to report respiratory activity and discovered that the presence of phenazines also had a profound effect on dye reduction during growth on specific carbon sources. I then focused my experiments on three carbon sources of particular interest (glucose, succinate, and tryptone) and found that biofilm morphology, matrix production, terminal oxidase expression, phenazine production, and phenazine utilization were all affected by carbon source identity. My results show that the earliest steps in catabolism (i.e., initial oxidations or transformations of the electron donor) influence the latest steps (i.e., reduction of the terminal electron acceptor) an that these primary metabolic pathways do not function in the purely modular way that they are often presented in textbooks. Although we can elucidate the mechanistic details of a pathway by studying it in isolation, attempts to control bacterial growth require that we take a global view of

metabolism and the relationships between pathways that may, at first, appear to function independently.

5:4: Other pathways of energy generation in *Pseudomonas aeruginosa* and the contribution of redox state to biofilm formation in *Bacillus subtilis*

The experiments described in Chapter 4 were conducted for the collaborations in which I participated as part of my thesis work. Some of this research explored other pathways of energy generation in *P. aeruginosa* and illustrates other facets of *P. aeruginosa* metabolic flexibility. First, I considered the fate of pyruvate, an important intermediate of central metabolism that can be modified in a variety of ways. While Chapters 2 and 3 describe pathways that lead to pyruvate oxidation through aerobic respiration, Chapter 4 investigated the contribution of pyruvate fermentation and carboxylation to *P. aeruginosa* growth under specific conditions. Through my collaborations with the Tong Lab, I was able to contribute *in vivo* functional data that elucidated the physiological roles of pyruvate and acetyl-CoA carboxylases.

My work with the Stanley-Wall Lab generated data that serve as another example of how redox state drives community behavior. I contributed evidence that the conditions found within *Bacillus subtilis* biofilms are amenable to spontaneous disulfide bond formation between BslA monomers, which leads to the formation of a hydrophobic coat at the surface of the biofilm. These data show how chemical gradients influence the construction of *B. subtilis* biofilms, much as they do in those of *P. aeruginosa*, emphasizing the universality of redox-dependent mechanisms that influence biofilm structure.

5:5: Concluding remarks

In conclusion, my thesis contributes to the growing body of evidence that *Pseudomonas aeruginosa* is a metabolic powerhouse, able to adjust its physiology in response to electron acceptor availability, carbon source, respiratory chain content, and mode of growth. The results presented in my thesis remind us that planktonic and biofilm growth are distinct, with specific

respiratory enzymes contributing differentially to optimal fitness in either condition. This highlights the need for more biofilm-based research when searching for anti-microbial compounds that might combat *P. aeruginosa* (and other bacterial) growth and biofilm-based infection in clinical settings. My thesis also serves a more fundamental purpose, to illustrate how bacteria are able to withstand major deviations in growth conditions and still grow efficiently. These “lesser” organisms are capable of fastidiously tuning their metabolism and have evolved to exploit diverse resources for survival and growth.

5.6: References

Arai, Hiroyuki, Takuro Kawakami, Tatsuya Osamura, Takehiro Hirai, Yoshiaki Sakai, and Masaharu Ishii. 2014. “Enzymatic Characterization and in Vivo Function of Five Terminal Oxidases in Pseudomonas Aeruginosa.” *Journal of Bacteriology* 196 (24): 4206–15.

Hirai, Takehiro, Tatsuya Osamura, Masaharu Ishii, and Hiroyuki Arai. 2016. “Expression of Multiple cbb3 Cytochrome c Oxidase Isoforms by Combinations of Multiple Isosubunits in Pseudomonas Aeruginosa.” *Proceedings of the National Academy of Sciences of the United States of America*, October. https://doi.org/10.1073/pnas.1613308113.

Jo, Jeanyoung, Krista L. Cortez, William Cole Cornell, Alexa Price-Whelan, and Lars Ep Dietrich. 2017. “An Orphan cbb3-Type Cytochrome Oxidase Subunit Supports Pseudomonas Aeruginosa Biofilm Growth and Virulence.” *eLife* 6 (November). https://doi.org/10.7554/eLife.30205.

Appendix

An Aerobic Exercise: Defining the Roles of Pseudomonas aeruginosa Terminal Oxidases

This chapter is adapted from a commentary article I co-authored in 2014 in the Journal of Bacteriology, which was written as a companion piece to a study published in the same issue that characterized *Pseudomonas aeruginosa*'s five terminal oxidases. This chapter is referred to in section 1.3.4.

The opportunistic pathogen *Pseudomonas aeruginosa* encodes a large and diverse complement of aerobic terminal oxidases, which is thought to contribute to its ability to thrive in settings with low oxygen availability. In this issue, Arai et al. present a thorough characterization of these five complexes, enabling a more detailed understanding of aerobic respiration in this organism.

Although the Earth's atmosphere contains approximately 21% oxygen, bacteria in environments that are ostensibly aerobic still encounter zones where the concentration is much lower, due to the effects of oxygen solubility, low diffusibility, and consumption by neighboring cells. Many bacteria cope with this in part through the use of branched respiratory chains that can be modulated in response to changing conditions (Poole and Cook 2000) . Aerobic terminal oxidases, which catalyze electron transfer from the respiratory apparatus to oxygen, vary in their affinities and efficiencies (Morris and Schmidt 2013). Five such enzymes have been identified in the opportunistic pathogen *Pseudomonas aeruginosa* (**Fig. 1**), and these are thought to contribute to its ability to thrive under hypoxia (Poole and Cook 2000; Matsushita et al. 1980; Comolli and Donohue 2004; Alvarez-Ortega and Harwood 2007; Kawakami et al. 2010; Williams, Zlosnik, and Ryall 2007; Arai 2011). A diverse collection of aerobic terminal oxidases may be especially critical for an organism that has a proficiency for persisting in biofilms, which are characterized by the formation of steep oxygen gradients (Xu et al. 1998; Dietrich et al. 2013; Wessel et al. 2014). In addition to contributing to *P. aeruginosa*'s growth under microaerobic conditions, some of these complexes have been implicated in its ability to cope with various stresses (Kawakami et al. 2010; Cunningham and Williams 1995). In this issue of the Journal of Bacteriology, Arai et al. conduct a comprehensive study of these complexes, probing their biochemical properties and contributions to aerobic growth (Arai et al. 2014). They

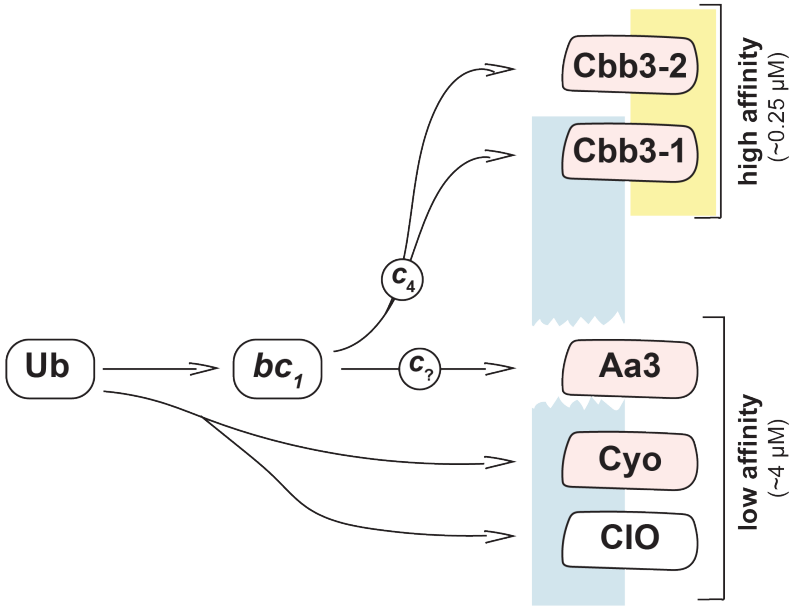

The *P. aeruginosa* membrane-bound electron transport chain can employ five different oxygen reductases. Ubiquinone (Ub) is reduced by a dehydrogenase (not shown) and acts as the electron donor for the cytochrome bc_1 complex, Cyo, or CIO. The cytochrome bc_1 complex reduces a *c*-type cytochrome, which then acts as the electron donor for Aa_3, Cbb_3-1 (or Cco1), or Cbb_3-2 (or Cco2). Heme-copper oxidases are represented by pink shapes. Oxidases that support growth better under microaerobic conditions are shaded yellow, while those that support growth better under typical conditions are shaded blue. These roles are influenced by intrinsic chemical properties and expression levels of the individual complexes. Approximate affinities for oxygen (K_m Values obtained amperometrically) are shown.

describe a systematic investigation of the attributes of each enzyme, which clarified many aspects of *P. aeruginosa*'s aerobic biology and revealed a new potential role for a particular high-affinity oxidase.

The *P. aeruginosa aerobic* terminal oxidases include enzymes that can use ubiquinol or cytochromes as electron donors, ones that have low or high affinities for O_2, and a cyanide-insensitive oxidase (CIO) that functions in the presence of this endogenously produced virulence factor (Cunningham and Williams 1995). Aside from CIO, the four other aerobic terminal oxidases encoded by the *P. aeruginosa* genome are the bo_3 oxidase (Cyo), the aa_3 oxidase (Aa_3), cbb_3 oxidase-1 (Cbb_3-1), and cbb_3 oxidase-2 (Cbb_3-2). Earlier studies predicted that Cyo and Aa_3 (which is most similar to the mitochondrial terminal oxidase) would have low affinities for oxygen and that CIO and the Cbb_3 enzymes would have high oxygen affinities (Comolli and Donohue 2004; Alvarez-Ortega and Harwood 2007; Kawakami et al. 2010; Bosma

et al. 1987; Winstedt and von Wachenfeldt 2000). In batch cultures grown under typical conditions (i.e., in nutrient-rich media and atmospheric oxygen, with vigorous shaking), the low-affinity enzymes Cyo and/or Aa_3 would thus be expected to play major roles during exponential growth, when oxygen is relatively abundant. The high-affinity enzymes Cbb_3-1 and Cbb_3-2 would be expected to function primarily in stationary phase, when oxygen is relatively scarce, and/or during growth in microaerobic conditions. Hypothetically, CIO would be particularly important in stationary phase, as it is the only terminal oxidase that functions in the presence of cyanide, which *P. aeruginosa* produces at high cell density (Williams, Zlosnik, and Ryall 2007; Cunningham and Williams 1995; Cunningham, Pitt, and Williams 1997).

Using gene expression and mutant analyses, previous studies have revised and clarified this working model of *P. aeruginosa* aerobic respiration. They have shown that the Aa_3 oxidase, which plays a major role in aerobic respiration in other bacteria ((Bosma et al. 1987; Winstedt and von Wachenfeldt 2000), is expressed primarily under nutrient-limited conditions and is otherwise a minor player under typical conditions (Kawakami et al. 2010). Rather, the Cbb_3-1, Cbb_3-2, and CIO oxidases play major roles, and their importance is exaggerated when oxygen becomes limiting and during growth in biofilms (Comolli and Donohue 2004; Alvarez-Ortega and Harwood 2007; Kawakami et al. 2010; Hamada et al. 2014). The two Cbb_3 oxidases are very similar at the amino acid level (with a similarity of 87% for the catalytic subunit in strain PAO1), but they are differentially regulated: the Cbb_3-1 complex is expressed constitutively, while the Cbb_3- 2 complex is induced by oxygen limitation (Comolli and Donohue 2004; Alvarez-Ortega and Harwood 2007). Critically, these studies also showed that oxidase gene expression can be compensatory, such that loss of one or more oxidases leads to induction of others (Kawakami et al. 2010).

To study the physiological roles of the *P. aeruginosa* aerobic terminal oxidases in isolation, Arai et al. took the important step of generating combinatorial mutants, each containing only one of these complexes, in strain PAO1. Growth experiments confirmed the unique primary physiological roles of the Cbb_3 complexes in this bacterium (Comolli and

Donohue 2004; Alvarez-Ortega and Harwood 2007; Kawakami et al. 2010). Under typical conditions, the strain containing the Cbb_3-1 oxidase grew like the wild type, while the strain containing the Cbb_3-2 oxidase showed a defect earlier in the growth experiment before "catching up" to the final wild-type density. This growth profile is consistent with the prior observation that Cbb_3-2 is induced specifically by oxygen limitation (Comolli and Donohue 2004); basal levels of expression could support initial growth before increased oxygen consumption by the denser culture brings the oxygen level down and thereby enhances expression. The growth phenotypes of the other individual single-oxidase strains also reflected what was known about regulation of the *P. aeruginosa* terminal oxidases (Comolli and Donohue 2004; Kawakami et al. 2010).

Prior work looking at expression of genes encoding putative *c*-type cytochromes had provided clues as to which of these proteins might carry electrons from the cytochrome bc_1 complex to the Cbb_3-type oxidases (Kawakami et al. 2010). Arai et al. used a genetic approach to determine that cytochrome *c*4, encoded by ORF *PA5490* in strain PAO1, is the predominant mediator functioning at this step in the electron transport pathway under typical and microaerobic conditions. This finding fills in an important gap that was remaining in our model of the *P. aeruginosa* aerobic respiratory chain.

To assess their positions in the electron transport chain and oxygen affinities, Arai et al. conducted in vitro studies with membranes prepared from strains producing each of the individual oxidases. Oxygen consumption assays confirmed the electron donor (ubiquinone or cytochrome *c*) predictions for each complex (Comolli and Donohue 2004), as well as the cyanide sensitivity of all of the oxidases but CIO. A battery of affinity assays also confirmed predictions for the relative affinities of the oxidases, with one exception: CIO, a cytochrome *bd*-type enzyme, was found to differ from the canonical *Escherichia coli* cytochrome *bd* (D'mello, Hill, and Poole 1996) in that it showed a low affinity for oxygen. The physiological consequences of the low oxygen affinity of CIO were examined by expressing the *P. aeruginosa cioAB* genes in an *E. coli* mutant lacking native terminal oxidases. The growth of this strain was compared to a

version of the same mutant expressing the *E. coli* cytochrome *bd* under the same promoter. Growth rates and yields for the two strains were similar under typical conditions, but the CIO-expressing strain showed a slower growth rate under microaerobic conditions, further supporting the conclusion that CIO functions optimally when oxygen availability is relatively high.

By generating *P. aeruginosa* mutants that each expressed only one terminal oxidase, Arai et al. were able to address outstanding questions regarding oxygen respiration and provide a more complete picture of the aerobic electron transport chain in this pathogen. A particularly intriguing feature of the *P. aeruginosa* system is that a high-affinity oxidase, Cbb_3-1, functions as the major oxygen reductase in well-aerated cultures (**Fig. 1**). The authors point out that this is a unique trait, as most other bacteria regulate high-affinity oxidases such that they are expressed specifically under low-oxygen conditions, with low-affinity enzymes similar to Aa_3 and/or Cyo acting as the major oxidase(s) under high-oxygen conditions (Bosma et al. 1987; Winstedt and von Wachenfeldt 2000; Ugidos et al. 2008). Even the closely related *Pseudomonas putida*, which also possess two Cbb_3-type enzymes, employs Cyo as its major oxidase under typical conditions (Ugidos et al. 2008). Though the measured proton translocation efficiency (protons translocated across the membrane per oxygen atom consumed) values of the Cbb_3-type oxidases were lower than that of the Aa_3 oxidase, they were higher than the efficiency value of CIO and comparable to that of the Cyo oxidase.

The critical role of Cbb_3-1 during exponential growth with relatively high oxygen availability raises the question of whether this enzyme contributes capabilities beyond oxygen reduction in typical *P. aeruginosa* cultures. The Cbb_3 oxidases differ from other heme-copper oxidases in their subunit and binuclear active site composition exhibiting structural similarities to nitric oxide reductases (NORs) (Buschmann et al. 2010; Pitcher and Watmough 2004). Cbb_3 oxidase purified from *P. stutzeri* has been shown to have NOR activity (Forte et al. 2001), and *P. aeruginosa*'s Cbb_3 oxidases have been implicated in anaerobic denitrification and NO-mediated effects on biofilm formation (Hamada et al. 2014). In diverse organisms, effects of the Cbb_3

oxidases on the expression of other metabolic genes and on biomineralization have suggested that they may be involved in sensing and responding to changes in redox homeostasis (Comolli and Donohue 2004; Oh and Kaplan 2000; Li et al. 2014) Finally, results from the current study and others suggest that modulation of the *P. aeruginosa* respiratory chain is strongly influenced by environmental stresses, and the different oxidases provide activity under distinct, specialized conditions (Kawakami et al. 2010; Williams, Zlosnik, and Ryall 2007; Cunningham, Pitt, and Williams 1997). Aa_3 is expressed during nutrient starvation, Cyo is expressed under iron starvation and in the presence of a NO-generating reagent, and CIO is induced by copper starvation and cyanide (Kawakami et al. 2010). As Arai et al. note, utilization of Cbb_3-1 during exponential growth may provide protection from reactive oxygen species or another unknown source of stress. Further investigation into the ecophysiology of *P. aeruginosa* biofilm formation and infection may uncover the significance of Cbb_3 activity for this bacterium, which utilizes oxygen preferentially and yet dominates in environments where it is in short supply.

Acknowledgement
Research done in our laboratory is supported by NIH/NIAID R01-AI103369 to L.E.P.D. We apologize to authors whose work could not be cited due to space limitations.

References

Alvarez-Ortega, Carolina, and Caroline S. Harwood. 2007. “Responses of Pseudomonas Aeruginosato Low Oxygen Indicate That Growth in the Cystic Fibrosis Lung Is by Aerobic Respiration.” *Molecular Microbiology* 65 (1): 153–65.

Arai, Hiroyuki. 2011. “Regulation and Function of Versatile Aerobic and Anaerobic Respiratory Metabolism in Pseudomonas Aeruginosa.” *Frontiers in Microbiology* 2 (May): 103.

Arai, Hiroyuki, Takuro Kawakami, Tatsuya Osamura, Takehiro Hirai, Yoshiaki Sakai, and Masaharu Ishii. 2014. “Enzymatic Characterization and in Vivo Function of Five Terminal Oxidases in Pseudomonas Aeruginosa.” *Journal of Bacteriology* 196 (24): 4206–15.

Bosma, G., M. Braster, A. H. Stouthamer, and H. W. van Verseveld. 1987. “Isolation and Characterization of Ubiquinol Oxidase Complexes from Paracoccus Denitrificans Cells Cultured under Various Limiting Growth Conditions in the Chemostat.” *European Journal of Biochemistry / FEBS* 165 (3): 657–63.

Buschmann, Sabine, Eberhard Warkentin, Hao Xie, Julian D. Langer, Ulrich Ermler, and Hartmut Michel. 2010. “The Structure of cbb3 Cytochrome Oxidase Provides Insights into Proton Pumping.” *Science* 329 (5989): 327–30.

Comolli, James C., and Timothy J. Donohue. 2004. “Differences in Two Pseudomonas Aeruginosa cbb3 Cytochrome Oxidases.” *Molecular Microbiology* 51 (4): 1193–1203.

Cunningham, L., M. Pitt, and H. D. Williams. 1997. “The cioAB Genes from Pseudomonas Aeruginosa Code for a Novel Cyanide-Insensitive Terminal Oxidase Related to the Cytochrome Bd Quinol Oxidases.” *Molecular Microbiology* 24 (3): 579–91.

Cunningham, L., and H. D. Williams. 1995. “Isolation and Characterization of Mutants Defective in the Cyanide-Insensitive Respiratory Pathway of Pseudomonas Aeruginosa.” *Journal of Bacteriology* 177 (2): 432–38.

Dietrich, Lars E. P., Chinweike Okegbe, Alexa Price-Whelan, Hassan Sakhtah, Ryan C. Hunter, and Dianne K. Newman. 2013. “Bacterial Community Morphogenesis Is Intimately Linked to the Intracellular Redox State.” *Journal of Bacteriology* 195 (7): 1371–80.

D’mello, R., S. Hill, and R. K. Poole. 1996. “The Cytochrome Bd Quinol Oxidase in Escherichia Coli Has an Extremely High Oxygen Affinity and Two Oxygen-Binding Haems: Implications for Regulation of Activity in Vivo by Oxygen Inhibition.” *Microbiology* 142 (Pt 4) (April): 755–63.

Forte, E., A. Urbani, M. Saraste, P. Sarti, M. Brunori, and A. Giuffrè. 2001. “The Cytochrome cbb3 from Pseudomonas Stutzeri Displays Nitric Oxide Reductase Activity.” *European Journal of Biochemistry / FEBS* 268 (24): 6486–91.

Hamada, Masakaze, Masanori Toyofuku, Tomoki Miyano, and Nobuhiko Nomura. 2014. “cbb3-Type Cytochrome c Oxidases, Aerobic Respiratory Enzymes, Impact the Anaerobic Life of Pseudomonas Aeruginosa PAO1.” *Journal of Bacteriology* 196 (22): 3881–89.

Kawakami, Takuro, Miho Kuroki, Masaharu Ishii, Yasuo Igarashi, and Hiroyuki Arai. 2010. “Differential Expression of Multiple Terminal Oxidases for Aerobic Respiration in Pseudomonas Aeruginosa.” *Environmental Microbiology* 12 (6): 1399–1412.

Li, Yingjie, Oliver Raschdorf, Karen T. Silva, and Dirk Schüler. 2014. “The Terminal Oxidase cbb3 Functions in Redox Control of Magnetite Biomineralization in Magnetospirillum Gryphiswaldense.” *Journal of Bacteriology* 196 (14): 2552–62.

Matsushita, K., M. Yamada, E. Shinagawa, O. Adachi, and M. Ameyama. 1980. “Membrane-Bound Respiratory Chain of Pseudomonas Aeruginosa Grown Aerobically.” *Journal of Bacteriology* 141 (1): 389–92.

Morris, Rachel L., and Thomas M. Schmidt. 2013. “Shallow Breathing: Bacterial Life at Low O(2).” *Nature Reviews. Microbiology* 11 (3): 205–12.

Oh, J. I., and S. Kaplan. 2000. “Redox Signaling: Globalization of Gene Expression.” *The EMBO Journal* 19 (16): 4237–47.

Pitcher, Robert S., and Nicholas J. Watmough. 2004. “The Bacterial Cytochrome cbb3 Oxidases.” *Biochimica et Biophysica Acta* 1655 (1-3): 388–99.

Poole, R. K., and G. M. Cook. 2000. “Redundancy of Aerobic Respiratory Chains in Bacteria? Routes, Reasons and Regulation.” *Advances in Microbial Physiology* 43: 165–224.

Ugidos, Ana, Gracia Morales, Eduardo Rial, Huw D. Williams, and Fernando Rojo. 2008. “The Coordinate Regulation of Multiple Terminal Oxidases by the Pseudomonas Putida ANR Global Regulator.” *Environmental Microbiology* 10 (7): 1690–1702.

Wessel, Aimee K., Talha A. Arshad, Mignon Fitzpatrick, Jodi L. Connell, Roger T. Bonnecaze, Jason B. Shear, and Marvin Whiteley. 2014. “Oxygen Limitation within a Bacterial Aggregate.” *mBio* 5 (2): e00992.

Williams, Huw D., James E. A. Zlosnik, and Ben Ryall. 2007. “Oxygen, Cyanide and Energy Generation in the Cystic Fibrosis Pathogen Pseudomonas Aeruginosa.” *Advances in Microbial Physiology* 52: 1–71.

Winstedt, L., and C. von Wachenfeldt. 2000. “Terminal Oxidases of Bacillus Subtilis Strain 168: One Quinol Oxidase, Cytochrome aa(3) or Cytochrome Bd, Is Required for Aerobic Growth.” *Journal of Bacteriology* 182 (23): 6557–64.

Xu, K. D., P. S. Stewart, F. Xia, C. T. Huang, and G. A. McFeters. 1998. “Spatial Physiological Heterogeneity in Pseudomonas Aeruginosa Biofilm Is Determined by Oxygen Availability.” *Applied and Environmental Microbiology* 64 (10): 4035–39.